University of Glasgow

McDowall, Daniel (2022) *A study of the complex relationship between self-assembly, activity and material properties of low molecular weight gelators.* PhD thesis.

https://theses.gla.ac.uk/83209/

Copyright and moral rights for this work are retained by the author

A copy can be downloaded for personal non-commercial research or study, without prior permission or charge

This work cannot be reproduced or quoted extensively from without first obtaining permission from the author

The content must not be changed in any way or sold commercially in any format or medium without the formal permission of the author

When referring to this work, full bibliographic details including the author, title, awarding institution and date of the thesis must be given

Enlighten: Theses
https://theses.gla.ac.uk/
research-enlighten@glasgow.ac.uk

A study of the complex relationship between self-assembly, activity and material properties of low molecular weight gelators

Daniel McDowall

Submitted in fulfilment of the requirements for the

Degree of Doctor of Philosophy

School of Chemistry

College of Science and Engineering

University of Glasgow

July 2022

Abstract

The self-assembly of small organic molecules can lead to interesting materials such as non-Newtonian fluids and gels. These have potential applications ranging from cell culturing to organic electronics. In this work, a selection of molecules that self-assemble and form low molecular weight gels are studied. In a high throughput photocatalysis experiment, five amino acid functionalised perylene bisimides under a range of variables were tested for the photocatalytic hydrogen evolution reaction from water. The results showed that the formation of 1D nanofibres with a specific molecular packing and surface charge produced optimum rates of H_2. Two gelator molecules that formed 1D nanofibres but possessed a different molecular packing were inactive, highlighting the importance and sensitivity of the self-assembly process for any potential application.

As well as manipulating the self-assembled structures that form, the ordering of those nanostructures can be controlled through the formation of so called ‘gel noodles’. The influence that nanostructure alignment would have on photocatalysis was of interest but PBIs did not readily form gel noodles. Using a model system of a functionalised dipeptide (1ThNapFF), it was determined that pre-gel solutions containing 1D nanofibres that result in viscous shear-thinning fluids were required to form gel noodles. Highly aligned gel noodles with a uniform size distribution could be prepared by using a spinning technique to subject the pre-gel solution to a stretching and narrowing of diameter (extensional deformation).

In the literature, an isoleucine-functionalised PBI (PBI-I) was reported to form highly viscous pre-gel solutions. These solutions were tested. Aligned gel noodles were prepared without the need for the spinning technique. The subtle change in molecular structure resulted in vastly different shear viscosities, facilitating the formation of the gel noodles. Un-aligned gel noodles could be prepared through delayed gelation. However, no definitive conclusion as to whether or not alignment improved hydrogen evolution could not be drawn.

A third, more aligned sample, was of interest for the photocatalysis but attempts using the spinning technique on the PBI-I solutions were unsuccessful. The PBI-I pre-gel solution did not stretch during spinning. Instead resulted in numerous broken-up small lengths of unaligned gel noodle. It was hypothesised that this was due to the PBI-I solution possessing a low extensional viscosity relative to 1ThNapFF. A literature technique (called ‘dripping-onto-substrate’) to measure extensional relaxation time was setup, validated and used to show that the 1ThNapFF solutions behave as elastic fluids with long extensional relaxation times. whereas the PBI-I solutions did not. While both solutions self-assembled to form wormlike micelles with a similar shear viscosity, they still possessed fundamental differences in fluid properties, highlighting the complexity of studying and manipulating

these systems. It is evident that there is no ‘catch all’ approach to analysing them, and a range of techniques are required.

Table of Contents

Chapter 1 13

1 Preface 14

2 Introduction to low molecular weight gels 14

2.1 Self-assembly 16

2.1.1 Fundamentals of self-assembly mechanism 16

2.1.2 Self-assembly in pre-gel solutions 17

2.2 Gelation 20

2.2.1 Gelation triggers 20

3 Chemical structure of LMWGs 23

3.1 Peptides 24

3.1.1 Functionalised peptides 25

3.1.2 π-gelators 26

4 Applications of LMWGs 28

4.1 Organic electronics 28

4.2 Photochemical reactions 30

4.3 Photocatalytic water splitting reactions 30

5 Conclusions 33

6 This thesis 34

7 References 35

Chapter 2 43

Acknowledgements 44

1 Introduction 46

1.1 Organic Photocatalysis 46

1.2 Perylene bisimides 47

1.3 Introduction to the work in this Chapter 51

2 Results 52

2.1 High throughput photocatalysis 52

2.2 Self-assembled structure 56

2.2.1 PBI-A 57

2.2.2 PBI-V 60
2.2.3 PBI-F 63
2.2.4 PBI-Y 66
2.2.5 PBI-H 68
2.2.6 Summary 71
2.3 Molecular packing 71
2.4 Nanofibre surface charge 73
3 Experimental 77
3.1 Synthesis 77
3.1.1 Amino acid functionalised perylene bisimides 77
3.1.2 Polyvinylpyrrolidone capped platinum nanoparticles 78
3.2 Characterisation and methods 81
3.2.1 pH measurements 81
3.2.2 PBI solution preparation 81
3.2.3 Small angle X-ray scattering 81
3.2.4 Dynamic light scattering 82
3.2.5 Inductively coupled plasma-optical emission spectrometry 82
3.2.6 Nuclear magnetic resonance (NMR) experiments 82
3.2.7 Electrochemistry 83
3.2.8 UV-Vis Absorption Spectroscopy 83
3.2.9 High throughput photocatalysis studies 83
4 References 85
Chapter 3 89
1 Literature review 92
1.1 Introduction 92
1.2 Aims 107
2 Results and discussion 109
2.1 1ThNapFF solution characterisation 109
2.1.1 Shear viscosity measurements 109
2.1.2 Small angle X-ray scattering 110

2.2 Formation and control of gel noodles 115
2.2.1 Noodle analysis 115
2.2.2 Preliminary noodle formation using pipettes 115
2.2.3 Syringe pump – static formed noodles 121
2.2.4 Syringe pump - spun noodles 126
2.2.5 Concentric flow 129
2.3 Nanoindentation 134
3 Conclusions 138
4 Experimental 140
4.1 Materials 140
4.1.1 PBI-L synthesis 140
4.2 Solution preparation 140
4.3 Bulk gel preparation 141
4.4 Viscosity measurements 142
4.5 Pipette filament formation 142
4.5.1 Pipettes used 142
4.5.2 Static filament formation 143
4.5.3 Dragging pipette 144
4.6 Syringe pump filament formation 144
4.6.1 Syringe pump 144
4.6.2 Static filament formation 144
4.6.3 Spinning aligned filaments 145
4.6.4 Concentric flow setup 146
4.7 Optical microscopy 148
4.8 ImageJ analysis 149
4.9 Nanoindentation 150
4.10 Small angle X-ray scattering 150
4.10.1 Fitting data 151
5 References 153
Chapter 4 157

1 Introduction 160
1.1 The importance of extensional deformations 162
1.1.1 Polymers 162
1.1.2 Silks 163
1.1.3 Hydrogel filaments 165
1.1.4 Other nanomaterials 165
1.2 Measuring fluids under extensional deformation 167
1.3 Dripping-onto-substrate 168
1.3.1 Worm-like micelles 171
2 Results and discussion 174
2.1 Perylene bisimide gel noodles 174
2.1.1 PBI gel noodles 175
2.1.2 PBI-I photocatalysis 178
2.2 Dripping-onto-substrate 181
2.2.1 DoS: setup 181
2.2.2 DoS: Validation 183
2.2.3 DoS: 1ThNapFF 186
2.2.4 DoS: PBI-I 188
2.2.5 DoS: 2NapFF 190
3 Conclusions 194
4 Experimental 195
4.1 Sample preparation 195
4.1.1 Solution preparation 195
4.2 Photocatalysis experiments 196
4.2.1 Photocatalysis sample preparation 196
4.2.2 Lamp setup 197
4.2.3 Gas chromatography 197
4.3 Rotational rheometer measurements 197
4.4 Optical microscopy 197
4.5 Portable CPOM setup 197

4.6 Dripping-onto-substrate 198
4.6.1 Setup 198
4.6.2 Measurement 198
4.6.3 Data processing 199
4.6.4 Data analysis 200
5 References 201
Chapter 5 205
1 Conclusions 206

List of abbreviations

List of abbreviations for commonly used terms within the thesis.

aQDM	Amphiphilic naphtho-*p*-quinodimethane
AFM	Atomic force microscopy
CaBER	Capillary break-up extensional rheometer
CNT	Carbon nanotube
CPCl/NaSal	Cetylpyridinium chloride/sodium salicylate
CMP	Conjugated microporous polymers
COF	Covalent organic frameworks
CPOM	Cross polarised optical microscopy
DMSO	Dimethyl sulfoxide
FF	Diphenylalanine
D-A	Donor-acceptor
DoS	Dripping-onto-substrate
EC	Elasto-capillary
FiSER^™	Filament stretching extensional rheometerTM
GdL	Glucono-delta-lactone
g-C3N4	Graphitic carbon nitride
GI-SAXS	Grazing incidence small angle X-ray scattering
HSP	Hansen solubility parameter
HOMO	Highest occupied molecular orbital
HER	Hydrogen evolving reaction
ITO	Indium doped tin oxide
ICP-OES	Inductively coupled plasma-optical emission spectrometry
IC	Inertia-capillary
EDH	L-histidine terminated bolaamphiphile
LED	Light emitting diode
LMWG	Low molecular weight gel
LUMO	Lowest unoccupied molecular orbital
MIF	Materials innovation factory
MeOH	Methanol
MNC	Minimum noodling concentration
NMR	Nuclear magnetic resonance
OTAB/NaOA	Octyl trimethylammonium bromide/sodium oleate
1D	One dimensional
OFET	Organic field effect transistor
OSC	Organic solar cell
OER	Oxygen evolving reaction
PBI	Perylene bisimide
PMI	Perylene monoimide
PEO	poly(ethylene oxide)
PAM	Polyacrylamide
PA6	Polyamide-6
PEG	Polyethylene glycol
PET	Polyethylene terephthalate
Pdots	Polymer dots
PVP	Polyvinylpyrrolidone

RQC	Residual quadrupolar coupling
SEM	Scanning electron microscopy
SANS	Small angle neutron scattering
SAXS	Small angle X-ray scattering
SWV	Square wave voltammetry
TBA	Tetrabutylammonium hydroxide
TCE	Tetrachloro ethane
TEM	Transmission electron microscopy
TEA	Triethanolamine
TTA-UC	Triplet-triplet annihilation up-conversion
UV-Vis	Ultraviolet-visible
WAXS	Wide angle X-ray scattering
WLM	Wormlike micelle

Acknowledgements

I would like to thank the Leverhulme Trust (grant number 75014) for funding the joint PhD studentship between myself and my collaborator Ben Greeves. I'd also like to thank the University of Glasgow and all the staff in the department who helped with various experiments.

It was a privilege working with many great scientists throughout my PhD. I would like to thank all the current and past members of the Adams and Draper research groups for all the fun times throughout my PhD. The lab has always been a great environment to work in and I am sad to be leaving. Especially now there is so much more space! I'd particularly like to thank Lisa, Becky and Jakki for all the adventures and fun times.

I would like to thank Ben Greeves and Professor Alex Cowan for hosting me at the University of Liverpool on many occasions. The visits were always productive and it was great to come to Liverpool. Ben and I were always able to work well together, bounce ideas off each other and in the evenings watch the odd Champions League game on TV.

Much of my research was made possible with the power of small angle scattering experiments! I thank all the beamline scientists at Diamond Light Source and ISIS Neutron and Muon source who helped me with measurements and analysis. To add to that I'd like to thank Dr Annela Seddon and her GANESHA instrument at the University of Bristol for the X-ray scattering experiments and advice.

I'd like to thank all my family and friends for their support during my PhD. Many of them made the long trip from home to visit and we had many great times together. I'd like to thank my parents for all their support and encouragement through the years. Finally I'd like to thank my wife, Beth, for being a rock in my life and for sharing in many adventures in Scotland with me.

Declaration

All work in this thesis was carried out by the author unless otherwise explicitly stated and described in the acknowledgements at the start of each chapter. Chapter 1 was prepared by the author alone.

Chapter 1

Introduction

1 Preface

In the past century, there have been enormous advances in soft materials towards various applications such as organic electronics, cell cultivation and medicine.[1–3] One particular research area is that of low molecular weight gels (LMWGs), in which there is enormous scope for research. LMWGs have attracted a large amount of interest with applications from medicine to nanoelectronics.[4–6] Low molecular weight gels are formed by the self-assembly of small molecules into larger, typically one dimensional (1D), structures that entangle and crosslink to result in gelation. Self-assembly is ubiquitous both in nature and in modern materials, offering remarkable properties. For example, self-assembly underpins the formation of the phospholipid bilayer in cells of almost all living organisms. It is therefore unsurprising that the self-assembly of small organic molecules presents a rich field for materials research.

2 Introduction to low molecular weight gels

LMWGs are small compounds that can self-assemble via non-covalent interactions to form supramolecular structures that result in gelation.[7,8] The process relies on the build-up of the molecular units into nanostructures (commonly 1D structures, such as nanofibers). Gelation then occurs when the cross-linking and entanglement of supramolecular structures form a network that entraps solvent and imparts solid-like characteristics (Figure 1). Importantly, for some systems, the pre-gel solution also contains self-assembled nanostructures. LMWGs and the materials from which they are made are of interest for potential applications including photocatalysis[9,10], organic electronics[11], cell culturing[12], water purification[13] and thread-like materials.[14]

Self-assembly and gelation is a highly sensitive process, where numerous variables (such as concentration, temperature, ionic strength etc) can determine whether or not gelation will occur as well as modulating the properties of a gel.[15] While this can present a challenge to researchers, it also presents an opportunity, where changes to seemingly minor variables can be used to form materials with vastly different properties.[16,17] This often means that instead of using the materials, time and money to synthesise a new molecule, simple and easily implemented changes can have the same desired effect. Materials can be designed to form gels in organic solvents (forming organogels) or in water (forming hydrogels). Gelation can be triggered by various means such as pH, a solvent switch or use of metal salts among others.

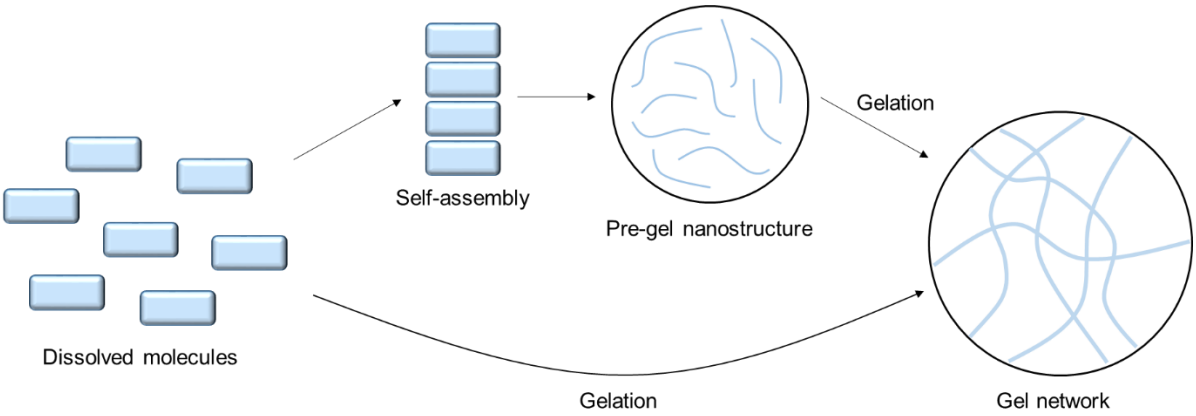

Figure 1. Cartoon diagram of the self-assembly and gelation process from dissolved molecules of gelator. The process can go directly from dissolved molecules to a gel or *via* a pre-gel solution with self-assembled nanostructures.

The formation of a gel is dependent on a range of processes and length scales from molecular interactions to the long-range entanglement of the 1D structures in the network. As such, a range of techniques are needed to probe the gel characteristics at these different length scales and a quick summary of commonly used techniques is given below. For compounds that absorb in the relevant regions of light, UV and Visible light (UV-Vis) spectroscopy is widely used to probe self-assembly and packing at the molecular level.[18] NMR spectroscopy can be used to study gelation kinetics[19] but often the solid-like phase of the gel is not-observable by conventional NMR. Rheology can be used to study gel formation and bulk mechanical properties of a gel.[20] Probing the size and morphology of the nanostructures can be achieved through scanning electron microscopy/transmission electron microscope (SEM/TEM) or confocal microscopy. SEM/TEM often require drying which can lead to artefacts and they also only probe a small area of the sample.[21] Small angle neutron scattering (SANS) and small angle X-ray scattering (SAXS) are widely used in soft matter research to characterise the size and morphology of nanostructures.[22] The nanostructures are studied *in situ* and samples do not need to be dried, meaning that gels can be studied in a solvated state. A relatively large volume of sample is irradiated, giving an averaged representation of the nanostructures present. These factors mean that a representative image of the gel is given as compared with localised microscopy techniques. Data analysis for these scattering techniques can be very informative but can be complex and prone to errors (such as over-fitting).[23] Most of the above techniques are also relevant for the effective study of the pre-gel solutions formed from these materials. It is clear that a full characterisation requires a wide range of techniques.

2.1 Self-assembly

2.1.1 Fundamentals of self-assembly mechanism

The self-assembly process is controlled by numerous variables that must be thoroughly investigated and controlled. Firstly, the molecular structure determines the nature of the interactions between molecules, where subtle changes (such as chirality) can have a significant impact and the presence of certain groups can introduce new interactions (such as hydrogen bonding).[24–26] In LMWGs, the main non-covalent interactions that drive self-assembly are Van der Waals interactions, hydrogen bonding, π-stacking and dipole-dipole interactions.[15] The solvent plays a crucial role in the process, where often a solubility change triggered by an external variable is the driving force for gelation. In aqueous environments, hydrophobic forces play a significant role in driving self-assembly. Every small molecule gelator has a minimum gelation concentration (commonly in the region of 0.1 wt%), below which a gel will not form. This is either due to an insufficient number of self-assembled structures to form a network or a lack of self-assembly. Temperature is an overarching variable that directly influences these processes and thermal annealing is a common method for gelation triggering. The self-assembly of LMWGs has been described as a bottom-up process[8,27] and the interplay of these variables leaves researchers with a very wide and exciting landscape to investigate. Desired properties can either be achieved through the synthesis of novel compounds (which is often time consuming and resource intensive) or by modulating the self-assembly, such as through changes in ionic strength or pH.

Predicting and designing small molecule gelators remains a challenge, and many new gelators are often discovered serendipitously. Hansen solubility parameters (HSPs) are one approach to predicting the behaviour of a specific molecule in a specific solvent/solvent system.[28–30] For small molecular gelators, HSPs use an additive approach of the functional groups within a molecule and the solvent, assessing the dispersive, polar and hydrogen bonding interactions of the components. There have been computational attempts to predict which structures will form gels and which will not. These methods use real-world data of previously discovered gelators. For example, an *in silico* screening of 2025 dipeptides by Gupta *et al* identified 9 candidates as potential gelators.[31] When these were synthesised and tested, the model was correct and all 9 candidates formed gels.

2.1.2 Self-assembly in pre-gel solutions

It is of great importance to note that many LMWGs exist in a self-assembled state in the pre-gel solution, where aggregates such as worm-like micelles form (Figure 1).[6,32] Often, these are reported with no mention of gel formation but in the context of this work, both the pre-gel solutions and the gels they form are of relevance.

For example, a perylene monoimide (PMI) was synthesised on the hypothesis that the large aromatic perylene core would impart hydrophobicity and drive π-π stacking, thus leading to self-assembly in water.[33] At a PMI concentration of 11.5 mM this was indeed the case, where cryo-TEM images and a slope of -2 in the low Q region of SAXS data identified the presence of 40 nm wide and several micron long ribbon-like structures (Figure 2). Based on the data the authors suggested that the PMI forms bilayers within the ribbons and that the ribbons adopt a lamellar spacing of 27 nm (obtained from low Q peaks in the SAXS; Figure 2d). Gels were then formed from the aqueous solutions by the addition of salts that screen the negatively charged PMI ribbons.

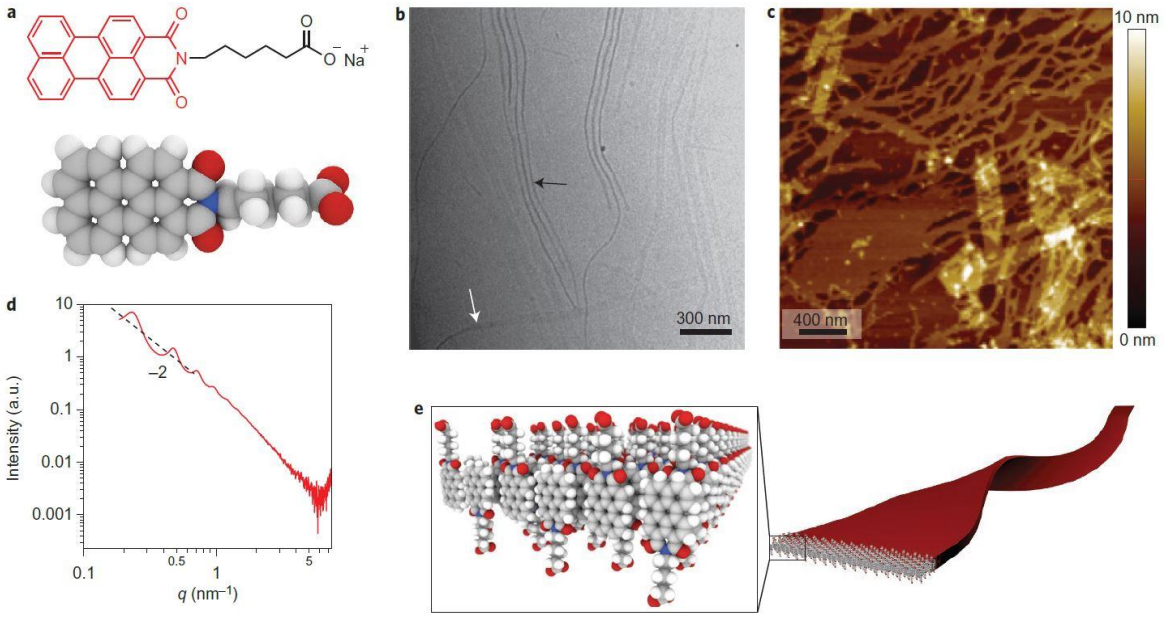

Figure 2. (a) Molecular structure of the PMI chromophore amphiphile; (b) cryo-TEM image of the PMI solution; (c) Atomic force microscopy (AFM) image of dilute PMI solution; (d) SAXS data of the PMI solution and (e) cartoon schematic of the structure and packing of the ribbons. Reprinted by permission from Springer Nature: A. S. Weingarten, R. V. Kazantsev, L. C. Palmer, M. McClendon, A. R. Koltonow, A. P. S. Samuel, D. J. Kiebala, M. R. Wasielewski and S. I. Stupp, Nat. Chem., 2014, 6, 964–970, Copyright© 2014.

Another example was shown in work by Clover *et al.*, in which the influence of amino acid chirality on the self-assembly of amphipathic peptides (Figure 3a) was investigated.[26] At a concentration of 0.25 mM, the Ac-FKFEFKFE-NH2 peptides self-assemble into fibrillar structures, but depending on the amino acid chirality, the self-assembled structures that formed were vastly different (Figure 3b to 3e). The LL and DD peptides form nanofibres whereas the LD and DL peptides form large helical tapes. At higher concentrations (10 mM), the fibrillar structures form gels that exhibit shear-thinning behaviour and show mechanical recovery after being subjected to high strains.

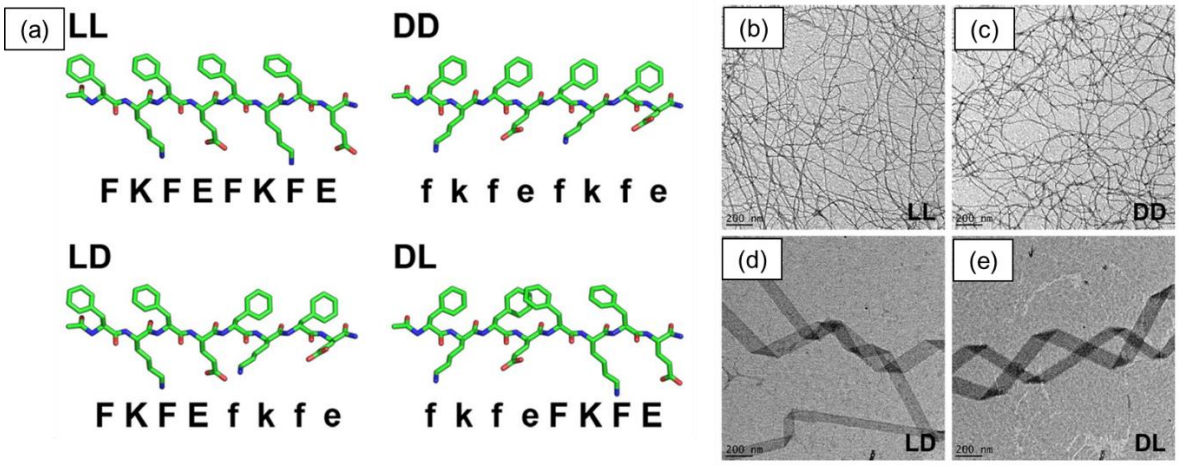

Figure 3. (a) Structures of the homochiral and heterochiral peptides studied; (b – e) TEM images of the different peptides (images labelled with peptide) at 0.25 mM in water. Reprinted with permission from the American Chemical Society under the ACS AuthorChoice agreement, T. M. Clover, C. L. O'Neill, R. Appavu, G. Lokhande, A. K. Gaharwar, A. E. Posey, M. A. White and J. S. Rudra, J. Am. Chem. Soc., 2020, 142, 19809–19813, Copyright© 2020.

In other work, the self-assembly of an amphiphilic naphtho-*p*-quinodimethane (aQDM; Figure 4a) was modulated through changing the amount of base added, resulting in either ribbons, helices or disordered filaments forming (Figure 4b to 4d).[34] Atomic force microscopy measurements were used to obtain an average thickness of the ribbons and helices, which inferred that the molecules form bilayers with the carboxylic acid groups on the external faces. SAXS measurements of the solutions supported the observed structures in TEM. Interestingly, in wide angle X-ray scattering (WAXS) measurements, crystalline peaks are observed for both the ribbon and helical structures, but then become less well defined at higher NaOH equivalents with the formation of disordered filaments. The peaks indicate high levels of molecular ordering within the ribbons and helices.

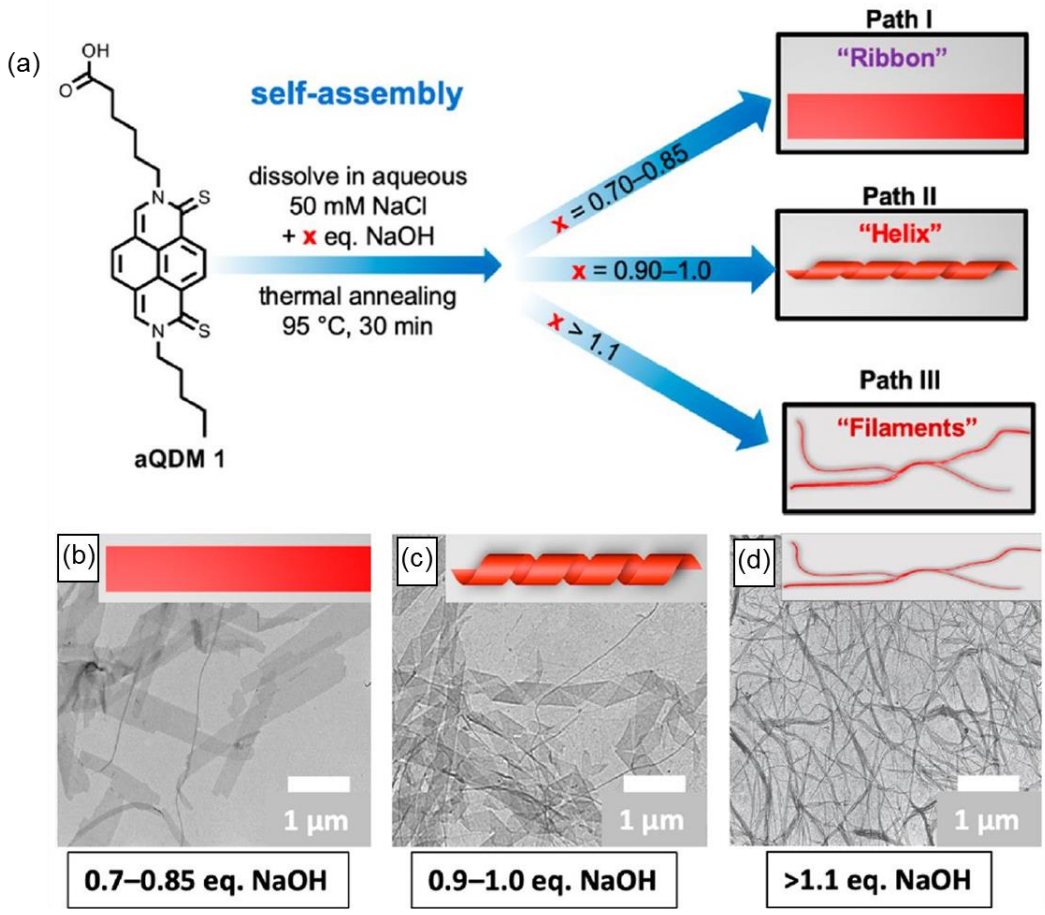

Figure 4. (a) Schematic of the pathways to different self-assembled structures by modifying NaOH; TEM images of self-assembled structures formed into (b) ribbons; (c) helical ribbons and (d) filaments. Adapted with permission from N. Grabicki, O. Dumele, H. Sai, N. E. Powers-Riggs, B. T. Phelan, M. H. Sangji, C. T. Chapman, J. V. Passarelli, A. J. Dannenhoffer, M. R. Wasielewski and S. I. Stupp, Chem. Mater., 2021, 33, 706–718, Copyright© 2021 American Chemical Society.

The self-assembled structures in solution allow for manipulation prior to any applications or gel formation. For example, self-assembled nanofibers can be aligned *via* magnetic fields[35] or by shear.[36] Through alignment of the nanostructure, researchers hope to enhance material properties, whether that be in organic electronic applications[37] or cell culturing.[38,39] Additionally, the self-assembly often results in fluids with vastly different properties to that of the solvent, a phenomena well-known in the surfactant literature.[40,41] The pre-gel self-assembly of aramid amphiphiles into nanoribbons facilitates the formation of macroscopic threads (multiple cm long) by drawing the threads during gelation.[14] The threads possess high tensile strength and flexibility, which is remarkable considering they are comprised of small molecules bound by non-covalent interactions. In many of these examples, the self-assembled structures modify the rheological properties of the fluids but this is seldom studied in great detail if at all. Worm-like micelles formed from functionalised dipeptides

have been shown to result in viscous, shear-thinning solutions that also exhibit high extensional relaxation times.[6,42] In summary, the pre-gel self-assembly of molecules that form LMWGs is extremely important for both the final gels as well as potential applications.

2.2 Gelation

Gelation occurs upon the entanglement and cross-linking of 1D structures that results in the immobilisation of the solvent. Often the inversion test is used to show whether or not a gel has formed, in which the vial containing the 'gel' is inverted.[43] If the 'gel' holds its weight and does not flow then it is assigned as a gel. While this test can be useful (and cheap!), it provides a deficient analysis on the material properties. Many very viscous liquids can pass the inversion test because the time scales over which they flow are longer than the measurement time. As such, ideally oscillatory rheology should be used to measure the solid-like (storage modulus, G′) and liquid-like (loss modulus, G″) properties. Where G′ is an order of magnitude greater than G″, then a true gel is considered to have formed.[44] Oscillatory rheology requires a fixed volume of gel in a specialist cup-shaped geometry to be measured. For samples with non-conventional morphologies other techniques such as nanoindentation can be used. Nanoindentation is a highly localised measurement which is repeated across a sample to build up an average.[45] It involves a tip performing a fixed depth indentation into the surface of a material while measuring force. The force-indentation curve can be analysed to obtain material parameters such as the Young's modulus.

2.2.1 Gelation triggers

There are a wide range of methods by which gelation can be triggered and it is important to recognise the strengths and weakness of each. The choice of gelation method is fundamentally important for biological applications, which are often sensitive to pH and solvent. They generally (but not always) involve decreasing the solubility of the gelator such that self-assembly is triggered.

2.2.1.1 pH triggers

Particular interest is shown to the formation of hydrogels for biological applications due to improved biocompatibility as compared to organogels. Often, hydrogels are designed with pH responsive moieties (such as carboxylic acid groups), meaning that self-assembly and gelation can be manipulated through the addition of acids or bases (Figure 5).[46,47] For example, gelators with COOH groups can be deprotonated at high pH, resulting in them dissolving in water. Furthermore, this process is typically reversible. Again, it must be pointed out that some gelators still self-assemble when "dissolved" at high pH forming, for example, worm-like micelle solutions. Upon a reduction in pH, the carboxylic acid group is protonated, reducing solubility and driving self-assembly to form a gel.

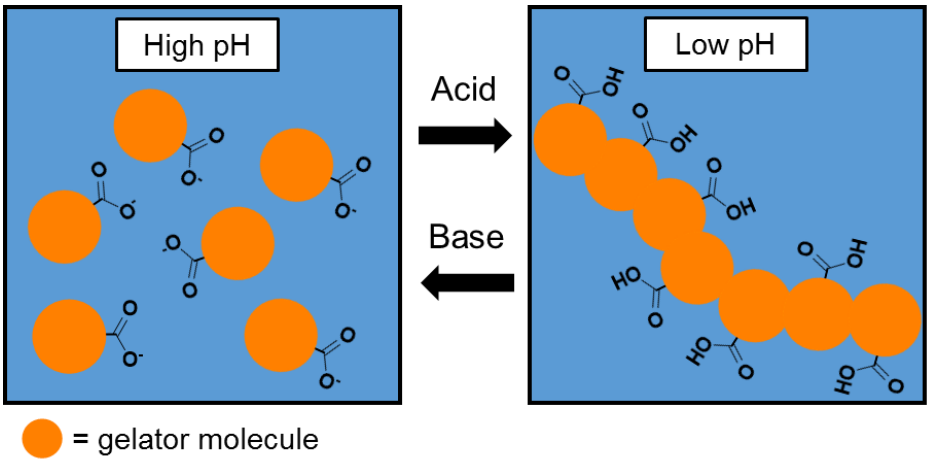

Figure 5. Cartoon schematic showing the protonation and gelation *via* an acid trigger.

Control over pH is essential when preparing pH triggered gels. For example, for a perylene bisimide (PBI) LMWG, which possesses two carboxylic acid groups, the initial pH determined whether one or both of the two carboxylic acid groups were deprotonated. In turn, the self-assembled structures in the pre-gel are different and only one of the solutions can be used to form a gel.[48] As such, accurate measurement of pH and knowledge of the pK_a of gelator both before and after gel formation can be crucial. It is important to note that determining the pK_a of these materials can be complex. It has been reported that the self-assembly of Fmoc-diphenylalanine into fibrils results in two apparent pK_a shifts that are higher than the theoretically calculated one.[49]

Hydrochloric acid can be used to trigger gelation but generally results in inhomogeneous gels. This is because it triggers gelation rapidly, before allowing the acid to mix homogeneously. To overcome this, triggers that reduce the pH slowly with time have been developed. These include the hydrolysis of anhydrides and lactones.[50,51] It is important to note that the method by which the gel is formed affects the material properties. For anhydride hydrolysis triggered gels, the primary structures are shown to be the same as when trigger with hydrochloric acid, but the mechanical properties of the gel are different.[51]

For systems where gelation occurs by a slow pH drop, pH can be measured with time to gain an understanding a gelation kinetics. Additional measurements (such as rheology and small angle scattering) can be performed in-tandem to correlate the pH and material changes. For example, gel-to-gel transitions can be monitored with pH and time.[52]

2.2.1.2 Salts

Counter-ions can be used to trigger gelation in some circumstances. Gelators that are dissolved in water at high pH *via* the deprotonation of a carboxylic acid group can self-assemble to form 1D structures such as worm-like micelles. The deprotonated carboxylic acid groups are negatively charged, resulting in a worm-like micelles with a net negative

charge. An appropriate positive counter-ion (such as Ca^{2+}) can be added that behaves as a cross-linking agent, resulting in gelation by the 'locking-in' of the worm-like micelle network (Figure 6). This can be achieved with various salts, and for metal chloride salts the gel stiffness correlated with the Hofmeister series.[53] This gelation method is widely used for the formation of gel 'noodles', novel structures with potential applications in cell culturing and organic electronics.[32,38] The use of buffer solutions and cell media (which often contain salts) to trigger hydrogelation is widely reported for biological applications.

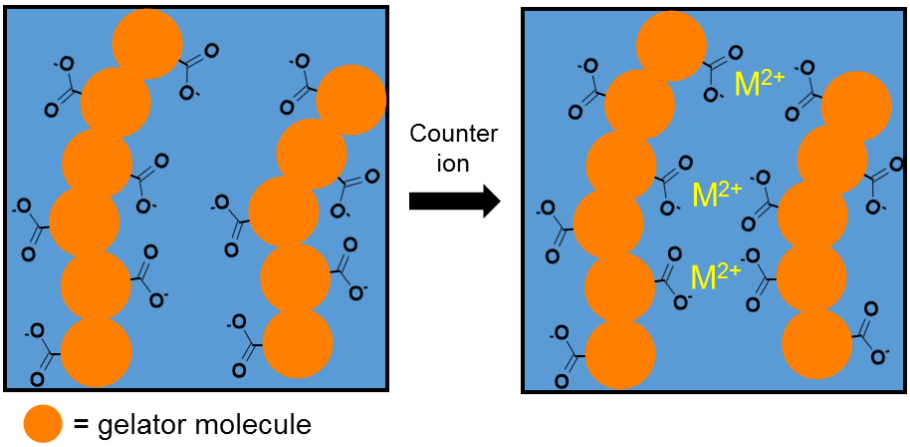

Figure 6. Cartoon schematic showing the gelation of negatively charged worm-like micelles by metal cation (M^+) cross-linking.

2.2.1.3 Annealing

Thermal annealing involves dissolving the gelator in hot solvent and then allowing it to cool. As it cools, the gelator solubility decreases, triggering self-assembly and network formation, resulting in gelation. This works on the principle that the gelator is more soluble at higher temperature, which is common, but not always the case.[54]

Annealing is solvent and concentration dependent, for example researchers screened the gelation propensity of a range of compounds in 31 solvents with different polarities.[55] The gelators were dissolved in hot solvent in an ultrasonic bath and then allowed to cool. Gels were formed in most (but not all) solvents and the compounds exhibited a range of minimum gelation concentrations. Thermal annealing is also applicable to hydrogels. For example, a fluorenylmethoxycarbonyl (Fmoc) group appended with phenylalanine formed hydrogels by dissolution in phosphate buffer solution (pH 7.46) with heating and then being allowed to cool.[56] After 15 minutes of cooling, a transparent gel formed.

2.2.1.4 Solvent switch

The solvent switch gelation trigger method involves dissolving the gelator in a solvent such that it is molecularly dissolved. Then a pre-defined volume of another solvent, in which the gelator is poorly soluble, is added. The final mix of two solvents creates an environment

which lowers the solubility, resulting in self-assembly and gel formation. A common example is a dimethyl sulfoxide (DMSO)-water solvent switch. For example, an Fmoc protected pentafluorophenylalanine gelator was dissolved in DMSO (at a concentration of 210 mM) and diluted in water to a concentration of 4.2 mM (0.2 wt%) gelator, resulting in gelation within minutes.[57]

3 Chemical structure of LMWGs

There is huge chemical diversity of LMWGs (Figure 7) including (but not limited to) peptides,[58] steroids,[59] synthetic bile salts,[60] carbohydrates,[61] and dyes.[62] As discussed above, it remains very difficult to predict which structures will behave as LMWGs and which will not, and the discovery of new compounds is often serendipitous.[63] Discovery of new LMWG molecules can be achieved by a library approach, in which a large number of candidates are synthesised and tested.[64,65] Often this involves structural modifications from a common structure and can be very time and resource intensive.

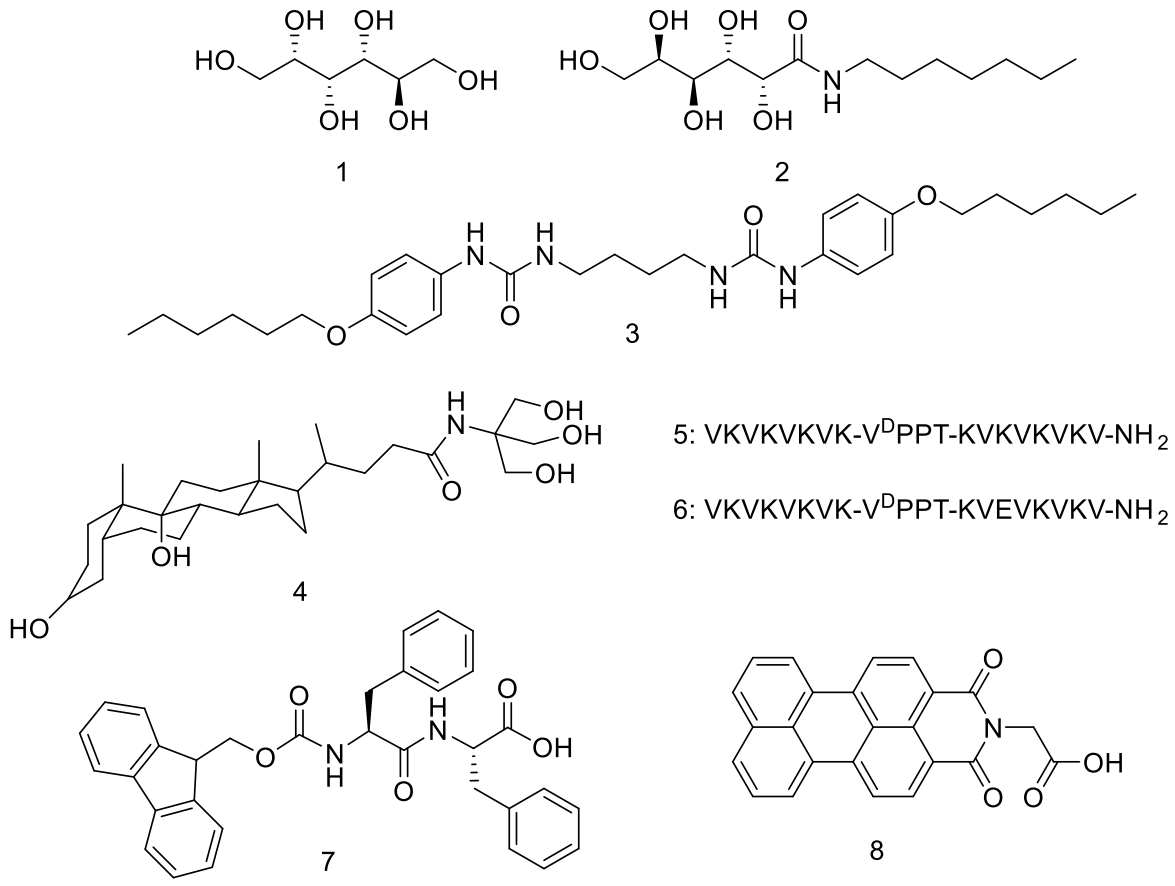

Figure 7. Chemical structures of small molecule gelators reported in the literature.[60,61,66–70]

3.1 Peptides

Amino acids are an essential building block of life which combine to form peptides, which underpin the workings of living organisms through the formation of proteins and enzymes. Peptides are widely known to assemble into supramolecular structures through the formation of α-helices and β-sheets and some form gels.[71,72] The self-assembly is sensitive to the specific order of the amino acid chain and even the chirality of the amino acid used can result in vastly different structures forming.[26] While investigating the self-assembly of peptides, Reches and Gazit discovered that one of the smallest peptides to self-assemble into 1D structures is diphenylalanine (FF).[73] This originated from the hypothesis that the stacking of aromatic residues at the heart of a β-amyloid polypeptide (Figure 8a) played a key role in the self-assembly. The FF residue self-assembled to form nanotubes (Figure 8b and 8c in 1,1,1,3,3,3-hexafluoro-2-propanol that were visualised using transmission electron microscope (TEM).

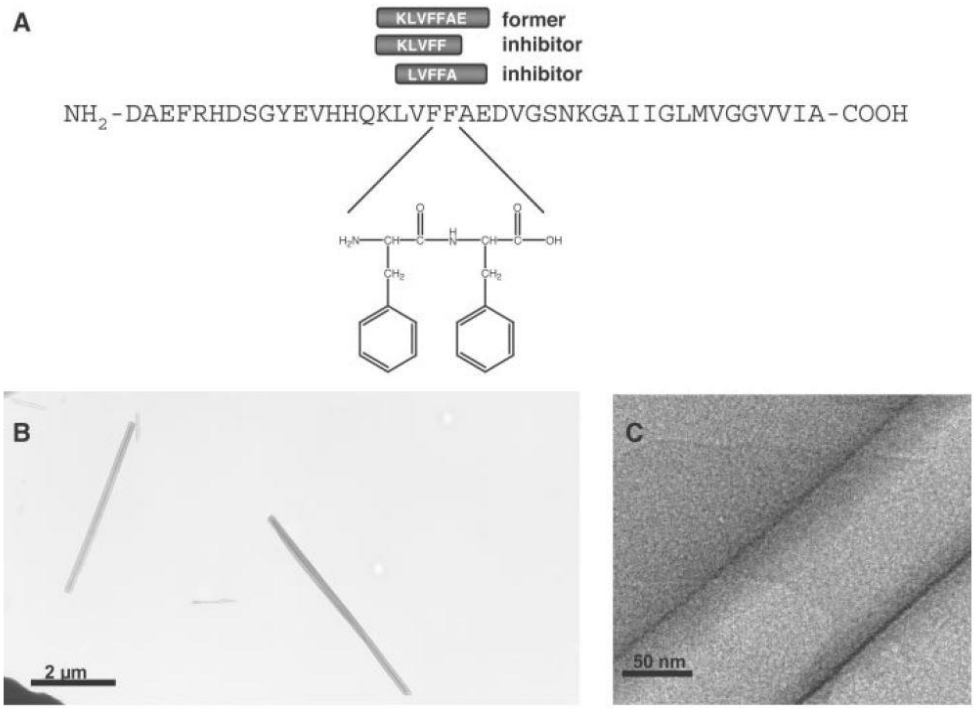

Figure 8. (a) β-amyloid polypeptide structure, highlighting the diphenylalanine aromatic core; (b) Negatively stained TEM of nanotubes formed from diphenylalanine; (c) High resolution TEM images of the nanotubes. From M. Reches and E. Gazit, Science, 2003, 300, 625–627, reprinted with permission from AAAS.

Peptides that are 4 – 20 amino acid units long with alternating hydrophobic and hydrophilic groups are highly effective at self-assembling.[74,75] These assemble in fibres that antiparallel β-sheet-rich fibres and form gels. As will be shown later, amino acids and peptides often form a key part of more structurally-complex gelators.

3.1.1 Functionalised peptides

Due to the effectiveness of peptides to self-assemble and form gels, a significant field of research now also focusses on functionalised peptides. This involves attaching additional chemical group(s) to a peptide sequence to impart certain qualities.[7,8] One approach is through the addition of aromatic moieties to the N-terminus of the peptide (usually connected *via* a linker group) is widely reported approach (Figure 9).[6,56] The rationale behind this is that aromatic interactions aid the self-assembly of the small molecules.[76,77] For example, it has been noted that the self-assembly of Fmoc-FF was similar to that of a much larger peptide sequence.[78]

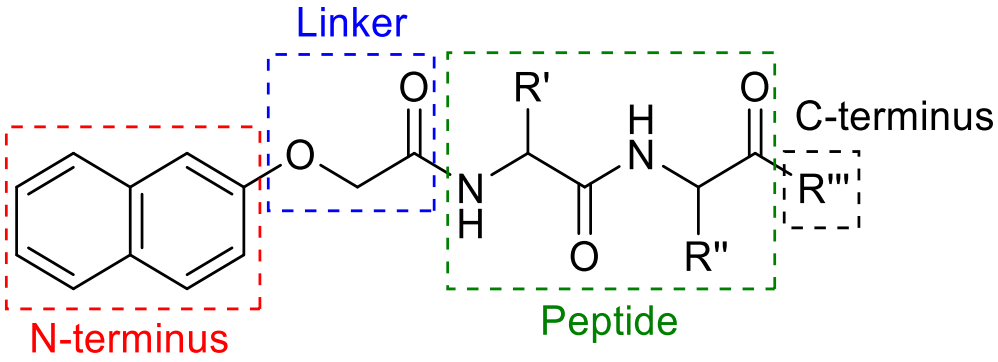

Figure 9. The general structure of an aromatic functionalised peptide. R' and R'' are determined by the amino acid used. R''' is commonly an –OH group.

As with many LMWG compounds, functionalised dipeptides are widely reported to form worm-like micelle solutions before gelation is triggered.[25] Functionalised dipeptides have been widely studied by many different researchers, with a view to many different applications.[25,65,79,80] In many instances, a given gelator molecule under a given set of conditions is presented. In recent years significant research into the influence of key variables underpinning the self-assembly in the pre-gel solutions has been investigated. For example, worm-like micelles in the pre-gel solution have been shown to undergo structural changes upon being subjected to a heat/cool cycle, leading to an increase in viscosity.[6] Typically, NaOH is used to deprotonate the carboxylic acid groups to solubilise the functionalised dipeptides. By changing the counter-ion used (such as LiOH and KOH), the self-assemble structures, shear viscosity and extensional relaxation time changed.[42] This work exemplifies how self-assembled structures can be modulated with simple changes.

3.1.2 π-gelators

A wide-range of low molecular weight gelators with π-conjugated systems have been reported, leading to specific optical and electronic properties as well as helping to promote self-assembly via π-π stacking.[81] These include perylenes,[82,83] naphthalenes,[84] oligothiophene[37,85] and oligophenylene[37] (Figure 10) among others. When molecularly dissolved (i.e. not self-assembled) such compounds often possess strong UV-Vis light absorption[86] and exhibit fluorescence.[87] Typically, the optoelectronic properties of these materials change upon self-assembly and aggregation,[86,87] a process that is highly dependent on the solvent.[88] The electronic structure of both the dissolved molecules and self-assembled structures can be probed and understood using UV-Vis spectroscopy.[87] These materials often behave as semiconductors and can transport charge upon certain stimuli. In the self-assembled state, the π-π interactions and co-facial packing of the molecules can enable intermolecular charge transport due of orbital overlap.

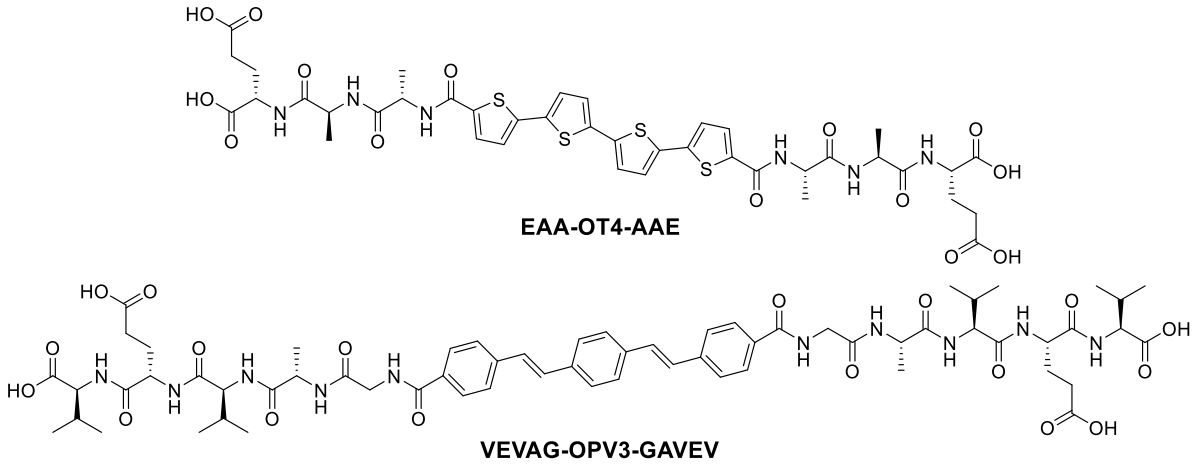

Figure 10. Chemical structures of oligothiophene and oligophenylene peptide-π-peptide gelators reported by Wall *et al.*

Materials based on the perylene core have been widely studied. Functionalisation can be performed either on the aromatic core or at the imide positions, leading to a large potential chemical diversity.[87] PMIs and PBIs are widely studied materials that typically self-assemble and form gels. Stupp and co-workers have studied PMI hydrogels where the presence of charged ribbons with a strong electronic coupling to the catalyst achieves light-driven hydrogen production in the presence of a sacrificial electron donor.[33] In other work, they also show hydrogen evolution from PMI-polyelectrolyte hybrid hydrogels.[9] Through functionalising the PMI core with a hydroxyl group, the material become more pH responsive which allows for tuning of the UV-Vis absorption as well as the self-assembled structure.[82] By either protonating/deprotonating the hydroxyl group, the PMI can be used

for either the hydrogen evolution reaction or CO_2 reduction reaction respectively, owing to a change in the energy level of the structures.

Draper and co-workers have widely studied PBIs, with a particular focus on studying the effect of the imide substituent, which has been functionalised with a range of different amino acids.[62,89,90] The PBIs form worm-like micelles at high pH and gels at low pH. They can be used to form photoconductive films due to the formation of the radical anion or dianion (Figure 11). The worm-like micelle solutions can be aligned by drying or gelling under shear, where directional dependence in the photoconductivity is found.[36]

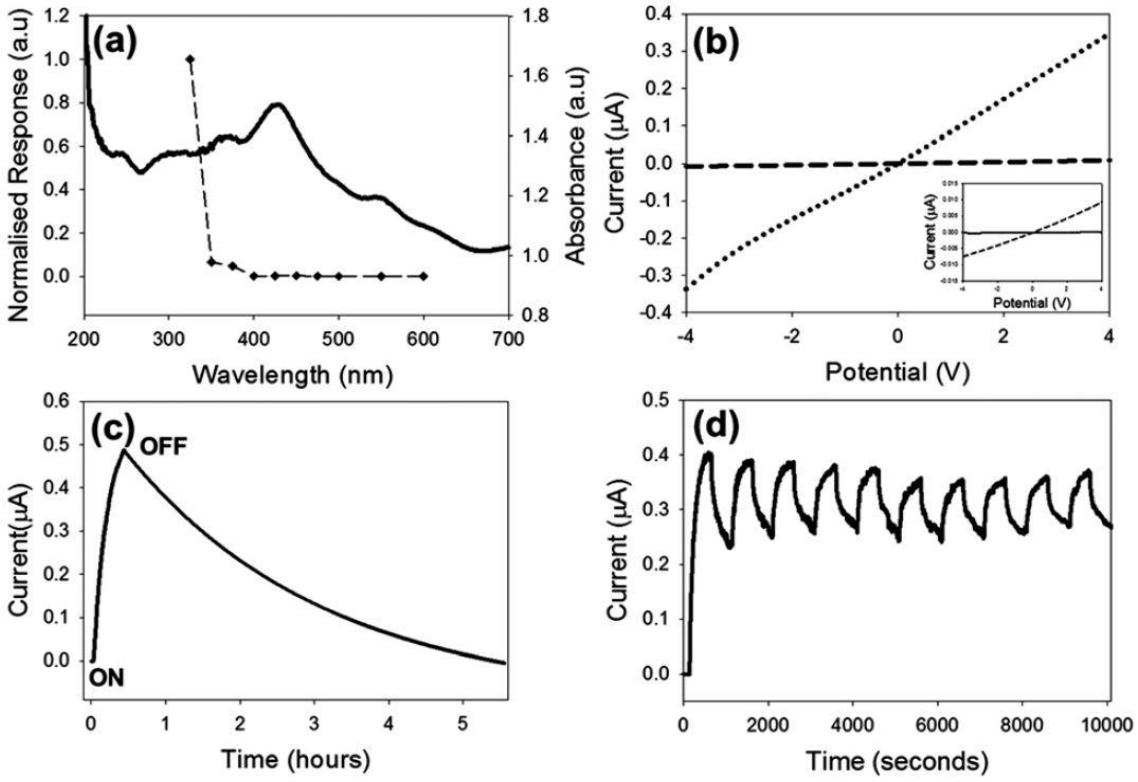

Figure 11. Dried solution and xerogel data for an L-alanine functionalised PBI. (a) Photocurrent (2 V potential difference) against irradiation wavelength for a dried solution overlaid with the UV-Vis absorption spectrum; (b) plot of current vs potential for a dried solution (dots) and a xerogel (dash) on 365 nm irradiation. Inset shows xerogel data under irradiation (dash) and in the dark (solid line); (c) Photo response with time with the switching on and off of a 365 nm lamp; (d) Photo response of a dried solution with cycling the 365 nm lamp on and off. Reproduced from E. R. Draper, J. J. Walsh, T. O. McDonald, M. A. Zwijnenburg, P. J. Cameron, A. J. Cowan and D. J. Adams, J. Mater. Chem. C, 2014, 2, 5570–5575, with permission from the Royal Society of Chemistry.

4 Applications of LMWGs

Low molecular weight gels have a wide range of potential applications including water purification,[13] cell culture[12,91] and drug delivery.[92,93] These are not of immediate relevance to this thesis however and will not be discussed in any detail. Applications of relevance are discussed below.

4.1 Organic electronics

Self-assembled materials and LMWGs have been widely investigated for use as organic semiconductors, with potential applications in photocataysis, photovoltaics, organic electronics, energy harvesting and sensing.[81] These have potential benefits including lower costs and increased mechanical flexibility as well as comprising from earth-abundant materials.[81] They have potential for high levels of tuneability where changes to the molecular structure or to the self-assembly and packing can modulate the activity.[94,95] A semiconductor is a material that is conductive under certain conditions. The principle works on the incorporation of optoelectronic functionalities (typically π-conjugated groups) into compounds that self-assemble into nano- and micro-scale assemblies.

For π-conjugated molecules, the highest occupied molecular orbital (HOMO) is determined by the π bonding orbitals and the lowest unoccupied molecular orbital (LUMO) is determined by the π antibonding orbitals. The semiconductor bandgap for these materials is therefore determined by the HOMO/LUMO energy gap. Upon irradiation with photons possessing energy greater than or equal to the band gap, electrons are promoted to the conduction band, leading to the formation of excitons, which can impart conductivity.[96] Organic semiconductors often possess small dielectric constants and photo-generated electrons and holes (Frenkel excitons) are held together by Coulombic interactions.[97] Typically, exciton recombination occurs rapidly but given the correct circumstances effective charge separation can occur.

The formation of self-assembled structures leads to electronic coupling between the individual units by π orbital overlap facilitating the delocalisation of charge along the structure. This can result in enhanced charge separation within the organic semiconductor material. The electronic and structural ordering of units within the self-assembled structure influences the distance over which charge transport occurs. These self-assembled nanostructures can be highly ordered and in some instances have fewer grain boundaries and reduced density of trapped states compared with traditional semiconductors.[98] Long range exciton transport of up to 4 μm along a single self-assembled fibre comprised of functionalised carbonyl-bridged triarylamine molecules has been reported.[99] In follow up work, a similar compound with the same core was shown to self-assemble into different

structures in different solvents (Figure 12).[100] The single supramolecular nanofibres (Figure 12a) exhibited higher exciton diffusivities. Alternatively, the specific packing and ordering may result in defects and trap the charge to a small domain.[101] Furthermore, reports of long range transport within a single self-assembled fibre or crystal do not necessarily speak to activity in a real-world device. Nevertheless, it is clear that the effectiveness of charge separation depends greatly on the specific molecular packing and self-assembled structure.

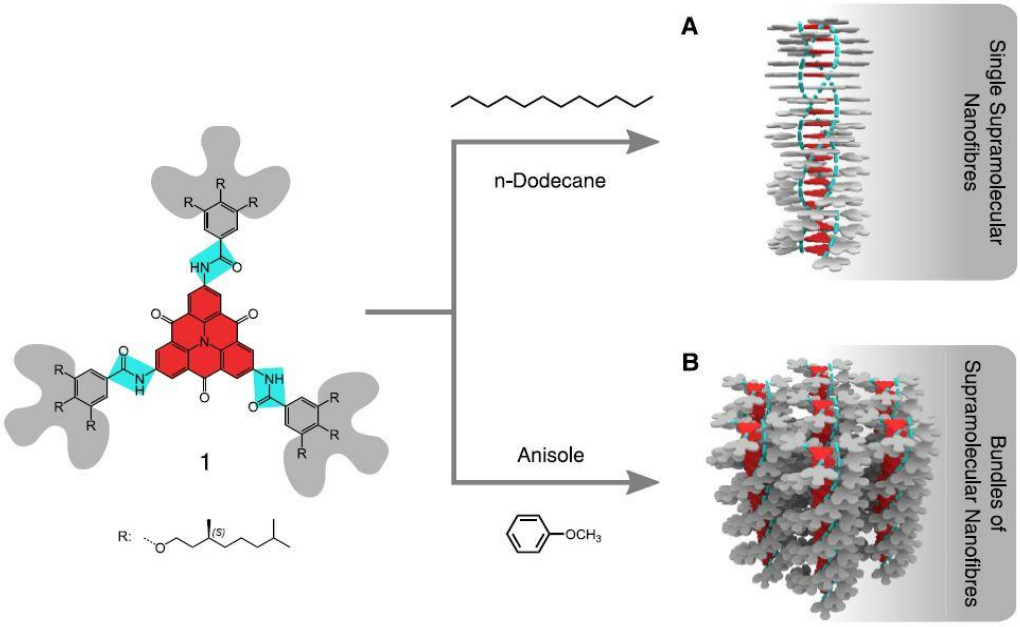

Figure 12. Molecular structure of a carbonyl-bridged triarylamine triamide that self-assembles into single nanofibres in n-dodecane or bundles of nanofibres in anisole. Reproduced from B. Wittmann, F. A. Wenzel, S. Wiesneth, A. T. Haedler, M. Drechsler, K. Kreger, J. Köhler, E. W. Meijer, H.-W. Schmidt and R. Hildner, J. Am. Chem. Soc., 2020, 142, 8323–8330, with permission from American Chemical Society Copyright© 2020, under the ACS Authors Choice CC-BY-NC-ND license.

There has been research into the use of LMWG and self-assembled materials for organic electronic applications in devices including organic solar cells (OSCs), organic field effect transistors (OFETs) and organic photodetectors.[11,102,103] For example, OSCs operate using the separation of electron-hole pairs that are formed upon irradiation with light. Bulk heterojunctions facilitate efficient charge separation using an interpenetrating donor-acceptor (D-A) layer between the electrodes.[104] LMWGs have been investigated for applications in bulk heterojunctions of OSCs due to the formation of a 3D network of fibres. For example, a D-A system comprised of a polymer and self-assembled organogel was used as part of an OSC.[105] The OSC was comprised of an organogel (PBI organogelator that forms nanofibers) and a hole conducting polymer. A doctor blade was used to form the layers which were dried, resulting in a xerogel. The devices made from this material showed

appreciable current density and voltage. As a control experiment, an electronically similar PBI that does not form gels was used to prepare a device, which then exhibited low current, voltage and efficiency. This suggests the formation of the interpenetrating gel network was crucial to activity. The work was a proof-of-concept for OSCs and the D-A layer combined good absorption properties with high charge carrier mobility.

4.2 Photochemical reactions

Self-assembled gels have been identified as a potential photochemical reaction media, where they have been described as a form of 'compartmentalised' environment, offering potential benefits including surface area, diffusion and tuneability.[106] The photocatalyst can by loaded into the gel network with the reagent or the photocatalyst being the material from which the gel network is comprised.

Both photooxidation and photoreduction reactions have been reported in LMWGs. Bachl *et al* performed the photooxidation of 1-(-4-methoxyphenyl)ethanol in a range of LMWG matrices as well as bio-polymer gels.[107] The reaction was performed with visible light in air using a riboflavin terraacetate catalyst. The photooxidation was successful in the wide range of media. The reaction efficiency was related to the mechanical properties of the gels, where the stronger gels with dense fibrillar networks (based on rheology and SEM data) exhibited lower efficiency. The cyclohexane-based bisamide LMWG afforded full conversion with no photodegradation of the catalyst observed. In other work, the photoreduction of an aryl halide (4-bromoacetophenone to acetophenone) was performed in a LMWG *via* a triplet-triplet annihilation up-conversion (TTA-UC) mechanism.[108] A photosensitiser and emitter were present within the gel network to drive the TTA-UC process. The results obtained in the aerobic gel phase were comparable to those obtained for the same reaction in solution under an inert atmosphere, demonstrating that the gel provides a specific environment.

4.3 Photocatalytic water splitting reactions

One particular area of interest is using LMWGs and self-assembled systems as part of photocatalytic water splitting systems.[10,109,110] Water splitting occurs *via* a redox reaction comprised of two half-reactions, the water oxidation reaction (equation (2)) and the proton reduction reaction (equation (3)). Traditionally, water splitting can be achieved by electrolysis where electricity is used to drive the reaction, where hydrogen production occurs at the cathode and oxygen production occurs at the anode. The minimal potential needed to drive the proton reduction reaction is 1.23 V and 0 V for water oxidation *vs* a normal hydrogen electrode,[111] although in practice a larger potential (an overpotential) is typically required due to losses.

$$(1) \quad H_2O \rightarrow H_2 + \frac{1}{2}O_2$$

$$(2) \quad H_2O \rightarrow \frac{1}{2}O_2 + 2H^+ + 2e^-$$

$$(3) \quad 2H^+ + 2e^- \rightarrow H_2$$

There is significant interest in the solar driven water splitting reaction for potential routes to generate hydrogen as a green fuel or produce the useful chemical reagents of hydrogen and oxygen. For energy applications, solar driven hydrogen production could be used as a store of energy as opposed to converting solar energy directly into electricity.[112] Overall water splitting results in both hydrogen and oxygen are being generated. Alternatively, the half reactions can be run individually, to form either one of the products.

Organic semiconductors have been widely investigated for solar based water splitting with graphitic carbon nitride,[113] covalent organic frameworks,[114] organic polymers[115] and porous organic polymers[116] among others. For complete water splitting (forming both hydrogen and oxygen), various device configurations can be used with some generating the voltage to drive electrolysis and others used in direct contact with the aqueous electrolyte (Figure 13).[115]

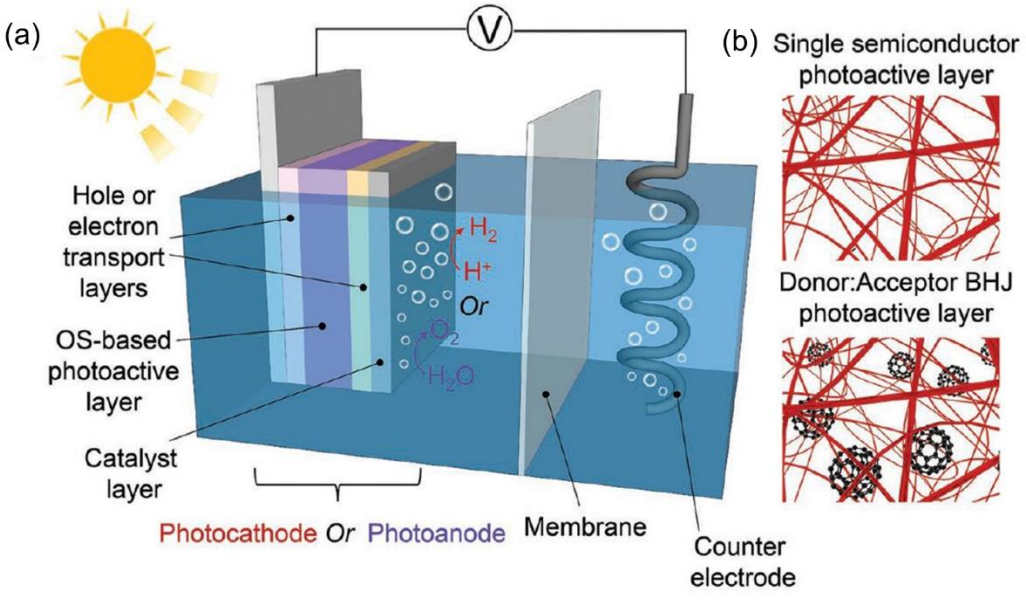

Figure 13. (a) Cartoon schematic of a photo-electrochemical cell using an organic semiconductor photocathode or photoanode in direct contact with the aqueous electrolyte. This setup requires the applications of an external voltage; (b) cartoon representation of both a single semiconductor layer and a donor:acceptor (polymer:fullerene) bulk heterojunction. Reproduced from L. Yao, A. Rahmanudin, N. Guijarro and K. Sivula, Adv. Energy Mater., 2018, 8, 1–18, with permission from John Wiley and Sons, Copyright© 2018.

For self-assembled systems and LMWGs to perform solar driven water splitting, materials must meet certain criteria. They must possess good visible light absorption, have long excited state lifetimes, correct frontier molecular orbital energies, possess good surface area for high reaction efficiency and be inexpensive and easy to synthesise.[10] There are numerous reports of LMWGs and self-assembled organic materials forming part of a photocatalytic system for hydrogen evolution from water.[10,33,117] In these systems the self-assembled organic material typically acts as the light harvester, so it must be designed appropriately for light absorption. Upon photo-excitation, an exciton forms which can delocalise along the self-assembled structure, helping charge separation. This depends on good packing and orbital overlap between the individual molecular units. For those used in direct contact with the aqueous electrolyte, the materials must be compatible with water. Co-catalysts are commonly employed and these are likely the site of the proton reduction. As such the charge generated on the self-assembled structure must be transported to the co-catalyst. As example, both platinum (in various forms)[10,110] and Mo_3S_{13}[118] have been used as a co-catalysts. Finally, when running hydrogen evolution half reaction on its own, a sacrificial hole scavenger (often methanol or triethanolamine) is required which aids with charge separation.

The exact mechanisms of such photocatalytic systems can be hard to determine, but with extensive experiments on a system, specific mechanisms can been devised (Figure 14).[119]

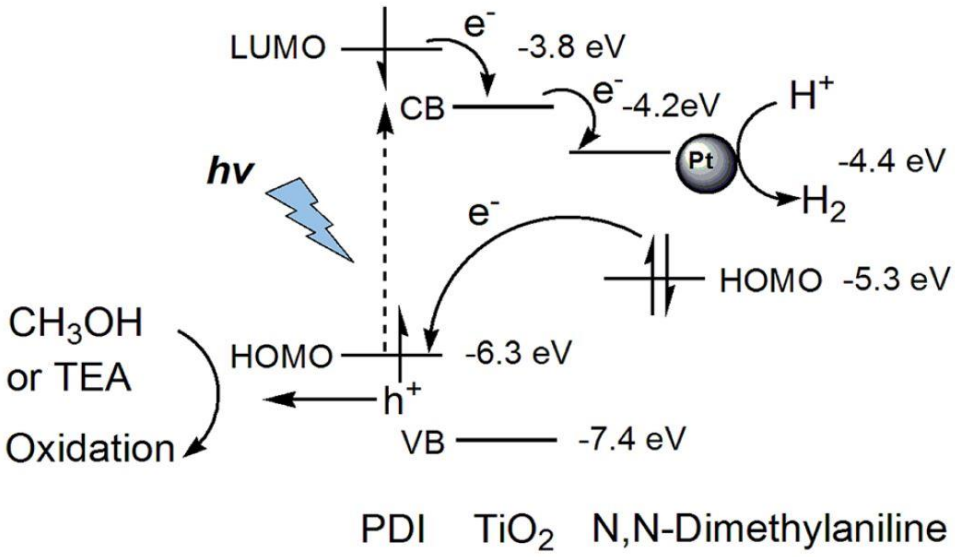

Figure 14. Schematic showing the proposed mechanism and energy levels (*vs.* vacuum level) for the hydrogen evolution reaction in PBI system. Reproduced from S. Chen, D. L. Jacobs, J. Xu, Y. Li, C. Wang and L. Zang, RSC Adv., 2014, 4, 48486–48491, with permission from the Royal Society of Chemistry, Copyright© 2014.

To cover some examples of such systems, a self-assembled trilateral cationic cyanostilbene system has been used to perform photocatalytic hydrogen evolution from water with the addition of an iodide source and platinum co-catalyst.[10] While the mechanism of the reaction and the influence of different additives, the exact structure of the self-assembled structures and the impact that has on the photocatalysis is not investigated in detail. Perylene-based compounds are a specific class of molecules that are frequently used for photocatalytic hydrogen evolution.[82,120]

5 Conclusions

To conclude, the field of low molecular weight gels is an active research area being directed towards many potential applications ranging from cell culturing, water purification and organic electronics. The chemical structure plays a significant role in determining the self-assembly and whether or not a material will form gels. Often new gelators are discovered serendipitously, but there are successful studies where new gelators are predicted computationally. The field of LMWGs often draws upon nature, where amino acids play an important role in the underlying chemistry and interactions that drive self-assembly. Unsurprisingly, when more complex and functionalised gelators have been synthesised (such as π-gelators and functionalised dipeptides), amino acids and peptides often form a key part of those structures.

The self-assembled structure is fundamental to the gels mechanical properties and often self-assembled structures are also present in pre-gel solutions. While it is clear that molecular structure dictates self-assembly and gelation, other variables such as concentration, salt, pH and temperature are also very important. This range of variables offers many avenues to tune the material properties.

π-gelators and the self-assembled structures that form in pre-gel solutions have widely been investigated for applications in organic electronics, photovoltaics and photocatalysis among others. At present, there is not specific work focussing on manipulating nanofibre alignment for enhanced photocatalysis.

6 This thesis

The work in this thesis focusses on controlling and understanding the self-assembly of LMWGs and pre-gel solutions in order to tune the material properties and activity to a specific purpose. The overarching aim of the research has been to understand and improve materials for self-assembled photocatalysis.

The first research chapter investigates five different amino acid functionalised PBIs for solar driven evolution of hydrogen from water. A range of pH and methanol concentrations were studied in high throughput experiments, in which hundreds of samples were measured in a short space of time. To compliment this, the self-assembled structures were investigated using SAXS experiments. This data was drawn together to link self-assembled structure to optimised hydrogen evolution. Coupled with data from surface charge NMR experiments and UV-Vis spectroscopy, it was concluded that optimum charge separation (and hence hydrogen evolution) occurred when long 1D structures, with a specific molecular packing and surface charge were present.

Following from this, it was hypothesised that charge separation and photocatalytic activity would be enhanced by introducing long-range alignment to the 1D nanofibres. Inducing nanostructural alignment in such materials is a challenge but one method involves the formation of macroscopic gel filaments (so-called gel ‘noodles’) which have been previously reported. Preparing gel noodles involves injecting pre-gel solution into a trigger medium bath. Initial attempts to form gel noodles with PBIs were unsuccessful, where inhomogeneous clumps of gel formed instead. To determine the properties that control formation and alignment of gel noodles, a model system of a functionalised dipeptide was studied. This formed gel noodles given a high enough solution viscosity and highly aligned gel noodles were successfully formed by a spinning technique.

In the final chapter, the formation of PBI gel noodles is investigated. Changing the amino acid that the PBI is functionalised with as well as controlling the solution pH resulted in sufficiently viscous solutions that formed gel noodles. While some alignment was found in these gel noodles, no difference in hydrogen evolution as compared to the unaligned noodles was seen. The PBI solutions were not robust enough to survive the spinning technique that induced very good alignment. It was hypothesised that this was due to the extensional viscosity of the fluids. A literature setup called ‘dripping-onto-substrate’ (DoS) that measures extensional relaxation time was built. The technique was validated against known fluids and then used to show that the functionalised dipeptide behaved like an elastic fluid with long extensional relaxation times whereas the PBI solution broke very quickly in extensional deformation.

7 References

1 H.-R. Lim, H. S. Kim, R. Qazi, Y.-T. Kwon, J.-W. Jeong and W.-H. Yeo, *Adv. Mater.*, 2020, **32**, 1901924.

2 T. Jiang, J. G. Munguia-Lopez, S. Flores-Torres, J. Kort-Mascort and J. M. Kinsella, *Appl. Phys. Rev.*, 2019, **6**, 11310.

3 K. Vithani, A. Goyanes, V. Jannin, A. W. Basit, S. Gaisford and B. J. Boyd, *Pharm. Res.*, 2019, DOI:10.1007/s11095-018-2531-1.

4 A. R. Hirst, B. Escuder, J. F. Miravet and D. K. Smith, *Angew. Chem. - Int. Ed.*, 2008, **47**, 8002–8018.

5 R. G. Weiss, *Gels*, 2018, DOI:10.3390/gels4020025.

6 E. R. Draper, H. Su, C. Brasnett, R. J. Poole, S. Rogers, H. Cui, A. Seddon and D. J. Adams, *Angew. Chem. - Int. Ed.*, 2017, **56**, 10467–10470.

7 E. K. Johnson, D. J. Adams and P. J. Cameron, *J. Mater. Chem.*, 2011, **21**, 2024–2027.

8 S. Fleming and R. V. Ulijn, *Chem. Soc. Rev.*, 2014, **43**, 8150–8177.

9 H. Sai, A. Erbas, A. Dannenhoffer, D. Huang, A. Weingarten, E. Siismets, K. Jang, K. Qu, L. C. Palmer, M. Olvera De La Cruz and S. I. Stupp, *J. Mater. Chem. A*, 2019, **8**, 158–168.

10 H.-J. Lee, J. Kim, A. Abudulimu, J. Cabanillas-Gonzalez, P. C. Nandajan, J. Gierschner, L. Lüer and S. Y. Park, *J. Phys. Chem. C*, 2020, **124**, 6971–6978.

11 S. S. Babu, S. Prasanthkumar and A. Ajayaghosh, *Angew. Chem. - Int. Ed.*, 2012, **51**, 1766–1776.

12 X. Yan, Y. R. Chen, Y. F. Song, J. Ye, M. Yang, B. B. Xu, J. Y. Zhang, X. Wang and J. K. Yu, *Front. Bioeng. Biotechnol.*, 2020, **8**, 1–13.

13 B. O. Okesola and D. K. Smith, *Chem. Soc. Rev.*, 2016, **45**, 4226–4251.

14 T. Christoff-Tempesta, Y. Cho, D.-Y. Kim, M. Geri, G. Lamour, A. J. Lew, X. Zuo, W. R. Lindemann and J. H. Ortony, *Nat. Nanotechnol.*, 2021, **16**, 447–454.

15 E. R. Draper and D. J. Adams, *Chem*, 2017, **3**, 390–410.

16 J. Raeburn, A. Z. Cardoso and D. J. Adams, *Chem. Soc. Rev.*, 2013, **42**, 5143–5156.

17 F. Tantakitti, J. Boekhoven, X. Wang, R. V. Kazantsev, T. Yu, J. Li, E. Zhuang, R.

Zandi, J. H. Ortony, C. J. Newcomb, L. C. Palmer, G. S. Shekhawat, M. O. De La Cruz, G. C. Schatz and S. I. Stupp, *Nat. Mater.*, 2016, **15**, 469–476.

18 W. Wei, S. Ouyang and Z. Tierui, *J. Semicond.*, 2020, **41**, 091708.

19 B. Escuder, M. LLusar and J. F. Miravet, *J. Org. Chem.*, 2006, **71**, 7747–7752.

20 K. A. Ramya, S. M. M. Reddy, G. Shanmugam and A. P. Deshpande, *Langmuir*, 2020, **36**, 13342–13355.

21 L. L. E. Mears, E. R. Draper, A. M. Castilla, H. Su, Zhuola, B. Dietrich, M. C. Nolan, G. N. Smith, J. Doutch, S. Rogers, R. Akhtar, H. Cui and D. J. Adams, *Biomacromolecules*, 2017, **18**, 3531–3540.

22 T. Narayanan and O. Konovalov, *Materials*, 2020, DOI:10.3390/ma13030752.

23 M. J. Hollamby, *Phys. Chem. Chem. Phys.*, 2013, **15**, 10566–10579.

24 Y. Li, Y. Sun, M. Qin, Y. Cao and W. Wang, *Nanoscale*, 2015, **7**, 5638–5642.

25 A. D. Martin, J. P. Wojciechowski, A. B. Robinson, C. Heu, C. J. Garvey, J. Ratcliffe, L. J. Waddington, J. Gardiner and P. Thordarson, *Sci. Rep.*, 2017, **7**, 1–6.

26 T. M. Clover, C. L. O'Neill, R. Appavu, G. Lokhande, A. K. Gaharwar, A. E. Posey, M. A. White and J. S. Rudra, *J. Am. Chem. Soc.*, 2020, **142**, 19809–19813.

27 R. Huang, Y. Wang, W. Qi, R. Su and Z. He, *Mater. Lett.*, 2014, **128**, 216–219.

28 J. Bonnet, G. Suissa, M. Raynal and L. Bouteiller, *Soft Matter*, 2014, **10**, 3154–3160.

29 N. Yan, Z. Xu, K. K. Diehn, S. R. Raghavan, Y. Fang and R. G. Weiss, *J. Am. Chem. Soc.*, 2013, **135**, 8989–8999.

30 D. A. Makeiff, J. –Y Cho, N. Godbert, B. Smith, K. Azyat, A. Wagner, M. Kulka and R. Carlini, *J. Mol. Liq.*, 2021, **339**, 116723.

31 J. K. Gupta, D. J. Adams and N. G. Berry, *Chem. Sci.*, 2016, **7**, 4713–4719.

32 S. Zhang, M. A. Greenfield, A. Mata, L. C. Palmer, R. Bitton, J. R. Mantei, C. Aparicio, M. O. De La Cruz and S. I. Stupp, *Nat. Mater.*, 2010, **9**, 594–601.

33 A. S. Weingarten, R. V. Kazantsev, L. C. Palmer, M. McClendon, A. R. Koltonow, A. P. S. Samuel, D. J. Kiebala, M. R. Wasielewski and S. I. Stupp, *Nat. Chem.*, 2014, **6**, 964–970.

34 N. Grabicki, O. Dumele, H. Sai, N. E. Powers-Riggs, B. T. Phelan, M. H. Sangji, C. T. Chapman, J. V. Passarelli, A. J. Dannenhoffer, M. R. Wasielewski and S. I. Stupp,

Chem. Mater., 2021, **33**, 706–718.

35 D. W. P. M. Löwik, I. O. Shklyarevskiy, L. Ruizendaal, P. C. M. Christianen, J. C. Maan and J. C. M. Van Hest, *Adv. Mater.*, 2007, **19**, 1191–1195.

36 E. R. Draper, O. O. Mykhaylyk and D. J. Adams, *Chem. Commun.*, 2016, **52**, 6934–6937.

37 B. D. Wall, S. R. Diegelmann, S. Zhang, T. J. Dawidczyk, W. L. Wilson, H. E. Katz, H. Q. Mao and J. D. Tovar, *Adv. Mater.*, 2011, **23**, 5009–5014.

38 M. T. McClendon and S. I. Stupp, *Biomaterials*, 2012, **33**, 5713–5722.

39 A. Li, A. Hokugo, A. Yalom, E. J. Berns, N. Stephanopoulos, M. T. McClendon, L. A. Segovia, I. Spigelman, S. I. Stupp and R. Jarrahy, *Biomaterials*, 2014, **35**, 8780–8790.

40 R. Omidvar, S. Wu and H. Mohammadigoushki, *J. Rheol.*, 2019, **63**, 33–44.

41 J. P. Rothstein and H. Mohammadigoushki, *J. Nonnewton. Fluid Mech.*, 2020, DOI:10.1016/j.jnnfm.2020.104382.

42 K. McAulay, P. A. Ucha, H. Wang, A. M. Fuentes-Caparrós, L. Thomson, O. Maklad, N. Khunti, N. Cowieson, M. Wallace, H. Cui, R. J. Poole, A. Seddon and D. J. Adams, *Chem. Commun.*, 2020, **56**, 4094–4097.

43 S. R. Raghavan and B. H. Cipriano, in *Molecular Gels*, eds. R. G. Weiss and P. Terech, Springer, Dordrecht, 2006, pp. 241–252.

44 C. Yan and D. J. Pochan, *Chem. Soc. Rev.*, 2010, **39**, 3528–3540.

45 I. Lüchtefeld, A. Bartolozzi, J. Mejía Morales, O. Dobre, M. Basso, T. Zambelli and M. Vassalli, *J. Nanobiotechnology*, 2020, **18**, 1–11.

46 B. Ding, Y. Li, M. Qin, Y. Ding, Y. Cao and W. Wang, *Soft Matter*, 2013, **9**, 4672–4680.

47 T. J. Moyer, J. A. Finbloom, F. Chen, D. J. Toft, V. L. Cryns and S. I. Stupp, *J. Am. Chem. Soc.*, 2014, **136**, 14746–14752.

48 B. J. Greeves, M. A. Zwijnenburg, E. R. Draper, D. J. Adams, M. Barrow and R. Schweins, *Chem*, 2017, **2**, 716–731.

49 C. Tang, A. M. Smith, R. F. Collins, R. V Ulijn and A. Saiani, *Langmuir*, 2009, **25**, 9447–9453.

50 D. J. Adams, M. F. Butler, P. Sanderson, L. Mullen, W. J. Frith and M. Kirkland, *Soft*

Matter, 2009, **5**, 1856.

51 E. R. Draper, L. L. E. Mears, A. M. Castilla, S. M. King, T. O. McDonald, R. Akhtar and D. J. Adams, *RSC Adv.*, 2015, **5**, 95369–95378.

52 S. Panja and D. J. Adams, *Chem. Commun.*, 2019, **55**, 10154–10157.

53 L. Chen, G. Pont, K. Morris, G. Lotze, A. Squires, L. C. Serpell and D. J. Adams, *Chem. Commun.*, 2011, **47**, 12071–12073.

54 M. Yan, S. K. P. Velu, M. Maréchal, G. Royal, J. Galvez and P. Terech, *Soft Matter*, 2013, **9**, 4428–4436.

55 H. Kumari, S. E. Armitage, S. R. Kline, K. K. Damodaran, S. R. Kennedy, J. L. Atwood and J. W. Steed, *Soft Matter*, 2015, **11**, 8471–8478.

56 S. Roy and A. Banerjee, *Soft Matter*, 2011, **7**, 5300–5308.

57 D. M. Ryan, S. B. Anderson, F. T. Senguen, R. E. Youngman and B. L. Nilsson, *Soft Matter*, 2010, **6**, 475–479.

58 T. Yucel, C. M. Micklitsch, J. P. Schneider and D. J. Pochan, *Macromolecules*, 2008, **41**, 5763–5772.

59 P. Terech and Y. Talmon, *Langmuir*, 2002, **18**, 7240–7244.

60 P. Terech, S. Dourdain, S. Bhat and U. Maitra, *J. Phys. Chem. B*, 2009, **113**, 8252–8267.

61 A. Chalard, P. Joseph, S. Souleille, B. Lonetti, N. Saffon-Merceron, I. Loubinoux, L. Vaysse, L. Malaquin and J. Fitremann, *Nanoscale*, 2019, **11**, 15043–15056.

62 E. R. Draper, J. J. Walsh, T. O. McDonald, M. A. Zwijnenburg, P. J. Cameron, A. J. Cowan and D. J. Adams, *J. Mater. Chem. C*, 2014, **2**, 5570–5575.

63 R. G. Weiss, *J. Am. Chem. Soc.*, 2014, **136**, 7519–7530.

64 D. R. Trivedi and P. Dastidar, *Chem. Mater.*, 2006, **18**, 1470–1478.

65 S. Awhida, E. R. Draper, T. O. McDonald and D. J. Adams, *J. Colloid Interface Sci.*, 2015, **455**, 24–31.

66 S. Grassi, E. Caretti, L. Dei, C. W. Branham, B. Kahr and R. G. Weiss, *New J. Chem.*, 2011, **35**, 445–452.

67 H. Kumari, S. E. Armitage, S. R. Kline, K. K. Damodaran, S. R. Kennedy, J. L. Atwood and J. W. Steed, *Soft Matter*, 2015, **11**, 8471–8478.

68 M. C. Branco, D. J. Pochan, N. J. Wagner and J. P. Schneider, *Biomaterials*, 2009, **30**, 1339–1347.

69 D. J. Adams, L. M. Mullen, M. Berta, L. Chen and W. J. Frith, *Soft Matter*, 2010, **6**, 1971–1980.

70 A. S. Weingarten, R. V. Kazantsev, L. C. Palmer, D. J. Fairfield, A. R. Koltonow and S. I. Stupp, *J. Am. Chem. Soc.*, 2015, **137**, 15241–15246.

71 V. Castelletto and I. W. Hamley, in *Peptide Self-Assembly: Methods and Protocols*, eds. B. L. Nilsson and T. M. Doran, Springer New York, New York, NY, 2018, pp. 3–21.

72 F. Sheehan, D. Sementa, A. Jain, M. Kumar, M. Tayarani-Najjaran, D. Kroiss and R. V. Ulijn, *Chem. Rev.*, 2021, **121**, 13869–13914.

73 M. Reches and E. Gazit, *Science*, 2003, **300**, 625–627.

74 S. Zhang, T. Holmes, C. Lockshin and A. Rich, *Proc. Natl. Acad. Sci. USA*, 1993, **90**, 3334–3338.

75 S. Zhang and M. Altman, *React. Funct. Polym.*, 1999, **41**, 91–102.

76 G. Fichman and E. Gazit, *Acta Biomater.*, 2014, **10**, 1671–1682.

77 S.-M. Hsu, Y.-C. Lin, J.-W. Change, Y.-H. Liu and H.-C. Lin, *Angew. Chem. - Int. Ed.*, 2014, **53**, 1921–1927.

78 A. Mahler, M. Reches, M. Rechter, S. Cohen and E. Gazit, *Adv. Mater.*, 2006, **18**, 1365–1370.

79 L. Chen, S. Revel, K. Morris, L. C. Serpell and D. J. Adams, *Langmuir*, 2010, **26**, 13466–13471.

80 W. Ji, C. Yuan, P. Chakraborty, P. Makam, S. Bera, S. Rencus-Lazar, J. Li, X. Yan and E. Gazit, *ACS Nano*, 2020, **14**, 7181–7190.

81 S. Ghosh, V. K. Praveen and A. Ajayaghosh, *Annu. Rev. Mater. Res.*, 2016, **46**, 235–262.

82 A. Dannenhoffer, H. Sai, D. Huang, B. Nagasing, B. Harutyunyan, D. J. Fairfield, T. Aytun, S. M. Chin, M. J. Bedzyk, M. Olvera de la Cruz and S. I. Stupp, *Chem. Sci.*, 2019, 5779–5786.

83 S. Roy, D. Kumar Maiti, S. Panigrahi, D. Basak and A. Banerjee, *RSC Adv.*, 2012, **2**, 11053–11060.

84 R. I. Randle, L. Cavalcanti, S. Sproules and E. R. Draper, *Mater. Adv.*, 2022, **3**, 3326–3331.

85 E. R. Jira, K. Shmilovich, T. S. Kale, A. Ferguson, J. D. Tovar and C. M. Schroeder, *ACS Appl. Mater. Interfaces*, 2020, **12**, 20722–20732.

86 C. Rehhagen, M. Stolte, S. Herbst, M. Hecht, S. Lochbrunner, F. Würthner and F. Fennel, *J. Phys. Chem. Lett.*, 2020, **11**, 6612–6617.

87 F. Würthner, C. R. Saha-Möller, B. Fimmel, S. Ogi, P. Leowanawat and D. Schmidt, *Chem. Rev.*, 2016, **116**, 962–1052.

88 L. Xu, M. Zhang, X. Zhu, C. Xue, H.-X. Wang and M. Liu, *ACS Appl. Mater. \& Interfaces*, 2022, **14**, 1765–1773.

89 J. G. Egan, G. Brodie, D. McDowall, A. J. Smith, C. J. C. Edwards-Gayle and E. R. Draper, *Mater. Adv.*, 2021, **2**, 5248–5253.

90 M. J. Farooqi, M. A. Penick, J. Burch, G. R. Negrete and L. Brancaleon, *Spectrochim. Acta - Part A Mol. Biomol. Spectrosc.*, 2016, **153**, 124–131.

91 E. V. Alakpa, V. Jayawarna, A. Lampel, K. V. Burgess, C. C. West, S. C. J. Bakker, S. Roy, N. Javid, S. Fleming, D. A. Lamprou, J. Yang, A. Miller, A. J. Urquhart, P. W. J. M. Frederix, N. T. Hunt, B. Péault, R. V. Ulijn and M. J. Dalby, *Chem*, 2016, **1**, 298–319.

92 P. Zhang, A. G. Cheetham, Y. A. Lin and H. Cui, *ACS Nano*, 2013, **7**, 5965–5977.

93 M. J. Webber, J. B. Matson, V. K. Tamboli and S. I. Stupp, *Biomaterials*, 2012, **33**, 6823–6832.

94 F. Kong, M. Lin and T. Qiu, *Luminescence*, 2018, **33**, 1209–1216.

95 P. Chal, A. Shit, D. Levy, S. Das, S. Mondal and A. K. Nandi, *Colloids Surfaces A Physicochem. Eng. Asp.*, 2019, **577**, 480–492.

96 S. M. J. Rogge, A. Bavykina, J. Hajek, H. Garcia, A. I. Olivos-Suarez, A. Sepúlveda-Escribano, A. Vimont, G. Clet, P. Bazin, F. Kapteijn, M. Daturi, E. V. Ramos-Fernandez, F. X. I. Llabrés Xamena, V. Van Speybroeck and J. Gascon, *Chem. Soc. Rev.*, 2017, **46**, 3134–3184.

97 K. H. Park, W. Kim, J. Yang and D. Kim, *Chem. Soc. Rev.*, 2018, **47**, 4279–4294.

98 Q. Cui, Y. Hu, C. Zhou, F. Teng, J. Huang, A. Zhugayevych, S. Tretiak, T. Q. Nguyen and G. C. Bazan, *Adv. Funct. Mater.*, 2018, DOI:10.1002/adfm.201702073.

99 A. T. Haedler, K. Kreger, A. Issac, B. Wittmann, M. Kivala, N. Hammer, J. Köhler, H. W. Schmidt and R. Hildner, *Nature*, 2015, **523**, 196–199.

100 B. Wittmann, F. A. Wenzel, S. Wiesneth, A. T. Haedler, M. Drechsler, K. Kreger, J. Köhler, E. W. Meijer, H.-W. Schmidt and R. Hildner, *J. Am. Chem. Soc.*, 2020, **142**, 8323–8330.

101 J. L. Brédas, E. H. Sargent and G. D. Scholes, *Nat. Mater.*, 2016, **16**, 35–44.

102 Y. Yao, Y. Chen, H. Wang and P. Samorì, *SmartMat*, 2020, **1**, 1–16.

103 S. S. Babu, V. K. Praveen and A. Ajayaghosh, *Chem. Rev.*, 2014, **114**, 1973–2129.

104 C. J. Brabec, N. S. Sariciftci and J. C. Hummelen, *Adv. Funtional Mater.*, 2001, **11**, 15–26.

105 A. Wicklein, S. Ghosh, M. Sommer, F. Würthner and M. Thelakkat, *ACS Nano*, 2009, **3**, 1107–1114.

106 B. Maiti, A. Abramov, R. Pérez-Ruiz and D. Díaz Díaz, *Acc. Chem. Res.*, 2019, **52**, 1865–1876.

107 J. Bachl, A. Hohenleutner, B. B. Dhar, C. Cativiela, U. Maitra, B. König and D. D. Díaz, *J. Mater. Chem. A*, 2013, **1**, 4577–4588.

108 M. Häring, R. Pérez-Ruiz, A. J. Von Wangelin and D. D. Díaz, *Chem. Commun.*, 2015, **51**, 16848–16851.

109 A. J. Dannenhoffer, H. Sai, B. Harutyunyan, A. Narayanan, N. E. Powers-Riggs, A. N. Edelbrock, J. V. Passarelli, S. J. Weigand, M. R. Wasielewski, M. J. Bedzyk, L. C. Palmer and S. I. Stupp, *Nano Lett.*, 2021, **21**, 3745–3752.

110 X. Li, X. Lv, Q. Zhang, B. Huang, P. Wang, X. Qin, X. Zhang and Y. Dai, *J. Colloid Interface Sci.*, 2018, **525**, 136–142.

111 A. J. Bard and L. R. Faulkner, *Electrochemical methods: Fundamentals and Applications*, Wiley, New Jersey, 2nd edn., 2000.

112 H. Song, S. Luo, H. Huang, B. Deng and J. Ye, *ACS Energy Lett.*, 2022, **7**, 1043–1065.

113 G. Liao, Y. Gong, L. Zhang, H. Gao, G. J. Yang and B. Fang, *Energy Environ. Sci.*, 2019, **12**, 2080–2147.

114 T. Banerjee, K. Gottschling, G. Savasci, C. Ochsenfeld and B. V. Lotsch, *ACS Energy Lett.*, 2018, **3**, 400–409.

115 L. Yao, A. Rahmanudin, N. Guijarro and K. Sivula, *Adv. Energy Mater.*, 2018, **8**, 1–18.

116 R. S. Sprick, J. X. Jiang, B. Bonillo, S. Ren, T. Ratvijitvech, P. Guiglion, M. A. Zwijnenburg, D. J. Adams and A. I. Cooper, *J. Am. Chem. Soc.*, 2015, **137**, 3265–3270.

117 K. Kong, S. Zhang, Y. Chu, Y. Hu, F. Yu, H. Ye, H. Ding and J. Hua, *Chem. Commun.*, 2019, **55**, 8090–8093.

118 A. S. Weingarten, A. J. Dannenhoffer, R. V. Kazantsev, H. Sai, D. Huang and S. I. Stupp, *J. Am. Chem. Soc.*, 2018, **140**, 4965–4968.

119 S. Chen, D. L. Jacobs, J. Xu, Y. Li and C. Wang, 2014, 1–10.

120 M. C. Nolan, J. J. Walsh, L. L. E. Mears, E. R. Draper, M. Wallace, M. Barrow, B. Dietrich, S. M. King, A. J. Cowan and D. J. Adams, *J. Mater. Chem. A*, 2017, **5**, 7555–7563.

Chapter 2

High throughput investigation into the photocatalytic activity of perylene bisimides

Acknowledgements

This chapter is based on work in a publication ‘Controlling Activity by Self-Assembly – Tuning Perylene Bisimide Photocatalysts for the Hydrogen Evolution Reaction’ (D. McDowall, B.J. Greeves, R. Clowes, K. McAulay, A.M. Fuentes-Caparrós, L. Thomson, N. Khunti, N. Cowieson, M.C. Nolan, M. Wallace, A.I. Cooper, E.R. Draper, A.J. Cowan and D.J. Adams, Adv. Energy Mater., 2020, DOI:10.1002/aenm.202002469)

This work was carried out as part of a collaboration with Benjamin Greeves and Dr Alex Cowan at the University of Liverpool. As such, much of this Chapter relies on data and work that was not solely performed by the author. The work from collaborators is required to present this work. As such, detailed below is exactly who did what piece of work and it will be made clear in the text also. Both Daniel McDowall and Ben Greeves performed the high throughput photocatalysis together. This involved preparing solutions, setting up and running the equipment as well as analysing and plotting the data. We thank both Professor Andy Cooper and Rob Clowes (University of Liverpool) for providing access and support for the high throughput setup. Ben Greeves carried out the electrochemistry and UV-Vis spectroscopy sample preparation, data collection, analysis and plotting. Daniel McDowall performed the synthesis and characterisation of PBIs and Pt nanoparticles. Daniel McDowall prepared samples for the small angle X-ray scattering (SAXS) as well as analysed and plotted the data.

The SAXS samples were measured on the B21 beamline at Diamond Light Source. They were run by Adams group members Dr Kate McAulay, Ana-Maria Fuentes-Caparros and Lisa Thomson with the assistance of the B21 beamline scientists.

Daniel McDowall prepared samples for and performed the NMR surface charge experiments. The NMR software programmes were written by Dr Matthew Wallace (University of East Anglia), who also assisted greatly with the data analysis.

Abstract

A high throughput experimental setup has been used to screen perylene bismide (PBI) low molecular weight gelators for the light-driven hydrogen evolution reaction from water. By using a high throughput setup, a range of variables including functionalisation, pH and methanol concentration were investigated, resulting in ~350 individual samples being studied in a matter of weeks. Primarily, samples containing 20 v/v% MeOH were studied, where it was found that three of the five PBIs were active and produced peak hydrogen at pH 5. At both low and high pH, minimal hydrogen was produced. Two of the PBIs were inactive, producing minimal hydrogen at all pH values studied. Through a combination of electrochemistry, small angle X-ray scattering, UV-Vis spectroscopy and NMR spectroscopy, it was determined that the formation of 1D nanofibres with a specific molecular packing and charged surfaces provided optimum hydrogen evolution, highlighting both the importance and sensitivity of the self-assembly process for specific applications.

1 Introduction

To combat the effects of greenhouse gas emissions and global warming there is significant research to develop new technologies that reduce our reliance on fossil fuels. One such avenue involves harnessing photons from solar radiation to drive chemical reactions. Of significant interest is the photocatalytic splitting of water (an abundant resource!) which offers a potential route to clean and renewable energy from H_2 and O_2.[1] H_2 and O_2 are valuable chemicals that are used in many chemical processes. Aside from water splitting there is also scope to utilise solar energy for a wide range of other reactions such as CO_2 reduction and photochemistry.[2,3]

To make such systems viable, they must be efficient and cheap to produce. Strong absorption in the solar spectrum of light as well as the correct energy levels to drive the reaction in question are required. For water splitting other considerations such as spatial separation of H_2 and O_2 evolution (to prevent the formation of potentially explosive mixtures) are also required. The first work (in 1972) reporting the photocatalytic splitting of water to form H_2 and O_2 gas used TiO_2 as a photocatalyst.[4] Since then there has been a large amount of research into the design of materials that can perform water splitting. Many of these are based on inorganic systems, such as doped TiO_2[5] but there is also research into organic compounds that can be used to perform the photocatalytic splitting of water.[6] These have the benefits of often being cheaper to make and are comprised of earth abundant materials.

1.1 Organic Photocatalysis

Organic photocatalysts for the solar energy driven water oxidation, hydrogen evolving reaction (HER) and oxygen evolving reaction (OER) have been subject to significant amounts of research.[7–10] Organic photocatalysts are highly desirable due to being comprised of earth abundant materials. There have been many reported organic photocatalysts such as graphitic carbon nitride (g-C_3N_4),[10,11] polymer dots (Pdots),[12] conjugated microporous polymers (CMPs)[13] and covalent organic frameworks (COFs).[14]

g-C_3N_4 was first reported for hydrogen evolution from water in 2009.[11] The researchers achieved steady metal-free H_2 evolution from water under visible light ($\lambda > 420$ nm) with triethanolamine (TEA) as a sacrificial electron donor. However, the metal-free H_2 activity exhibited variation in repeats, a problem which they improved through adding Pt nanoparticles. The nanoparticles facilitate electron localisation from the carbon nitride conduction band, leading to increased H_2 production. This is attributed to H_2 elimination from Pt-H surface bonds being favoured over elimination from the carbon nitride surface.

COFs were first reported in 2005, comprising of molecular building blocks connected by covalent bonds to form crystalline structures.[15] The synthesis of "COF-1" (Figure 1) involved the dehydration of diboronic acid molecules. This created a new class of rigid, highly porous organic polymers with 2D or 3D structures which typically exhibit good thermal stabilities. The first report of a COF being used for photocatalytic H_2 production was published in 2014.[16] This used a hydrazine-based COF (TFPT-COF) built from 1,3,5-tris-(4-formyl-phenyl)triazine and 2,5-diethoxy-terepthalohydrazide.

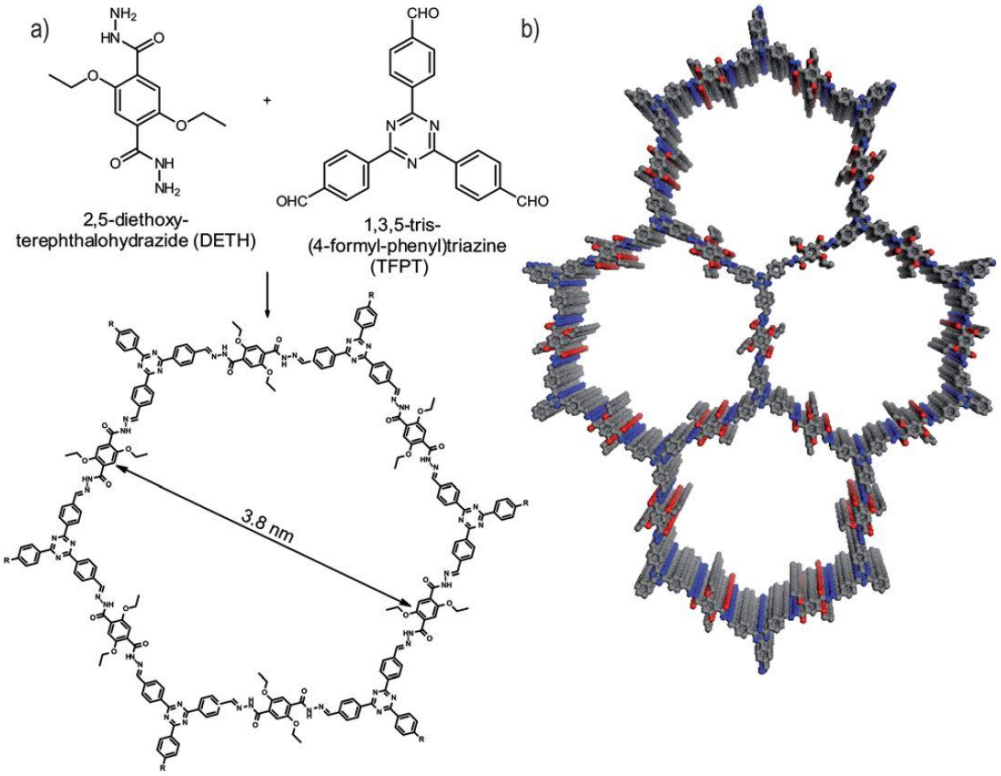

Figure 1. (a) Scheme showing the condensation of the monomers to form a covalent organic framework; (b) A cartoon showing the hexagonal structure of the COF. Reproduced from L. Stegbauer, K. Schwinghammer and B. V. Lotsch, Chem. Sci., 2014, 5, 2789–2793, with permission from The Royal Society of Chemistry (Copyright © 2014) under the Creative Commons Attribution 3.0 Unported (CC BY-NC 3.0) licence.

1.2 Perylene bisimides

Perylene tetracarboxylic diimides (Figure 2, left side), also known as PBIs and their derivatives have received a significant amount of interest both in industrial dye and pigment applications as well as in academic research.[17–20] For many years, PBIs have been used in industrial pigments due to their strong colour (commonly deep reds and purple), low

solubility and chemical and thermal stability. The colour of PBIs depends on chemical functionalisation, concentration and aggregation.

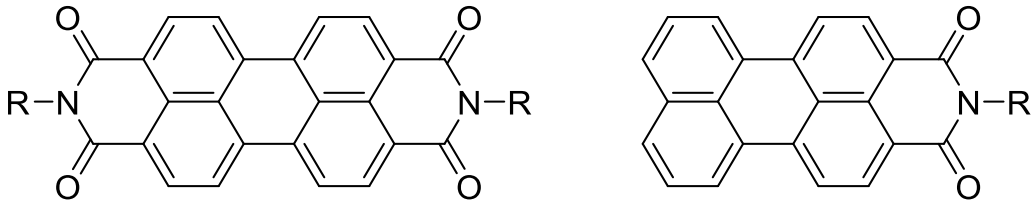

Figure 2. Chemical structures of PBI (left) and PMI (right). They can be readily functionalised at the imide position (R group).

PBIs have been used in organic electronics, photovoltaic devices and photocatalytic applications.[21,22] PBIs frequently exhibit n-type semiconductor behaviours and have large absorption coefficients in the visible light region.[18,23] Depending on how they are functionalised, the material properties of PBIs can be modulated. Functionalising the aromatic perylene core typically changes the energy levels of the molecule. For example, electron withdrawing substituents can allow for the tuning of the PBIs LUMO levels.[24] Changing the imide position substituent does not tend to significantly change the optical and electronic properties but plays an important role in the solubility and non-covalent interactions. Many PBIs can self-assemble and form gels, a process driven by non-covalent interactions such as π-π stacking, hydrogen bonding and Van der Waals forces.[17,25–27] One particular area of interest for PBIs, as well as other derivatives such as PMIs (Figure 1, right side), is the field photochemical reactions.[23,28,29] Generally, the perylene component acts to harvest light and generate an exciton.

In work reported in 2006, an organic bilayer composed of a PBI (n-type semiconductor) and a pthalocyanine (p-type semiconductor) with an outer surface of IrO_2 was used as a photoanode for O_2 evolution from an aqueous solution of KOH (Figure 3).[30] The PBI layer efficiently harnesses visible light, resulting in exciton formation. Charge separation then occurs at the p/n interface with hole conduction through the phthalocyanine interface and O_2 evolution at the IrO_2/H_2O interface.

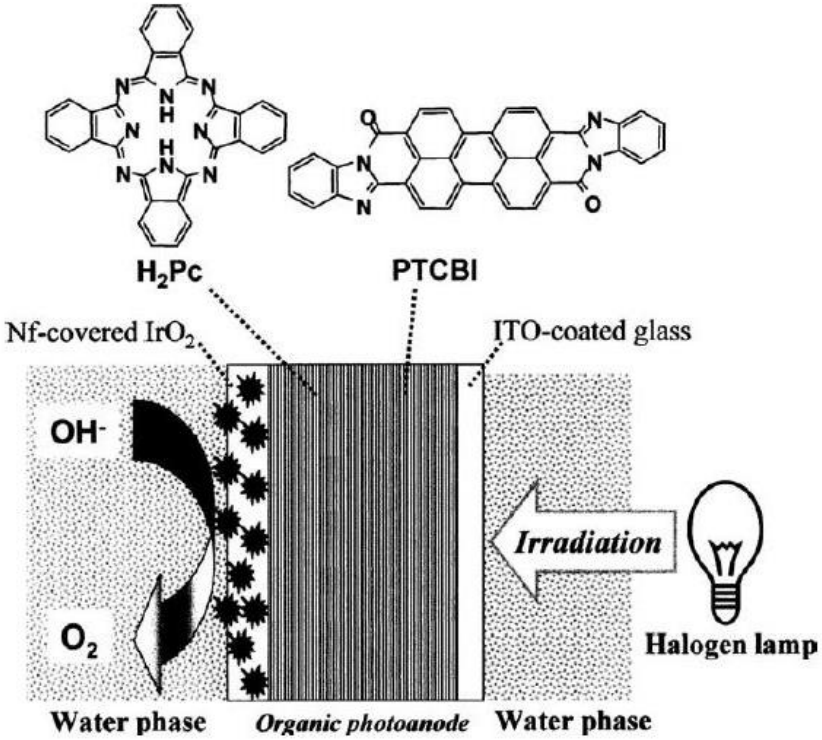

Figure 3. Chemical structures of the PBI (PTCBI in the figure) and phthalocyanine derivates used for the p/n bilayer with a schematic for light driven O_2 evolution. Reprinted from T. Abe, K. Nagai, T. Ogiwara, S. Ogasawara, M. Kaneko, A. Tajiri and T. Norimatsu, J. Electroanal. Chem., 2006, 587, 127–132, Copyright© 2006 with permission from Elsevier.

Similarly, a phosphonic acid functionalised PBI was used on an ITO/PBI/CoO_x electrode for the visible-light-driven oxidation of water to produce O_2.[28] Control experiments without the CoO_x yielded no O_2. In this paper, the PBI plays the role of absorbing the light and then transporting the exciton to the CoO_x. The authors found that if the films were significantly thicker than a typical exciton diffusion length, lower photocurrents were observed. They attribute this to the majority of excitons formed undergoing a relaxation process before they can dissociate into useable charges. They performed control experiments with a similar PBI that did not have a phosphonic acid group. ITO/PBI/CoO_x anodes made with this PBI showed photocurrents an order of magnitude lower than the phosphonic acid PBI. These findings are interesting because they suggest the phosphonic acid groups are important in efficiently linking the organic film to the CoO_x catalyst.

Visible-light-driven H_2 evolution from water was performed using 1D nanofibre composites with dodecyl and/or dimethylaniline functionalised PBIs.[31] Self-assembly and fibre formation was driven by a solvent switch from a good to a bad solvent. Pt and/or TiO_2 was then deposited onto the nanofibres. These fibres were dispersed into an aqueous solution of 10 % of either MeOH or TEA and irradiated under a 400 W xenon lamp with a filter removing any light below 420 nm. H_2 evolution was observed from each of the three PBIs studied,

however, the dimethylaniline functionalised PBIs showed more H_2 evolution compared to the dodecyl functionalised PBI. The proposed mechanism for the process is as follows. The PBI acts as the photocatalyst and, upon excitation with visible light, there is an electronic transition from the PBIs HOMO to LUMO, generating a hole. Where the electron donating dimethylaniline substituent is present, this transfers an electron to fill the hole, resulting in a charge separation between the PBI backbone and the now positively charged aniline substituent. The 1D nanofibre with π-π stacking between PBI molecules allows for the delocalisation of the electron along the nanofibre which reduces charge recombination and allows for more efficient transfer to the TiO_2. The TiO_2 was employed as an electron relay to transfer the electron to the Pt which then acts as the location at which water is reduced to form H_2. The positive charge on the dimethylaniline is neutralised by the MeOH or TEA, which are employed as sacrificial electron donors. This work is interesting as it demonstrates the importance of the PBI functionalisation as well as the role of the 1D nanostructures in the photocatalytic process.

One group used the self-assembled structures of an un-substituted PBI (a hydrogen atom on the imide nitrogen i.e. R=H in Figure 1, left side) for the photodegradation of phenol and cationic and anionic dyes.[32] The self-assembled structures were also used for visible light ($\lambda > 420$ nm) splitting of water to form O_2 in the presence of $AgNO_3$ as an electron acceptor. In this work the self-assembly was triggered by a switch from a good solvent to a bad one. The powders of self-assembled PBI were then dispersed in aqueous media for use as a photocatalyst. This work is interesting as it does not employ the use of Pt, TiO_2 or CoO_x as is commonly used in PBI photocatalysis systems.

In other work, researchers used self-assembled nanoribbons formed from a PMI for photocatalysis.[33] The PMI formed nanoribbons in solution and underwent gelation upon the addition of salts. For photocatalytic H_2 production, they chose a nickel catalyst ($[Ni(P_2N_2)_2](BF_4)_2(NiP_2N_2)$) and used ascorbic acid as a sacrificial electron donor. Interestingly, they found that the nickel catalyst also induced the crystallisation and formation of a hydrogel. The addition of the nickel catalyst to the PMI solution resulted in a large blue shift in the absorbance, which is attributed to a strong coulombic coupling between the nickel catalyst and the light-harvesting PMI assemblies. It is suggested that the carboxylate-terminated nanoribbons present binding sites for the nickel catalyst. They observed that all gels produced significantly more H_2 when compared with the solid precipitate of the protonated PMI, which demonstrates the importance of the hydrated gel structure.

1.3 Introduction to the work in this Chapter

The aim of this work was to continue on from a previous study using amino acid functionalised PBIs. In this work, the photocatalytic production of H_2 from an aqueous system of a phenylalanine functionalised PBI in the presence of polyvinylpyrrolidone (PVP) capped Pt nanoparticles (co-catalyst) and MeOH has been reported within our group.[34] The interesting finding in this work is the strong pH dependence on the amount of H_2 produced. The self-assembly of this PBI is triggered by pH (owing to the carboxylic acid groups) thus suggesting a relationship between pH induced self-assembly of the PBIs and photocatalytic performance. This work hypothesises that the nanofibres are critical in transporting the electron to the Pt nanoparticles where the reaction can then take place.[34] Here, as with many other reported systems, MeOH is used as a sacrificial electron donor. The self-assembly and gelation as well as photoconductivity of these amino acid functionalised PBIs has been studied previously.[27,35] The photoconductivity arises from the formation of the PBI radical anion and this only occurs with wavelengths of light < 400 nm. Small angle neutron scattering (SANS) data show significant variation in the diameters and lengths of the self-assembled fibres. The work showed that different amino acid groups had a large impact on the optoelectronic properties of the PBIs, which is likely due to differences in the self-assembly and molecular packing. It is therefore reasonable to expect that differences may also be seen in the photocatalytic activity of these PBIs.

The first steps were to test a wider range of PBIs for photocatalytic water splitting and investigate the underlying cause of any trends seen in the photocatalytic activity. Five amino acid functionalised PBIs were synthesised and screened using high throughput methods to determine which were most effective. The high throughput studies allow for hundreds of samples to be screened with relative ease, meaning that optimum conditions can be identified. Then, investigations into the molecular packing, supramolecular structure and nanofibre surface charge were used to correlate the key variables that lead to the higher activity. The work here is focussed on understanding the supramolecular chemistry that governs the effectiveness of these materials as photocatalysts. At this stage the absolute values of H_2 produced are not important, but rather it is the comparison between the amounts formed that is useful.

2 Results

2.1 High throughput photocatalysis

Previous work has shown the photocatalytic water splitting to produce H_2 from PBI-F.[34] Building upon this work, 5 mg/mL solutions of PBI-A, F, V, Y and H (Figure 4) at a range pH values in the presence of 1 mol% PVP capped Pt nanoparticles and 20 %vol MeOH were studied.

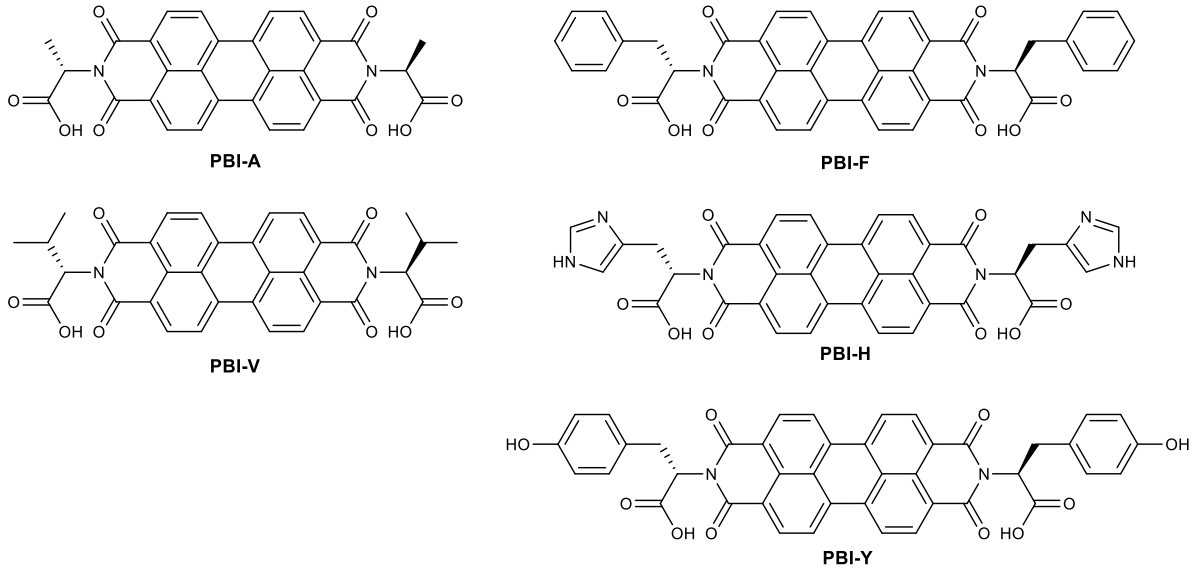

Figure 4. The five PBIs studied in this work for photocatalytic splitting water to produce H_2

To screen hundreds of samples in a short space of time, experiments were performed with our collaborators at the Materials Innovation Factory (MIF), University of Liverpool. The setup at the MIF enabled automation, and hence significantly improved time efficiency (Figure 5). All of the components were combined in glass vials and then pH adjusted with either HCl or NaOH (depending on the desired pH) under rigorous stirring. The samples were purged with N_2 and capped in an automated system and then irradiated under a solar simulator for 3 hours. These were then analysed using a headspace gas chromatography instrument fitted with an autosampler to test for H_2, CH_4 and CO gas. The pH values studied were 2.0, 3.0, 3.5, 4.0, 4.5, 5.0, 6.0, 7.0, 8.0 and 10.0. A particular focus was placed on the pH range of 3 to 5 (with smaller pH increments studied) as published work studying PBI-F showed this to be important.[34] At pH 6.0 and above, all the samples were solutions whereas at pH 5.0 and below all samples formed large aggregates (visible to the eye) that were formed as a result gelation occurring under stirring. The exception to this is the PBI-H sample at pH 2, which re-dissolved due to the protonation of the imidazole ring.

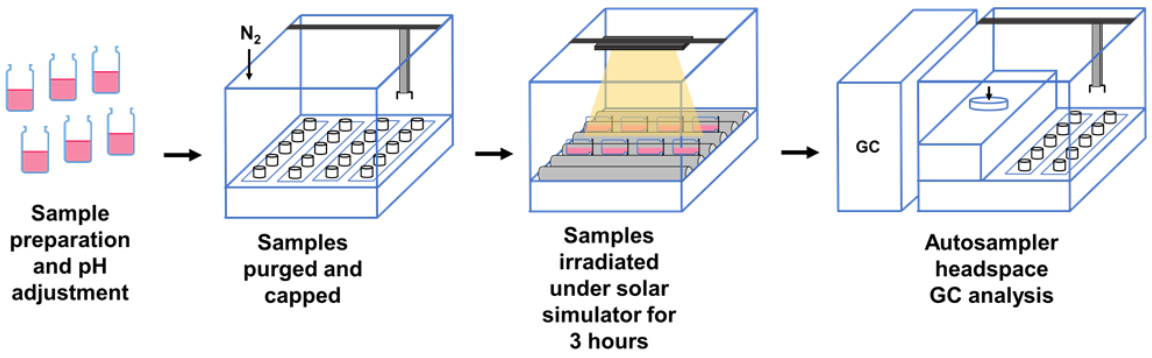

Figure 5. Cartoon schematic of sample preparation and analysis performed at the MIF. Reproduced from D. McDowall, B.J. Greeves, R. Clowes, K. McAulay, A.M. Fuentes-Caparrós, L. Thomson, N. Khunti, N. Cowieson, M.C. Nolan, M. Wallace, A.I. Cooper, E.R. Draper, A.J. Cowan and D.J. Adams, Adv. Energy Mater., 2020, DOI:10.1002/aenm.202002469 with permission from Wiley-VCH Verlag GmbH & Co. KGaA (Copyright © 2020) under the Creative Commons CC-BY (version 4.0) license.

Across all these samples H_2 was seen in significant amounts for PBI-A, -F and -V, in which there was a clear dependence on sample pH (Figure 6). At pH >5 negligible amounts of H_2 were seen. The transition from pH 6 to pH 5 represents a “switching-on” of H_2 production for all three of these compounds. After pH 5, the H_2 produced decreases steadily until none is produced at pH 2. For PBI-Y and -H, negligible H_2 is produced at all pH values, and these PBIs are designated as inactive. With this result, 5 chemically similar PBIs exhibit different photocatalysis behaviour, falling into one of two groups, active or inactive. The transition from pH 6 to pH 5 represents a switching-on of photocatalysis and coincides with a transition from solution to gel.

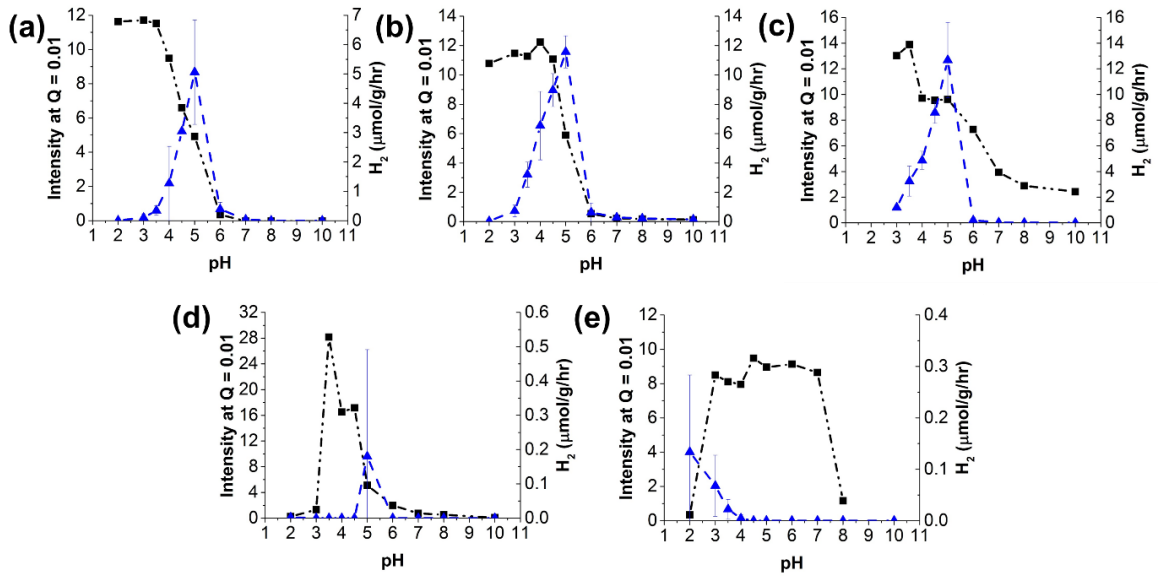

Figure 6. H_2 evolution data overlaid with SAXS intensity at Q = 0.01 $Å^{-1}$ for (a) PBI-A; (b) PBI-F; (c) PBI-V; (d) PBI-Y and (e) PBI-H. Reproduced from D. McDowall, B.J. Greeves, R. Clowes, K. McAulay, A.M. Fuentes-Caparrós, L. Thomson, N. Khunti, N. Cowieson, M.C. Nolan, M. Wallace, A.I. Cooper, E.R. Draper, A.J. Cowan and D.J. Adams, Adv. Energy Mater., 2020, DOI:10.1002/aenm.202002469 with permission from Wiley-VCH Verlag GmbH & Co. KGaA (Copyright © 2020) under the Creative Commons CC-BY (version 4.0) license.

The influence of the MeOH sacrificial electron donor was also investigated and the results are summarised in contour plots (Figure 7). For PBI-A, the rate of H_2 is broadly unaffected and remains (relatively) high from 5 – 40 v/v% MeOH. There is a subtle impact of the pH, where peak H_2 is seen at pH 4 for 10 v/v% MeOH. The greatest rate of H_2 produced is seen at pH 5 with 30 v/v% MeOH. At 0 v/v% MeOH the rate of H_2 production is very low, showing the importance of the sacrificial electron donor. In the absence of the MeOH, it is probable that fast carrier recombination occurs, preventing charge transfer to the Pt.[36] For PBI-Y, the rate of H_2 production is very low across the contour plot but where H_2 is seen it peaks at pH 5.

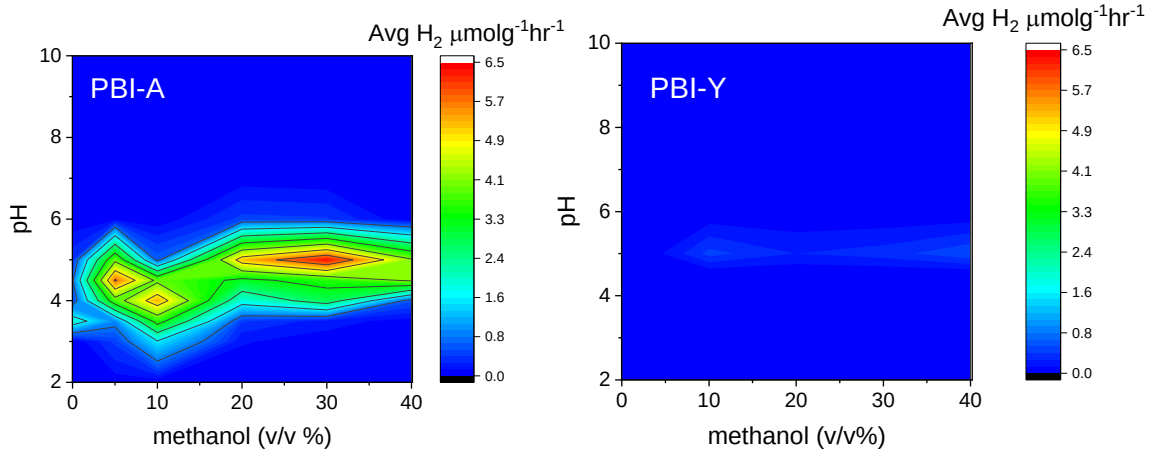

Figure 7. Contour maps showing the rates of H_2 production across the variables of both pH and methanol for PBI-A (left) and PBI-Y (right). Reproduced from D. McDowall, B.J. Greeves, R. Clowes, K. McAulay, A.M. Fuentes-Caparrós, L. Thomson, N. Khunti, N. Cowieson, M.C. Nolan, M. Wallace, A.I. Cooper, E.R. Draper, A.J. Cowan and D.J. Adams, Adv. Energy Mater., 2020, DOI:10.1002/aenm.202002469 with permission from Wiley-VCH Verlag GmbH & Co. KGaA (Copyright © 2020) under the Creative Commons CC-BY (version 4.0) license.

The factors that determine the observed trends in H_2 rate were then investigated in greater detail, with a particular focus on PBI-A and PBI-Y as both active and inactive materials respectively. To start with the electrochemical feasibility of the HER was investigated. The proposed mechanism of the hydrogen reduction derives from the generation of the PBI radical anion ($PBI^{\bullet-}$) and dianion (PBI^{2-}). Square wave voltammetry (SWV) was used to measure the reduction potentials from pH 10 to 4.5. Lower pH samples could not be measured due to the formation of a gel network. For PBI-A, electrochemical measurements show that the HER is thermodynamically possible from the anion ($PBI^{\bullet-}$) and dianion (PBI^{2-}) species below pH 8 (Figure 8a). For PBI-Y (Figure 8b), the HER is thermodynamically possible from below pH 7 (singly reduced species) and below pH 6 (doubly reduced species). The feasibility of the HER reaction does not correlate with the observed switching on of the H_2 production. As such, other factors including molecular packing, self-assembled structure and nanofibre surface charge were investigated.

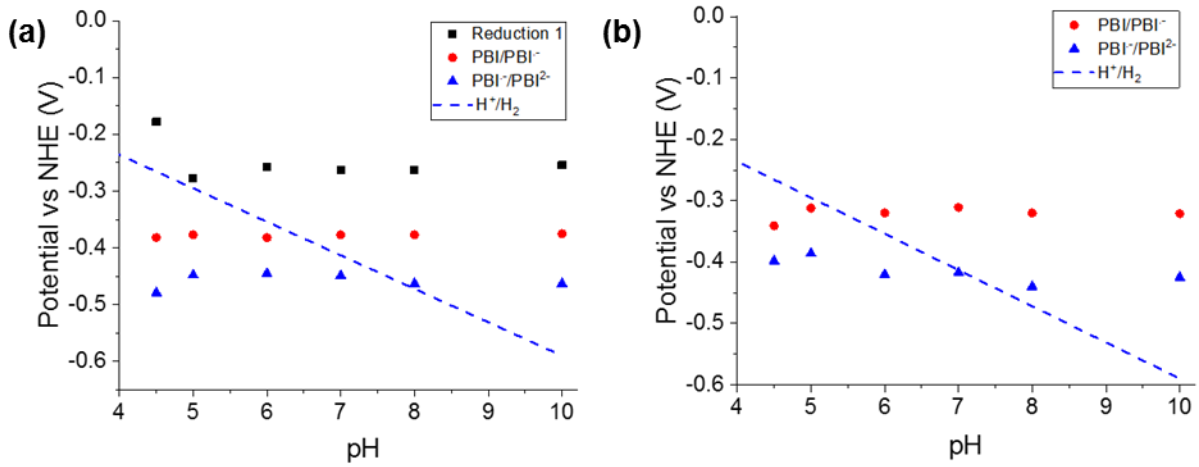

Figure 8. Reduction potentials of (a) PBI-A and (b) PBI-Y with pH. Potentials were determined from square wave voltammetry (SWV). H^+/H_2 line represents the potential for proton reduction to occur at each pH. SWV experiments were performed by Benjamin Greeves. Reproduced from D. McDowall, B.J. Greeves, R. Clowes, K. McAulay, A.M. Fuentes-Caparrós, L. Thomson, N. Khunti, N. Cowieson, M.C. Nolan, M. Wallace, A.I. Cooper, E.R. Draper, A.J. Cowan and D.J. Adams, Adv. Energy Mater., 2020, DOI:10.1002/aenm.202002469 with permission from Wiley-VCH Verlag GmbH & Co. KGaA (Copyright © 2020) under the Creative Commons CC-BY (version 4.0) license.

2.2 Self-assembled structure

Based on previous literature, it was hypothesised that the self-assembled structures would be an important factor in the photocatalysis.[34] For these PBIs, the transition from pH 6 to pH 5 represents the onset of gelation. In this instance, the pH is lowered during stirring, which prevents the formation of a self-supporting gel network, but aggregates of gel were formed. It is assumed that the primary structures are unaffected by the stirring. Conventional methods of studying nanomaterials, such as scanning electron microscopy (SEM), are commonly unsuitable for self-assembled nanostructures due to drying artefacts.[37] Additionally, they only allow the probing of a very small area of sample, which may not be representative. Small angle X-ray scattering (SAXS) is a technique that enables the nanostructures (on the size range of 5-500 nm) to be probed *in situ* and in a hydrated state. A large sample area is analysed, where commonly the X-ray beam impinging on the sample is of the size range of 1 mm x 0.5 mm. Consequently, the information gained is representative of all of the structures present in the samples. SAXS data is typically plotted as a scattering vector (Q) vs intensity (I) plot. Scattering at low Q is derives from larger structures, as such, an increase in scattering intensity would be associated with an increase in the presence of large self-assembled structures. It was hypothesised that the self-

assembly of the PBIs into larger aggregates would improve charge separation and transport, and lead to increased H_2 production rates.

As a simple analysis, the scattering intensity at low Q can be plotted with pH and H_2 evolution (Figure 5). For the three active PBIs, there is a correlation between the increase in scattering at Q = 0.01 $Å^{-1}$ (scattering from larger structures) and the onset of significant H_2 evolution, which supports the hypothesis. While helpful, this analysis is overly simplistic because the scattering intensity reaches a maximum which is maintained to pH 2, where no H_2 produced. For more in-depth analysis, the scattering data at each pH were fitted to structural models in SasView, a fitting software for scattering data.[38] Model fitting is a widely used method to analyse scattering data.[39]

2.2.1 PBI-A

For PBI-A the scattering data (Figure 9) at pH 10 – 7 show an increase in scattering intensity until a plateau at Q = 0.1 $Å^{-1}$, at which point it decreases again with no scattering detected at lowest Q. This high pH data was best fit to the sphere model (Table 1), depicting small spherical aggregates with a radius of 1.0 nm. Then at pH 6, a combined model of a sphere and power law were required to fit the data, suggesting a co-existence of small spherical aggregates as well as some larger structures, resulting in higher low Q scattering. There is a clear transition in the scattering patterns from pH 6 to pH 5 the bump at high Q is largely lost and the scattering intensity at low Q increases by approximately an order of magnitude. Additionally, the shape of the scattering curve changes significantly, indicating a change of structure.[40]

To fit the data at pH 5, a combined model of flexible cylinder and sphere was required. The fit depicts flexible cylindrical fibres with a radius of 3.5 nm, a length of 120 nm and a Kuhn length of 22 nm. The Kuhn length is a term that represents the stiffness of the cylindrical structure, where larger Kuhn lengths depict more rigid cylinders. A polydispersity of radius was required to fit the data, indicating a size distribution in the nanofibre radius. Also, the fibre length obtained from the fitting is outside the length scale that can be probed by SAXS meaning that value is less accurate. SEM images in previous work on PBI-A has shown that the nanofibres persist over lengths of 1000-2000 nm.[27,35] The subsequent fitting for the pH 4.5 and 4.0 data depict similar structures but do not require a spherical component. Any small aggregates present at pH 5.0 appear to have aggregated further with the lowering of pH. Finally, the structures depicted from pH 4.0 to 2.0 show similar structures but the addition of a power law component to the model was required. The power law captures the increased scattering intensity at low Q and is often associated with scattering from a gel network.

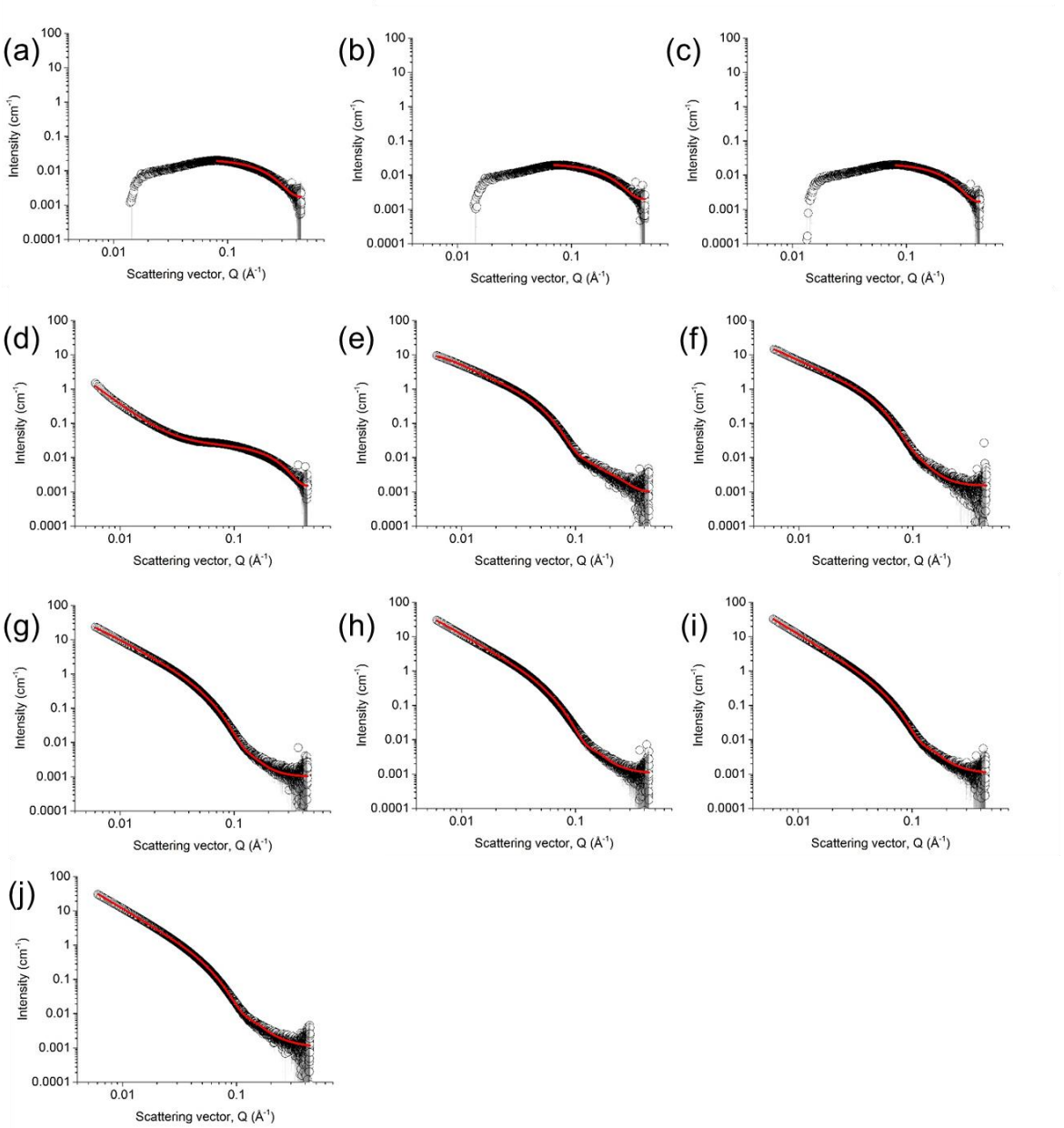

Figure 9. SAXS data for PBI-A showing scattering vector vs scattering intensity (open black circles) with the corresponding model fits (solid red lines; models used are described in Table 1). 5 mg/mL PBI-A with 20 v/v% MeOH at pH (a) 10; (b) 8; (c) 7; (d) 6; (e) 5; (f) 4.5; (g) 4; (h) 3.5; (i) 3; (j) 2. Reproduced from D. McDowall, B.J. Greeves, R. Clowes, K. McAulay, A.M. Fuentes-Caparrós, L. Thomson, N. Khunti, N. Cowieson, M.C. Nolan, M. Wallace, A.I. Cooper, E.R. Draper, A.J. Cowan and D.J. Adams, Adv. Energy Mater., 2020, DOI:10.1002/aenm.202002469 with permission from Wiley-VCH Verlag GmbH & Co. KGaA (Copyright © 2020) under the Creative Commons CC-BY (version 4.0) license.

pH	Model	Length / nm	Kuhn length / nm	Cylinder radius / nm	Sphere radius / nm	Power law	Reduced Chi squared
2	Flexible cylinder with a polydispersity of radius 0.2 + power law	680*	5.9 ± 0.08	3.2 ± 0.01	-	2.7 ± 0.00	3.4
3	Flexible cylinder with a polydispersity of radius 0.2 + power law	680*	5.7 ± 0.07	3.1 ± 0.01	-	2.7 ± 0.00	1.3
3.5	Flexible cylinder with a polydispersity of radius 0.2 + power law	680*	5.6 ± 0.06	3.0 ± 0.01	-	2.7 ± 0.00	3.7
4	Flexible cylinder with a polydispersity of radius 0.25	680*	6.3 ± 0.05	3.0 ± 0.00	-	-	3.9
4.5	Flexible cylinder with a polydispersity of radius 0.3	220 ± 2.7	24.3 ± 0.07	3.5 ± 0.00	-	-	3.4
5	Flexible cylinder with a polydispersity of radius 0.25 + Sphere	130 ± 0.52	22 ± 0.08	3.5 ± 0.00	1.0†	-	2.7
6	Sphere + Power law	-	-	-	1.0 ± 0.00	2.6 ± 0.01	1.0
7	Sphere	-	-	-	1.0 ± 0.00	-	<1
8	Sphere	-	-	-	1.0 ± 0.00	-	<1
10	Sphere	-	-	-	1.0 ± 0.00	-	<1

Table 1. Model fitting results for PBI-A at 5 mg/mL and 20 v/v% MeOH at a range of pH. * No fitting error available. Length increased to an unrealistically large number with further fitting. Length set to 680 nm and a power law added to capture the intensity at low Q. This suggests the presence of structures longer than measurable by this SAXS setup. † No fitting error available. Bump at high Q attributed to small aggregates as seen at high pH. Sphere radius set to 1.0 nm based on the high pH fitting.

2.2.2 PBI-V

For PBI-V, similar trends to PBI-A are seen, but there is a greater low Q scattering intensity at high pH (Figure 10). At all pH, the data required a cylindrical model to adequately fit the data, however for pH >5.0, a spherical model was also required in the fit. For pH 7 – 10, the fits depict cylindrical structures with a radius of around 7 nm (Table 2). This is consistent with the co-existence worm-like micelles and small spherical aggregates at high pH. PBI-V has previously been reported to form worm-like micelles at high pH.[27] At pH 6.0, the data were best fit to a flexible elliptical cylinder model with a spherical component. The fit depicts cylinders that are of a radius of 2.9 nm and an axis ratio of 4.6. This shows a transition from relatively wide cylindrical nanofibres to belt-like nanofibres with the lowering of pH. At pH 6.0, there are spherical aggregates present, evidenced by the large bump at high Q and requirement for a spherical model.

At pH 5.0, the data were fitted to a flexible elliptical cylinder model, without the requirement for a spherical model. This suggests that any small spherical aggregates that were present at pH 6.0 have now self-assembled to form 1D structures. The pH 6.0 to pH 5.0 transition is also accompanied by an increase in scattering intensity at low Q, although this is less pronounced than is seen for PBI-A and PBI-F. For PBI-V, the requirement for an elliptical component as pH is lowered is indicative of the lateral association of the 1D structures. This may occur as carboxylate groups are protonated with decreasing the pH, resulting in a reduction in surface charge. From pH 5.0 to pH 3.0, the self-assembled structures present remain largely unchanged. The fitting suggests an increase in the Kuhn length of the fibres as pH is lowered, but there is not a significant shift in structure.

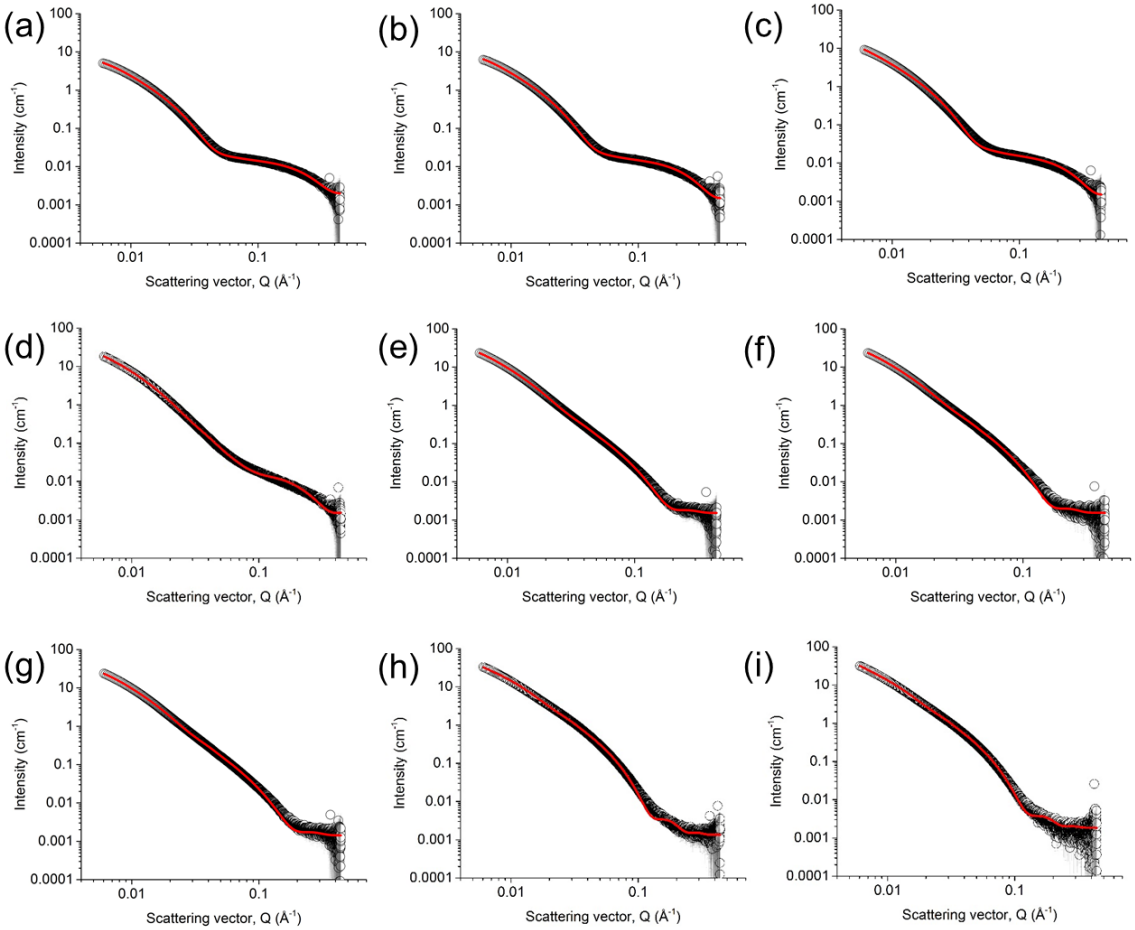

Figure 10. SAXS data for PBI-V showing scattering vector vs scattering intensity (open black circles) with the corresponding model fits (solid red lines; models used are described in Table 2). 5 mg/mL PBI-V with 20 v/v% MeOH at pH (a) 10; (b) 8; (c) 7; (d) 6; (e) 5; (f) 4.5; (g) 4; (h) 3.5; (i) 3; (j) 2. Reproduced from D. McDowall, B.J. Greeves, R. Clowes, K. McAulay, A.M. Fuentes-Caparrós, L. Thomson, N. Khunti, N. Cowieson, M.C. Nolan, M. Wallace, A.I. Cooper, E.R. Draper, A.J. Cowan and D.J. Adams, Adv. Energy Mater., 2020, DOI:10.1002/aenm.202002469 with permission from Wiley-VCH Verlag GmbH & Co. KGaA (Copyright © 2020) under the Creative Commons CC-BY (version 4.0) license.

pH	Model	Length / nm	Kuhn length / nm	Cylinder radius / nm	Axis ratio	Sphere radius / nm	Reduced Chi squared
3	Flexible elliptical cylinder	280 ± 0.00	70.5 ± 0.66	2.7 ± 0.00	7.1 ± 0.01	-	4.8
3.5	Flexible elliptical cylinder	370 ± 0.00	93 ± 2.43	2.7 ± 0.00	7.2 ± 0.01	-	10.4
4	Flexible elliptical cylinder	280 ± 2.00	13.4 ± 0.04	1.7 ± 0.00	8.0 ± 0.02	-	3.3
4.5	Flexible elliptical cylinder	240 ± 2.28	19.5 ± 0.08	1.9 ± 0.00	7.7 ± 0.02	-	4.1
5	Flexible elliptical cylinder	290 ± 2.18	13.2 ± 0.03	1.7 ± 0.00	8.1 ± 0.02	-	2.6
6	Flexible elliptical cylinder + Sphere	580 ± 20.33	5.9 ± 0.28	2.9 ± 0.03	4.6 ± 0.04	1.0*	1.9
7	Flexible cylinder with a polydispersity of radius 0.25 + Sphere	405 ± 13.41	11.7 ± 0.55	7.3 ± 0.05	-	1.0*	5.8
8	Flexible cylinder with a polydispersity of radius 0.25 + Sphere	314 ± 14.06	10.8 ± 0.69	7.3 ± 0.06	-	1.0*	2.3
10	Flexible cylinder with a polydispersity of radius 0.25 + Sphere	282 ± 15.10	10.2 ± 0.79	7.0 ± 0.07	-	1.0*	2.5

Table 2. Model fitting results for PBI-V at 5 mg/mL and 20 v/v% MeOH at a range of pH. *No fitting error available. Bump at high Q attributed to small aggregates. High Q bump region fitted independently to sphere model and this radius used as a fixed value in the fit of the whole Q range.

2.2.3 PBI-F

For PBI-F (Figure 11) at pH 7.0 to pH 10.0, the SAXS data were fitted to both a sphere and a power law. As before, the sphere components depict small spherical aggregates. Here, the data show a small but not insignificant scattering intensity at low Q, meaning that a power law component was required (as was seen for PBI-A pH 6.0). Here, the two models were fitted to the two regions separately (Table 3) due to the decrease in scattering intensity from the sphere model region (high Q) to the power law region (low Q). This should not be present in an “ideal” data set and meant that the data could not be fitted with one combined model. This could be due to the background subtraction on a sample that exhibits relatively low scattering intensity. At pH 6.0, a combined model of a sphere with a flexible cylinder was required to fit the data which, as before, indicates the co-existence of two structures. From pH 6.0 to pH 5.0, a transition occurs, where the spherical component is no longer required. There is also a stark transition in the self-assembled cylinders present. As well as the requirement for an elliptical component in the cylinder model, there is a reduction in the radius of the cylinder. Moving to pH 4.5 and lower, there is a transition from elliptical cylinders back to spherical cross-section cylinders. Additionally, there is an increase in the cylinder radius. Crucial to the interpretation of this is that a relatively high polydispersity of radius (0.3) is required to fit the data. This suggests the association of cylinders present at pH 5.0 into poorly defined (in terms of radius) cylindrical aggregates.

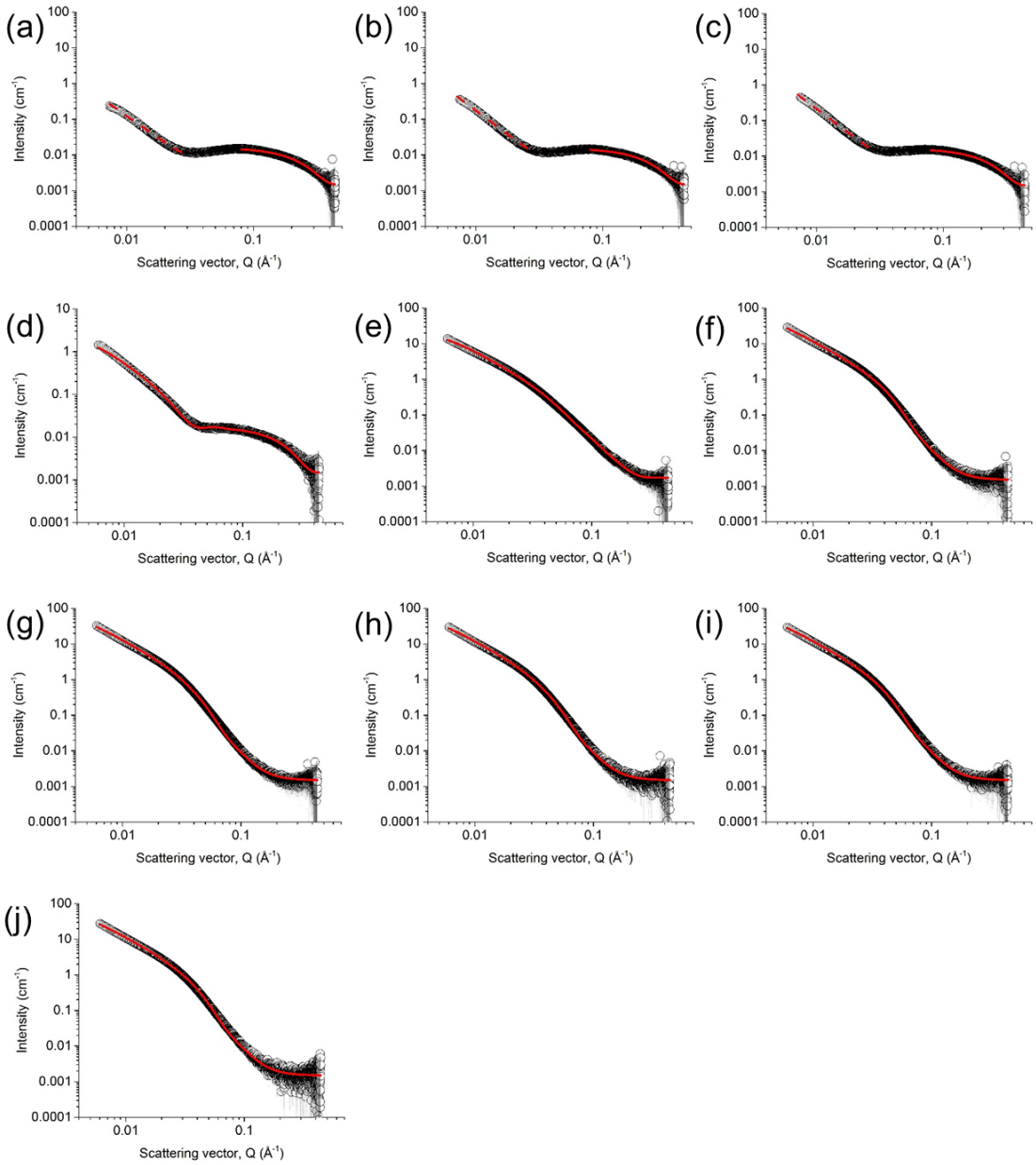

Figure 11. SAXS data for PBI-F showing scattering vector vs scattering intensity (open black circles) with the corresponding model fits (solid red lines; models used are described in Table 3). 5 mg/mL PBI-F with 20 v/v% MeOH at pH (a) 10; (b) 8; (c) 7; (d) 6; (e) 5; (f) 4.5; (g) 4; (h) 3.5; (i) 3; (j) 2. For the pH 10, 8 and 7 data, two regions were fitted separately, here the power law fits are displayed by dashed red lines. Reproduced from D. McDowall, B.J. Greeves, R. Clowes, K. McAulay, A.M. Fuentes-Caparrós, L. Thomson, N. Khunti, N. Cowieson, M.C. Nolan, M. Wallace, A.I. Cooper, E.R. Draper, A.J. Cowan and D.J. Adams, Adv. Energy Mater., 2020, DOI:10.1002/aenm.202002469 with permission from Wiley-VCH Verlag GmbH & Co. KGaA (Copyright © 2020) under the Creative Commons CC-BY (version 4.0) license.

pH	Model	Length / nm	Kuhn length / nm	Cylinder radius / nm	Axis ratio	Sphere radius / nm	Power law	Reduced Chi squared
2	Flexible cylinder with a polydispersity of radius 0.3	400*	13.0 ± 0.06	5.0 ± 0.01	-	-	-	7.5
3	Flexible cylinder with a polydispersity of radius 0.3	420*	13.7 ± 0.05	4.8 ± 0.00	-	-	-	8.6
3.5	Flexible cylinder with a polydispersity of radius 0.3	470*	9.4 ± 0.08	4.5 ± 0.01	-	-	-	8.9
4	Flexible cylinder with a polydispersity of radius 0.3	500*	9.4 ± 0.08	4.6 ± 0.01	-	-	-	9.8
4.5	Flexible cylinder with a polydispersity of radius 0.3	400*	13.9 ± 0.04	4.6 ± 0.00	-	-	-	10.3
5	Flexible elliptical cylinder	700 ± 21.73	2.7 ± 0.10	1.1 ± 0.01	4.6 ± 0.01	-	-	3.4
6	Sphere + Flexible cylinder	300*	13.5 ± 0.70	8.5 ± 0.04	-	1.0†	-	1.2
7	Sphere	-	-	-	-	1.0 ± 0.00	-	<1
7	Power law	-	-	-	-	-	2.7 ± 0.01	<1
8	Sphere	-	-	-	-	1.0 ± 0.00	-	<1
8	Power law	-	-	-	-	-	2.7 ± 0.01	<1
10	Sphere	-	-	-	-	1.0 ± 0.00	-	<1
10	Power law	-	-	-	-	-	2.5 ± 0.02	<1

Table 3. Model fitting results for PBI-F at 5 mg/mL and 20 v/v% MeOH at a range of pH. * No fitting error available. Further fitting of the length went to an unrealistically large number. Length left and other parameters fitted to finish the fitting. This suggests that the length is larger than can be measured with this SAXS setup. †No fitting error available. Bump at high Q attributed to small aggregates as seen at high pH. Sphere radius set to 1.0 nm based on the high pH fitting.

2.2.4 PBI-Y

The SAXS data for one of the inactive materials, PBI-Y, showed some similar trends to those seen for the active PBIs (Figure 12). At pH 10.0, the data were best fitted to a combined model of a sphere and power law (Table 4), suggesting a combination of small aggregates and the presence of larger aggregates (resulting in low Q scattering). At pH 8.0 and 7.0, the data were best fitted to a flexible cylinder and a sphere which is consistent with the presence of worm-like micelles as well as small aggregates. At pH 6.0 and 5.0, a combined model of a flexible elliptical cylinder and sphere were required. Here, small aggregates (modelled by the spherical component) are still present however the cylinder model now requires an elliptical component. This could be indicative of the lateral association of the 1D structures present at pH 7.0, into sheet-like structures. At pH 4.5, only a flexible elliptical cylinder model was required to fit the data, suggesting that the small aggregates have self-assembled into larger structures. It is also noted that the fit had a larger reduced chi^2, suggesting a poorer quality of fit. The subsequent data at pH 4.0 and 3.5 could not be adequately fitted to any models, while still exhibiting a high scattering intensity. This suggests underlying changes within the sample that progressively cause the data to be harder to fit from pH 4.5 to 3.5. Then, at pH 2.0 and 3.0, the scattering intensity drops off significantly, but gel-like aggregates were still visible (the PBI did not re-dissolve). The decrease in scattering intensity could either be caused by the aggregation into structures that are larger than can be resolved by SAXS or due to a highly dense network from which there is insufficient contrast from which X-ray scattering can occur.

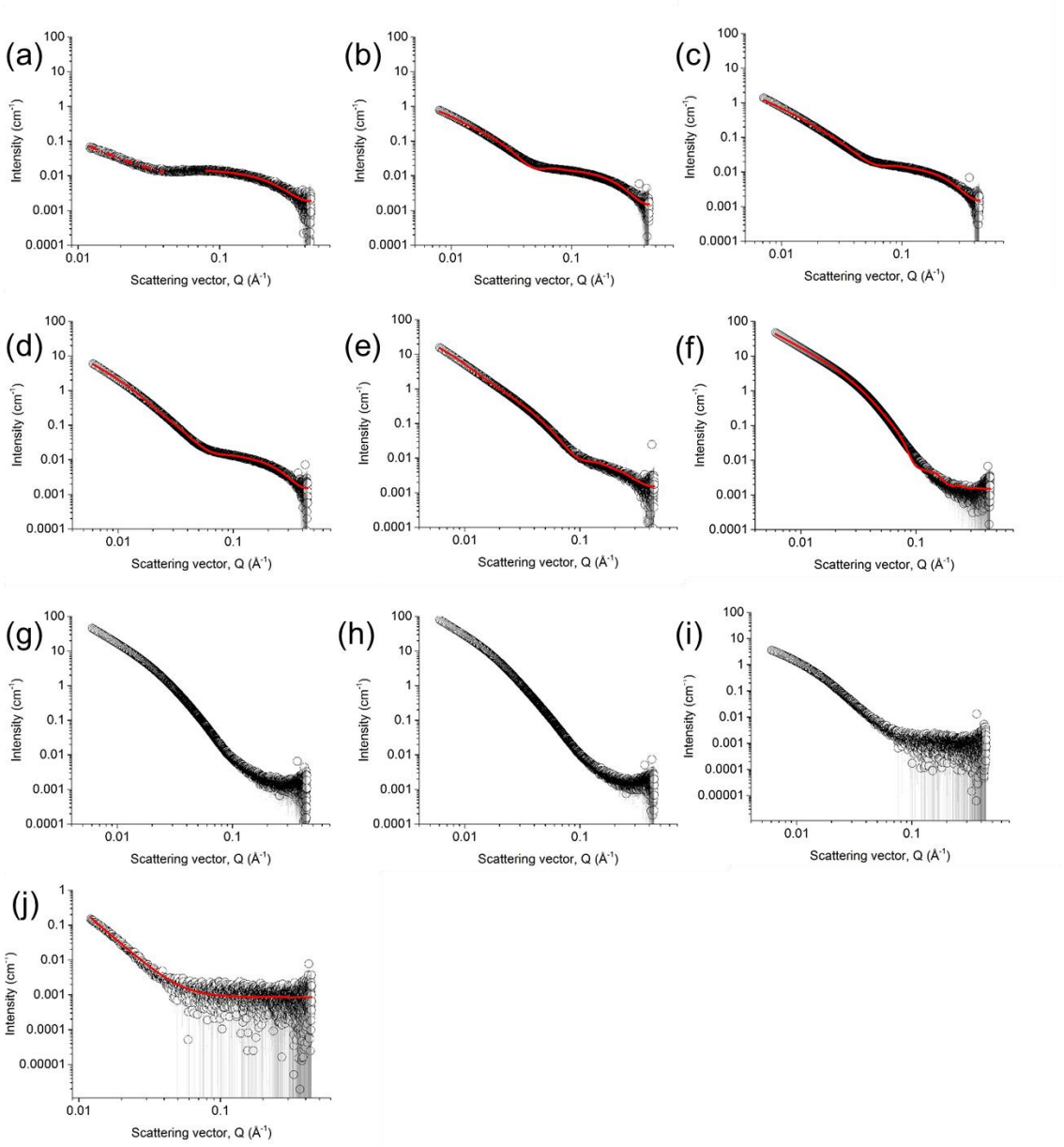

Figure 12. SAXS data for PBI-Y showing scattering vector vs scattering intensity (open black circles) with the corresponding model fits (solid red lines; models used are described in Table 4). 5 mg/mL PBI-Y with 20 v/v% MeOH at pH (a) 10; (b) 8; (c) 7; (d) 6; (e) 5; (f) 4.5; (g) 4; (h) 3.5; (i) 3; (j) 2. Reproduced from D. McDowall, B.J. Greeves, R. Clowes, K. McAulay, A.M. Fuentes-Caparrós, L. Thomson, N. Khunti, N. Cowieson, M.C. Nolan, M. Wallace, A.I. Cooper, E.R. Draper, A.J. Cowan and D.J. Adams, Adv. Energy Mater., 2020, DOI:10.1002/aenm.202002469 with permission from Wiley-VCH Verlag GmbH & Co. KGaA (Copyright © 2020) under the Creative Commons CC-BY (version 4.0) license.

pH	Model	Length / nm	Kuhn length / nm	Cylinder radius / nm	Axis ratio	Sphere radius / nm	Power law	Reduced Chi squared
2	Power law	-	-	-	-	-	3.5 ± 0.02	<1
3	Not fitted							
3.5	Not fitted							
4	Not fitted							
4.5	Flexible elliptical cylinder	640*	12.2 ± 0.07	3.3 ± 0.00	-	-	-	11.3
5	Flexible elliptical cylinder + Sphere	640 ± 0.18	64.0 ± 13.08	3.2 ± 0.00	8.0 ± 0.03	1.0†	-	2.1
6	Flexible elliptical cylinder + Sphere	570*	27.7 ± 0.43	4.7 ± 0.01	3.7 ± 0.02	1.0†	-	1.1
7	Flexible cylinder + Sphere	300*	10.9 ± 0.29	5.8 ±0.02	-	1.0†	-	1.6
8	Flexible cylinder + Sphere	130 ± 0.00	31.8 ± 0.80	7.0 ± 0.02	-	1.0†	-	1.8
10	Sphere	-	-	-	-	1.0 ± 0.00	-	<1
10	Power	-	-	-	-	-	1.9 ± 0.07	<1

Table 4. Model fitting results for PBI-Y at 5 mg/mL and 20 v/v% MeOH at a range of pH. The pH 3 to 4 data could not be adequately fitted to a model. This is believed to be due to scattering from the fibre network, which also results in the observed drop in scattering intensity at pH 3 and pH 2. * No fitting error available. Further fitting of the length went to an unrealistically large number. Length left and other parameters fitted to finish the fitting. This suggests that the length is larger than can be measured with this SAXS setup. † No fitting error available. Bump at high Q attributed to small aggregates as seen at pH 10. Sphere radius set to 1.0 nm based on the high pH fitting.

2.2.5 PBI-H

Finally, the SAXS data for PBI-H show similar trends but with some differences (Figure 13). At pH 10.0 the data is best fitted to a sphere model (Table 5), as is seen at high pH for many of the PBIs and depicts small aggregates.

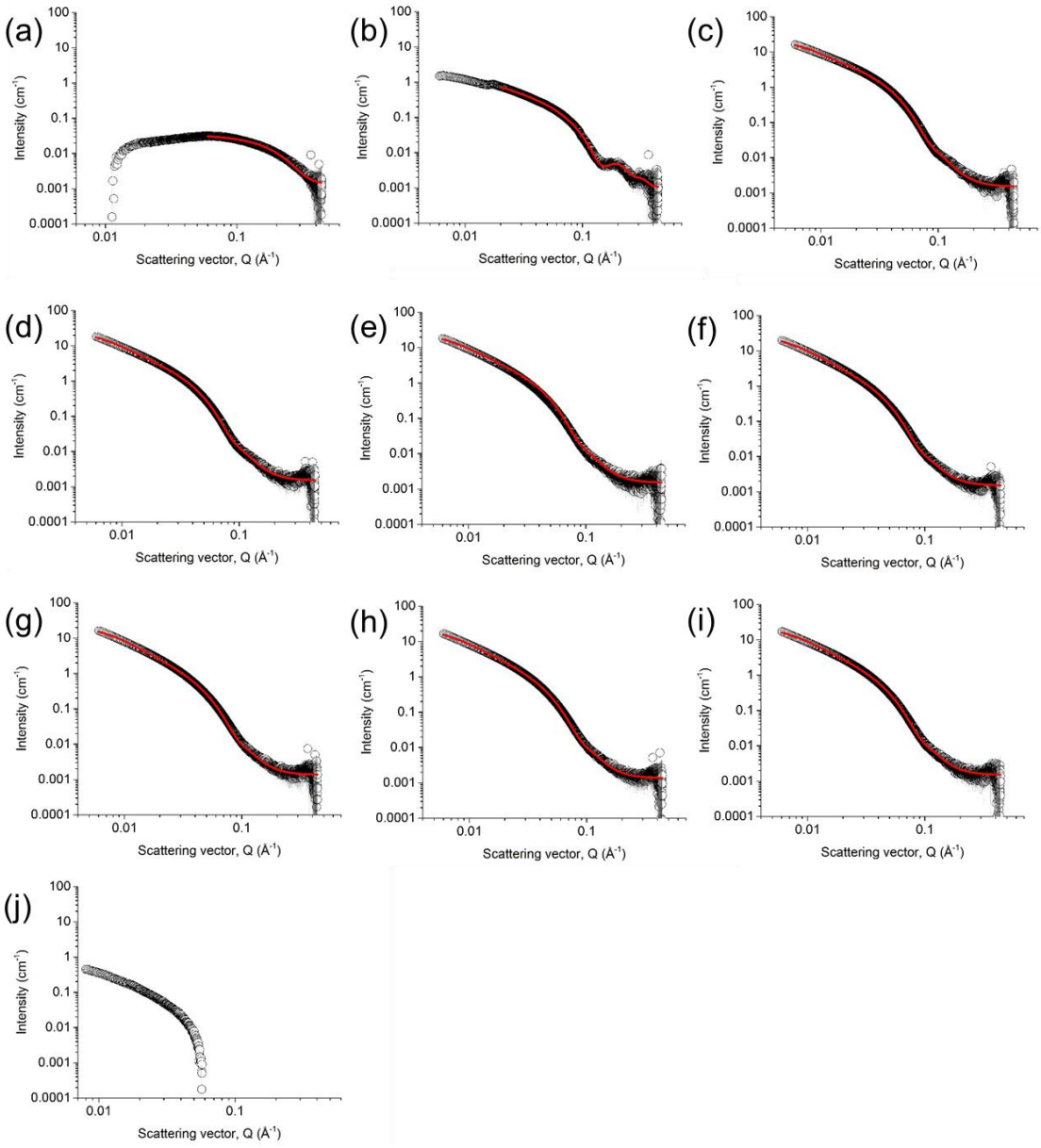

Figure 13. SAXS data for PBI-H showing scattering vector vs scattering intensity (open black circles) with the corresponding model fits (solid red lines; models used are described in Table 1). 5 mg/mL PBI-F with 20 v/v% MeOH at pH (a) 10; (b) 8; (c) 7; (d) 6; (e) 5; (f) 4.5; (g) 4; (h) 3.5; (i) 3; (j) 2. It was not possible to adequately fit the pH 2 data. Reproduced from D. McDowall, B.J. Greeves, R. Clowes, K. McAulay, A.M. Fuentes-Caparrós, L. Thomson, N. Khunti, N. Cowieson, M.C. Nolan, M. Wallace, A.I. Cooper, E.R. Draper, A.J. Cowan and D.J. Adams, Adv. Energy Mater., 2020, DOI:10.1002/aenm.202002469 with permission from Wiley-VCH Verlag GmbH & Co. KGaA (Copyright © 2020) under the Creative Commons CC-BY (version 4.0) license.

Moving to pH 8.0 a combined model of a cylinder and a sphere achieved the best fit, depicting a cylinder of approximately 4 nm in radius. From pH 7.0 to 3.0, the model fitting depicts nearly identical structures of flexible cylinders with a polydisperse radius. At pH 2.0,

there is very little scattering intensity due to PBI-H being re-dissolved due to the protonation of the imidazole group on the amino acid.

pH	Model	Length / nm	Kuhn length / nm	Cylinder radius / nm	Sphere radius / nm	Reduced Chi squared
3	Flexible cylinder with polydispersity of radius 0.25	152 ± 0.60	15.2 ± 0.00	4.0 ± 0.00	-	4.06
3.5	Flexible cylinder with polydispersity of radius 0.25	157 ± 0.70	15.7 ± 0.00	4.1 ± 0.00	-	1.96
4	Flexible cylinder with polydispersity of radius 0.25	179 ± 0.42	12.7 ± 0.05	3.9 ± 0.00	-	4.30
4.5	Flexible cylinder with polydispersity of radius 0.25	181 ± 0.41	13.5 ± 0.05	4.1 ± 0.00	-	4.64
5	Flexible cylinder with polydispersity of radius 0.25	175 ± 0.39	13.0 ± 0.05	4.1 ± 0.00	-	4.56
6	Flexible cylinder with polydispersity of radius 0.25	130 ± 0.41	22.6 ± 0.07	4.2 ± 0.00	-	3.22
7	Flexible cylinder with polydispersity of radius 0.25	88 ± 0.29	40.0 ± 0.10	4.3 ± 0.00	-	3.89
8	Cylinder + Sphere	51 ± 0.55	-	25.5 ± 0.00	0.9*	<1
10	Sphere	-	-	-	0.9 ± 0.00	1.00

Table 5. SAXS fitting results for PBI-H at 5 mg/mL with 20 v/v% MeOH at different pH. *No fitting error available. Sphere radius fixed based on pH 10 fit.

2.2.6 Summary

The SAXS data across the five PBIs all show distinct behaviour but also some commonality. All PBIs show the presence of nanofibres at pH 5.0, with varying morphology and dimensions. As has already been alluded to, the SAXS data do not give the whole story. It is clearly not the case that the formation of long 1D structures results in a switching on of the photocatalysis. It is instead one part of the story. For example, the SAXS data don't explain why PBI-H or PBI-Y (which form long 1D structures at pH 5.0) are inactive or why the system is so sensitive to methanol concentration (Figure 7).

2.3 Molecular packing

UV-Vis spectroscopy is a powerful technique that can be used to study the electronic environment and molecular packing.[23,41,42] As such, a UV-Vis spectroscopy study was conducted to understand the local electronic environment of the PBIs at each pH. The UV-Vis experiments were performed and the data analysed by Benjamin Greeves. Due to the highly absorbing character of PBIs in the UV-Vis regions of light, conventional cuvettes could not be used. Instead, the sample was confined between two optical windows resulting in a thin film, allowing data to be collected. This method meant a consistent path length could not be formed and therefore the data were normalised. As representative samples for both active and inactive PBIs, PBI-A and PBI-Y were studied in-depth with UV-Vis spectroscopy. Both identical samples to those used for high throughput photocatalysis (5 mg/mL) were studied as well as highly diluted solutions (10^{-6} mol/L).

For PBI-A at pH 10.0, increasing the concentration from 10^{-6} mol/L to 5 mg/mL (9.4×10^{-3} mol/L) results in a decrease in the ratio of the first two vibronic peak intensities (Figure 14a), which is commonly attributed to the formation of self-assembled H-aggregates.[43] For the photocatalysis solutions of PBI-A, the UV-Vis spectra fall into three distinct categories, for pH 10.0 – 6.0 the spectra are similar. Moving to pH 5.0 – 3.0 there is peak broadening and a shift in the intensity maxima (Figure 14b). There is a hypsochromic shift from 502 nm at pH 10.0 to 478 nm at pH 4.0 as well as a bathochromic shifted band appearing at 571 nm. At pH 2.0 there is a further broadening of the spectra, indicating further aggregation of the supramolecular structures.

A fitting approach that has previously been used to identify different aggregate types in peptide functionalised PBIs was applied to the UV-Vis spectra.[44] The spectra for PBI-A can be modelled as a linear combination of the aggregates present at three different pH using the aggregates present at pH 10.0 (denoted Type 1), pH 4.0 (type 2) and pH 2.0 (type 3). Fitting the data for PBI-A shows that where significant H_2 production is seen, the spectra are predominantly comprised of Type 2 aggregates (Figure 14c).

For the inactive material, PBI-Y, the UV-Vis spectra show a different pH dependency (Figure 14e). None of the type 2 aggregates, that are present for the active materials, are seen (Figure 14f). For PBI-Y at pH 10.0 – 6.0, sharp peaks are seen and the fitting shows that type 1 aggregates dominate. From pH 5.0 to 4.5, the relative contribution of Type 1 aggregates diminishes and those of type 3 aggregates increase until type 3 dominates at pH 4.0.

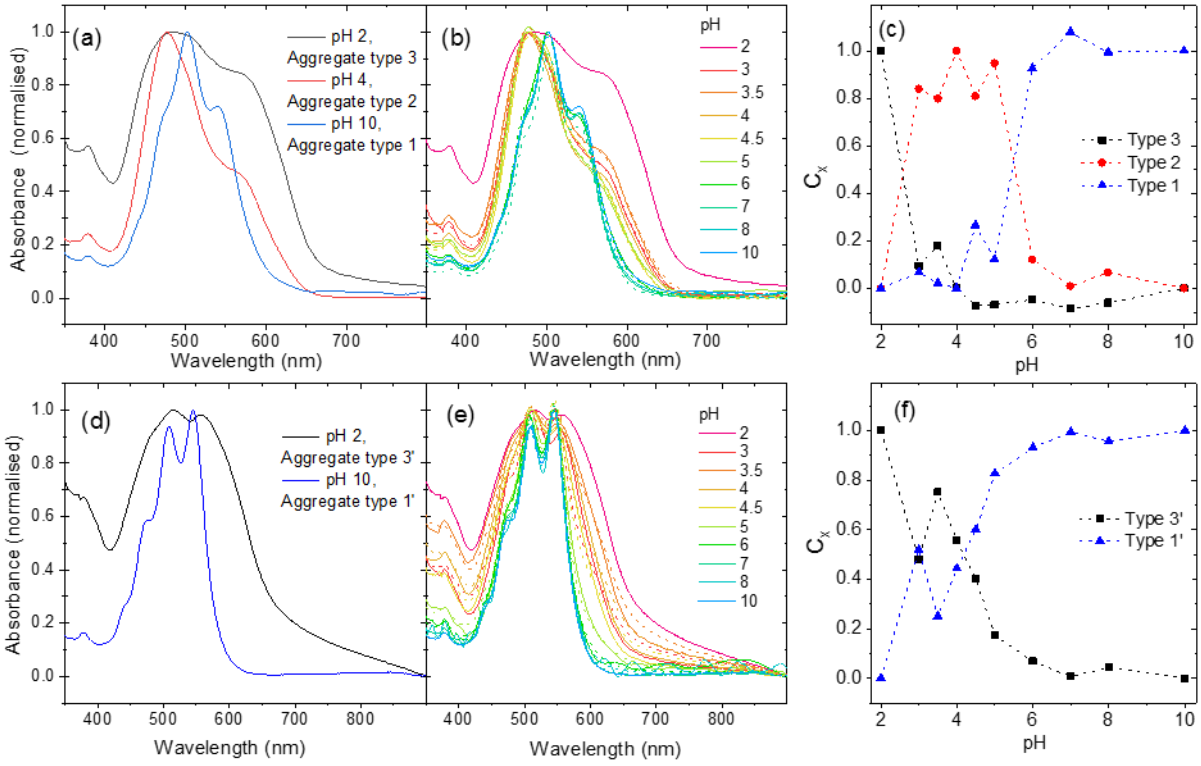

Figure 14. UV-Vis spectra for PBIs at 5 mg/mL and 20 v/v% MeOH at a range of pH. (a) Active PBI-A and inactive (d) PBI-Y at selected pH values that represent distinct aggregate types. The spectra at all pH values of (b) PBI-A and (e) PBI-Y can be fitted to a linear combination of the spectra shown in panels (a) and (d) using equation 1. Experimental data is shown with solid lines and fits shown with dashed lines. (c) and (f) are the coefficient for each component spectrum used in the fitting of the is plotted in (e) PBI-A and (f) PBI-Y. Reproduced from D. McDowall, B.J. Greeves, R. Clowes, K. McAulay, A.M. Fuentes-Caparrós, L. Thomson, N. Khunti, N. Cowieson, M.C. Nolan, M. Wallace, A.I. Cooper, E.R. Draper, A.J. Cowan and D.J. Adams, Adv. Energy Mater., 2020, DOI:10.1002/aenm.202002469 with permission from Wiley-VCH Verlag GmbH & Co. KGaA (Copyright © 2020) under the Creative Commons CC-BY (version 4.0) license.

2.4 Nanofibre surface charge

The surface charge on the self-assembled structures is another potentially important variable that can govern the photocatalysis. One method by which the surface charge can be probed is through nuclear magnetic resonance (NMR) spectroscopy. Typically, the self-assembly of small molecules results in them becoming NMR silent, but in recent years the use of residual quadrupolar couplings (RQCs) in both ^{23}Na and ^{2}H spectra have been used to probe the surface charge of worm-like micelles.[45,46] RQCs are satellite peaks that appear in the spectra of the probe molecule/ion when studying aligned and anisotropic structures that interact with the probe. The magnitude of the RQC depends on both the degree of anisotropy of the supramolecular structures as well as the strength of the probe-structure interaction. Here, the self-assembled PBI structures can be aligned in strong magnetic fields (such as those found in an NMR spectrometer) due to their high diamagnetic anisotropy. The technique requires the use of probe molecules (such as Na^+ and dioxane-d_8) that interact with the structures. For PBI solutions ^{23}Na is ideal because it is already added to the solution (in the form of NaOH) to deprotonate the carboxylic acid. Additional probes such as dioxane-d_8 and D_2O can also be used.

To probe the surface charge on the self-assembled structures, the RQCs for PBI-A and PBI-Y at the different pH were studied. The pH needed to be lowered slowly to allow for time between sample preparation on the lab bench and loading the sample into the NMR spectrometer. If a gel formed before being exposed to the magnetic field the structures would be “locked-in”, not align and RQCs would not be seen. As such, a strong acid trigger such as HCl cannot be used. To achieve this, a widely used acid trigger that reduces the pH slowly, glucono-delta-lactone (GdL), was used. The process occurred over the course of 10+ hours and simultaneous experiments in the lab measuring the change in pH at the same time that RQCs in the NMR spectrometer were measured. At the start of the experiment for both PBI-A and PBI-Y, the pH was around 6.5 (Figure 15b & 15e), which rapidly fell until an apparent pK_a at around 100 – 200 minutes into the experiment. After this the pH gradually fell over the course of 8 hours to a value around pH 4.0. For both PBI-A and PBI-Y, no RQCs were observed for either the dioxane-d_8 or D_2O probe molecules, suggesting that neither sample ordered around the supramolecular structures in a manner that resulted in a signal.

In the ^{23}Na spectra, RQCs are determined by the appearance of satellite peaks either side of the Na peak. For PBI-A, no RQC peaks are seen within the first 300 minutes of the experiment (Figure 15a). Instead, a broadening of the central peak is observed until just after 300 minutes. The peak broadening may be due to the presence of relatively small aggregates that have limited alignment in the magnetic field.[47] After this point, at pH 5.22,

peaks can be resolved and RQCs calculated (Figure 15c), where the magnitude of the RQC is around 250 Hz. The data suggest that at this pH, there are 1D aggregates aligned in the magnetic field and are interacting with Na^+ ions. This suggests the presence of charged nanofibres at the most active pH for H_2 evolution. During the subsequent drop in pH, the magnitude of the RQC decreases until around 70 Hz at pH 4.17. The decrease in the RQC magnitude means that either the interaction of Na^+ with the nanofibres is decreasing due to a reduction in the surface charge. Alternatively, the alignment of the nanofibres is simply being lost. In this instance, the former is more likely because it is less feasible that the nanofibres would de-align while being exposed to the strong magnetic field.

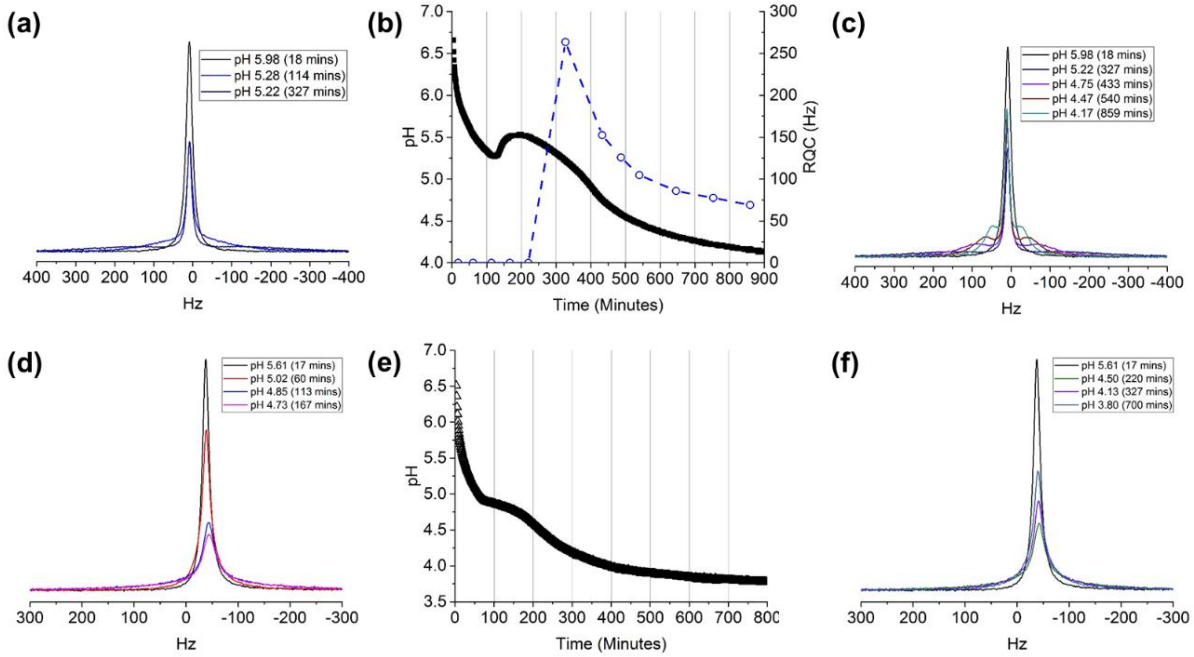

Figure 15. Experimental data for 5 mg/mL PBI-A with 10 mg/mL GdL and 20 v/v% methanol-d_4 (a – c) and for 5 mg/mL PBI-Y with 10 mg/mL GdL and 20 v/v% methanol-d_4 (d – f). (a) ^{23}Na spectra from 18 to 327 minutes, showing the appearance of the RQCs; (b) Change in pH with time (hollow black circles) and the corresponding change in ^{23}Na RQC with time (hollow blue diamonds, with a dashed line to guide the eye); (c) ^{23}Na spectra from 327 to 645 minutes (with the first spectra, 18 mins, for reference); (d) ^{23}Na spectra from 17 to 167 minutes; (e) pH change with time (hollow black triangles); (f) change in ^{23}Na spectra from 220 to 700 minutes. 17 minutes is included for reference. Reproduced from D. McDowall, B.J. Greeves, R. Clowes, K. McAulay, A.M. Fuentes-Caparrós, L. Thomson, N. Khunti, N. Cowieson, M.C. Nolan, M. Wallace, A.I. Cooper, E.R. Draper, A.J. Cowan and D.J. Adams, Adv. Energy Mater., 2020, DOI:10.1002/aenm.202002469 with permission from Wiley-VCH Verlag GmbH & Co. KGaA (Copyright © 2020) under the Creative Commons CC-BY (version 4.0) license.

For PBI-Y, across the pH range a broadening of the central peak is seen but no ^{23}Na RQCs are observed (Figure 15d & 15f). The peak broadening reaches a maximum at the apparent pK_a, at pH 4.73 (167 minutes). For PBI-Y, the manner by which the peak is broadened is different to that observed for PBI-A (Figure 16). For PBI-A, the broadening occurs at the base of the peak, and the central transition remains relatively sharp. For PBI-Y, both the central and satellite peaks are broadened, which is consistent with the interaction of Na^+ with unaligned nanofibres.[48] This suggests that interactions between the fibres and probe molecule are occurring but that aggregation was too extensive by the time the sample entered the magnetic field (a few minutes were required to transfer the sample from the lab to the spectrometer). As such, the nanofibres were hindered from aligning. This finding is consistent with the SAXS data, where at pH 7.0 a combined model of a flexible cylinder and sphere were required to fit the data. By contrast, the SAXS data suggests smaller structures are present at pH 7.0 and pH 6.0 for PBI-A.

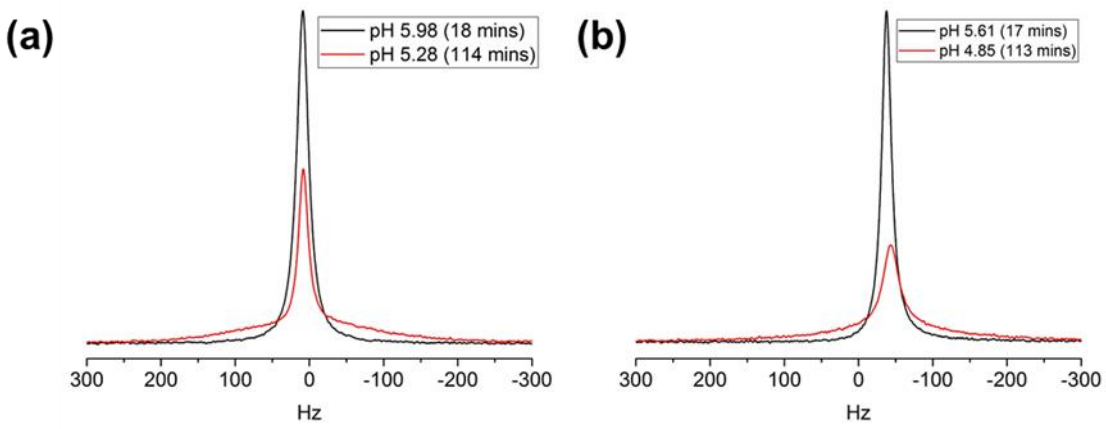

Figure 16. ^{23}Na spectra for (a) 5 mg/mL PBI-A with 10 mg/mL GdL and 20 v/v% methanol-d_4; (b) 5 mg/mL PBI-Y with 10 mg/mL GdL and 20 v/v% methanol-d_4. The first spectrum from each experiment is shown (black line) along with a spectrum showing the broadened peak (red line). Reproduced from D. McDowall, B.J. Greeves, R. Clowes, K. McAulay, A.M. Fuentes-Caparrós, L. Thomson, N. Khunti, N. Cowieson, M.C. Nolan, M. Wallace, A.I. Cooper, E.R. Draper, A.J. Cowan and D.J. Adams, Adv. Energy Mater., 2020, DOI:10.1002/aenm.202002469 with permission from Wiley-VCH Verlag GmbH & Co. KGaA (Copyright © 2020) under the Creative Commons CC-BY (version 4.0) license.

Conclusions

To conclude, the power of high throughput experimental setup was used to investigate the relationship between self-assembled structure and photocatalytic hydrogen evolution. The high throughput setup enabled ~350 samples to be measured in a few weeks where it would have taken months by conventional methods. The effect of changing amino acid, pH and methanol concentration was investigated, allowing for the structure-activity relationship to be investigated in great detail.

Three of the five PBIs studied were active for the hydrogen evolution reaction. For the active PBIs, pH 5.0 represented the optimum rate of hydrogen evolution, which was correlated with the presence of self-assembled nanofibres by using small angle X-ray scattering. At both high and low pH, minimal hydrogen production was observed for the active PBIs. The results showed that self-assembled nanofibres were not the only determining factor in efficient photocatalysis. For the active PBIs, nanofibres were present at low pH but no hydrogen was seen. For the inactive PBIs, nanofibres were formed but no hydrogen was generate. Clearly, the picture was more nuanced. The study was expanded and UV-Vis spectroscopy, NMR spectroscopy and electrochemistry was used to determine that efficient photocatalysis required both specific molecular packing and surface charge on the nanofibers.

3 Experimental

3.1 Synthesis

3.1.1 Amino acid functionalised perylene bisimides

Amino acid functionalised perylene bisimides were synthesised using previously reported methods.[27,49] A library of PBIs functionalised with 5 different amino acids, L-alanine, L-phenylalanine, L-valine, L-histidine and L-tyrosine were synthesised.

For example, in the synthesis of PBI-A, 2.00 g (5.1 mmol) perylene-3,4,9,10-tetracarboxylic dianhydride (PTCDA) was reacted with 0.91 g (10.2 mmol) L-alanine using 3.47 g (51.0 mmol) imidazole as a solvent. The reagents were mixed thoroughly in a Schlenk flask, purged with N_2 for 15 minutes and then heated to 120°C for 5 hours. The temperature was then lowered to 90°C and 20 mL deionised water added *via* needle through the septum. This solution was left to stir for 1 hour and then lowered to room temperature. The Schlenk flask was then filled with deionised water and the solution filtered under gravity. The filtrate was collected, the pH lowered to <4 (pH 5 in the case of L-histidine, which re-dissolves at very low pH) with 2M HCl triggering precipitation of the PBI product. This was then filtered under vacuum, washed with 2M HCl and then deionised water. The collected solid was dried under vacuum and then refluxed in 50 mL 2M HCl for 5 hours to remove any residual imidazole. This mixture was lowered to 80°C and then vacuum filtered, washed three times with 10 mL 2M HCl, 3 times with 10 mL deionised water and dried under vacuum. ^{1}H and ^{13}C NMR spectroscopy was used to characterise the compounds.

PBI-A

^{1}H NMR 500 MHz, (DMSO-d_6, 80°C): δ (ppm) = 12.40 (br, 1H;-OH); 8.47 (d, 4H); 8.36 (d, 4H); 5.64 (q, 2H, J = 7.0 Hz); 1.70 (d, 6H, J = 7.0 Hz)

^{13}C (126 MHz, DMSO-d_6, 80°C): δ (ppm) = 171.4 (COOH); 162.6 (C=O); 134.3, 131.4, 128.8, 125.8, 124.2, 122.8 (perylene core C); 49.3 (CH); 15.0 (CH_2).

PBI-F

^{1}H NMR 500 MHz, (DMSO-d_6 and TFA, 80°C): δ (ppm) = 8.54 (d, 4H, J = 7.9 Hz); 8.38 (d, 4H, J = 7.9 Hz); 7.24 (d; J = 7.5 Hz); 7.16 (t, J = 7.5 Hz); 7.07 (t, J = 7.5 Hz); 5.94 (dd, 2H); 3.67 (dd, 2H, J = 14.3 Hz); 3.46 (dd, 2H, J = 14.3 Hz)

^{13}C (126 MHz, DMSO-d_6 and TFA, 80°C): δ (ppm) = 170.7 (COOH); 162.8 (C=O); 134.6, 131.6, 128.9, 126.1, 124.3, 122.6 (perylene core); 138.5, 129.4, 128.6, 126.7 (aromatic C); 116.7, 114.5 (TFA); 54.7 (CH); 35.1 (CH_2).

PBI-V

^{1}H NMR 500 MHz, (DMSO-d_6, 80°C): δ (ppm) = 12.41 (br, 1H; OH); 8.65 (d, 4H, J = 7.9 Hz); 8.49 (d, 4H, J = 7.9 Hz); 5.25 (d, 2H); 2.79 (m); 1.29 (d, 6H); 0.83 (d, 6H).

^{13}C NMR 126 MHz, (DMSO-d_6, 80°C): δ (ppm) = 170.7 (COOH); 163.2 (C=O); 134.7, 131.9, 129.1, 126.2, 124.5, 122.6 (perylene core); 59.0 (CH); 27.7 (CH): 22.5 (CH_3); 19.6 (CH_3)

PBI-Y

^{1}H NMR 500 MHz, (DMSO-d_6, 80°C): δ (ppm) = 12.63 (br, 1H, OH); 8.76 (br, 2H); 8.40 (dd, 4H); 8.34 (dd, 4H); 7.04 (d, 4H); 6.57 (d, 4H); 5.89 (dd, 2H); 3.55 (dd, 2H, J = 14.5 Hz); 3.39 (dd, 2H, J = 14.5 Hz)

^{13}C NMR 126 MHz, (DMSO-d_6, 80°C): δ (ppm) = 170.9 (COOH); 162.8 (C=O); 156.3 (aromatic C-OH), 134.5, 131.6, 128.8, 126.0, 124.2, 122.6 (perylene core); 130.3, 128.5, 115.6 (aromatic C); 54.9 (CH); 34.1 (CH_2).

PBI-H

^{1}H NMR 500 MHz, (DMSO-d_6 and TFA, 25°C): δ (ppm) = 14.30 (d, 4H); 8.94 (d, 2H); 8.84 (d, 4H); 8.52 (d, 4H); 7.47 (s, 2H); 5.86 (dd, 2H); 3.71 (dd, 2H, J = 15.7 Hz); 3.45 (dd, 2H, J = 15.7 Hz)

^{13}C NMR 126 MHz, (DMSO-d_6 and TFA, 80°C): δ (ppm) = 169.9 (COOH); 162.9 (C=O); 134.8, 131.9, 129.1, 126.2, 124.6, 122.7 (perylene core C); 134.3, 130.9, 117.5 (5-membered ring C); 53.3 (CH); 24.9 (CH_2)

3.1.2 Polyvinylpyrrolidone capped platinum nanoparticles

The synthesis of PVP-capped platinum nanoparticles was carried out based on a previously reported synthesis.[50] This involves the reduction of chloroplatinic acid. The nanoparticles formed were reported to be stable for over half a year.

A 20 mL solution of 0.5 wt% potassium L-tartrate monobasic was brought to reflux under rigorous stirring. A 20 mL solution of 1 wt% polyvinylpyrollidone and 1mM chloroplatinic acid hexahydrate was added to the mixture. After 5 minutes, the pale brown/yellow solution turned a dark brown colour with no further change. After 1 hour, the reaction mixture was cooled to room temperature and the resulting solutions spin filtered. The solutions were centrifuged at 4700 rpm for 30 minutes, which resulted in 0.5 – 2.0 mL of dark brown solution remaining above the filter and a clear and colourless filtrate collected in the bottom. The filtrate was removed, the dark brown solution diluted to 20 mL with deionised water and centrifuged again. This washing process was repeated three times for each synthesis. After this process the 0.5 – 2.0 mL dark brown solution remaining above the filter was collected

and freeze-dried. The freeze-dried solid was then readily re-dispersed into deionised water to make a resulting solution of 1 mM Pt. The freeze dried nanoparticles were characterised by 3Inductively coupled plasma-optical emission spectrometry (ICP-OES) and dynamic light scattering (DLS) to obtain a Pt percentage by mass.

The nanoparticles in the original publication were found to have an average diameter of 3.5 nm by transmission electron microscopy (TEM).[50] In the work presented here particle sizing was performed by DLS on nanoparticles from 7 separate syntheses. From this, a mean hydrodynamic diameter of 16.6 ± 1.1 nm was obtained. The intensity distribution (Figure 17b) is dominated by a peak representing particles of around 15 nm in diameter. Additionally, in the intensity distributions peaks at around 200 nm diameter and 5000 nm diameter were seen. These are smaller than the main peak at ~15 nm. In DLS, larger particles scatter to a much greater extent than smaller particles, therefore a relatively small population of large particles can come to dominate the intensity distribution.[51] As can be seen in the volume and number distributions (Figure 17c and 17d), the larger peaks seen in the intensity distribution are not present because there is a significantly larger number of the ~15 nm particles present. It can therefore be concluded that while there are larger particles present in the nanoparticles used, they are relatively few in number. While further tests have not been performed, these are assumed to be either dust or nanoparticle aggregates.

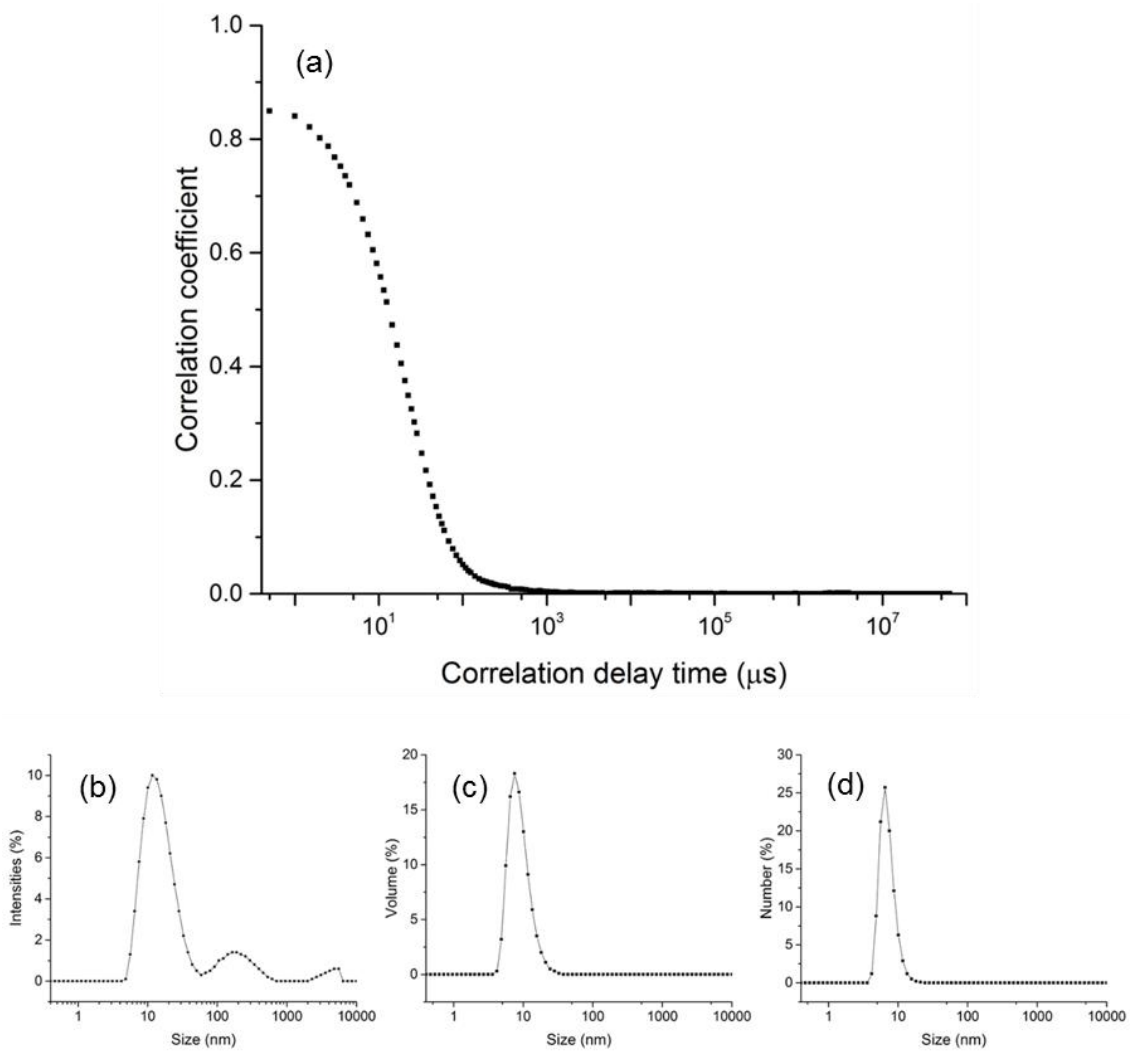

Figure 17. (a) A typical correlation function obtained for these nanoparticles; (b) Intensity; (c) volume and (d) number distributions from one data set obtained for these nanoparticles.

The reason of the discrepancy between the reported particle diameter from the 2003 paper and the nanoparticles synthesised here may be due to numerous reasons. It is common for two different sizing techniques to give different particle diameters.[52] Firstly, the PVP capping agent has a low electron density relative to the platinum, therefore may not be observed in TEM. A diameter of only the metal core of the nanoparticle is reported. In DLS, the calculated diameter is related to how the particle diffuses within the fluid and is thus referred to as the hydrodynamic diameter. This will therefore be affected by any surface structures on the particle (such as PVP capping agent) as well as the ionic strength of the media.

3.2 Characterisation and methods

3.2.1 pH measurements

pH measurements were made using Hanna instruments HI 8424 microcomputer pH meter with FC200 pH probes. The probe was calibrated with Hanna Instruments buffer solutions at pH 4.01, 7.01 and 10.01 prior to each use.

3.2.2 PBI solution preparation

For the preparation of PBI solutions in water, 2 molar equivalents of NaOH were added to a suspension of PBI in water and the solution stirred overnight with a magnetic stirrer. The next day the solutions were checked to ensure all of the solid had dissolved. Then the pH was checked and adjusted to the required pH using 2 M HCl and/or 2 M NaOH. Care was taken during the addition of acid and/or base to homogenise localised areas of different pH (for example a “clump” of PBI aggregates forming upon initial addition of HCl).

3.2.3 Small angle X-ray scattering

SAXS experiments were performed at the Diamond Light Source synchrotron. The scattering experiments were performed by Kate McAulay, Lisa Thomson and Ana Maria Fuentes Caparros. Comparable samples to those used in the photocatalysis were prepared and studied with SAXS. The platinum nanoparticles were not included because heavy atoms scatter strongly and could hinder the analysis of the self-assembled structures.

The pH adjusted solutions were loaded into the instrument differently depending on whether they had formed visible aggregates or not. Typically, the samples prepared at pH 7.0 and above were solutions that could be pipetted into a 96-well plate from which an autosampler took an aliquot for measurement. The samples at pH 5 and below contained aggregates and structures due to self-assembly. These were manually loaded into quartz capillaries to avoid clogging the autosampler. This was also done for the pH 6 samples. The samples were analysed in the X-ray beam of the B21 beamline (Diamond Light Source, Oxfordshire, UK). This beamline operates at a fixed energy of 12.4 keV and a camera length of 4.014 m, resulting in a Q range of 0.004 – 0.44 Å-1. Measurement times were 15 s for each sample. An aqueous solution of 20 v/v% MeOH was used as the background for these experiments

3.2.4 Dynamic light scattering

DLS measurements were performed on a Malvern Zetasizer nanoseries nanoseries Nano-ZS. As these measurements were performed in water, which is highly prone to picking up dust from the atmosphere, all solutions used were passed through 0.20 µm syringe filters (regenerated cellulose membrane within polypropylene housing) immediately before use. Measurements were made in disposable polystyrene cuvettes with a path length of 1 cm. Experiments were run at 25°C. 5 sets of 10 runs (10 s each run) were performed for each sample. The correlation functions were fitted with single exponentials to obtain a mean size and polydispersity.

3.2.5 Inductively coupled plasma-optical emission spectrometry

Platinum content measurements were performed by Jim McIver at the University of Glasgow using an Agilent Technologies 5100 ICP-OES. To prepare the samples for analysis, 1 mg of the freeze-dried nanoparticles were digested in a mixture of 1.0 mL deionised water and 0.8 mL Aqua Regia. To ensure complete digestion the mixtures were heated to boiling for at least 30 seconds. During this the solutions changed from the characteristic brown colour to colourless and clear, indicating destruction of the nanoparticles. This mixture was then diluted to a total volume of 10 mL with deionised water resulting in a 100 ppm solution of digested nanoparticles. These samples were then analysed. Standard solutions of 1 – 50 ppm Pt and a blank of 0.8 mL Aqua Regia in 10 mL deionised water were also used.

3.2.6 Nuclear magnetic resonance (NMR) experiments

For the characterisation after the synthesis of PBIs, NMR measurements were carried out on a Bruker 500 MHz spectrometer. PBI was dissolved in approximately 700 µL DMSO-d_6 at 1 mg/mL concentration for ^{1}H experiments and 10 mg/mL for ^{13}C experiments. For PBI-H and PBI-F, 2 µL trifluoroacetic acid was added to aid solubility. Due to PBI aggregation resulting in broadened signals, hot (80°C) NMRs were run when necessary, which improved the spectra. Where NMRs were performed at 80°C, spectra were first measured at 25°C.

Surface charge experiments were carried out on a Bruker 400 MHz spectrometer using periodic experiments that measure spectra at set intervals.[45,53] The experimental setup for the NMR spectrometer software was created by Dr Matthew Walker (University of East Anglia). ^{1}H, ^{2}H and ^{23}Na experiments were run overnight as the pH was lowered slowly with GdL. 6.25 mg/mL PBI solutions were prepared and diluted down with methanol-d_4 to a concentration of 5 mg/mL PBI and 20 v/v% methanol-d_4. Two 2 mL samples were prepared for each PBI, one for the NMR experiment and one for the pH experiment. These were run simultaneously overnight. Each 2 mL sample contained 20 mg GdL, 5 µL EtOH, 18 µL

dioxane-d_8 and 2 µL D_2O. For the NMR experiment 600 µL was removed from the 2 mL sample and pipetted into an NMR tube. ^{23}Na spectra were acquired in 256 scans using a 12 µs 90-degree pulse, a signal acquisition time of 0.3 s, a relaxation delay of 0.1 s and a sweep width of 120 ppm. ^{2}H spectra were recorded *via* the lock channel with 128 scans, a 200 µs 90-degree pulse, signal acquisition time of 2.0 s, a relaxation delay of 0.2 s and a sweep width of 10 ppm. ^{1}H spectra were acquired using the perfect echo WATERGATE sequence of Adams *et al.*[54] incorporating the double echo W5 sequence of Liu *et al.*[55] The acquisition time was set at 2.5 s. The delay between successive hard pulses of the selective pulse train was set at 333 µs corresponding to a 3000 Hz spacing between the null points. The relaxation delay was set at 1 s. 4 dummy scans and 16 scans were acquired.

3.2.7 Electrochemistry

Electrochemical measurements were performed by Benjamin Greeves using an Emstat potentiostat. Measurements were performed in a 40 mL vial, and used a three-electrode setup. PBI gelator solution (5 mL, 5 mg/mL) was placed into a 40 mL vial, and the pH was adjusted to the required pH using 0.1 M HCl. A supporting electrolyte of 0.1 M NaCl was also used. A glassy carbon disk electrode was used as the working electrode, with a platinum wire as the counter electrode, and a Ag/AgCl reference electrode with a double junction. The vial was sealed with an upturned septum, and purged under N_2 for 30 minutes.

Cyclic voltammograms were performed between +0.3 V to -1.0 V (scan rate 100 mVs^{-1}), with an equilibration time of 30 seconds. Square wave voltammogram measurements used a 1 second equilibration time, 0.01 amplitude and a frequency of 1 Hz.

3.2.8 UV-Vis Absorption Spectroscopy

UV-Vis absorption spectroscopy was carried out by Benjamin Greeves using a Shimadzu UV-2600 spectrophotometer. Due to high extinction coefficients, standard cuvettes were not used. 2 x 1 mm microscope slides were pressed together with gelator solution between them. The slides were sealed further with Parafilm, and placed inside the spectrophotometer with ‘Blu-tac’ to ensure alignment. Dilution experiments started with a standard 5 mg/mL (~0.01 M) PBI-A solution, which was diluted by a factor of 10 for each measurement.

3.2.9 High throughput photocatalysis studies

High throughput photocatalysis studies were performed at the Materials Innovation Factory (MIF) at the University of Liverpool with the help of Rob Clowes. 48 samples of 5 mL solution were prepared in 10 mL glass GC vials at a time. The vials were then purged for 3 hours with N_2, capped and crimped in a ChemSpeed Technologies SWING system. The vials

were then transported onto a set of rollers and illuminated under a solar simulator (Newport Oriel Sol3A class AAA with a 12 x 12 inch output beam). Headspace gas analysis was then performed by a Shimadzu Trace 2010 with a BID detector and an HS-20 headspace sampler. The GC was setup to detect H_2, CO and CH_4. H_2, CO and CH_4 calibrant gases were used for quantification. A Restek Rt-Msieve 5A PLOT fused silica capillary column (30 m x 0.53 mm, 50 µm) was used as the stationary phase.

4 References

1 J. Qi, W. Zhang and R. Cao, *Adv. Energy Mater.*, 2018, DOI:10.1002/aenm.201701620.

2 X. Li, J. Yu, M. Jaroniec and X. Chen, *Chem. Rev.*, 2019, **119**, 3962–4179.

3 D. Cambié, J. Dobbelaar, P. Riente, J. Vanderspikken, C. Shen, P. H. Seeberger, K. Gilmore, M. G. Debije and T. Noël, *Angew. Chem. Int. Ed.*, 2019, **131**, 14512–14516.

4 K. Fujishima, A., & Honda, *Nature*, 1972, **238**, 37–38.

5 T. Jafari, E. Moharreri, A. S. Amin, R. Miao, W. Song and S. L. Suib, *Molecules*, 2016, DOI:10.3390/molecules21070900.

6 L. Yao, A. Rahmanudin, N. Guijarro and K. Sivula, *Adv. Energy Mater.*, 2018, DOI:10.1002/aenm.201802585.

7 J. Jayakumar and H.-H. Chou, *ChemCatChem*, 2020, **12**, 689–704.

8 M. Z. Rahman, M. G. Kibria and C. B. Mullins, *Chem. Soc. Rev.*, 2020, **49**, 1887–1931.

9 Y. Wang, A. Vogel, M. Sachs, R. S. Sprick, L. Wilbraham, S. J. A. Moniz, R. Godin, M. A. Zwijnenburg, J. R. Durrant, A. I. Cooper and J. Tang, *Nat. Energy*, 2019, **4**, 746–760.

10 G. Liao, Y. Gong, L. Zhang, H. Gao, G. J. Yang and B. Fang, *Energy Environ. Sci.*, 2019, **12**, 2080–2147.

11 X. Wang, K. Maeda, A. Thomas, K. Takanabe, G. Xin, J. M. Carlsson, K. Domen and M. Antonietti, *Nat. Mater.*, 2009, **8**, 76–80.

12 L. Wang, R. Fernandez-Teran, L. Zhang, D. Fernandes L.A., L. Tian, H. Chen and H. Tian, *Angew. Chem. Int. Ed.*, 2016, **55**, 12306–12310.

13 R. S. Sprick, J. X. Jiang, B. Bonillo, S. Ren, T. Ratvijitvech, P. Guiglion, M. A. Zwijnenburg, D. J. Adams and A. I. Cooper, *J. Am. Chem. Soc.*, 2015, **137**, 3265–3270.

14 T. Banerjee, K. Gottschling, G. Savasci, C. Ochsenfeld and B. V. Lotsch, *ACS Energy Lett.*, 2018, **3**, 400–409.

15 A. P. Côté, A. I. Benin, N. W. Ockwig, M. O'Keeffe, A. J. Matzger and O. M. Yaghi, *Science*, 2005, **310**, 1166–1170.

16 L. Stegbauer, K. Schwinghammer and B. V. Lotsch, *Chem. Sci.*, 2014, **5**, 2789–2793.

17 F. Würthner, *Chem. Commun.*, 2004, **4**, 1564–1579.

18 F. Würthner, C. R. Saha-Möller, B. Fimmel, S. Ogi, P. Leowanawat and D. Schmidt, *Chem. Rev.*, 2016, **116**, 962–1052.

19 H. Zollinger, *Color Chemistry*, VCH, Weinham, 3rd edn., 2003.

20 W. Herbst and K. Hunger, *Industrial Organic Pigments: Production, Properties, Applications*, Wiley-VCH, 2nd edn., 1997.

21 C. Li and H. Wonneberger, *Adv. Mater.*, 2012, **24**, 613–636.

22 A. Nowak-Król, K. Shoyama, M. Stolte and F. Würthner, *Chem. Commun.*, 2018, **54**, 13763–13772.

23 W. Wei, S. Ouyang and Z. Tierui, *J. Semicond.*, 2020, **41**, 091708.

24 G. Battagliarin, Y. Zhao, C. Li and K. Müllen, *Org. Lett.*, 2011, **13**, 3399–3401.

25 D. Görl, X. Zhang and F. Würthner, *Angew. Chem. - Int. Ed.*, 2012, **51**, 6328–6348.

26 S. Chen, P. Slattum, C. Wang and L. Zang, *Chem. Rev.*, 2015, **115**, 11967–11998.

27 E. R. Draper, J. J. Walsh, T. O. McDonald, M. A. Zwijnenburg, P. J. Cameron, A. J. Cowan and D. J. Adams, *J. Mater. Chem. C*, 2014, **2**, 5570–5575.

28 J. T. Kirner, J. J. Stracke, B. A. Gregg and R. G. Finke, *ACS Appl. Mater. Interfaces*, 2014, **6**, 13367–13377.

29 A. Dannenhoffer, H. Sai, D. Huang, B. Nagasing, B. Harutyunyan, D. J. Fairfield, T. Aytun, S. M. Chin, M. J. Bedzyk, M. Olvera de la Cruz and S. I. Stupp, *Chem. Sci.*, 2019, 5779–5786.

30 T. Abe, K. Nagai, T. Ogiwara, S. Ogasawara, M. Kaneko, A. Tajiri and T. Norimatsu, *J. Electroanal. Chem.*, 2006, **587**, 127–132.

31 S. Chen, D. L. Jacobs, J. Xu, Y. Li, C. Wang and L. Zang, *RSC Adv.*, 2014, **4**, 48486–48491.

32 D. Liu, J. Wang, X. Bai, R. Zong and Y. Zhu, *Adv. Mater.*, 2016, **28**, 7284–7290.

33 A. S. Weingarten, R. V. Kazantsev, L. C. Palmer, M. McClendon, A. R. Koltonow, A. P. S. Samuel, D. J. Kiebala, M. R. Wasielewski and S. I. Stupp, *Nat. Chem.*, 2014, **6**, 964–970.

34 M. C. Nolan, J. J. Walsh, L. L. E. Mears, E. R. Draper, M. Wallace, M. Barrow, B.

Dietrich, S. M. King, A. J. Cowan and D. J. Adams, *J. Mater. Chem. A*, 2017, **5**, 7555–7563.

35 E. R. Draper, L. J. Archibald, M. C. Nolan, R. Schweins, M. A. Zwijnenburg, S. Sproules and D. J. Adams, *Chem. - A Eur. J.*, 2018, **24**, 4006–4010.

36 C. L. Smith, L. L. E. Mears, B. J. Greeves, E. R. Draper, J. Doutch, D. J. Adams and A. J. Cowan, *Phys. Chem. Chem. Phys.*, 2019, **21**, 26466–26476.

37 L. L. E. Mears, E. R. Draper, A. M. Castilla, H. Su, Zhuola, B. Dietrich, M. C. Nolan, G. N. Smith, J. Doutch, S. Rogers, R. Akhtar, H. Cui and D. J. Adams, *Biomacromolecules*, 2017, **18**, 3531–3540.

38 SasView, https://www.sasview.org/, (accessed 21 September 2021).

39 B. J. Greeves, M. A. Zwijnenburg, E. R. Draper, D. J. Adams, M. Barrow and R. Schweins, *Chem*, 2017, **2**, 716–731.

40 M. J. Hollamby, *Phys. Chem. Chem. Phys.*, 2013, **15**, 10566–10579.

41 F. Kong, M. Lin and T. Qiu, *Luminescence*, 2018, **33**, 1209–1216.

42 P. Chal, A. Shit, D. Levy, S. Das, S. Mondal and A. K. Nandi, *Colloids Surfaces A Physicochem. Eng. Asp.*, 2019, **577**, 480–492.

43 F. C. Spano, *Acc. Chem. Res.*, 2010, **43**, 429–439.

44 G. L. Eakins, J. K. Gallaher, R. A. Keyzers, A. Falber, J. E. A. Webb, A. Laos, Y. Tidhar, H. Weissman, B. Rybtchinski, P. Thordarson and J. M. Hodgkiss, *J. Phys. Chem. B*, 2014, **118**, 8642–8651.

45 M. Wallace, J. A. Iggo and D. J. Adams, *Soft Matter*, 2015, **11**, 7739–7747.

46 M. Wallace, J. A. Iggo and D. J. Adams, *Soft Matter*, 2017, **13**, 1716–1727.

47 G. Lindblom, B. Lindman and G. J. T. Tiddy, *J. Am. Chem. Soc.*, 1978, **100**, 2299–2303.

48 H. Gustavsson, B. Lindman and T. Bull, *J. Am. Chem. Soc.*, 1978, **100**, 4655–4661.

49 S. Roy, D. Kumar Maiti, S. Panigrahi, D. Basak and A. Banerjee, *RSC Adv.*, 2012, **2**, 11053–11060.

50 Y. Tan, X. Dai, Y. Li and D. Zhu, *J. Mater. Chem.*, 2003, **13**, 1069–1075.

51 J. Stetefeld, S. A. McKenna and T. R. Patel, *Biophys. Rev.*, 2016, **8**, 409–427.

52 R. F. ; B. Domingos, M. A. ; Ju-Nam, Y. ; Reid, M. M. ; Tufenkji, N. ; Lead, J. R. ;

Leppard, G. G. ; Wilkinson and K. J., *Env. Sci Technol*, 2009, **43**, 7277−7284.

53 M. Wallace, J. A. Iggo and D. J. Adams, *Soft Matter*, 2017, **13**, 1716–1727.

54 R. W. Adams, C. M. Holroyd, J. A. Aguilar, M. Nilsson and G. A. Morris, *Chem. Commun.*, 2013, **49**, 358–360.

55 M. Liu, X. A. Mao, C. Ye, H. Huang, J. K. Nicholson and J. C. Lindon, *J. Magn. Reson.*, 1998, **132**, 125–129.

Chapter 3

Controlling the formation and alignment of low molecular weight gel ‘noodles’

Acknowledgements

This chapter is based on work in a publication ‘Controlling the formation and alignment of low molecular weight gel ‘noodles’, from D. McDowall, M. Walker, M. Vassalli, M. Cantini, N. Khunti, C. J. C. Edwards-Gayle, N. Cowieson and D. J. Adams, Chem. Commun., 2021, 57, 8782–8785.

I would like to thank Professor Dave Adams for the synthesis the 1ThNapFF gelator that was used in this work.

I would like to thank both Dr Matthew Walker and Dr Massimo Vassalli of the School of Engineering at the University of Glasgow for running, analysing and giving insight into the nanoindentation measurements on the gel noodles.

I would like to thank the B21 beamline scientists (Diamond Light Source, UK) for running the samples that were sent *via* mail-in. I would also like to specifically thank Dr Nathan Cowieson for his insightful conversations as to how to analyse the SAXS data.

Abstract

Aligning the nanostructure within a low molecular weight gel has applications from cell culturing to organic electronics. Of particular interest to this project is aligning the nanostructure of perylene bisimides based photocatalysis and photoelectrode systems. One simple method that has been reported involves the injection of the pre-gel solution into a trigger medium, resulting in the formation of a gel filament with an aligned nanostructure. This has been performed with a diverse range of low molecular weight gelators but there has yet to be a rigorous study on the influence of key variables such as concentration. In the work presented here, the functionalised dipeptide 1ThNapFF is studied as a model system from which gel filaments were successfully formed. By simply injecting the gelator into a trigger solution, as is reported in the literature, alignment was not achieved consistently. By employing syringe pumps, better control over the structures could be achieved. To align the nanostructure within the gel filaments, a spinning technique was developed that stretched the structures as they formed. This produced aligned gel filaments approximately 0.1 mm in diameter. Two syringe pumps were used to create a concentric flow and access a ‘noodle-in-noodle’ morphology.

1 Literature review

1.1 Introduction

In Chapter 2, five perylene bismide (PBI) low molecular weight gelators were studied for photocatalytic hydrogen evolution. The photocatalytic system used the PBIs in both the liquid and gel state but at the onset of gelation (at pH 5) greatest amount of hydrogen was formed.[1] In Chapter 2, it was shown that the formation of 1D structures was a crucial component for photocatalytic efficiency. PBIs have previously been used as part of photoelectrode systems in the literature.[2–4] With no external stimulus, the nanofibers from which the gel is comprised generally adopt a random arrangement (Figure 1). An interesting question is, how would the alignment of the nanostructure influence the photocatalytic or photoelectrode efficiency? One hypothesis is that the perpendicular alignment of the 1D structures (Figure 1) may enhance charge separation and transport to the electrode surface and increase efficiency. Conversely, a parallel alignment of the 1D structures relative to the electrode surface (Figure 1) may hinder charge separation and transport. Achieving alignment of the 1D nanostructures within a gel is a challenge but it can be achieved using magnetic fields,[5–8] electric fields[9] and shear.[9,10] Alignment of the 1D nanostructures has attractive benefits from cell culturing to organic electronics.[11–13]

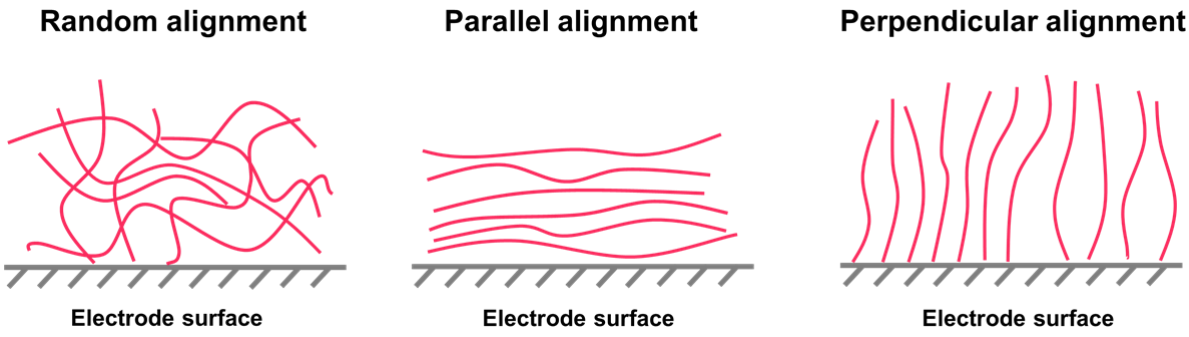

Figure 1. Cartoon of different alignment of the constituent 1D structures on an electrode surface.

The approach applied to achieve nanostructure alignment within a self-assembled gel is sample dependent. Some self-assembled gels form from molecularly dissolved units that aggregate into the 1D structures when gelation is triggered. The alignment must be induced during the formation of those 1D structures, such that they grow in an aligned manner. Otherwise the network will be 'locked-in' and cannot be aligned. Other self-assembled gels are formed from worm-like micelle solutions and the micelles are cross-linked to result in a gel. This means that these structures must be aligned prior to and/or during gelation. For example, shear has been used to align the worm-like micelles in solution parallel to a surface prior to and during gelation.[10] This utilised a slow pH drop using glucono-delta-

lactone (GdL) which, coupled with continuous shear, allowed for the formation of shear-aligned gels.[14] The shear must be maintained throughout the gelation process because alignment can be lost within a fraction of a second of the shear force stopping. In another example, peptide amphiphile nanoribbons have been aligned in magnetic fields ranging from 5 – 20 T, with greatest alignment achieved at 20 T.[7] To demonstrate the alignment, the samples are shown to extinguish light when positioned perpendicularly to a linear polariser. While highly effective, magnetic field alignment is impractical due to the specialist equipment required to obtain very strong magnetic fields. Shear alignment has been achieved by Stupp and co-workers by passing liquid-crystal like peptide amphiphile pre-gel solutions containing 1D nanostructures through a 40 μm pore size mesh that resulted in aligned self-assembled gels.[15] In further work, they used the aligned scaffold for neurite outgrowth and directed cell migration.[16] This method has advantages for this application because types of alignment such as high voltages or directional freezing are not viable for cell culturing.

For PBIs specifically, many of the methods described above can be used to align the 1D nanostructures. As well as forming hydrogels, PBIs also readily form worm-like micelles.[10,17] For the specific application of PBI photocatalysis, hydrogels offer an advantage over worm-like micelle solutions because of the aforementioned “locking-in” of the alignment. Xerogels and dried solutions offer another route to “lock-in” aligned structures but are undesirable. The aqueous environment in hydrated PBI samples (such as a hydrogel) has been shown to be favourable for charge stabilisation and separation relative to dried films and xerogels.[18] Strong magnetic fields can be used to align PBIs but were not readily accessible and generally have very restricted area in which to work (Figure 2).[8]

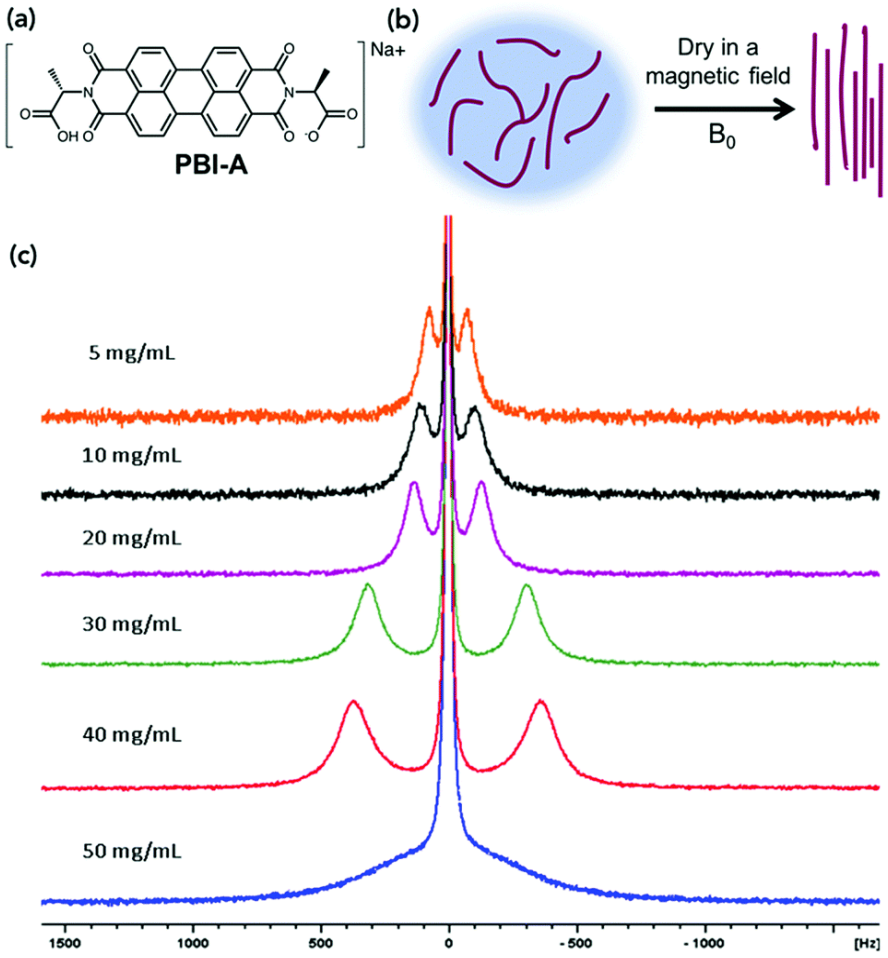

Figure 2. (a) Chemical structure of PBI-A; (b) cartoon schematic of drying and alignment of worm-like micelles in a magnetic field; (c) ^{23}Na NMR data at a range of concentrations exhibiting residual quadrupolar couplings that indicate alignment of the worm-like micelles in the magnetic field. Reproduced from E. R. Draper, M. Wallace, D. Honecker and D. J. Adams, Chem. Commun., 2018, 54, 10977–10980 with permission from the Royal Society of Chemistry under the CC BY 3.0 license.

Forming an aligned gel on an electrode surface presents an additional challenge, therefore other alignment methods excluding the electrode surface were investigated. One very important example is the formation of macroscopic self-assembled gel noodles and dried macroscopic filaments with both aligned and unaligned nanostructures.[19,20] This can be achieved by simple processes given the correct solution conditions (such as self-assembled structure). The macroscopic self-assembled gel noodles are on the order of 0.1 – 1.0 mm in diameter. In the gel noodles, different alignment orientations of the 1D structures have been reported. This can be unaligned (Figure 3a), aligned parallel to the long axis of the noodle (Figure 3b) or perpendicular to the long axis of the noodle (Figure 3c).

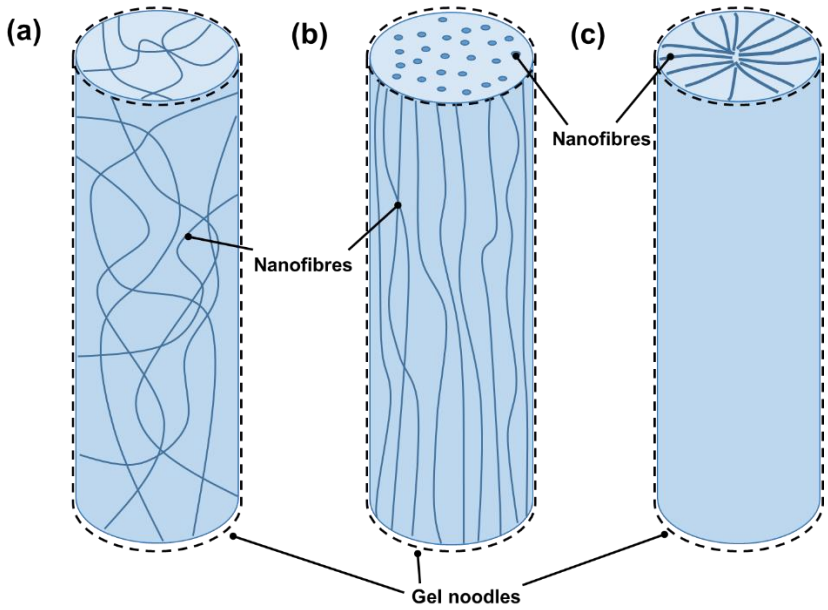

Figure 3. Cartoon of nanostructure alignment types within a gel noodle. (a) Random nanofiber alignment; (b) nanofiber alignment along the long axis of gel noodle and (c) radial alignment of the nanofibres. The schematic is not to scale.

PBIs possess similarities to the materials used in the formation of self-assembled gel noodles in the literature. PBIs can self-assemble into worm-like micelles at high pH and can be gelled *via* salt and acid triggers. As such, the formation of PBI gel noodles was attempted but preliminary experiments were unsuccessful. It was noticed that the literature clearly lacked a rigorous study on how to form these self-assembled gel noodles and the solution conditions required among other variables. Before working with PBIs which are generally lower viscosity, a model system, the functionalised dipeptide 1ThNapFF, was selected and used to understand the fundamental requirements for effective noodle formation.

The formation of self-assembled macroscopic gel strands was first reported in 2010 with a view to study the effect of alignment on cell growth and tissue engineering.[19] Researchers studied a peptide amphiphile with an alkyl tail ($C_{15}H_{31}CO$-VVVAAAEEE(COOH)) which self-assembles into 1D nanofibers in aqueous solution and can form gels. Noodle-like strings were formed by dispensing the self-assembled amphiphile solution from a pipette into a $CaCl_2$ solution that triggered gelation. This resulted in mechanically strong strings (or so-called “noodles”) of gel (Figure 4a). The diameter of these strings was typically on the order of 100 – 500 μm. Initially, unaligned gel noodles were formed. When the solutions were heat-treated to 80°C prior to being drawn into strings, alignment of the nanostructure parallel to the long direction of the noodle-like strings was seen. The alignment is attributed to a heat-induced change in self-assembled structure. The authors hypothesise that the heating process dehydrates the nanofibers present in solution. The subsequent rehydration results in the formation of thin plaque-like structures up to a micrometre wide in both length and

width. The heat/cool also resulted in a threefold viscosity increase of the solutions. It is suggested that both the formation of plaque-like structures and the viscosity increase meant that the shear forces experienced by the solution as it passes through the pipette tip aligned the nanostructure.

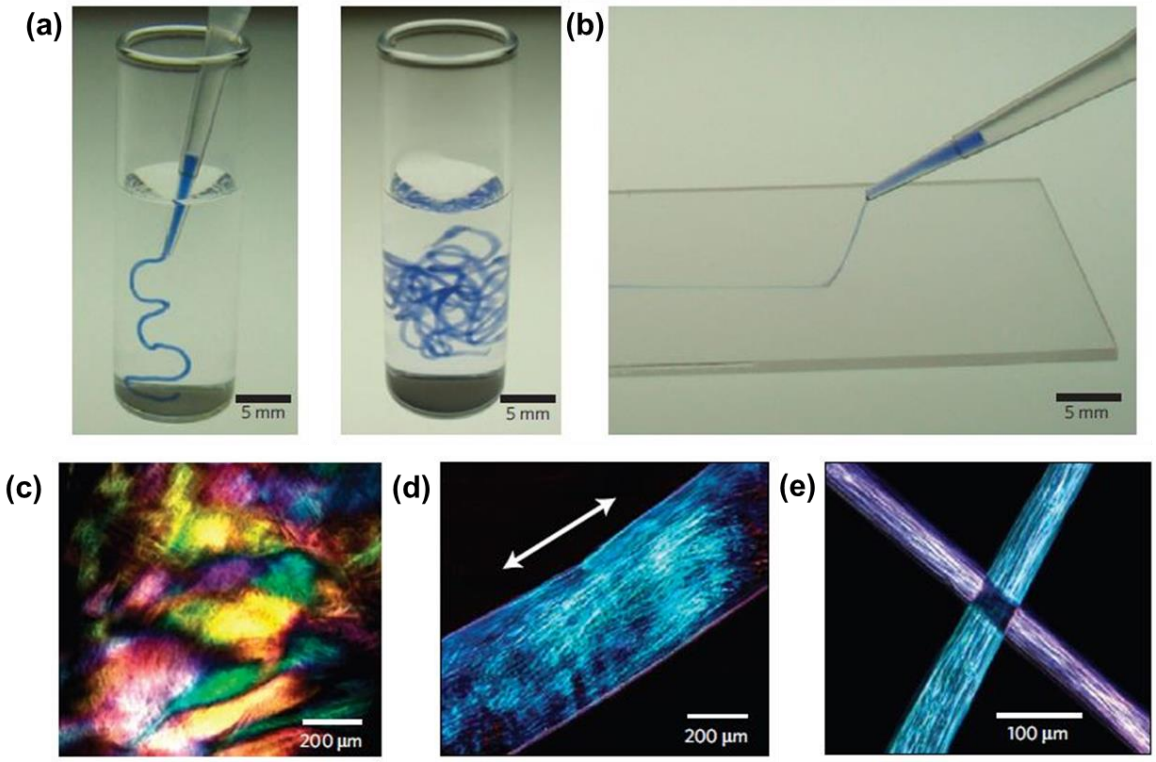

Figure 4. (a) Peptide amphiphile gel noodles; (b) a gel noodle dragged through aqueous $CaCl_2$; cross polarised optical microscope images of (c) peptide amphiphile gel film showing birefringence; (d) a gel noodle; (e) two crossed gel noodles showing light extinction. Reprinted by permission from Springer Nature: Nature Materials, S. Zhang, M. A. Greenfield, A. Mata, L. C. Palmer, R. Bitton, J. R. Mantei, C. Aparicio, M. O. De La Cruz and S. I. Stupp, Nat. Mater., 2010, 9, 594–601, Copyright© 2010.

Nanostructure alignment was determined by a combination of techniques including cross polarised optical microscopy (CPOM), scanning electron microscopy (SEM) and small angle X-ray scattering (SAXS). Uniform birefringence along the length of the aligned gel strings was observed in CPOM images (Figure 4d and 4e) and alignment of the nanostructure was seen in SEM images. For the comparable unaligned gel noodles, the SEM images show an isotropic network of nanofibers. 2D SAXS data of the aligned gel strand showed anisotropic scattering. The authors show that the noodle-like gel strings could be used to encapsulate cells. Additionally, the gel strands could be loaded with carbon nanotubes, resulting in electrical conductivities of 1 – 10 S/cm. No measurement of the mechanical strength of the gel noodles was made but a video in the supplementary information shows that they are sufficiently mechanically robust to be handled with tweezers and tied into a simple knot.

Using a custom-built setup in later work, both un-aligned and circumferentially aligned macroscopic gel tubes were formed.[21] The custom-built device allowed for rotation while the gel tubes were drawn, imparting rotational shear to the pre-gel solution resulting in circumferential alignment. Strictly speaking, the mechanism of gel formation is slightly different to that originally reported in 2010 and is of less relevance to this work but it demonstrates an example of the importance of shear as well as the interesting morphologies that can be accessed. Smooth muscle cells were encapsulated within the gel tubes without hindering cell viability. After 2 days, the cells orientated themselves with the alignment of the gel in an analogous manner to alignment seen in real arteries.

In 2013, a group published work studying a PBI with oligopeptide-polymer substituents at the imide positions.[22] A compound with a quarterthiophene core with oligopeptide-polymer substituents was studied. There is no mention of the compounds forming gels. However, the PBI-based compound does self-assemble into nanofibrils from which they prepared aligned noodle-like structures (Figure 5). Filaments were obtained (which were similar in nature to a gel noodle) by injecting a thermally-annealed solution of the oligopeptide-π-oligopeptide compound in tetrachloroethane (TCE) into MeOH. To form the filaments, the plunger was gently pushed to bring the TCE solution in the needle into contact with the MeOH. This triggered a continuous flow (without further pushing of the plunger) of the TCE solution into the MeOH, forming the filament in the process. They report filament diameters of 18.7 ± 1.6 μm, 10.0 ± 1.6 μm and 5.7 ± 1.2 μm from needles of inner diameters 495 μm, 318 μm and 241 μm respectively. The PBI-based filaments exhibited birefringence in CPOM images. SEM, SAXS and wide angle X-ray scattering (WAXS) was used to show that the microfiber filaments were comprised of aligned nanofibrils. The 2D SAXS and WAXS plots both showed anisotropic scattering patterns. The thermal annealing was required for the formation of reproducible, long, and uniform nanofibrils from which the noodle was composed.

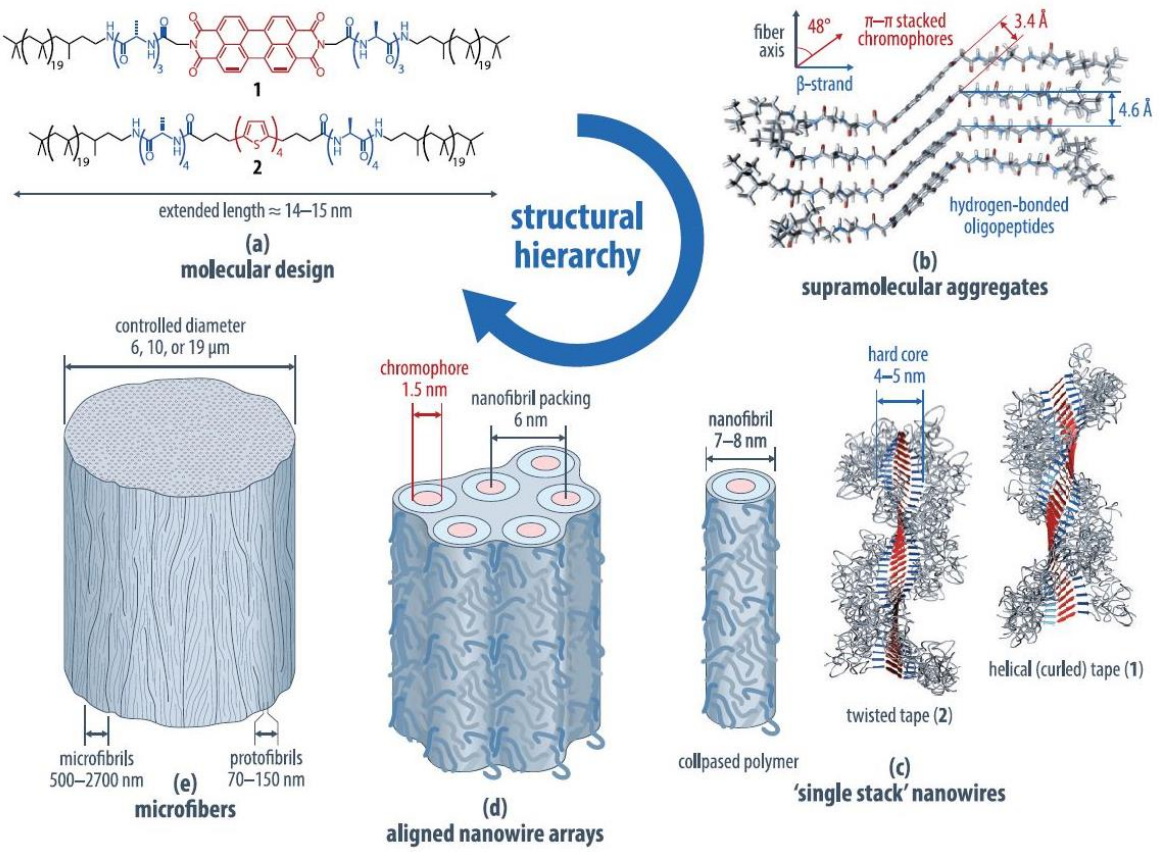

Figure 5. Chemical structures and cartoon schematics of the hierarchical self-assembly into nanofibrils and microfibers. Reprinted with permission from R. Marty, R. Szilluweit, A. Sánchez-Ferrer, S. Bolisetty, J. Adamcik, R. Mezzenga, E. C. Spitzner, M. Feifer, S. N. Steinmann, C. Corminboeuf and H. Frauenrath, ACS Nano, 2013, 7, 8498–8508. Copyright 2013 American Chemical Society.

This work highlights the importance of length scale in relation to nanostructure alignment. A macroscopic noodle is comprised of hierarchical building blocks from molecular interactions to fibrillary structures. Probing the gels on every length scale represents a challenge and many methodologies must be used. The filaments formed were significantly smaller than the needle diameters. They do not detail what the driving force of the formation of highly aligned filaments is. The method of production does not appear to involve a dragging or shear, which is typically attributed to the source of alignment.[10,19,23] It may be due to density differences between TCE and MeOH, being 1.60 g/mL and 0.79 g/mL respectively.[24] A similar effect has been reported when forming gel strands at a DMSO/water interface, where the DMSO “dives” to the bottom of the tank due to solvent density differences.[25]

Other researchers have also produced aligned gel noodles using peptide-π-peptide LMWGs (Figure 6a).[13] The π functionalities provide potential organic electronics applications. The noodles showed birefringence in CPOM images as well as alignment in

SEM images. Here they injected the pre-gel solution into a pool of trigger medium on a glass slide whilst dragging the needle through the pool. The authors report that one of the materials pre-gel solutions did not require a heat/cool treatment to obtain aligned noodle structures. This shows that the thermal annealing is not essential and that the material already had the right properties (such as self-assembled structure) to form aligned gels.

Alignment within the noodle structures resulted in global directionality of the π-stacked chromophores (Figure 6b and 6c) leading to unique photophysical and anisotropic electrical responses when compared to hydrogels with randomly oriented nanostructures. The authors observed that the aligned and non-aligned hydrogels have distinct spectral signatures. Sharper and higher energy band edges were found for the aligned structures, suggesting greater electronic order. These observations are related to differences in intermolecular and nanostructural packing. The gel noodles were dried and the orientational– and gate field- dependent conductance studied. When the electrical contacts were positioned parallel to the alignment, the hole mobility was approximately 21 times larger than when positioned perpendicular. A randomly orientated hydrogel showed no anisotropy in hole mobility.

Studies on two oligopeptide compounds (DFAG and DFAA; also π functionalised materials) with oligo(p-phenylenevinylene) (OPV) cores has also been published.[26] The manual method of dispensing through a pipette by hand is limited due to reproducibility issues and no fine control of flow rates. Seeking better control of the supramolecular assembly, the researchers utilised a microfluidic devices for the formation of aligned oligopeptides.[26,27] The microfluidic device operated using a cross-slot setup at which the oligopeptide solution and acid trigger meet. This created a planar extensional flow, which induced supramolecular alignment through an extensional/compressional flow character. The resulting aligned gel structures that then leave the device by two channels perpendicular to the inlets. In later work, the microfluidic setup was improved with chevron patterns in the ceiling and floor of the flow cell which act to focus the peptide solution stream before it reaches the cross slot.[27] In the work using the microfluidic devices, there is no extensive discussion on the use of the assembled fibres after they have left the device outlet. Instead, the assembly process and structure formation occurring *in situ* was predominantly studied.

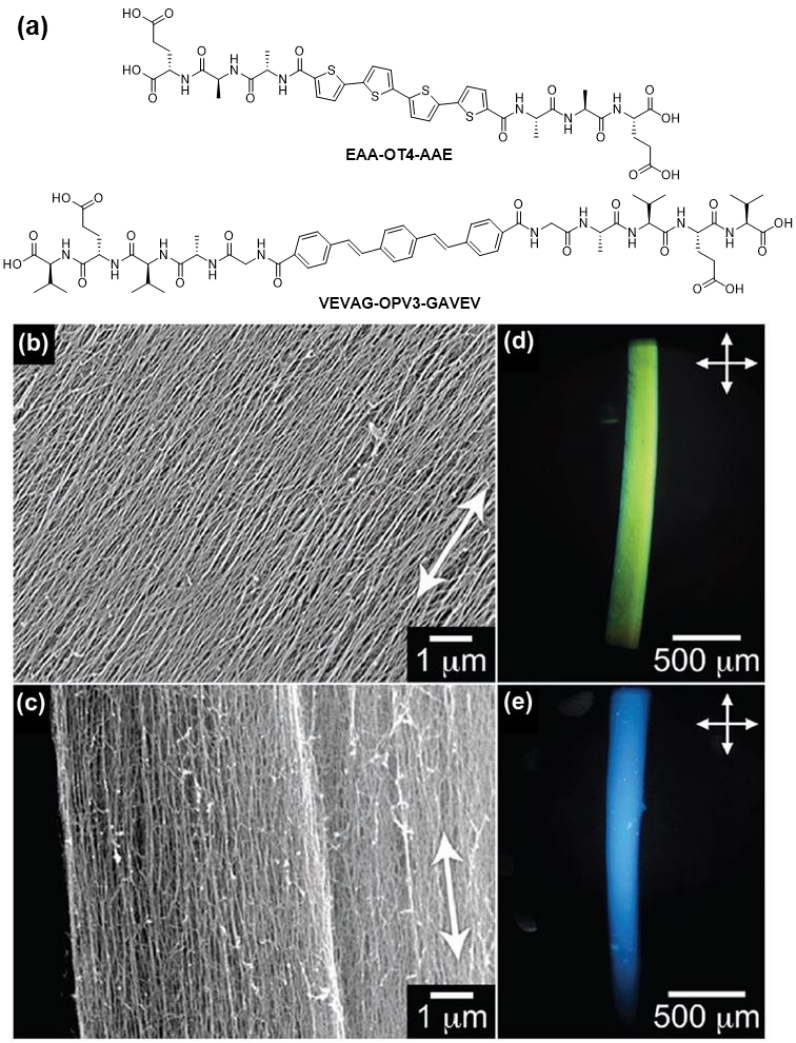

Figure 6. (a) Chemical structures of peptide-π-peptide compounds; (b – c) SEM images of the gel noodles formed from each compound (d – e) cross polarised optical microscopy images of the gel filaments from from each compound, showing birefringence. The arrows denote the orientation of the polarisers. Reprinted with permission from John Wiley and Sons, Advanced Materials, B. D. Wall, S. R. Diegelmann, S. Zhang, T. J. Dawidczyk, W. L. Wilson, H. E. Katz, H. Q. Mao and J. D. Tovar, Adv. Mater., 2011, 23, 5009–5014. Copyright © 2011.

Peptide-π-peptide compounds allow for gels that are manipulated with light.[28] Gel noodles were prepared using a peptide-π-peptide compound containing a diacetylene core, which undergoes photopolymerisation when exposed to the correct wavelength of light. The gel noodles were made and appeared colourless but upon photopolymerisation with UV light, the gel noodles turned a blue colour (Figure 7a). The noodles show birefringence in CPOM both before and after photopolymerisation (Figure 7b). By using a TEM grid as a shadow mask, they could selectively photopolymerise different regions of the noodles, resulting in different colours in the CPOM images (Figure 7c and 7d). A small description in the supporting information details the procedure used to form the gel noodles. 10 μL of pre-gel

solution was extruded from a 30-gauge (inner diameter of 0.159 mm) and syringe pump into a 1M HCl trigger bath at a flow rate of 20 cm/s. No comment is made on the diameter distribution of the filaments formed and the microscope images clearly show a range of noodle diameters.

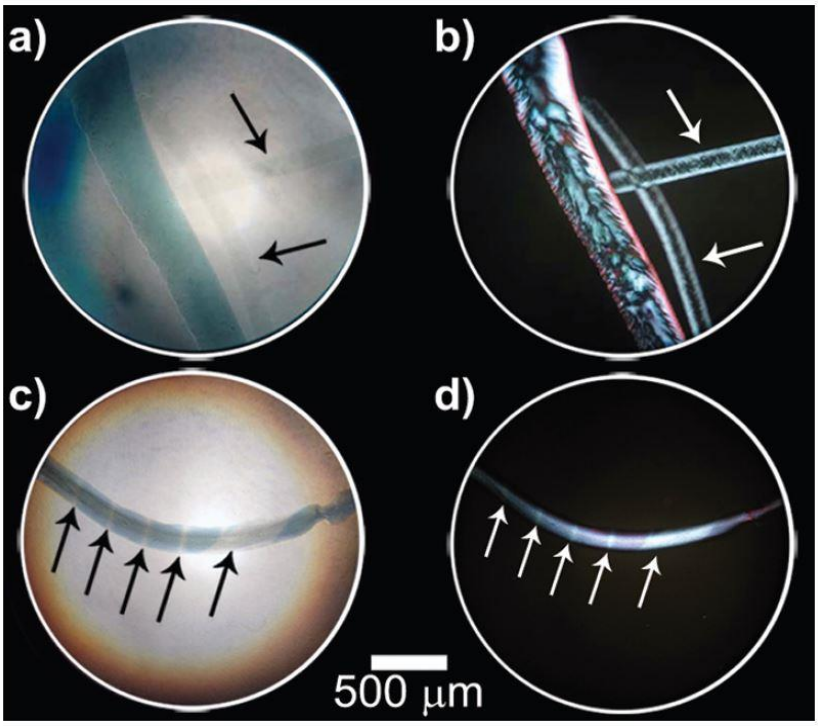

Figure 7. Optical microscope images of hydrogel noodles before (colourless) and after (blue) diacetylene polymerisation under both (a) normal light and (b) cross polarised light. Demonstration of spatially controlled UV polymerisation inside the gel noodles under both (c) normal light and (d) cross polarised light by masking with arrows indicating regions shielded from UV light. Reprinted with permission from S. R. Diegelmann, N. Hartman, N. Markovic and J. D. Tovar, J. Am. Chem. Soc., 2012, 134, 2028–2031, Copyright© 2012 American Chemical Society.

In other work, a highly ordered donor/acceptor material was prepared using ionic self-assembly.[29] A π-extended tetrathiafulvate (electron donor) and a PBI (electron acceptor) were self-assembled forming both p- and n-type nanofibres. The researchers performed a co-assembly of the two components through the injection of concentrated solutions of each component into each other. This resulted in the formation of ordered sacs and membranes. In contrast to solid films of the individual components, films made from the co-assembled compounds showed effective photo charge carrier generation with long (>3 μs) lifetimes. This suggests that the exciton formed at the p/n heterojunction was charge separated and freely transferred along the π stack. Macroscopic alignment of the co-assembled nanofibers was induced by a rubbing protocol. The researchers also prepared macroscopically aligned filaments of these self-assembled structures by the manual injection of a solution of one

component into a solution of the other through a pipette tip. This co-assembled noodle structure was studied and showed birefringence along the length of the strand with CPOM. While an aligned filament of the co-assembled material was successfully made there was no study of the charge transport within this specific structure.

A series of tri- and hexa-β^3-peptides with N-terminal acetyl groups were synthesised.[30] These incorporated design elements to promote the supramolecular self-assembly (Figure 8a). The peptide lengths were chosen for stable 14-helix formation and a total of six axially arranged donor-acceptor interactions. Remarkably, upon dissolution in either water or methanol, the N-acetylated β^3-peptides rapidly formed macroscopic fibres with no further stimulus. These grew up to three centimetres in length within 1 hour and were approximately 250 μm in diameter and could be removed from solution, were flexible and mechanically robust enough to be handled (Figure 8b to 8d). The same peptides excluding the N-acetyl group, with a free N-terminus did not form fibres. The size of the self-assembled fibres strongly indicated a high degree of hierarchical self-assembly which is supported by atomic force microscopy (AFM) measurements. It is remarkable that such robust filaments form spontaneously, and it demonstrates the power of supramolecular self-assembly. The longitudinal alignment of the fibrils throughout the macroscopic filament is assumed and commented on based on the nature of the self-assembly mechanism.

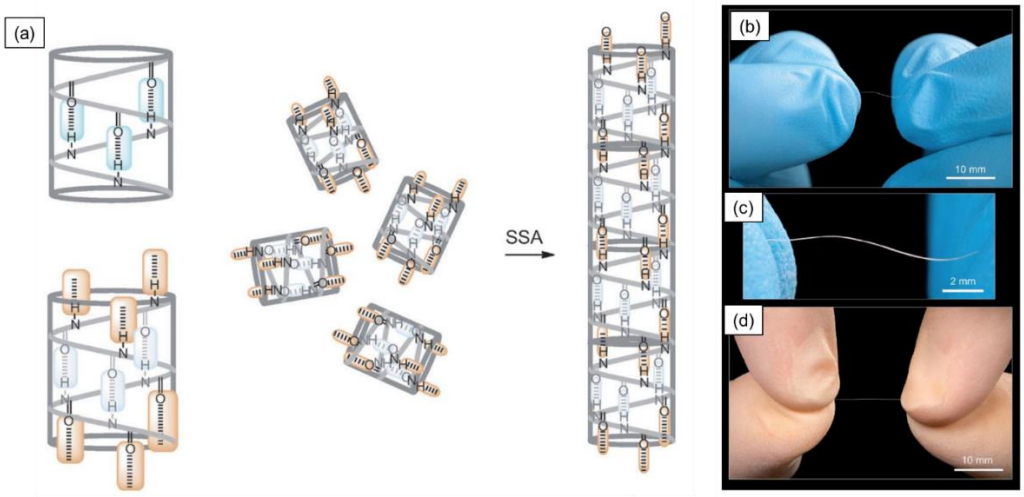

Figure 8. (a) Cartoon of the supramolecular self-assembly (SSA) of 14-helical β-peptides showing fibre formation; (b – d) Photographs of the macroscopic fibres formed from three of the different peptides studied. Reprinted with permission from John Wiley & Sons, M. P. Del Borgo, A. I. Mechler, D. Traore, C. Forsyth, J. A. Wilce, M. C. J. Wilce, M. I. Aguilar and P. Perlmutter, Angew. Chem. Int. Ed., 2013, 52, 8266–8270, Copyright© 2013.

Hydrogel noodle formation has also been reported with a C_{12}-GAGAGAGY peptide amphiphile.[31] The PA was dissolved in water using 0.05 M NaOH and then the pH adjusted. A range of pH values were studied. From pH 11 to pH 8, the self-assembled structures

changed from cylindrical nanofibers to nanoribbons (the nanoribbons also laterally aggregated in bundles). A further decrease to pH 4 resulted in hydrogel formation. The PA solution at pH 11 showed no birefringence in CPOM, even when the solution was sheared. At pH 8, the solution demonstrated birefringence which could be orientated with the application of a shear force between a microscope slide and cover slip. The behaviour was consistent with a nematic liquid crystal phase. The shear orientation of liquid crystal phase inspired the researched to form macroscopic gel noodles by injecting the fluid into an acid gelation bath. This formed gel noodles (approximately 200 μm diameter) that exhibited uniform birefringence in CPOM. This demonstrates the requirement of a specific self-assembled structure and solution behaviour to form gel noodles. Subtle changes to variables such as pH can impact the formation of noodles.

Supramolecular nanotube yarns have been spun from a pH 8.5 aqueous solution of 0.1 wt% L-histidine terminated bolaamphiphile (EDH).[32] Inspired by the spinning of silk from silkworms, the macroscopic yarns can be drawn directly from the aqueous solution by lifting carefully lifting a needle out of the solution. While different to the conventional formation of wet gel noodles, this work is relevant and interesting. A pH 8.5 solution of EDH that was heated and then kept for several days at ambient temperature formed randomly distributed and discrete nanotubes with internal diameters of 22 nm and wall thickness of 12-14 nm (imaged with cryo-TEM). They hypothesise that the alkaline environment would charge the surfaces, leading to a straightening of the nanotubes. The macroscopic yarns possess a uniform diameter of 1.5-5 μm and are highly aligned (seen with CPOM imaging). A home-built setup was used to measure the tensile strength of the yarns. While the yarns can be air-dried quickly, not all the water is. They hypothesise that the tube interior bound water could weaken the self-assembly so water is removed by 48 hours of vacuum drying. The vacuum-dried nanotube yarns show tensile strengths of 45-60 MPa and Young's moduli of 6.8-9.9 GPa, which is almost comparable to that of wool fibres.

Ortony and co-workers studied aramid amphiphile compounds that self-assemble in water to form high-aspect-ratio nanoribbons (Figure 9).[20] When fitting SAXS data of the solutions, they are best depicted by a lamellar bilayer model. Interestingly, the nanoribbons elongate upon sonication, reaching width-to-length aspect ratios of 4000:1. The mechanical properties of individual nanoribbons were investigated using AFM. The Young's modulus was calculated by using a statistical topographical analysis of AFM images and the tensile strength measured in the same manner following horn-sonication-induced scission. One of the compounds was used to form macroscopic threads. The nanoribbon suspension was annealed and drawn out from a pipette tip to form the long macroscopic threads in a gelation medium that show birefringence in CPOM images. The threads can be readily lifted out of the trigger medium and are mechanically robust. The gel threads were air dried, maintaining

structural integrity, and could be handled and bent without breaking as well as supporting up to 200 times its weight. Tensile tests on the dried macroscopic threads showed that out of two divalent anions, that with the higher charge density resulted in threads with a greater Young's modulus. The dried threads showed highly anisotropic SAXS patterns, confirming alignment of the nanoribbons.

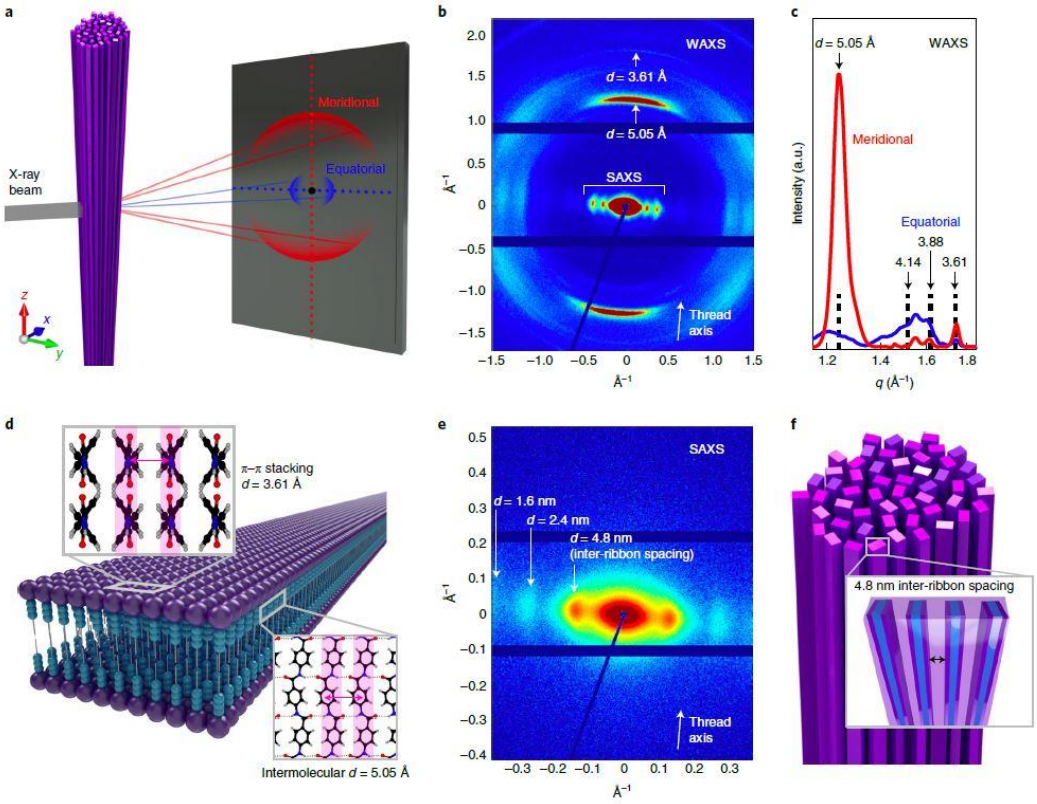

Figure 9. Cartoon schematics for the self-assembled threads. SAXS and WAXS data for solid state threads showing intense anisotropic scattering. Reprinted with permission from Springer Nature, Nature Nanotechnology, T. Christoff-Tempesta, Y. Cho, D.-Y. Kim, M. Geri, G. Lamour, A. J. Lew, X. Zuo, W. R. Lindemann and J. H. Ortony, Nat. Nanotechnol., 2021, 16, 447–454., Copyright© 2021.

A "supramolecular muscle" comprised of a self-assembled amphiphilic molecular motors was reported in 2017.[23] Here, they also used shear flow through a pipette into calcium trigger medium to form aligned nanofiber noodles. The molecular motor undergoes a photochemical isomerisation when irradiated with UV light (λ = 365 nm), resulting in an unstable isomer that undergoes a subsequent irreversible thermal inversion. The photoisomerisation was tracked using NMR spectroscopy. They report phototriggered actuation of the string in both aqueous solution and in air. Through a combination of CPOM, SAXS and grazing incidence small angle X-ray scattering (GI-SAXS) they show that the nanofiber bundles are aligned parallel to the long axis of the gel strings. They also form gel strings using a syringe pump at a flow rate of 0.75 μL/s (2.7 mL/hr) but since they state this

offers no significant benefit over using a pipette they take this no further. In follow on work, multicomponent gel noodles were prepared with iron nanoparticles attached the surface of one type of the nanofiber.[33] These gel strands can be actuated by both light as well as a magnetic field. This allowed for a dual controlled cargo transport experiment in which a piece of paper was moved. The photoactuation curved the gel strand and “collected” the piece of paper. A magnet was then used to move this gel-paper vessel.

Such a study does exist for the formation of radially aligned gel filaments by wet spinning N-heptyl-D-galactonamide (Figure 10).[25] This work operates *via* a solvent switch gelation triggering method, which is very different to those discussed above. The use of a syringe pump allowed the variables that control both the macrostructure and the nanostructure to be comprehensively studied. N-heptyl-D-galatonamide was dissolved in DMSO and then injected vertically downward into water. As the stream of DMSO passes into the water, the DMSO diffuses out and the solvent-switch results in gelation. By varying flow rate, needle diameter and gelator concentration a comprehensive phase diagram was produced to show that a “sweet spot” of flow rates was required. Too high a flow rate and the gel strand did not form and too slow the needle clogged. Using a combination of optical microscopy and cryo-SEM, the researchers show that the gel filaments are arranged radially. This demonstrates the value of using a syringe pump to comprehensively study the variables that control the noodle formation. To the best of our knowledge, a syringe pump has not been used for the formation of LMWG noodles with a nanostructure aligned parallel to the long axis of noodle before.

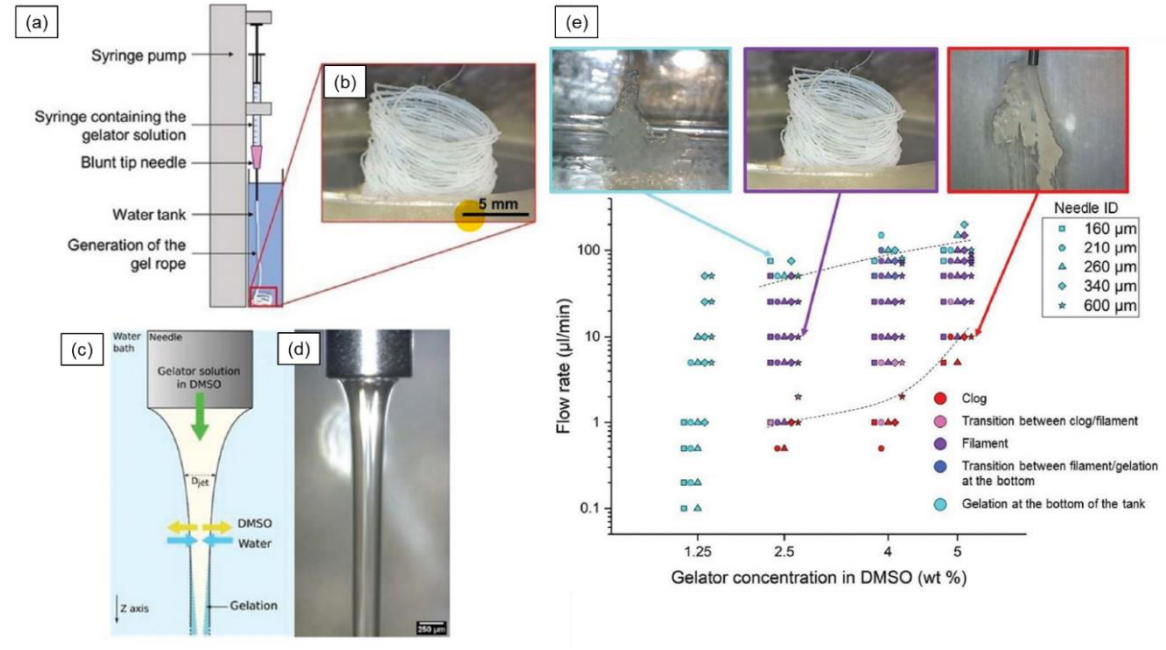

Figure 10. (a) Cartoon schematic of the experimental setup used; (b) Coiled gel filaments; (c) Cartoon schematic of the gelation mechanism; (d) Photograph of the DMSO jet; (e) Phase diagrame of the gelator concentration vs flow rate, with representative photographs of the gels that form. Reproduced from A. Chalard, P. Joseph, S. Souleille, B. Lonetti, N. Saffon-Merceron, I. Loubinoux, L. Vaysse, L. Malaquin and J. Fitremann, Nanoscale, 2019, 11, 15043–15056, with permission from The Royal Society of Chemistry (Copyright © 2019) under the Creative Commons Attribution-NonCommercial 3.0 Unported (CC BY-NC 3.0) licence.

1.2 Aims

The purpose of this research was to form PBI gel noodles with the nanostructure both unaligned and aligned parallel to the long axis of the noodle. Then perform photocatalysis on those structures to determine how nanostructure alignment influences photocatalytic efficiency. PBIs generally form solutions that possess relatively low viscosity even when worm-like micelles are formed meaning that initial attempts to form noodles were unsuccessful. A 10 mg/mL L-leucine functionalised perylene bisimide (PBI-L; Figure 11b) was used and the solution initially possessed a noodle-like shape when dispensed, but this was quickly lost resulting in an inhomogeneous mass of gel (Figure 11a). Either a specific functionalisation of PBI, set of solution conditions or equipment to make noodles may be required.

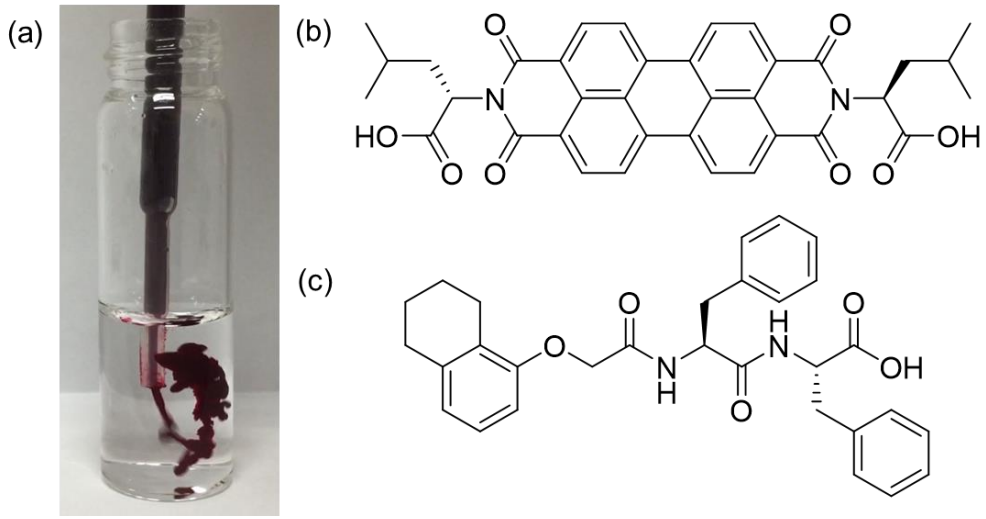

Figure 11. (a) Attempted gel noodle formation with 10 mg/mL PBI-L at pH 6.00 into 50 mM $CaCl_2$; Chemical structures of (b) PBI-L and (c) 1ThNapFF.

From the literature discussed above, it is clear that the self-assembled structure in the pre-gel solution is crucial to gel noodle formation and in determining the alignment. Also, the literature demonstrates the chemical diversity that can be used to form these structures. Unfortunately, many solutions are presented without discussing in detail how variables such as concentration etc were chosen and how they influence noodle formation and alignment. Also, it is not clear to what extent the method used to prepare noodles determines whether or not they will form and how aligned they will be. Much of the research to date uses injection by hand which is inherently irreproducible and is reflected in the diameter variation seen in the microscope images reported. Some work does use syringe pumps but typically uses one specific flow rate. For real world applications, control over the structures that form as well as reproducibility and scalability are vital. As such, a mechanised device (such as a syringe pump) is ideal for forming gel noodles but variables such as solution flow rate and

nozzle diameter have not been widely investigated. A study to this end for the formation of solvent switch triggered gels has previously been presented and such a study is required for this field.[25] While there is a relatively large volume of literature on the formation of LMWG noodles, there is yet to be a rigorous study on the parameters that control LMWG noodle formation, alignment and morphology.

In order to investigate these parameters with the aim of forming PBI gel noodles, a model system was first investigated to determine the required solution properties for effective noodle formation. With this knowledge a targeted approach to PBI noodle formation could then be carried out. The chosen model system was the functionalised dipeptide 1ThNapFF (Figure 11c) because it forms worm-like micelles at high pH, resulting in highly viscous and shear-thinning solutions.[34,35]

2 Results and discussion

2.1 1ThNapFF solution characterisation

2.1.1 Shear viscosity measurements

For 1ThNapFF, it was expected that the self-assembly and viscosity would change as the concentration was increased. Shear viscosity measurements were performed and show an increase in viscosity with concentration from 1 – 20 mg/mL (Figure 12). The 1 mg/mL solution behaved as a Newtonian fluid (in this measurement regime) and possessed a viscosity of 1 mPa.s (which is comparable to water) across the shear rate range studied. All concentrations >1 mg/mL exhibited shear-thinning behaviour.

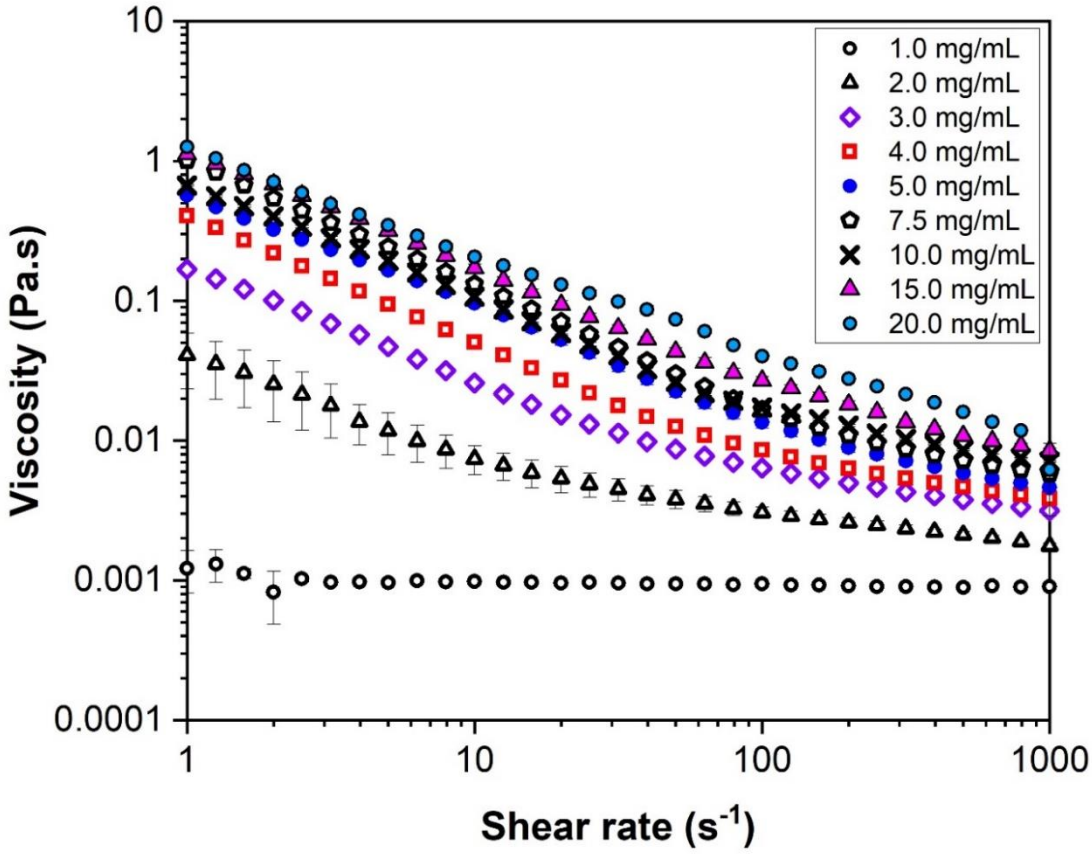

Figure 12. Viscosity of 1ThNapFF solutions at different concentrations at pH 11.3 across a shear rate of 1 to 1000 s^{-1}. Error bars are the standard deviation of triplicate measurements. Reproduced from D. McDowall, M. Walker, M. Vassalli, M. Cantini, N. Khunti, C. J. C. Edwards-Gayle, N. Cowieson and D. J. Adams, Chem. Commun., 2021, 57, 8782–8785, with permission from the Royal Society of Chemistry.

By plotting solution concentration against viscosity at both 10 and 100 s^{-1} the relationship is more clearly visualised (Figure 13). The data show an abrupt increase in viscosity with

concentration after 1 mg/mL and then levelling off at 7.5 and 10 mg/mL. The viscosity then increases with concentration from 15 and 20 mg/mL.

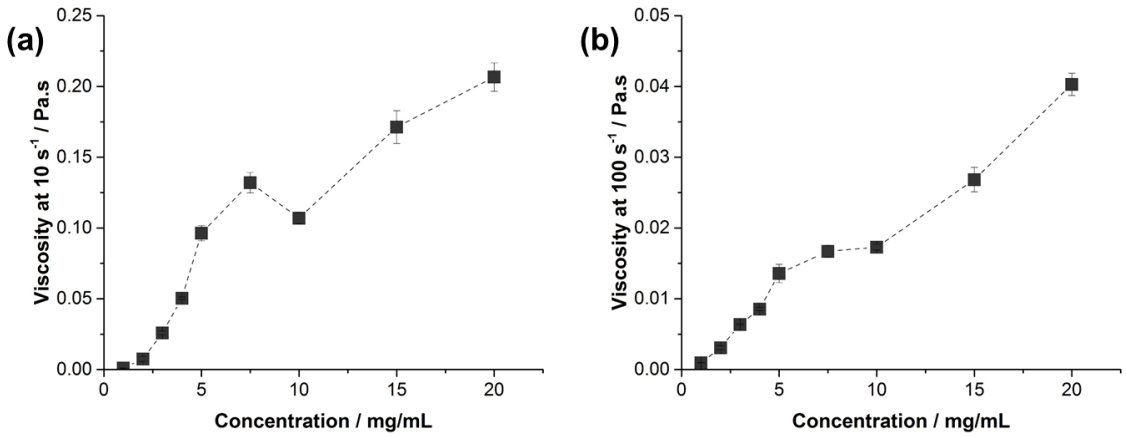

Figure 13. Concentration vs viscosity for solutions of 1ThNapFF at pH 11.3 at different shear rates (a) 10 s^{-1} and (b) 100 s^{-1}.

The heat/cool process for the peptide amphiphile in Stupp and co-workers original work resulted in a viscosity change from 5 – 15 mPa.s.[19] Both of these viscosities were adequate to form noodles, although the shear rate used for the measurement is not given. Based on shear viscosity alone, 1ThNapFF solutions of 2 mg/mL and above should be suitable to form noodles based on this analysis, but the relationship is likely more complex than reaching a certain viscosity.

2.1.2 Small angle X-ray scattering

Shear viscosity measurements across a concentration range from 1 to 20 mg/mL showed a general increase in viscosity with concentration. All concentrations of 1ThNapFF at 2 mg/mL and greater showed shear-thinning behaviour. SAXS data was collected to correlate with the shear viscosity findings. SAXS experiments were performed *via* mail-in at the B21 beamline at the Diamond Light Source synchrotron by Dr Nathan Cowieson. The raw data was then obtained from Diamond and processed. The 2D scattering patterns are shown in Figure 14. Most of the scattering patterns show a large degree of anisotropy, which is attributed to the alignment of the worm-like micelles during sample loading into the capillaries. To best understand this set of SAXS data, the 2D scattering patterns collected by the detector must first be studied.

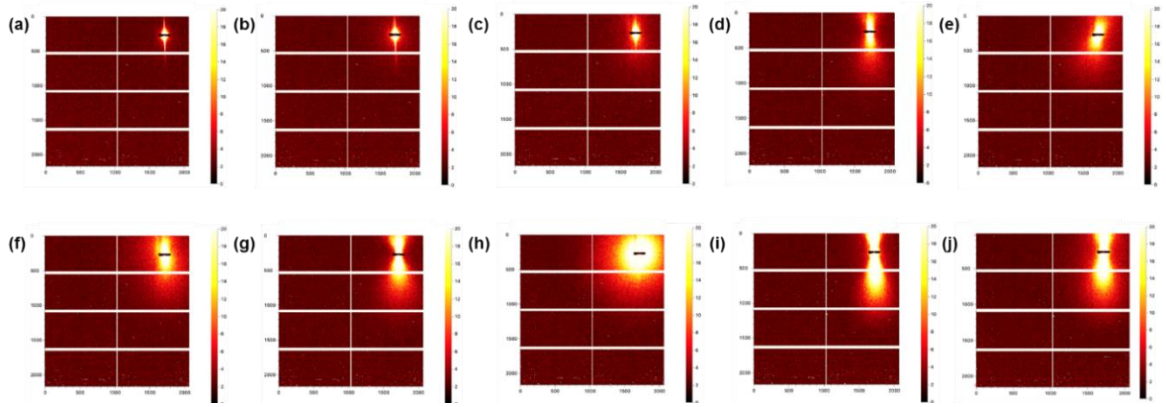

Figure 14. 2D scattering plots of aqueous 1ThNapFF at pH 11.3 at a range of concentrations. (a) 1.0 mg/mL; (b) 1.5 mg/mL; (c) 2.0 mg/mL; (d) 2.5 mg/mL; (e) 3.0 mg/mL; (f) 4.0 mg/mL; (g) 5.0 mg/mL; (h) 7.5 mg/mL; (i) 10 mg/mL; (j) 15 mg/mL. Reproduced from D. McDowall, M. Walker, M. Vassalli, M. Cantini, N. Khunti, C. J. C. Edwards-Gayle, N. Cowieson and D. J. Adams, Chem. Commun., 2021, 57, 8782–8785, with permission from the Royal Society of Chemistry.

At 1.0 and 1.5 mg/mL the scattering intensity is low and almost completely isotropic. To demonstrate this point, a radial integration across the Q range of 0.02-0.034 $Å^{-1}$ (relatively close to the beamstop) was performed on the 2D data. Figure 15 shows the data for 1.0 – 2.5 mg/mL (note the extreme data points at approximately -100° and 80° are due to capillary misalignment flare). At 2.0 and 2.5 mg/mL, the data are highly anisotropic, which is consistent with an increased degree of aligned self-assembled structures. As concentration is increased from 2.5 mg/mL, the data show an increased scattering intensity and all data (except 7.5 mg/mL) show anisotropic scattering.

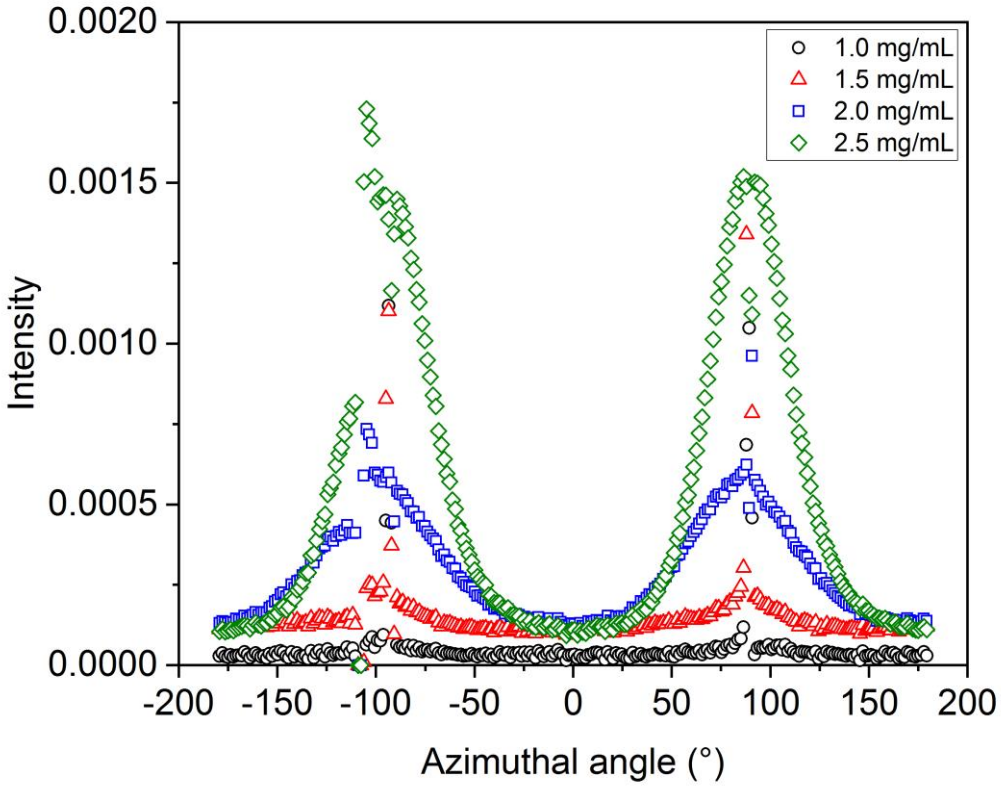

Figure 15. Radial integrations for 1ThNapFF solutions from 1.0 – 2.5 mg/mL across a Q range of 0.02-0.034 $Å^{-1}$. Kinks in the data at 90° and -90° are due to X-ray detector module boundaries.

An appropriate approach to processing anisotropic scattering data is to perform segment or bow-tie integrations over both the areas of low and high scattering intensity.[36] As such, two data sets are generated for each sample and an example is given in Figure 16.

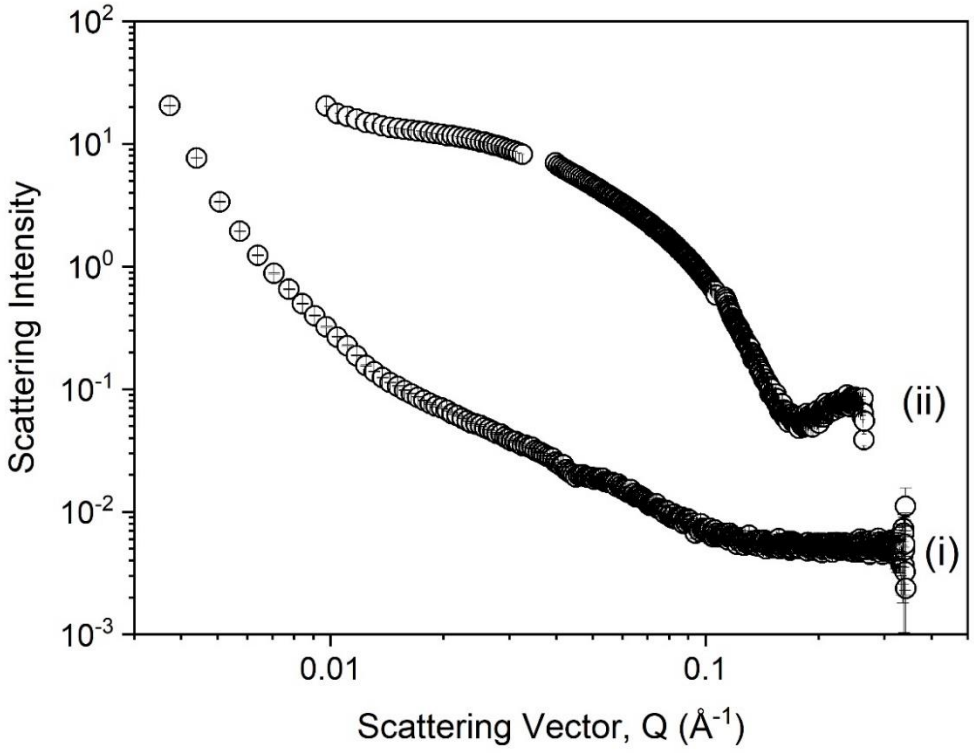

Figure 16. SAXS (bow-tie integration) data for solutions of 1ThNapFF at a concentration of 10 mg/mL at pH 11.3. (i) the low intensity scattering regions obtained from a horizontal bow-tie integration and (ii) the high intensity scattering regions obtain from a vertical bow-tie integration. The kinks and missing data points in each data occur due to integration around the detector module boundaries. Reproduced from D. McDowall, M. Walker, M. Vassalli, M. Cantini, N. Khunti, C. J. C. Edwards-Gayle, N. Cowieson and D. J. Adams, Chem. Commun., 2021, 57, 8782–8785, with permission from the Royal Society of Chemistry.

The 1D scattering data for all samples is shown in Figure 17. For anisotropic data, the high intensity scattering bow-tie integration is shown. This data was analysed in SasView (version 5.0.2)[37] and fitted to structural models (Table 1). The SAXS data shows trends that correlate with the viscosity data. The data at 1.0 and 1.5 mg/mL show isotropic, low scattering intensity (Figure 17). These data were not fitted to any structural models (due to low intensity) and correlate with either no or a very low concentration of self-assembled structures. At concentrations of 2 mg/mL and greater, the samples scatter strongly and were fitted to either the cylinder or flexible cylinder models (Table 1). These data depict long cylindrical structures with radii of around 2.1 nm at all concentrations of ≥2 mg/mL, suggesting no significant change in the fibre cross-sections with concentration. From a concentration of 5 mg/mL and above, the addition of a flexible component to the fitting model was required. In all cases the models depict cylinders with lengths of <80 nm but the true length of these structures is likely much longer and only the persistence length (related to

the flexibility of the structure) is seen. Many of the data sets required the addition of a power law to capture the upturn in intensity at low Q. The rheology and SAXS data show that the more concentrated solutions possessed self-assembled 1D structures and higher viscosities and so it was expected that these would be most suited to forming gel noodles.

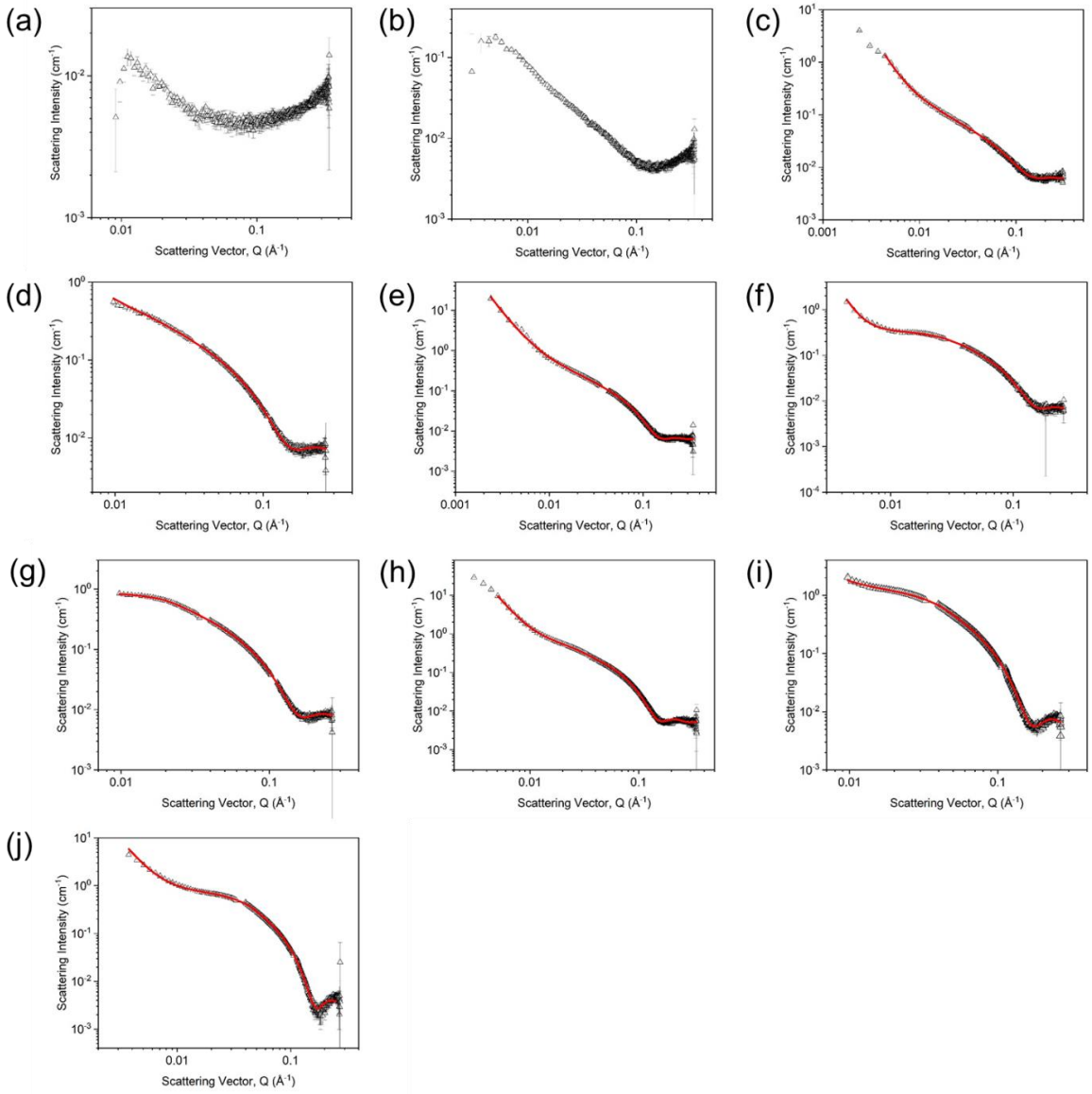

Figure 17. SAXS data (black hollow triangles) and fits (red lines) from the vertical bow-tie integrations of the 1ThNapFF concentration series at pH 11.3. Concentrations of (a) 1.0 mg/mL, (b) 1.5 mg/mL, (c) 2.0 mg/mL, (d) 2.5 mg/mL, (e) 3 mg/mL, (f) 4 mg/mL, (g) 5 mg/mL, (h) 7.5 mg/mL, (i) 10 mg/mL, (j) 15 mg/mL. Reproduced from D. McDowall, M. Walker, M. Vassalli, M. Cantini, N. Khunti, C. J. C. Edwards-Gayle, N. Cowieson and D. J. Adams, Chem. Commun., 2021, 57, 8782–8785, with permission from the Royal Society of Chemistry.

Table 1. Model fitting parameters obtained for 1ThNapFF solutions.

Concentration / mg/mL	2.0	2.5	3.0	4.0	5.0	7.5	10.0	15.0
Processing type	Vertical bow-tie integration	Vertical bow-tie integration	Vertical bow-tie integration	Vertical bow-tie integration	Vertical bow-tie integration	Isotropic	Vertical bow-tie integration	Vertical bow-tie integration
Fitting model	Cylinder + power law	Cylinder	Cylinder + power law	Cylinder + power law	Flexible cylinder	Flexible cylinder + power law	Flexible cylinder + power law	Flexible cylinder + power law
Cylinder scale	0.000001	0.000646	0.000493	0.000752	0.001381	0.000964	0.002830	0.001737
Cylinder scale error	0.00000001	0.0000025	0.0000017	0.0000035	0.0000027	0.0000015	0.0000103	0.0000042
Background	0.000035231	0.0070	0.0063	0.0066	0.0075	0.0048	0.0052	0.0027
Background error	0.0000002	0.00005	0.00003	0.00008	0.00005	-	0.00010	0.00005
Radius / Å	21.8	22.4	22.7	22.9	22.2	19.4	21.7	22.1
Radius error / Å	0.14	0.06	0.05	0.07	0.03	0.02	0.03	0.04
Length / Å	798.2	581.1	808.4	133.7	199.9	295.4	149.5	138.7
Length error / Å	59.9	19.9	23.1	0.6	0.7	0.7	0.9	0.9
Kuhn length / Å	-	-	-	-	162.08	73.84	82.43	76.10
Kuhn length error / Å	-	-	-	-	1.34	0.00	0.34	0.54
Power law scale	$3.1x10^{-11}$	-	$7.54x10^{-8}$	$8.54x10^{-12}$	-	$3.08x10^{-8}$	$4.79x10^{-6}$	$2.64x10^{-7}$
Power law scale error	$7.9x10^{-12}$	-	$3.41x10^{-9}$	$3.05x10^{-12}$	-	$6.55x10^{-10}$	$2.38x10^{-6}$	$3.97x10^{-8}$
Power law	3.51	-	3.21	4.74	-	3.70	2.52	3.00
Power law error	0.04887	-	0.0081	0.0689	-	0.0042	0.11	0.03
Reduced Chi^2	0.33	0.86	5.49	1.90	1.73	25.51	3.85	3.56

2.2 Formation and control of gel noodles

2.2.1 Noodle analysis

Optical microscopy was used to image and then measure the diameter of the gel filaments. The microscope had functionality to view the samples under cross polarised light. CPOM is a widely used technique to image materials with anisotropic structures and has been widely used for gel noodles.[13,19] Using CPOM, aligned structures exhibit birefringence and appear bright in an otherwise dark image. Patchy bright regions indicate discrete domains with alignment whereas uniform birefringence along the noodle indicates continuous alignment throughout the structure. A dark image with no visible birefringence suggests no alignment.

2.2.2 Preliminary noodle formation using pipettes

A concentration of 10 mg/mL was selected to form gel noodles at the first attempt based on the viscosity and SAXS data, which showed it formed a highly viscous shear-thinning solution with worm-like micelles present. In previous literature, pipettes were often used to form the gel noodles as they are easily accessible and can make a pre-defined volume of gel. However, details of the exact pipettes used to prepare optimal filaments are often not detailed. The effect of using different pipettes and therefore changing the pipette tip

diameter from which the solution is dispensed (among other variables) was investigated first. 2-20 µL, 20-200 µL and 100-1000 µL (1 mL) pipettes were tested. A 20 µL injection used for the two smaller volume pipettes and a 100 µL injection for the 100-1000 µL pipette.

It was found that gel noodles could be readily formed with the 10 mg/mL 1ThNapFF solution with all pipettes. Noodles could be formed with both acidic (HCl) triggers and ionic ($CaCl_2$) triggers. 50 mM $CaCl_2$ is used in the literature[19] and unless otherwise stated, was used as the gelation trigger for all noodles. It should be noted that any conclusions drawn from this point on may not translate to being applicable for an acid trigger because gelation occurs by a different mechanism for the acid trigger.[14,38]

An initial observation was that the speed of injection from the pipette was important for noodle formation. If the wrong speed was used, noodles did not form. The effect of this variable was tested (Figure 18) in 7 mL vials by varying the rate of depressing the pipette plunger by hand. A faster rate of pressing the plunger, the faster the flow rate of the dipeptide solution leaving the pipette tip. The test was could not be accurately controlled or quantified because it was performed by hand, but it gave a valuable insight into the effect of injection speed. It was found that with a slow injection the pipette tip would block, or a 'ball' of gel would form at the tip (Figure 18a). For the 2-20 µL pipette, this was not seen and at very slow injection rates noodles were still formed. When injected too quickly, turbulence created from the rapid injection resulted in inhomogeneous noodles (Figure 18c). With intermediate injection speeds all three pipettes could form continuous, uniform filaments (Figure 18b). With relative ease a range of noodle diameters could be accessed by using different pipettes.

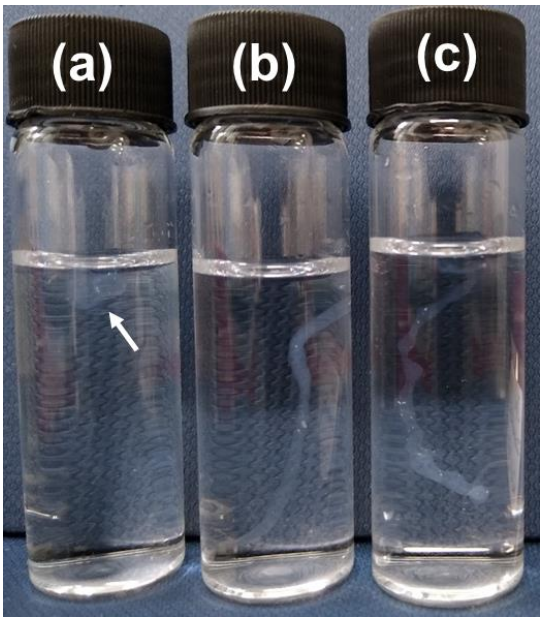

Figure 18. Pictures of gel noodles formed with 100-1000 µL pipette at different injection speeds (a) slow; (b) intermediate and (c) fast. For (a) a white arrow has been added to guide the eye to the ball of gel.

2.2.2.1 Static formed noodles

Noodles formed by direct injection into a trigger bath using the pipettes (referred to as static formed noodle) were studied with microscopy. To image the noodles on the microscope, the 1ThNapFF solution was dispensed into a 100 mL bath of 50 mM $CaCl_2$ with a microscope slide at the bottom. The excess trigger medium was removed and the slide with the noodle on it lifted out and imaged. The resulting noodles formed from intermediate injection speeds were imaged on an optical microscope under both normal and cross polarised light (Figure 20). Four noodles were made using each pipette and imaged, resulting in >20 representative microscope images. ImageJ was used to measure filament diameter in each microscope image and the result plotted as a histogram (Figure 19). The results show a relatively wide distribution of filament diameters for the 20-200 µL (0.55 to 1.20 mm) and 1 mL pipette (0.85 to 1.85 mm). The 2-20 µL pipette has a narrow distribution centred on 0.45-0.50 mm. In each case, all of the filaments were wider than the pipette tip used. The exact reason for this is unknown but it may be due to the die-swell phenomena.[39,40]

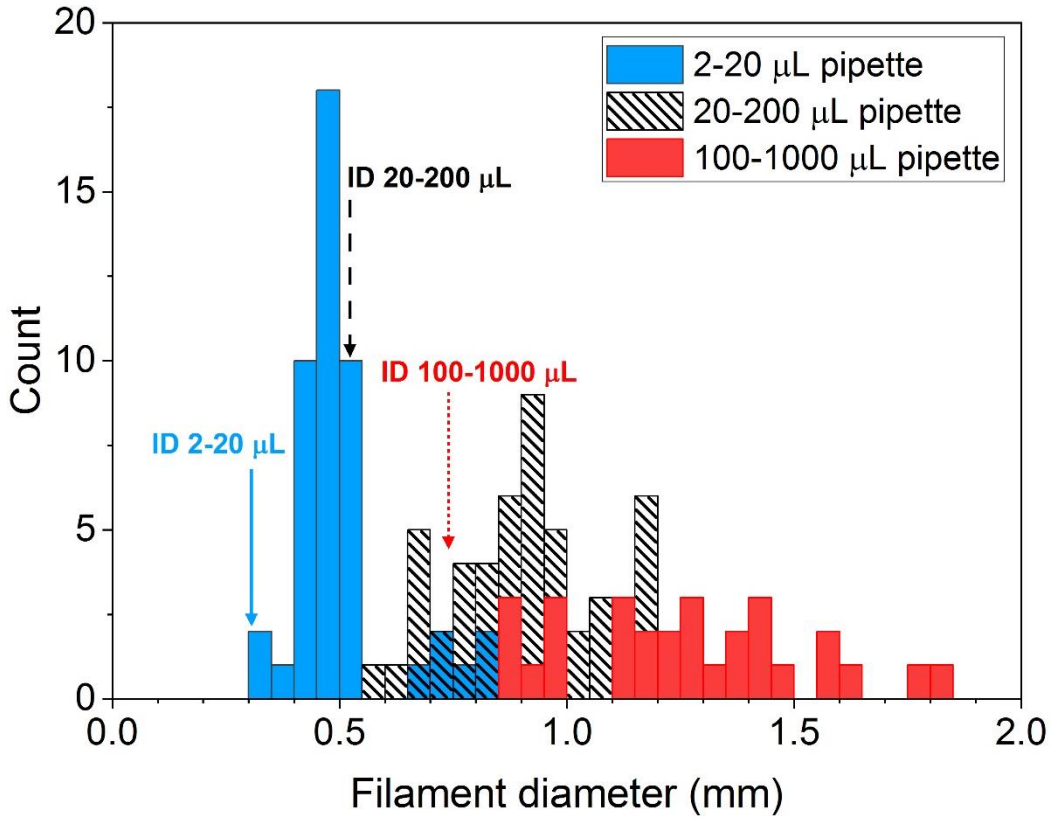

Figure 19. Histogram of noodle diameters formed with the three types of pipette. The inner diameter (ID) for each pipette tip is marked on the graph. Reproduced from D. McDowall, M. Walker, M. Vassalli, M. Cantini, N. Khunti, C. J. C. Edwards-Gayle, N. Cowieson and D. J. Adams, Chem. Commun., 2021, 57, 8782–8785, with permission from the Royal Society of Chemistry.

The extent of alignment within the noodle structures was probed with CPOM. For the noodles formed with the 2-20 pipette, only very faint birefringence was seen in the noodles (Figure 20a) and this was not uniform through the structures. For the 20-200 μL and 1 mL pipettes, a range of birefringence was observed. In some of the noodle regions, very little birefringence is seen but also both patchy and uniform birefringence is present (Figure 20b and 20c). The brightness of birefringence is dependent on the angle of the alignment relative to the polarisers. Initially, it was thought that the cause of dark regions was due to the alignment being at the wrong angle relative to the polarisers. This does not appear to be the case because both bright and dark noodles are seen that are in the same orientation relative to the polarisers. The results show that noodle regions with uniform birefringence were formed but this was not achieved consistently with the pipettes. A method that reproducibly forms aligned noodles is sought after.

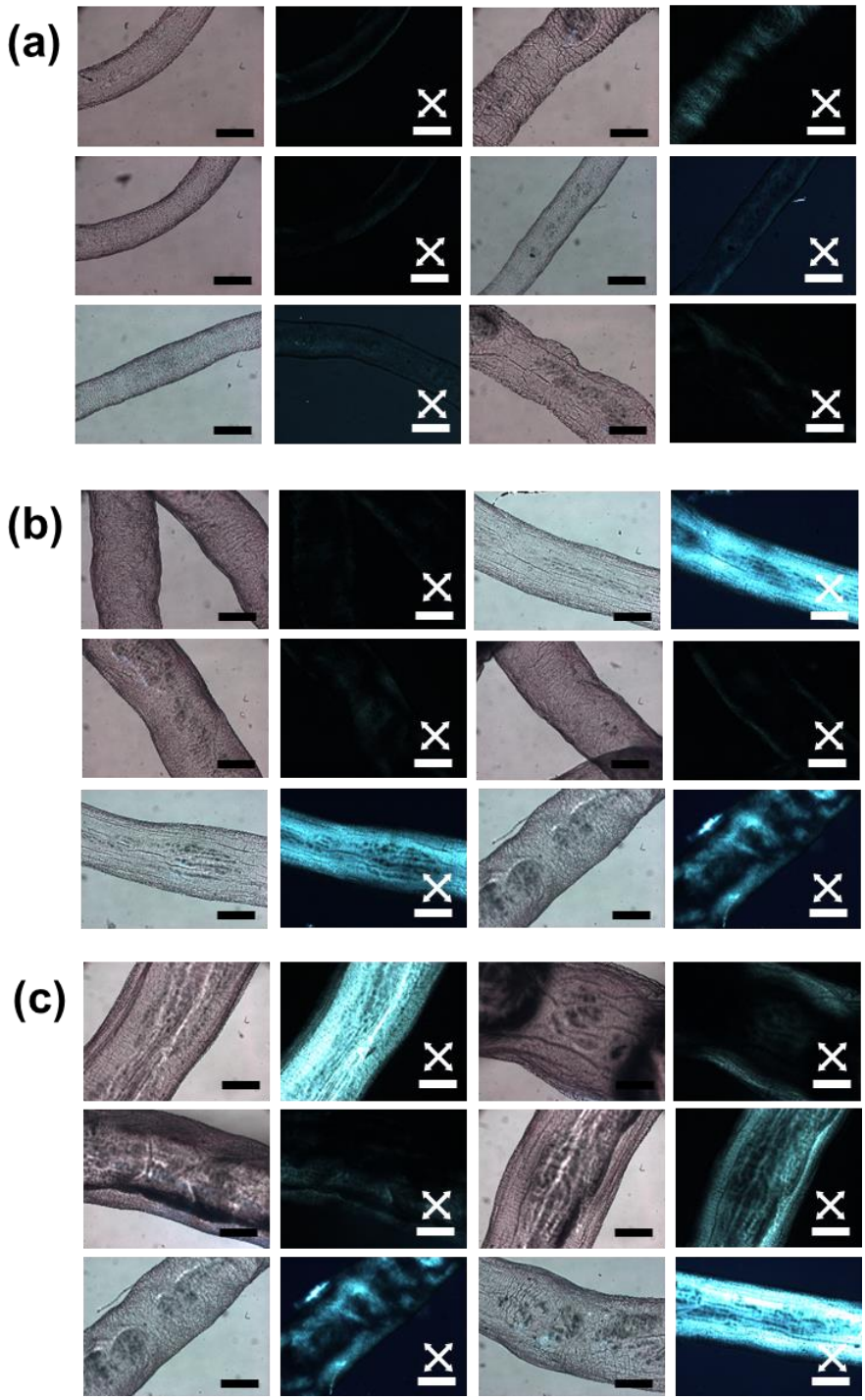

Figure 20. Microscope images of gel filaments formed from (a) a 2-20 µL pipette; (b) a 20-200 µL pipette and (c) a 100-1000 µL pipette under static conditions. Two images are given for each filament region that was imaged. One under normal light and the other under cross polarised light. In each set of images, the left hand images are under normal light, the right images are under cross polarised light. Scale bars represent 0.5 mm and white arrows indicate polariser direction.

Interestingly, the noodles were sufficiently mechanically robust to be lifted out of the trigger medium and remain intact (Figure 21).

Figure 21. Photograph of a gel noodle lifted out of the trigger bath using a spatula. Reproduced from D. McDowall, M. Walker, M. Vassalli, M. Cantini, N. Khunti, C. J. C. Edwards-Gayle, N. Cowieson and D. J. Adams, Chem. Commun., 2021, 57, 8782–8785, with permission from the Royal Society of Chemistry.

2.2.2.2 Dragged noodles

The aim of this work was to controllably form both un-aligned and aligned gel noodles. This could not be done consistently by static injection with pipettes alone. It was hypothesised that stretching the noodles as they form may help induce alignment. Therefore, noodles were made by a dragging process. This involves dragging the pipette tip through a pool of trigger medium whilst dispensing pre-gel solution. A similar technique (but not with the specific purpose of achieving stretching and alignment) has been reported previously in the literature, where a video can be seen in the ESI of that publication.[19] The speed at which the pipette is dragged will influence the filament that forms. The dragging technique showed a range of diameters in the same filament and could not be performed reproducibly. With a relatively fast drag, using both the 20-200 µL and 1 mL pipettes a reduction in filament diameter occurred in places. The thin filament regions showed uniform birefringence (Figure 22). The results suggest that an extensional process as the filaments form can effectively align the nanostructure. Extensional stresses have been shown to be important for the formation of synthetic spider silk, polymer crystallisation and the alignment of anisotropic particles.[41–43] This dragging technique was unsuitable for the 2-20 µL pipette as the filament was simply pulled along with the pipette. Dispensing by hand when using the pipettes was

easy but lacked reproducibility and consistency. Aligned regions were formed both under static and dragged conditions but this was difficult to control and resulted in very limited lengths of aligned filament.

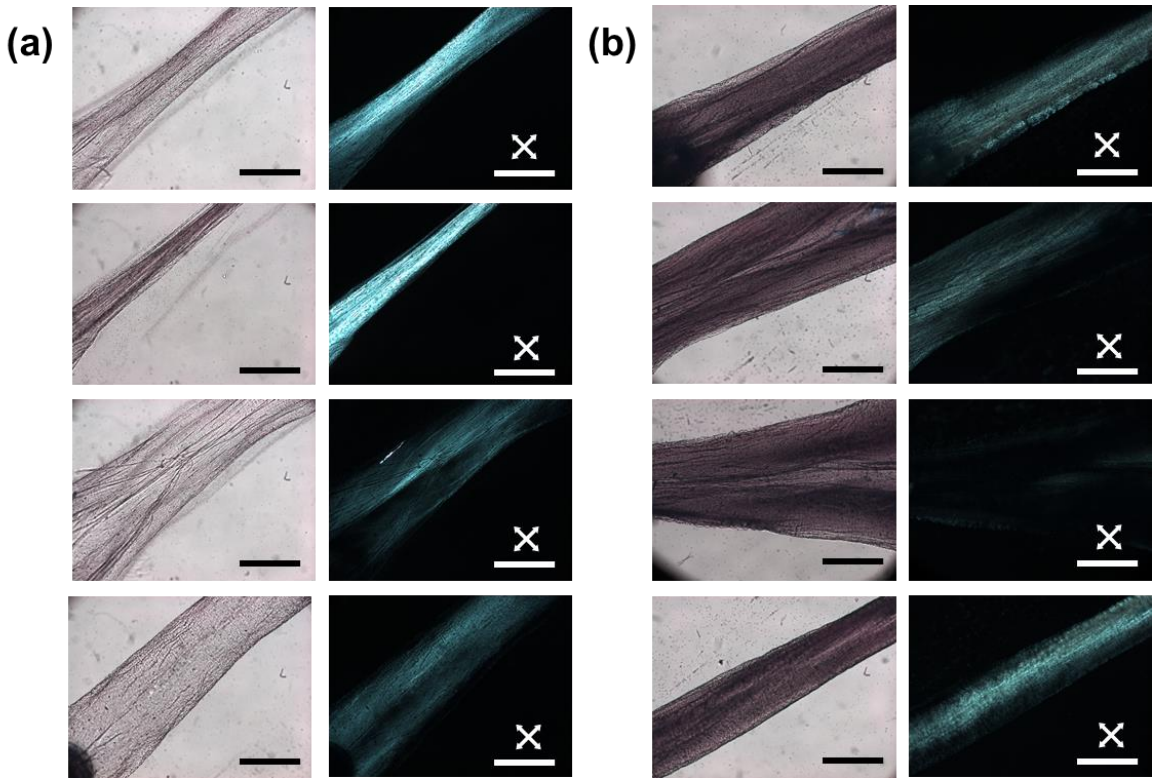

Figure 22. Microscope images of dragged gel filaments formed from (a) a 20-200 µL pipette and (b) a 100-1000 µL (1 mL) pipette. In each set of images the left hand images are under normal light, the right images are under cross polarised light. Scale bars represent 0.6 mm and white crosses indicate polariser direction.

2.2.3 Syringe pump – static formed noodles

To reproducibly control noodle formation, a syringe pump was employed. Briefly, a syringe containing gelator solution was attached *via* tubing to a flat-headed needle (413 um inner diameter) and connected to a syringe pump. The flow rate (in mL/hr) could be finely controlled with this equipment. With this setup the effect of flow rate and 1ThNapFF concentration were investigated. As with the pipettes, excessively slow (<5 mL/hr) and excessively fast flow rates (>200 mL/hr) did not form uniform noodles.

2.2.3.1 Minimum noodle concentration

The minimum concentration at which noodles could form was investigated to determine the minimum noodle concentration (MNC). A fixed flow rate was used as this was shown to affect whether or not noodles would form during preliminary experiments with the pipettes. Conceivably, the flow rate may be a significant factor for gel noodle formation when working at a concentration close to the MNC, but this is not investigated in great detail here. It was

found that noodles could form at a concentration of 5 mg/mL, but the structures formed were challenging to see by eye and on the microscope. For <5 mg/mL, it became increasingly challenging to see the structures without the addition of the dye, Nile blue A. The dye was added to the 1ThNapFF solutions at a concentration of 80 ppm to better visualise the gel structures that form. Concentrations of 1.0, 1.5, 2.0 and 4.0 mg/mL 1ThNapFF were then tested. At 4.0 and 2.0 mg/mL gel noodles were formed (Figure 23) and the dye aided in the visualisation. At concentrations of 1.5 and 1.0 mg/mL no noodles formed, instead inhomogeneous clumps of gel formed in the solutions. As such, the MNC is assigned as 2.0 mg/mL. This concentration links closely with both the onset of shear-thinning behaviour seen in the shear viscosity data as well as the presence of 1D nanofibres as derived from fitting the SAXS data.

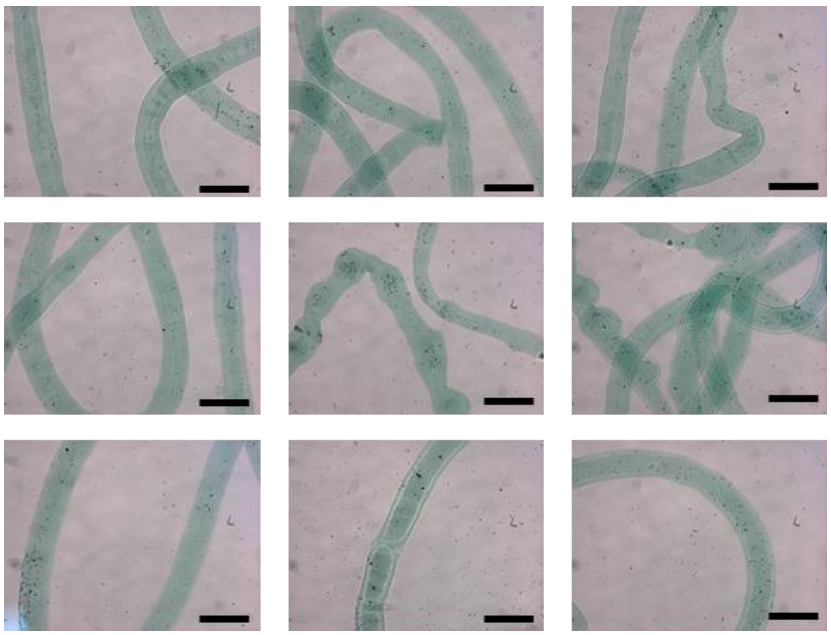

Figure 23. Optical microscope images of gel filaments made with 2 mg/mL 1ThNapFF with 80 ppm Nile Blue A at a flow rate of 10 mL/hr. Scale bars represent 0.6 mm. Reproduced from D. McDowall, M. Walker, M. Vassalli, M. Cantini, N. Khunti, C. J. C. Edwards-Gayle, N. Cowieson and D. J. Adams, Chem. Commun., 2021, 57, 8782–8785, with permission from the Royal Society of Chemistry.

2.2.3.2 Effect of 1ThNapFF concentration under static formation

With the MNC determined, the influence of 1ThNapFF concentration on filament diameter and alignment was investigated. Two flow rates, 10 mL/hr and 100 mL/hr were selected and concentrations of 5, 10 and 15 mg/mL were studied. Gel noodles were formed under static conditions in a 100 mL bath of 50 mM $CaCl_2$. Optical microscopy was used to assess the filament diameter and nanostructure alignment. At 10 mL/hr, the three different concentrations showed different distributions (Figure 24a), with noodle diameter increasing with concentration. At 100 mL/hr, all three concentrations had similar diameter distributions

centred at 0.80 to 0.95 mm (Figure 24e). Unsurprisingly, the larger flow rate lead to an increase in noodle diameter.

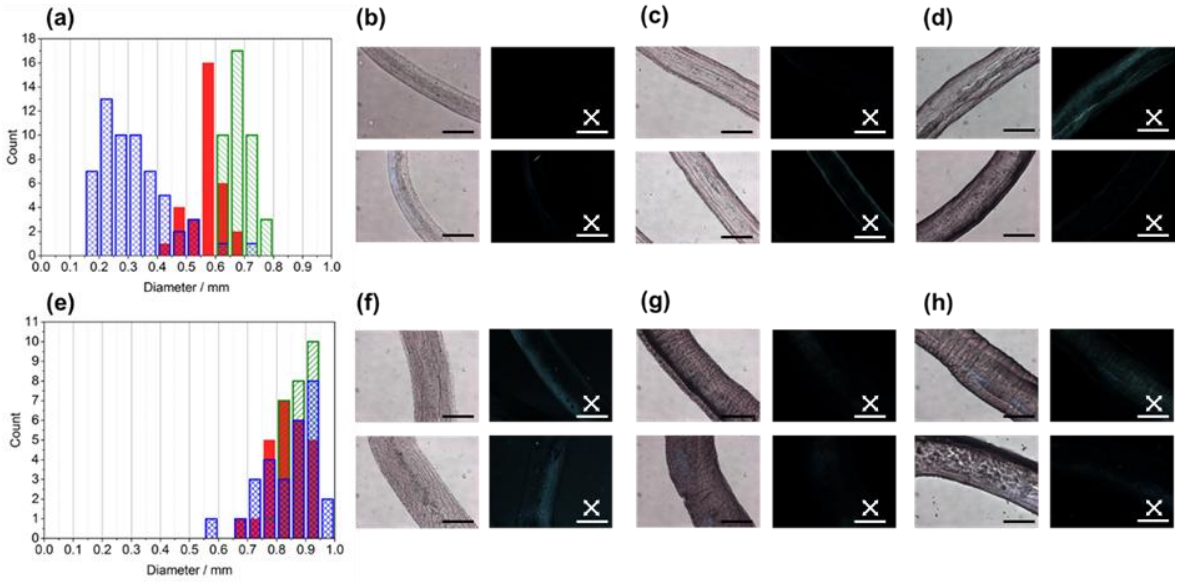

Figure 24. (a) Histogram of filament diameters for 5 mg/mL (blue, crisscrossed), 10 mg/mL (red, solid) and 15 mg/mL (green, dashed) 1ThNapFF at a flow rate 10 mL/hr with corresponding optical microscope images both normal and cross polarised light for (b) 5 mg/mL; (c) 10 mg/mL and (d) 15 mg/mL; (e) Histogram of filament diameters for 5 mg/mL (blue, criss crossed), 10 mg/mL (red, solid) and 15 mg/mL (green, dashed) 1ThNapFF at a flow rate 100 mL/hr with corresponding optical microscope images both normal and cross polarised light for (f) 5 mg/mL; (g) 10 mg/mL and (h) 15 mg/mL. Scale bars represent 0.6 mm and white crosses indicate polariser directions.

The reason for these differences are likely complex and will be linked to the fluid viscosities. The SAXS data shows that the self-assembled structures present are very similar at these three concentrations. The fluids are shear-thinning and show different viscosities at different shear rates but the viscosity profiles change with solution concentration. The two different flow rates will impart different shear forces on the fluid as they are dispensed, thus a complex relationship arises that cannot be easily deconvoluted. While the exact reasons are not understood, the findings offer a route to controlling the diameter of the gel filaments that are formed, which is relevant to potential applications. All noodles formed showed limited birefringence in CPOM images (Figure 24b to 24d and 24f to 24h), indicating that while noodles could be reproducibly formed and controlled using flow rate and concentration, alignment was not achieved with this setup.

2.2.3.3 Effect of flow rate under static formation

In the concentration series, the filament diameter could be controlled by changing the flow rate. This relationship was investigated further at a fixed concentration of 10 mg/mL. The results (Figure 25a) show that the filament diameter increased with an increasing flow rate. This allows for fine tuning of the structures formed.

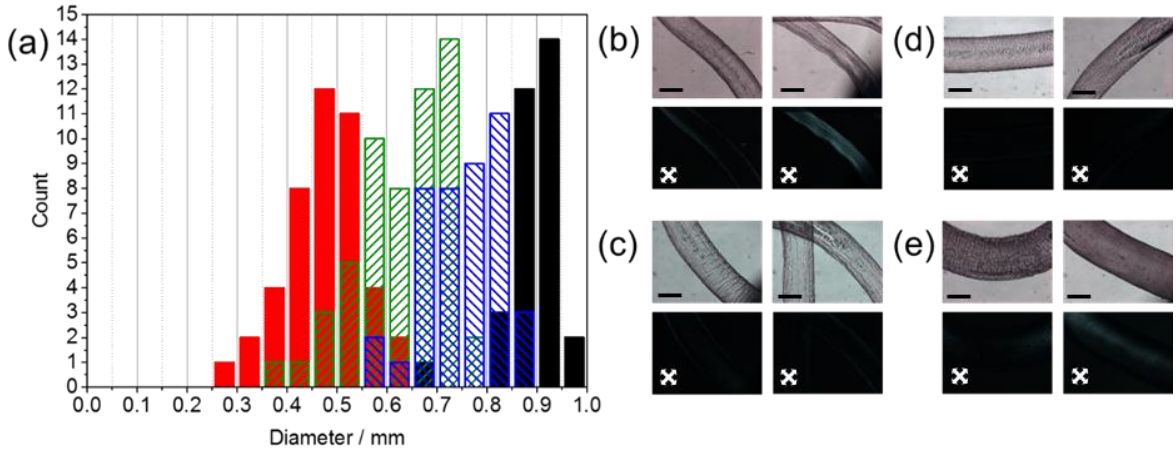

Figure 25. (a) Histogram of the filament sizes formed at flow rates of 10 mL/hr (solid red), 25 mL/hr (dashed green), 50 mL/hr (dashed blue) and 100 mL/hr (solid black); microscope images for (b) 10 mL/hr; (c) 25 mL/hr; (d) 50 mL/hr; (e) 100 mL/hr. Scale bars represent 0.5 mm. White crosses denote direction of the polarisers.

The CPOM images provide further evidence of the lack of alignment within the gel noodles formed during static injection into the trigger bath (Figure 25 and 26). A different approach is needed to form aligned structures.

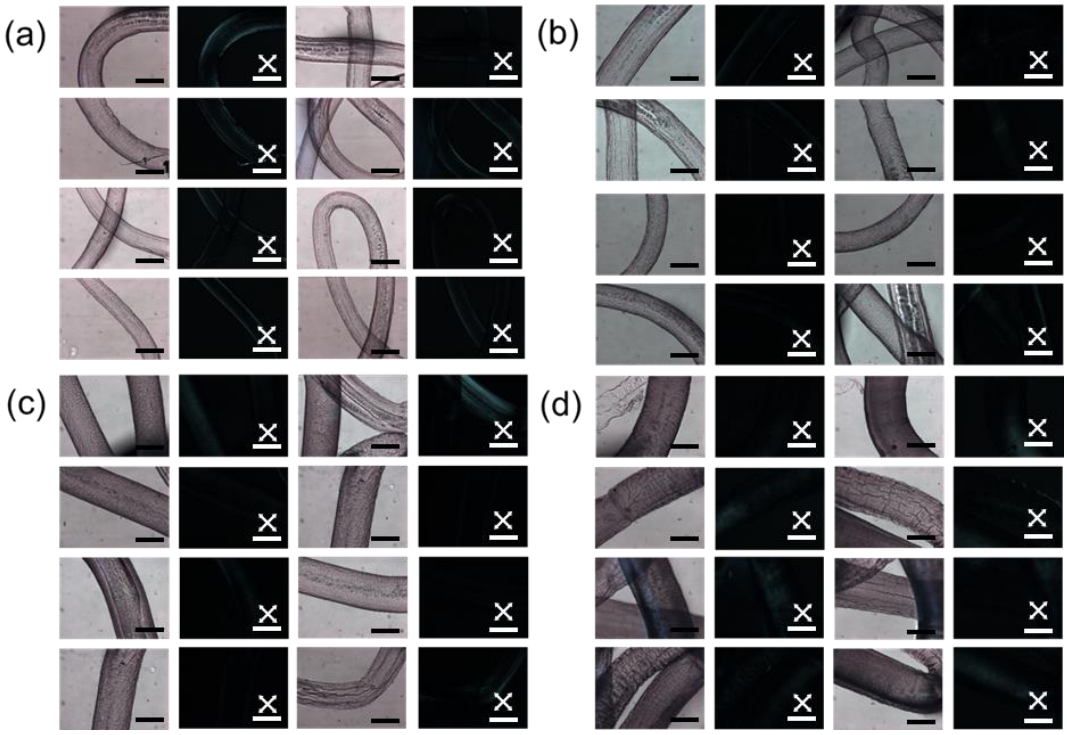

Figure 26. A selection of representative optical microscope images (both normal and cross polarised light) to compliment the data in Figure 20. The gel structures are formed from 10 mg/mL 1ThNapFF at pH 11.3 using the static procedure investigating the effect of flow rate. (a) 10 mL/hr; (b) 25 mL/hr; (c) 50 mL/hr and (d) 100 mL/hr. Scale bars represent 0.6 mm and white arrows indicate polariser direction.

2.2.3.4 Multi-meter long continuous filaments

Hypothetically, the syringe pump setup should be able to make infinitely long gel noodles dependent only on the volume of the 1ThNapFF solution reservoir and size of the trigger bath. To test whether multi-meter long filaments could be formed, a large $CaCl_2$ trigger bath (5 L) was setup in a large tray and a noodle formed. With this setup a multi-meter long gel filament could be formed (Figure 27). This is a relatively simple experiment, but nothing to this effect has been reported before.

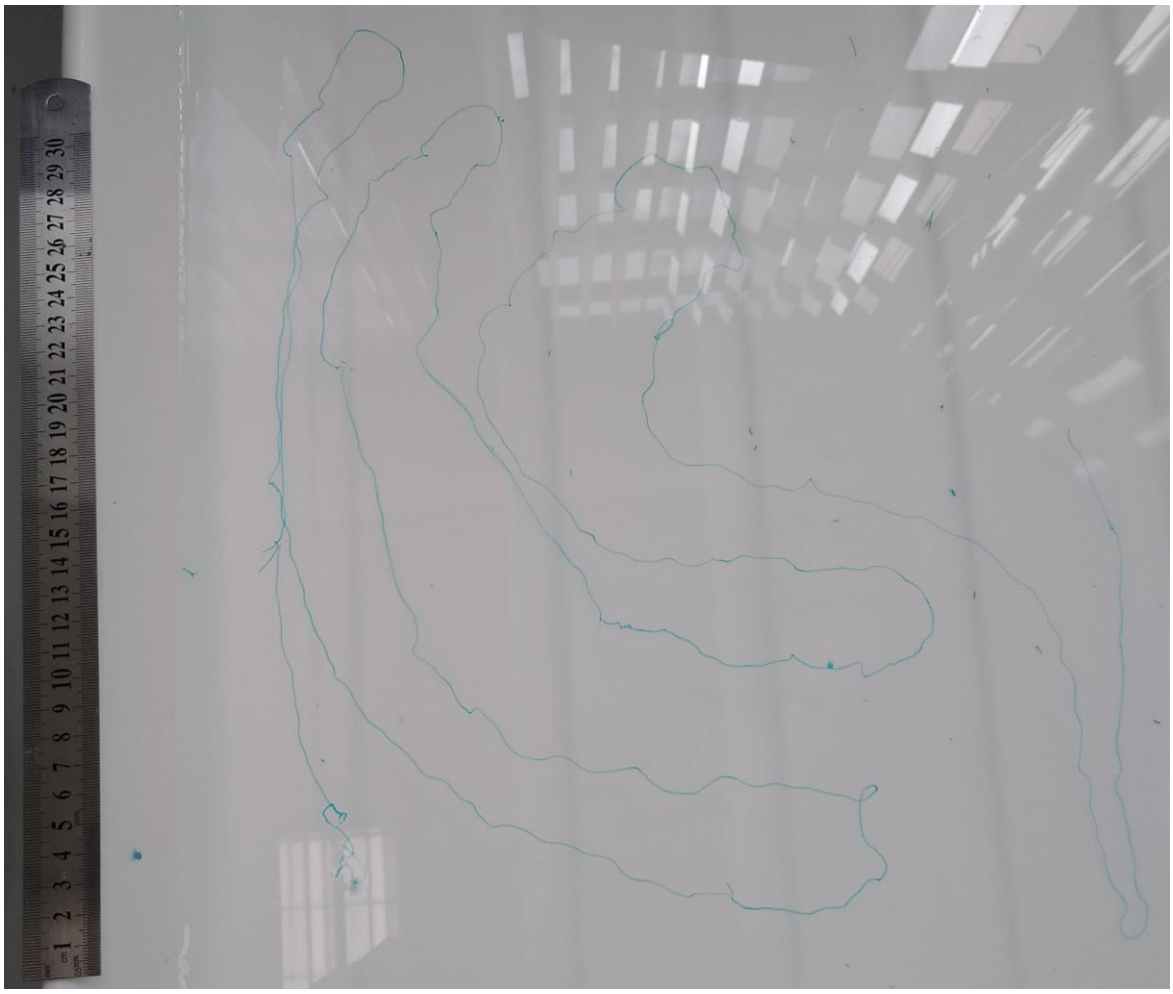

Figure 27. The full photograph of a multi-meter continuous gel filament (presented in the main paper) formed from a 10 mg/mL 1ThNapFF solution stained with 80 ppm Nile Blue A in a 50 mM $CaCl_2$ bath. A 30 cm ruler is placed to the left of the photograph for scale.

2.2.4 Syringe pump - spun noodles

Extensional flows are crucial for the alignment silk proteins in lab spun silk threads (obtained from silkworms).[41] Achieving good strength and elasticity required a careful balance of acidification and extensional stress. In other work, polymer crystals align under extensional flows during extrusion.[42] Furthermore, researchers formed aligned self-assembled gels by using cross-slot flow devices which impart extensional flows on the gel as it forms.[26]

For 1ThNapFF, worm-like micelles are present but do not align consistently under the formation of static gel noodles. Using pipettes, extensional deformation (stretching) the noodles as they formed induced alignment. It was hypothesised that given the correct conditions, the worm-like micelles within the gel noodles could be aligned and locked-in. To do this reproducibly, a spinning technique was developed (Figure 28a). This used a bath of trigger medium rotating at 100 rpm on a spin coater, into which the pre-gel solution was injected. The spinning procedure did not destroy the structures and instead resulted in a long single continuous noodle (Figure 28b).

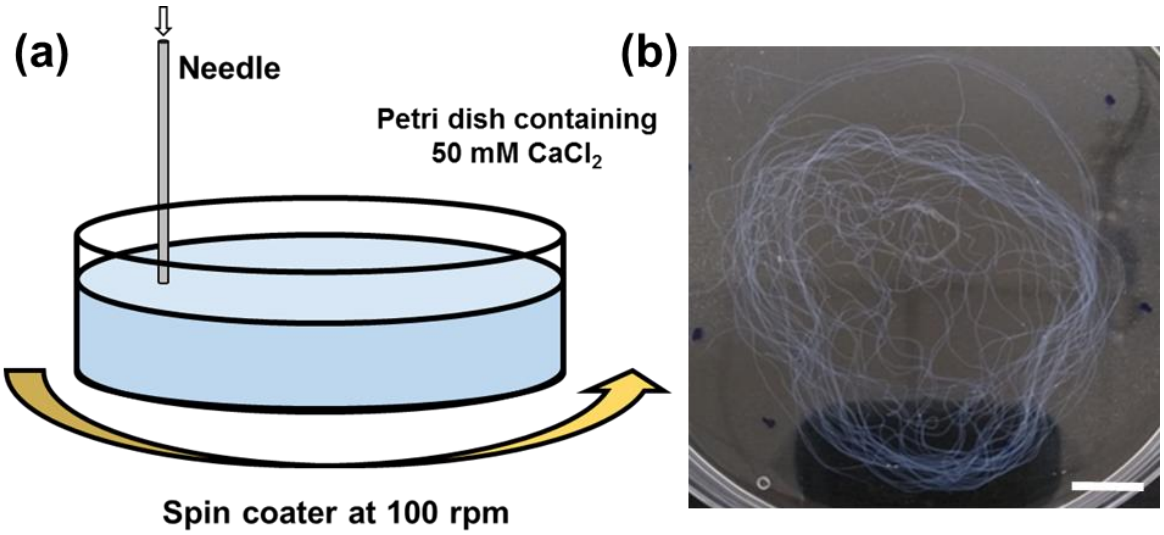

Figure 28. (a) Cartoon schematic of noodle spinning setup. (b) Photograph of a spun noodle in a Petri dish. The scale bar represents 10 mm. Reproduced from D. McDowall, M. Walker, M. Vassalli, M. Cantini, N. Khunti, C. J. C. Edwards-Gayle, N. Cowieson and D. J. Adams, Chem. Commun., 2021, 57, 8782–8785, with permission from the Royal Society of Chemistry.

2.2.4.1 10 mg/mL

At a 1ThNapFF concentration of 10 mg/mL, the spinning technique was tested extensively. The spinning technique resulted in bundles of thin filaments. The influence of syringe pump flow rate was investigated and showed that regardless of flow rate, the spun noodles had diameter distributions centred around 0.1 mm (Figure 29). This is a quarter of the inner diameter of the needle. At a spinning rate of 100 rpm, the solution/gel experiences a large degree of strain. It was remarkable that the solution/filaments could withstand this. As the 1ThNapFF pre-gel solution leaves the tip, it must be pulled by the passing trigger medium flow at the end of the needle and stretched. This results in the thin filaments which then gel. The non-Newtonian fluid behaviour, likely a high extensional viscosity, of 1ThNapFF solutions must facilitate the ability to withstand this process. 1ThNapFF worm-like micelle solutions have common features to many systems that can exhibit long extensional

relaxation times in uniaxial extensional flow. These include surfactant worm-like micelles,[44,45] polyelectrolytes[46] and polymer[47] solutions.

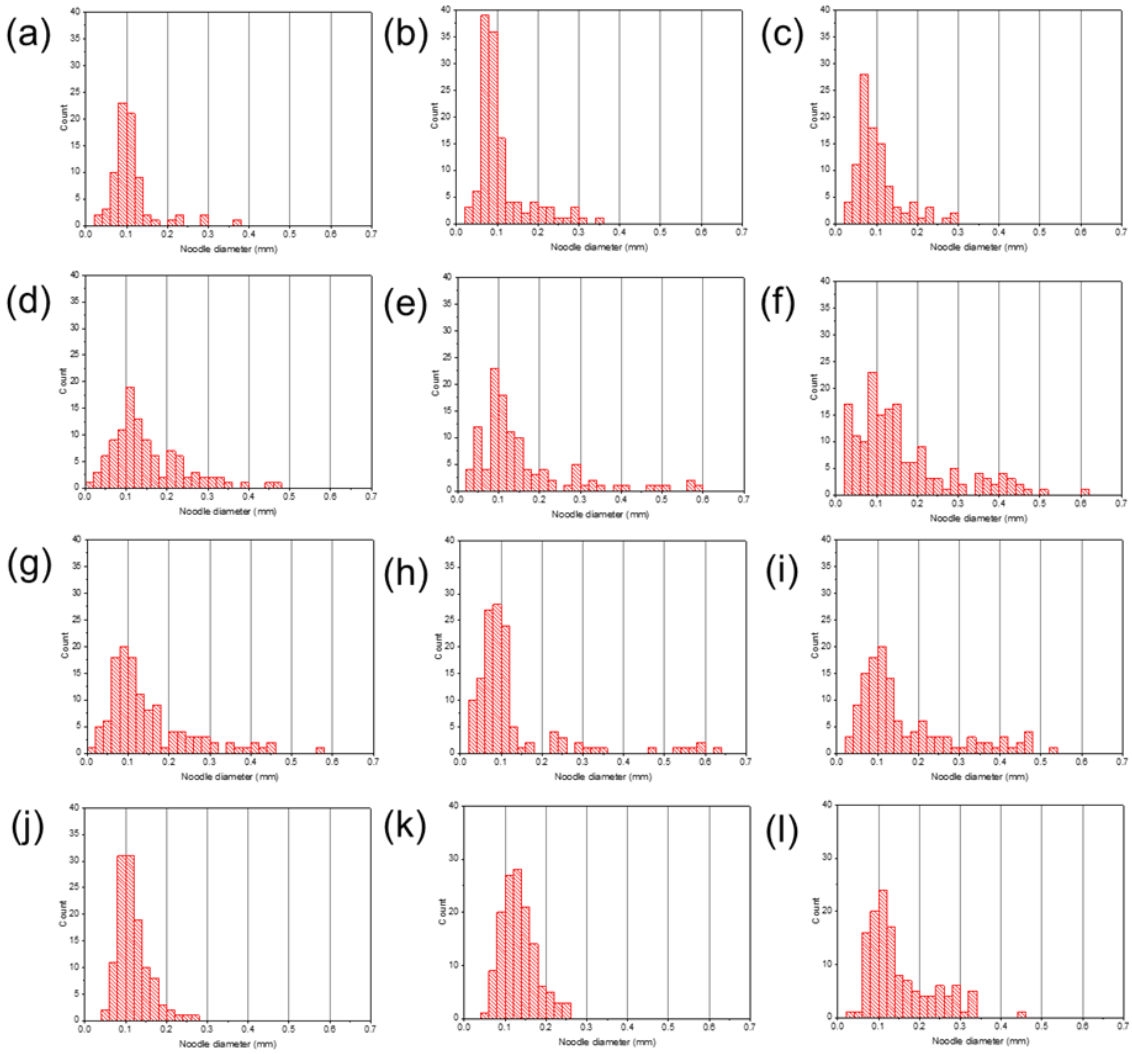

Figure 29. Histograms for the 100 rpm spinning technique. A 10 mg/mL 1ThNapFF pre-gel solution at pH 11.3 was used. (a – c) three repeats at 10 mL/hr; (d – f) three repeats at 25 mL/hr; (g – i) three repeats at 50 mL/hr and (j – l) three repeats at 100 mL/hr. Corresponding microscope images are shown in Figure S32. Reproduced from D. McDowall, M. Walker, M. Vassalli, M. Cantini, N. Khunti, C. J. C. Edwards-Gayle, N. Cowieson and D. J. Adams, Chem. Commun., 2021, 57, 8782–8785, with permission from the Royal Society of Chemistry.

The spun filaments almost all exhibited strong, uniform birefringence in CPOM measurements (Figure 30), indicating that the spun noodles have aligned nanostructures. In particular, the thinnest noodle regions show most birefringence. By spinning, gel noodles with a narrow size distribution and good alignment were reproducibly formed.

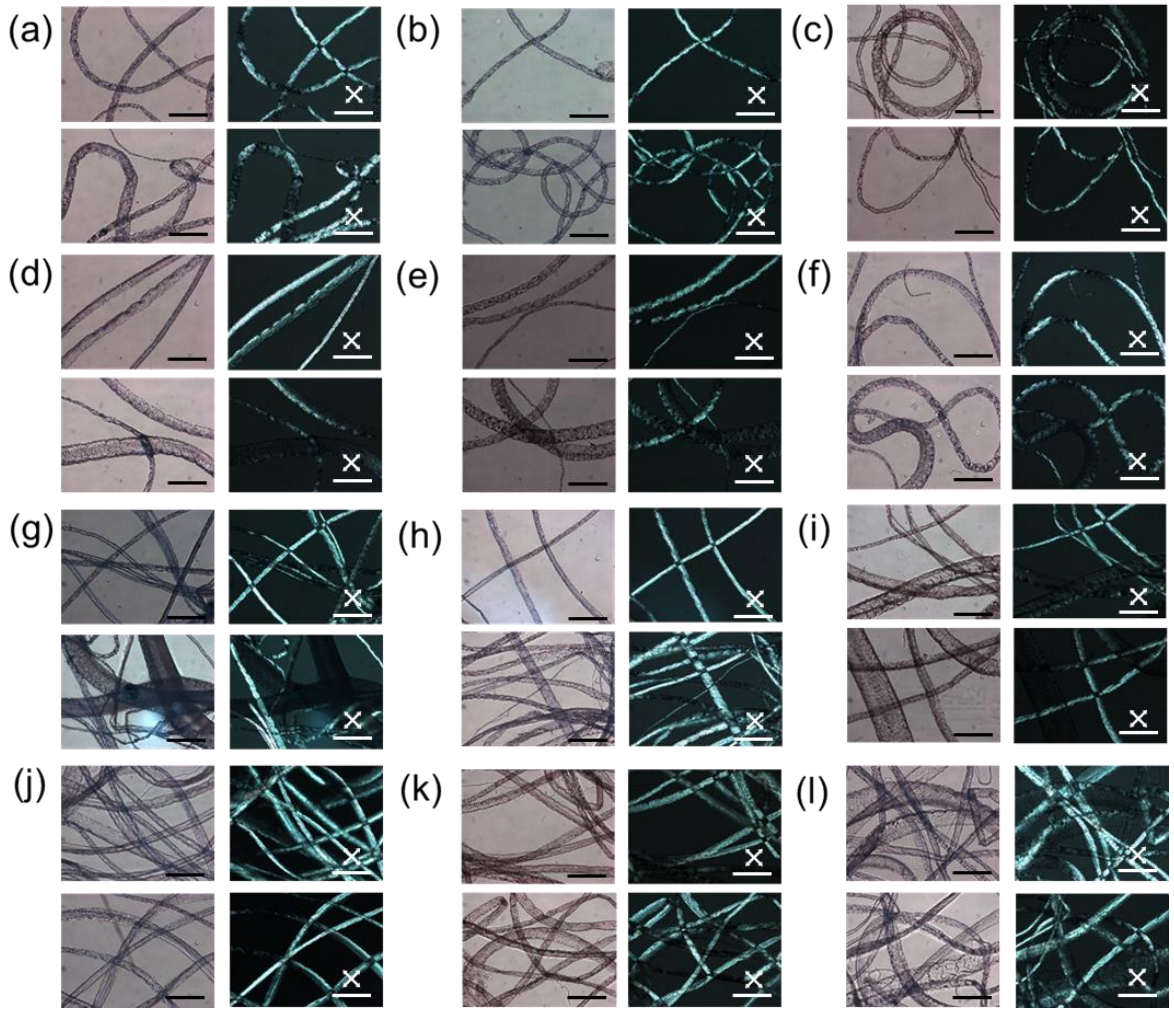

Figure 30. Corresponding optical microscope images (both normal and cross polarised light) for the 100 rpm spinning technique (histograms in Figure S31). A 10 mg/mL 1ThNapFF pre-gel solution at pH 11.3 was used. (a – c) three repeats at 10 mL/hr; (d – f) three repeats at 25 mL/hr; (g – i) three repeats at 50 mL/hr and (j – l) three repeats at 100 mL/hr. Scale bars represent 0.6 mm and white cross indicates polariser directions.

2.2.5 Concentric flow

A concentric flow setup was created to both align the filaments and access a filament in filament morphology. For the two applications two slightly different setups were used (Figure 31 and 33) but both utilise a needle pierced through tubing and then fixed with clamps. This resulted in two separate flows (each controlled by a syringe pump) aligned concentrically with each other that were then dispensed into the trigger bath.

2.2.5.1 Aligned filament formation

Work in the literature showed the alignment of gels comprised of vanadium oxide nanorods by using a sheath flow of gelation trigger medium that stretched the filaments as they formed.[48] A similar setup was created (Figure 31) such that using a sufficiently fast sheath flow of 50 mM $CaCl_2$ would stretch and align the gel filaments formed from a 10 mg/mL 1ThNapFF solution inner flow.

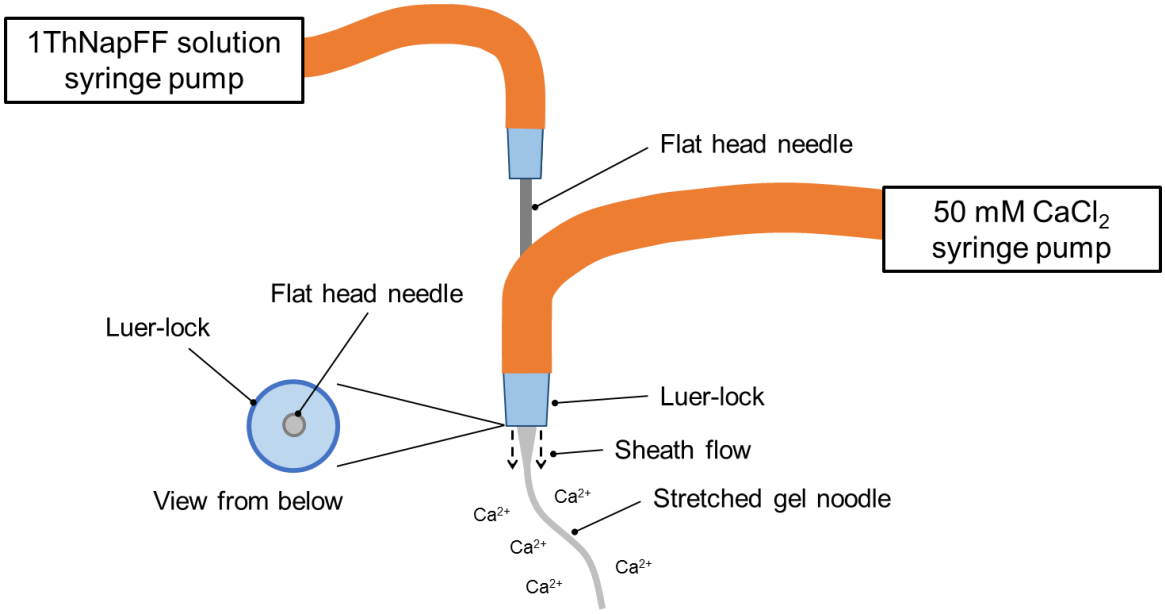

Figure 31. Cartoon schematic (not to scale) of the concentric flow setup used to form aligned gel filaments with a $CaCl_2$ sheath flow.

In preliminary work, the 50 mM $CaCl_2$ sheath flow rates accessible with the syringe pump were not fast enough to significantly stretch the gel filaments as they formed. To access faster sheath flow rates the syringe was instead driven by hand. To start with, the inner flow was started with no sheath flow and a length of filament formed (Figure 32a), then the sheath flow syringe was rapidly driven by hand, resulting in a significant thinning and enhanced birefringence of the filaments being formed (Figure 32b). The filament regions formed were collected in the glass dish containing 50 mM $CaCl_2$ and the filaments taken for imaging. These data reinforce the conclusion that a stretching process results in enhanced alignment within the gel structures. This could, in theory, be used to form very long aligned filaments, with the limiting factors being the volume of the syringes used.

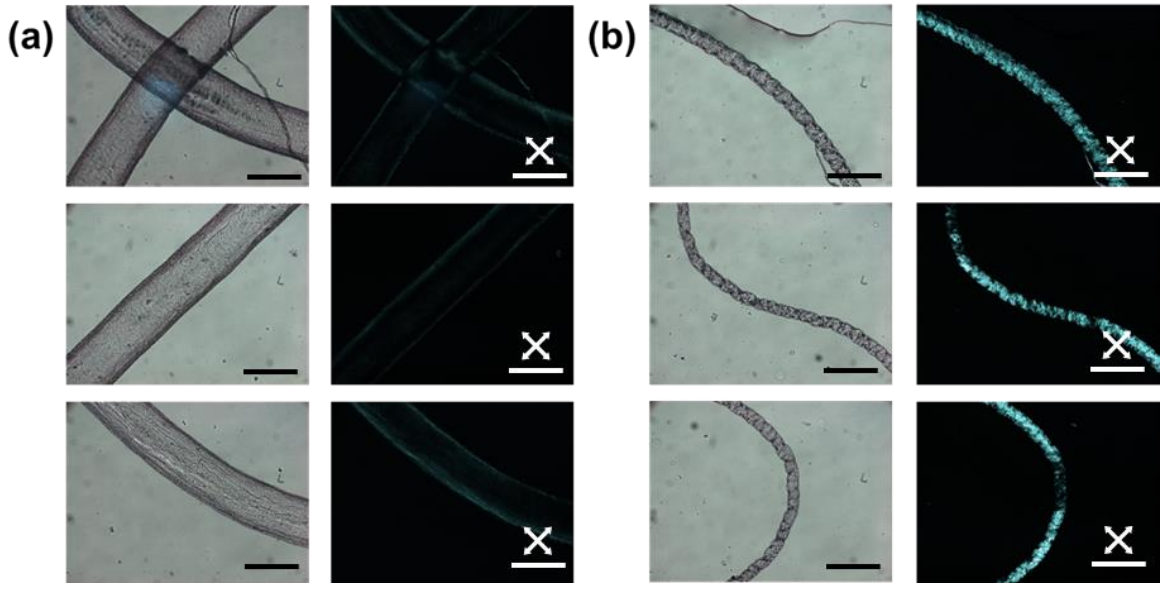

Figure 32. Gel filaments formed with the concentric flow setup with (a) no sheath flow and (b) a rapid, manually driven, sheath flow. Scale bars represent 0.5 mm and white crosses represent polariser directions.

2.2.5.2 Filament-in-filament morphology

Using the concentric flow setup, if both flows are loaded with gelator solutions, a noodle-in-noodle morphology can be accessed (Figure 33). The inner pre-gel solution was stained with Nile Blue A for visualisation.

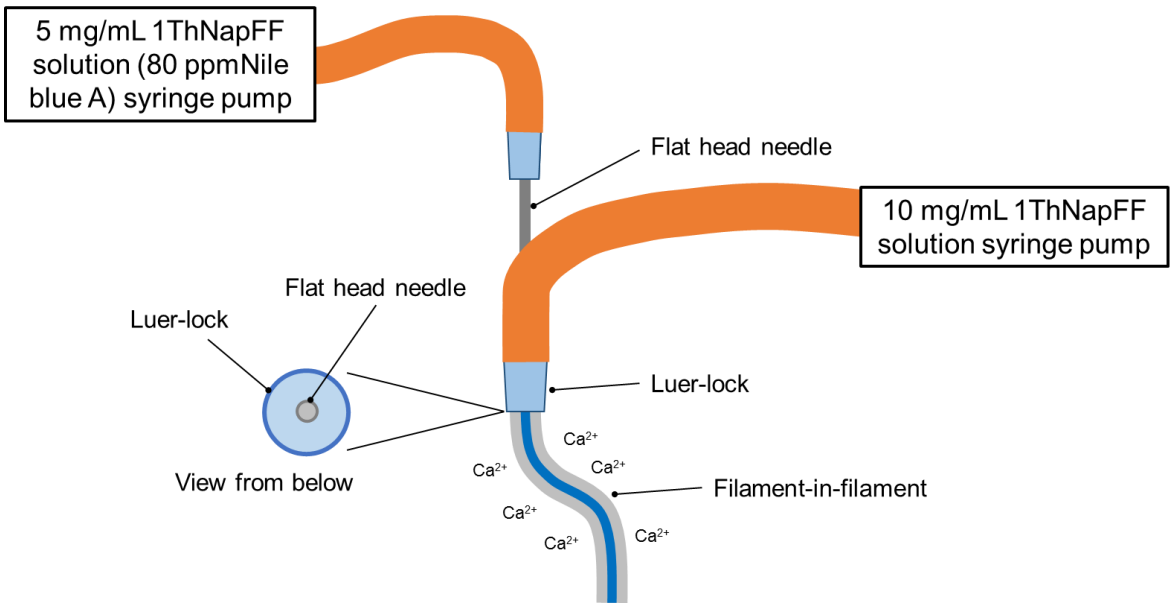

Figure 33. Cartoon schematic (not to scale) of the concentric flow setup used to form a filament-in-filament morphology.

The diameter of the inner noodle as well as the whole noodle can be controlled by varying the two flow rates. Cross-sections of the noodle-in-noodle were cut using a scalpel and imaged. A sheath flow solution of 10 mg/mL 1ThNapFF and an inner flow solution of 5 mg/mL 1ThNapFF with 80 ppm Nile Blue A was used.

Filament-in-filament **1**

Inner flow: 3 mL/hr

Sheath flow: 20 mL/hr

The setup successfully formed a filament-in-filament morphology with a thick inner filament clearly visible in photographs and microscope images (Figure 34).

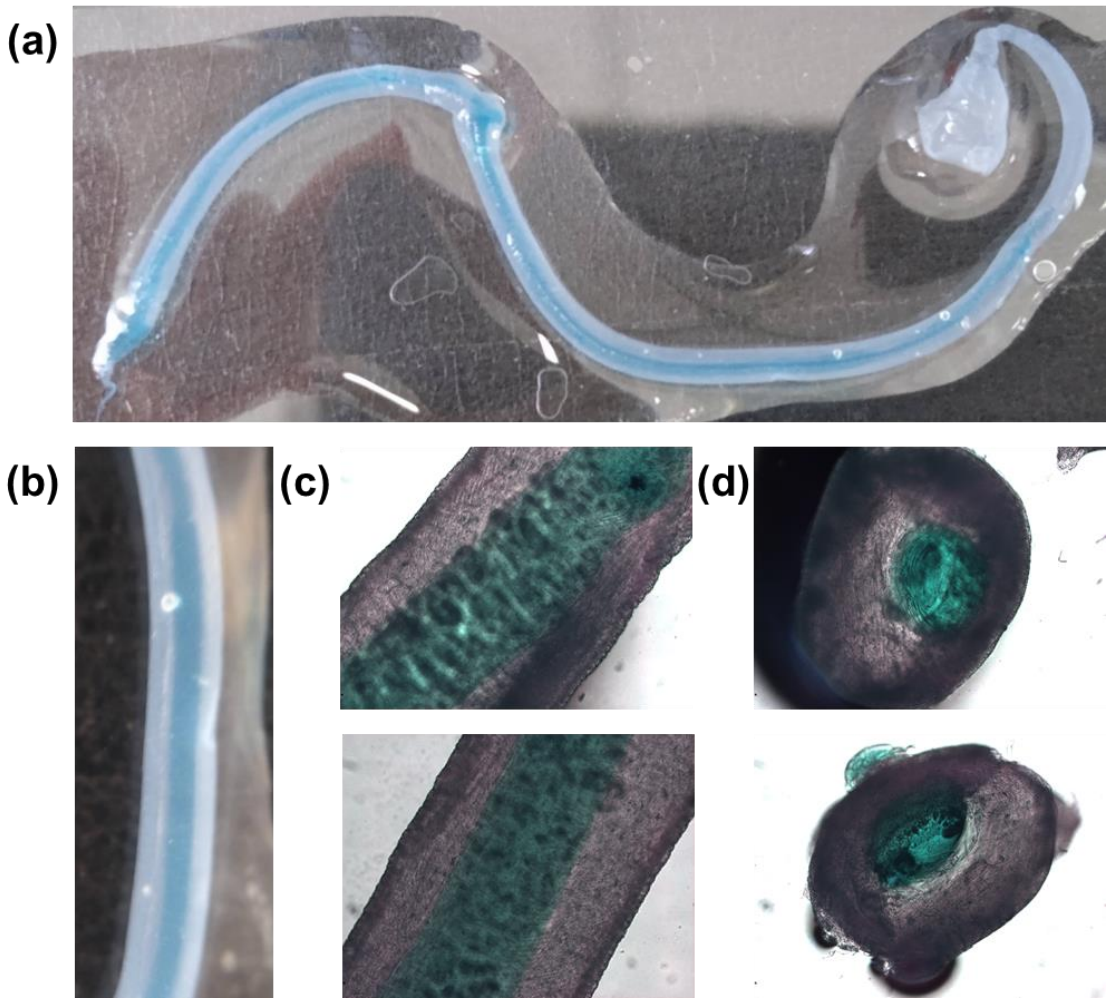

Figure 34. Various images of the filament-in-filament gel, (a) photograph of the whole length of the gel; (b) a close up macro lens photograph of the gel; (c) optical microscope images of the gel and (d) scalpel-cut cross-sections of the gel. Reproduced from D. McDowall, M. Walker, M. Vassalli, M. Cantini, N. Khunti, C. J. C. Edwards-Gayle, N. Cowieson and D. J. Adams, Chem. Commun., 2021, 57, 8782–8785, with permission from the Royal Society of Chemistry.

Filament-in-filament **2**

Inner flow: 10 mL/hr

Sheath flow: 50 mL/hr

A different set of flow conditions were used, resulting in slightly thicker filaments overall with a very thin inner filament (Figure 35 and 36)

Figure 35. Photographs of filament-in-filament **2** with a white and a black background with two expanded images on the right with arrows to guide the eye to the thin blue inner filament. Reproduced from D. McDowall, M. Walker, M. Vassalli, M. Cantini, N. Khunti, C. J. C. Edwards-Gayle, N. Cowieson and D. J. Adams, Chem. Commun., 2021, 57, 8782–8785, with permission from the Royal Society of Chemistry.

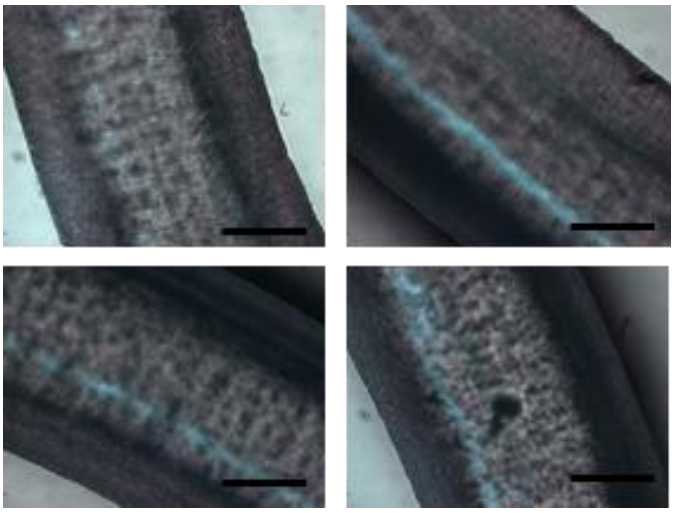

Figure 36. Optical microscope images of filament in filament **2**. For this sample, the inner blue filament cannot be seen in the microscope images. The blue shine on the surface of the filaments is an effect of the light. The scale bars represent 0.6 mm. Reproduced from D. McDowall, M. Walker, M. Vassalli, M. Cantini, N. Khunti, C. J. C. Edwards-Gayle, N. Cowieson and D. J. Adams, Chem. Commun., 2021, 57, 8782–8785, with permission from the Royal Society of Chemistry.

This work was performed as a proof of concept and significantly more research could be undertaken to optimise the filament-in-filament formation.

2.3 Nanoindentation

To the best of our knowledge, no previous work has studied the mechanical properties of LMWG gel noodles, although the tensile strength of self-assembled nanotube yarns that are drawn directly from solution has been previously studied.[32] Some LMWG noodles have been shown to be sufficiently mechanically robust to tie into a knot,[19] and the ones shown here are self-supporting if lifted out of the solution. Using conventional techniques (such as oscillatory rheology), the mechanical properties of the gel filaments cannot be measured due to the small size and 1D shape. Nanoindentation is a technique that can be used to measure the mechanical properties of a localised area (on the μm scale) of a material.[49] The nanoindenter tip is scanned across the gel surface and >20 individual measurements performed. The force-indentation curve for each measurement is fitted to give a Young's modulus and a median value is calculated for each gel. The data are presented in violin plots which show the distribution of the data, where the wide the part of the plot, the greater the frequency of data points at that value. The white dots representing the median, the thick dark blue bars represent the 1st and 3rd quartiles, the thin dark blue lines represent all the data excluding outliers and the light blue coloured violin-shaped regions represent the whole distribution of the Young's moduli values for each data set.

Nanoindentation was used to measure the mechanical properties of the gel filaments formed and bulk 1ThNapFF gels formed with $CaCl_2$. The gel noodles were formed and then passed to Dr Matthew Walker, who carried out the nanoindentation experiments and processed and analysed the data. The results (Figure 37) show that the Young's moduli for gel filaments at two different flow rates are similar at around 5 – 20 kPa. The Young's moduli are similar to those of the homogeneous bulk gel prepared with $CaCl_2$ (Figure 38c and 38d), which shows that the process of noodle formation does not significantly change the mechanical strength of the gels. With the nanoindentation setup available, the spun noodles were too small to be accurately measured.

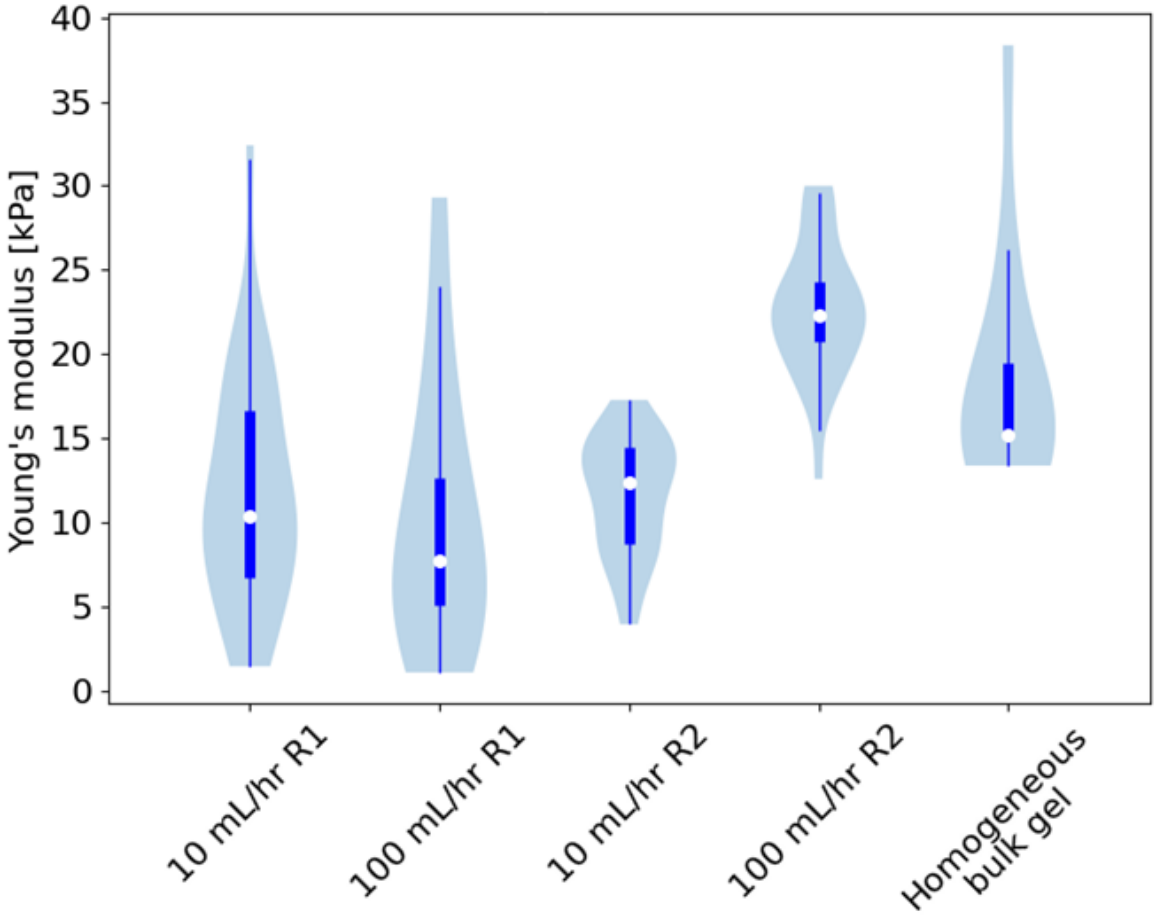

Figure 37. Violin plots of nanoindentation data for static formed noodles at two flow rates and a homogeneous bulk gel. Reproduced from D. McDowall, M. Walker, M. Vassalli, M. Cantini, N. Khunti, C. J. C. Edwards-Gayle, N. Cowieson and D. J. Adams, Chem. Commun., 2021, 57, 8782–8785, with permission from the Royal Society of Chemistry.

When preparing the bulk gels, a drop of concentrated $CaCl_2$ was added atop the 1ThNapFF solution. The gelation mechanism works via diffusion but for 1ThNapFF this process is extremely slow. As such, an inhomogenous gel was made and studied with nanoindentation. For the inhomogeneous gel, the transition from the stiff to the soft side can be clearly seen (Figure 38a) and at the extremes edge of the soft side, the sample is still a

liquid. In the nanoindentation data the stiff side of the gel had significantly greater Young's modulus values than the softer side of the gel (Figure 38). The median Young's modulus of the stiff side of the gel was approximately 130 kPa and the median value for the soft side was approximately 7 kPa. This highlights the importance of the Ca^{2+} concentration on the mechanical properties of the gel. The homogeneous 6 month old gel showed a median Young's modulus at around 15 kPa. Here the homogeneous bulk gel shows some inhomogeneity but is more homogeneous than the inhomogeneous example.

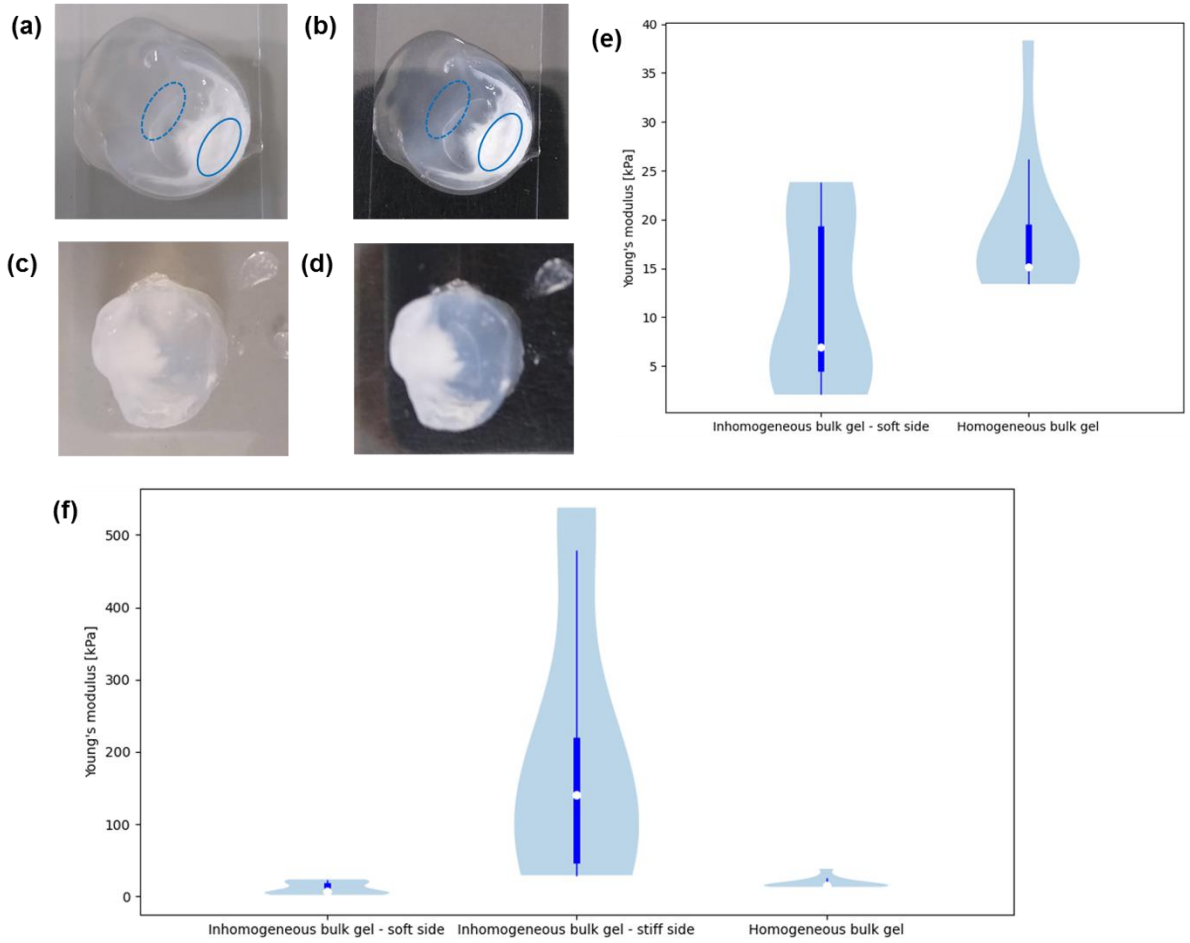

Figure 38. Photographs of the bulk gels studied with nanoindentation. A 7 day diffusion time bulk gel with a (a) white and (b) black background. For (a) and (b), the dotted blue circles represent the soft side and the solid line blue circles represent the stiff side of the inhomogeneous gel. A "homogeneous" 6 month diffusion time bulk gel with a (c) white and (b) black background. Violin plots of nanoindentation data for bulk gels of 1ThNapFF prepared with $CaCl_2$ shown for (e) the soft side of the inhomogeneous gel and the homogeneous gel (f) full scale plot with all regions studied.

All the noodles presented in this chapter are formed and studied on the day they are made. The effect of aging on the gel filaments was also investigated (Figure 39). The aging was only studied over a 24 hours period but showed that the Young's modulus fell over 24 hours from around 5 kPa to 2 kPa.

A cross-section of a filament-in-filament (shown in Figure 34) was cut using a scalpel blade and the mechanical properties of the two regions probed using nanoindentation (Figure 40). For this sample, the Young's moduli of the two regions are very similar and most of the data overlap. The difference in concentration does not significantly affect the Young's modulus of the gel.

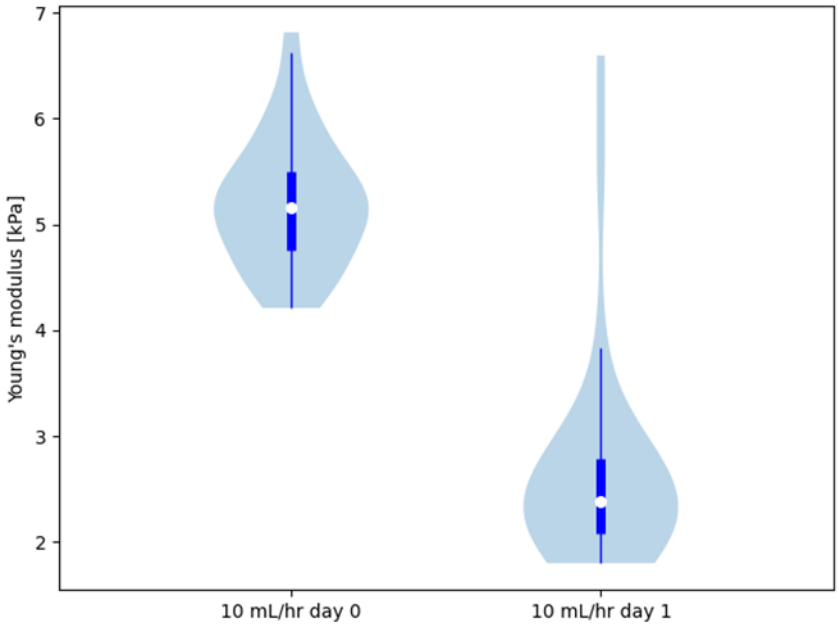

Figure 39. Violin plots for a gel filament formed with a syringe pump at a flow rate of 10 mL/hr on the day it was made (day 0) and 24 hours later (day 1). Reproduced from D. McDowall, M. Walker, M. Vassalli, M. Cantini, N. Khunti, C. J. C. Edwards-Gayle, N. Cowieson and D. J. Adams, Chem. Commun., 2021, 57, 8782–8785, with permission from the Royal Society of Chemistry.

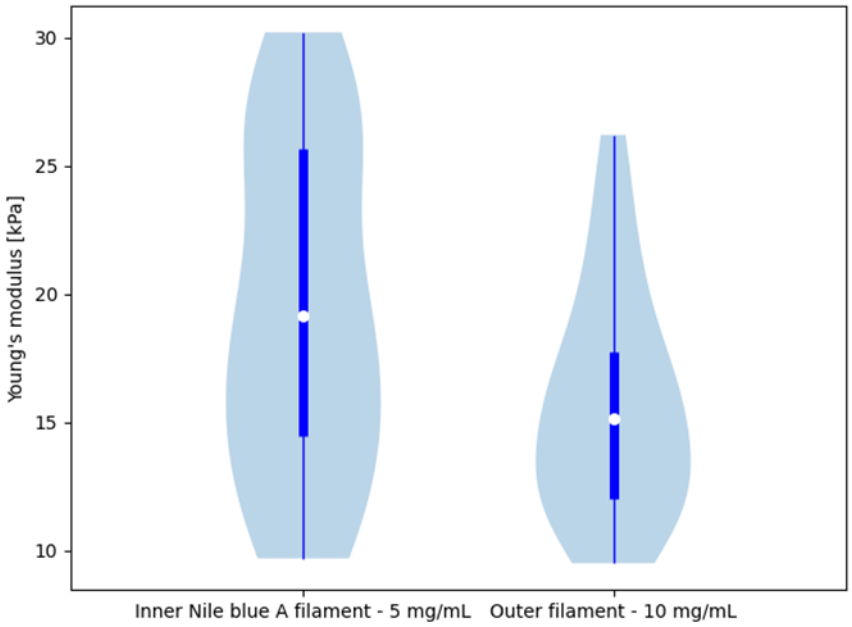

Figure 40. Violin plots of data collected from the cross-section of a filament-in-filament, allowing both the 10 mg/mL 1ThNapFF and 5 mg/mL 1ThNapFF (Nile blue A stained) regions to be measured. Reproduced from D. McDowall, M. Walker, M. Vassalli, M. Cantini, N. Khunti, C. J. C. Edwards-Gayle, N. Cowieson and D. J. Adams, Chem. Commun., 2021, 57, 8782–8785, with permission from the Royal Society of Chemistry.

3 Conclusions

To conclude, extensive research into the formation of LMWG noodles was performed with the functionalised dipeptide, 1ThNapFF, filling a gap in the literature. To start with, the relationship between 1D self-assembled structures, shear viscosity and gel noodle formation was shown to be crucial to effective noodle formation. Gel noodles could not be formed with low shear viscosity solutions containing a limited degree of self-assembled structures. Using the viscous, shear-thinning solution that formed at a concentration of 10 mg/mL, gel noodle formation with different pipettes was successfully performed. While this gave relatively poor control over both alignment and noodle diameter, it was a very easy method to use. By utilising a syringe pump, better control over noodle diameter could be achieved and significantly longer lengths of noodle were accessible. Up to this point, noodle alignment was not consistently achieved. To this end, a spinning method was developed that lead to the formation of highly alignment gel noodles with a narrow size distribution. By utilising the syringe pump, interesting morphologies such as a ‘noodle-in-noodle’ could then be accessed.

The research demonstrates that better control and longer noodles can be achieved by using a syringe pump, which is vital for real-world applications and scalability. Furthermore, the robust nature of gel noodles and morphologies was demonstrated.

The results in this work suggest that high viscosity solutions with worm-like micelles present are required to form gel noodles. As such, for the formation of PBI gel noodles, a PBI functionalisation or set of conditions (such as concentration) that would result in viscous, worm-like micelle solutions was sought after.

4 Experimental

4.1 Materials

1ThNapFF was synthesised by Professor Dave Adams according to a previously reported method.[50] $CaCl_2$ was obtained from Alfa Aesar and used with no further purification. Nile blue A was obtained from Sigma Aldrich and a solution in deionised water at a concentration of 8000 ppm was prepared from this.

4.1.1 PBI-L synthesis

L-Leucine functionalised perylene bisimide was synthesised using a previously reported method.[51] 2.00 g (5.1 mmol) perylene-3,4,9,10-tetracarboxylic dianhydride (PTCDA) was reacted with 1.34 g (10.2 mmol) L-leucine using 3.47 g (51.0 mmol) imidazole as a solvent. The reagents were mixed thoroughly in a Schlenk flask, purged with N_2 for 15 minutes and then heated to 120°C for 5 hours. The temperature was then lowered to 90°C and 20 mL deionised water added. This solution was left to stir for 1 hour and then lowered to room temperature. The Schlenk flask was then filled with deionised water and the solution filtered under gravity. The filtrate was collected, the pH lowered to <4 with 2M HCl triggering precipitation of the PBI product. This was then filtered under vacuum, washed with 2M HCl and then deionised water. The collected solid was dried under vacuum and then refluxed in 50 mL 2M HCl for 5 hours to remove any residual imidazole. This mixture was lowered to 80°C and then vacuum filtered, washed three times with 10 mL 2M HCl, 3 times with 10 mL deionised water and dried under vacuum. ^{1}H and ^{13}C NMR spectroscopy was used to characterise the compounds. The samples were run in DMSO-d_6 at high temperature (80°C) to aid solubility and reduce aggregation.

PBI-L

^{1}H NMR 500 MHz, (DMSO-d_6, 80°C): δ (ppm) = 12.49 (br, 1H;-OH); 8.89 (br, 4H); 8.60 (d, 4H, J = 7.1 Hz); 5.63 (dd, 2H, J = 5.1 and 8.6 Hz); 2.13 (m, 4H); 1.64 (m, 2H); 0.99 (d, 6H, J = 6.5 Hz); 0.92 (d, 6H, J = 6.4 Hz).

^{13}C (500 MHz, DMSO-d_6, 80°C): δ (ppm) = 171.4 (COOH); 162.9 (C=O); 134.5, 131.6, 129.0, 126.0, 124.2, 122.8 (perylene core C); 52.3 (CH); 38.5; 25.7; 23.2; 22.6.

4.2 Solution preparation

Aqueous solutions of 1ThNapFF were prepared as follows. 1ThNapFF was weighed into a 40 mL plastic Falcon tube followed by the addition of deionised water and then 2 equivalents of 2M NaOH in deionised water. The amounts used varied depending on the volume and concentration required. Solutions were typically prepared on a 10 mL scale. The solutions

were stirred overnight and then checked for undissolved solids the following morning and stirred further if required. Once dissolved, the solution pH was checked. The solution pH was adjusted to pH 11.3 ± 0.1 as required with 2M HCl and/or 2M NaOH. Generally, the initial pH >12 and was then lowered to pH 11.3. Care was taken to ensure homogeneity of the sample when pH adjusting. The viscous nature of 1ThNapFF solutions meant that insufficient mixing could result in localised pH differences. Once pH adjusted the solution was ready to use.

To stain the 1ThNapFF solutions blue for enhanced filament visibility when required, a calculated volume of 8000 ppm Nile blue A stock solution was added to achieve a final concentration of 80 ppm Nile blue A in the gelator solution.

10 mg/mL PBI-L solutions were prepared by weighing 50 mg of material into a 14 mL glass vial and then the required volume of deionised water. Finally 2 equivalents (relative to the PBI) of 1 mol/L NaOH was added. The total volume of both water and base added was 5 mL. A stirrer bar was added and the solution stirred overnight. The next day, when the PBI was fully dissolved, the pH was checked. Then the pH was adjusted down to pH 6.00 – 6.10 using 2 mol/L and 0.1 mol/L HCl.

4.3 Bulk gel preparation

Bulk gels were prepared for nanoindentation from 10 mg/mL 1ThNapFF solutions at pH 11.3. 2 mL of pre-gel solution was pipetted into an upside down plastic syringe with the top cut off, in a fashion as had previously reported.[52] This method is favourable because it means the gels can be easily removed once formed and taken for study using nanoindentation. Two equivalents of Ca^{2+} ions (in the form of an 8.9 µL drop of 200 mg/mL $CaCl_2$ in deionised water) was added near the centre of the pre-gel solution. The open top of the syringe was covered with Parafilm. Localised gelation where the $CaCl_2$ droplet was placed occurred instantly. For gelation to occur throughout the sample, the Ca^{2+} diffuses through the solution. For this particular system the diffusion was an extremely slow process and even when left for many months a completely homogeneous gel is not formed. For the nanoindentation experiments two bulk gels were studied. An inhomogeneous bulk gel, for which diffusion had been left for 7 days, and a homogeneous gel that was left for 6 months. Although it is noted that the homogeneous gel was still not entirely homogeneous by eye. For the 6-month diffusing gel, this was instead prepared on a 2 mL scale but in a 7 mL Sterilin vial to allow for an effective seal and prevent drying of the gel. The inverted syringe technique cannot be sealed effectively, especially for many months. Instead, the gels dry out.

4.4 Viscosity measurements

Viscosity measurements were made using an Anton Paar 301 rotational rheometer with a 50 mm cone and plate geometry. All measurements were performed at 25°C and a shear rate range of 1-1000 s^{-1}. To minimise the shear that the 1ThNapFF solutions are subjected to prior to the experiment, they were loaded onto the rheometer by pouring instead of using a pipette. Using a pipette can shear-align the sample and change the measured viscosity.

4.5 Pipette filament formation

All gel filaments were analysed on the day they were made unless stated otherwise.

4.5.1 Pipettes used

An Eppendorf 100-1000 µL (1 mL) pipette, SLS Lab Basics 20-200 µL pipette and SLS Lab Basics 2-20 µL pipette were used.

2-20 µL pipette tips: Fisherbrand SureOne aerosol barrier pipette tips (product code 11977714). Inner diameter 0.31 mm.

20-200 µL pipette tips: Eppendorf epTIPS standard pipettor tips (product code 11920537). Inner diameter 0.53 mm.

100-1000 µL pipette tips: Fisherbrand, polypropylene blue pipette tip (product code 10787524). Inner diameter 0.74 mm.

Pictures of the pipette and tips are shown in Figure 41.

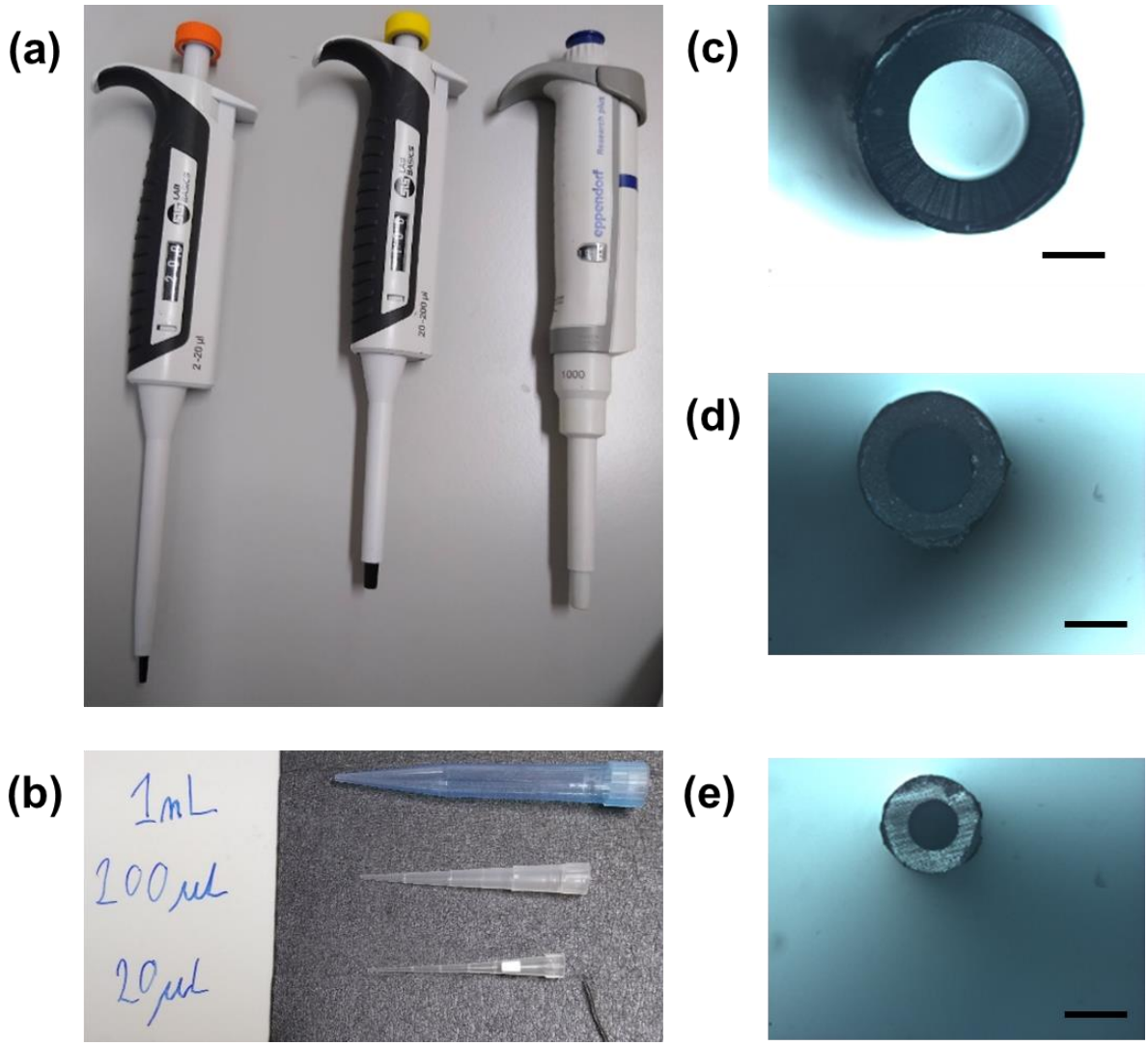

Figure 41. (a) Pipettes used. From right to left, 100-1000 µL (1 mL), 20-200 µL and 2-20 µL; (b) photograph of the pipette tips; Optical microscope images of pipette tips used (c) 100-1000 µL (1 mL); (d) 20-200 µL and (e) 2-20 µL. Images at 5X magnification, under normal light, in reflectance mode. Scale bars represent 0.4 mm.

4.5.2 Static filament formation

With 1ThNapFF solution loaded into a pipette, gel filaments were formed by submerging the pipette tip vertically into a 100 mL bath of 50 mM $CaCl_2$ and dispensing the pre-gel solution. This resulted in the formation of a continuous filament of gel until all the pre-gel solution was dispensed or the injection stopped. For the 2-20 µL pipette 20 µL of 1ThNapFF solution was used. For both the 1 mL and 20-200 µL pipettes, 100 µL 1ThNapFF solution was used. A process of trial and error to achieve an intermediate flow rate that result in uniform filaments was required for each pipette. The Ca^{2+} ions were in approximately a 1000 times excess relative to the 1ThNapFF molecules.

4.5.3 Dragging pipette

Filaments were formed by dragging the pipette tip along a microscope slide with a pool of 50 mM $CaCl_2$ atop whilst dispensing pre-gel solution. The general technique was inspired by a video in the supporting information of work by Zhang *et al.*,[19] but it was seemingly not performed with the intention of inducing alignment in that work. Here, a faster dragging than shown in that video was performed.

4.6 Syringe pump filament formation

All gel filaments were analysed on the day that they were made unless stated otherwise.

4.6.1 Syringe pump

An Alaris Carefusion syringe pump was used to control the flow rate of the 1ThNapFF pre-gel solutions. A 10 mL syringe was attached via a Luer lock fittings to 20 cm rubber tubing with a flat-headed needle (413 µm inner diameter) at the end. To load the syringe pump, the syringe was filled directly with gelator solution. The tubing was attached to the syringe and the pre-gel solution pumped manually until the tubing was full with pre-gel solution. The needle was then attached to the end of the tubing and the syringe loaded into the syringe pump. The rubber tubing and needle enabled movement of the needle to position it into the trigger medium. Next, the syringe pump was started until the pre-gel was coming out. During this process, care was taken to avoid the formation of bubbles within the tubing.

4.6.2 Static filament formation

To make gel filaments, a cylindrical Pyrex dish with a microscope slide at the bottom was filled with 100 mL 50 mM $CaCl_2$ trigger solution. A flow rate was selected and the infusion started. The first drops of pre-gel solution was dabbed onto tissue paper and then the needle moved and positioned vertically downwards into the trigger medium ~5 mm below the surface. The infusion was carried out for 15 s. To finish the needle was slowly moved to the edge of the dish and then dragged up the side to break the connection to the rest of the structure. As the filaments were generally one continuous structure, simply pulling the needle out may pull the whole structure and alter/damage it. After removing the needle, the syringe pump was stopped. Once formed the filament gel structures became more opaque over the course of a minute. The excess trigger solution was carefully removed manually from the dish with a 50 mL syringe. When the level of trigger solution was reduced to around 20 mL the floating gel structures were carefully positioned above the microscope slide. The remaining trigger solution was then slowly removed so that the gel structure “landed” on the microscope slide. The microscope slide was then taken for microscope imaging. The

filaments were never left to dry out and a few drops of trigger medium added atop the microscope slide to keep them hydrated.

The 1ThNapFF solutions, in ambient room lighting, were colourless and the filaments were difficult to see for the first few seconds but became slightly opaque as gelation occurred. A flashlight positioned at the side shining into the dish allowed for viewing of the filaments as they form. The syringe pump was always started before placing the needle into trigger solution. If the infusion was not started when the needle was placed in trigger solution the trigger could travel up the needle, forming a gel and blockage inside the needle. As the infusion was started before immersion in the trigger, there was often a droplet of gelator solution on the needle when it was placed into the trigger. When immersed into the trigger this droplet gelled resulting in a ball shaped gel structure on the tip. A small and fast shake of the needle tip in solution dislodged this allowing for the fluid to elute into solution and form filament structures. This shake did not affect the formation of the subsequent filament structures.

4.6.3 Spinning aligned filaments

Aligned gel filament structures were formed through a spinning technique. 20 mL trigger solution was pipetted into the bottom half of a 10 cm Petri dish. Dots were drawn on the underside of the Petri dish 1 cm in from the edge. This was secured with Blu-tack on a spin coater. It was important to position the Petri dish as close to the centre of rotation as possible to prevent the non-uniform flow of trigger medium. A speed of 100 rpm was used, resulting in a localised “velocity” of trigger medium around the needle of approximately 2136 cm/min.

The spin coater (from Ossila) was started and after a few seconds the solution in the Petri dish would reach an equilibrium point, forming a uniform ring of fluid around the edges of the dish. The infusion of the pre-gel solution from the syringe pump was started, and then placed vertically into the rotating trigger solution above the marked points 1 cm in from the edge of the dish. Any gel droplet present on the end of the needle was removed by the flow of fluid around the needle tip. The injection into the Petri dish was performed for 10 seconds. The needle was removed as closely to the top of the Petri dish as possible. Pulling the needle directly up and away may result in thin filaments of gel that fall into the solution, leading to unrepresentative results when imaged and measured. Following removal of the needle the spin coater was stopped. The bundle of gel filament structures could then be carefully manipulated in the trigger solution. A microscope slide was carefully placed in the Petri dish avoiding touching the gel structures. The gel filament structures were then carefully positioned over the microscope slide and the trigger slowly removed from the dish leaving the bundle of gel filaments on top of the slide ready to be imaged.

4.6.4 Concentric flow setup

Two concentric flows (an inner and a sheath flow) was created using two syringe pumps by taking the rubber tubing for the sheath flow and piercing it with the inner flow needle. Through careful alignment and clamping the needle and the sheath tubing can be concentrically aligned. A metal wire can be used to help shape the tubing and facilitate the positing and alignment of the tubing and needle (Figure 42). Care was taken to assure the two flows were concentrically aligned. This was done with the front camera of a mobile phone and a clip-on mcarolense to help focus on the small object. Pictures were taken to show the good alignment of the two nozzles (Figure 43 and 44). The exit nozzles of the concentric flows were submerged in a bath of trigger medium by raising the 50 mM $CaCl_2$ bath up to the static nozzles using a mechanical jack (Figure 43 and 44). As before, the syringe pump flow was started and run until drops were coming out prior to submersion in the trigger medium to prevent blockages. Again, any droplets of solution that may be present upon submersion and consequently gelled were removed by a spatula. After this the filament formation would start given sufficient flow rates.

Figure 42. Photograph showing the alignment of a needle within the rubber tubing and Luer-lock nozzle for the sheath flow. Note the metal wire is shaped to manipulate the rubber tubing to aid with this.

4.6.4.1 Formation of aligned filaments with the concentric flow setup

With the sheath flow as 50 mM $CaCl_2$ and the inner flow as 1ThNapFF solution, the sheath flow can be used to extensionally deform the 1ThNapFF filaments as they form, provided the sheath flow is fast enough. This is discussed more details in the results section.

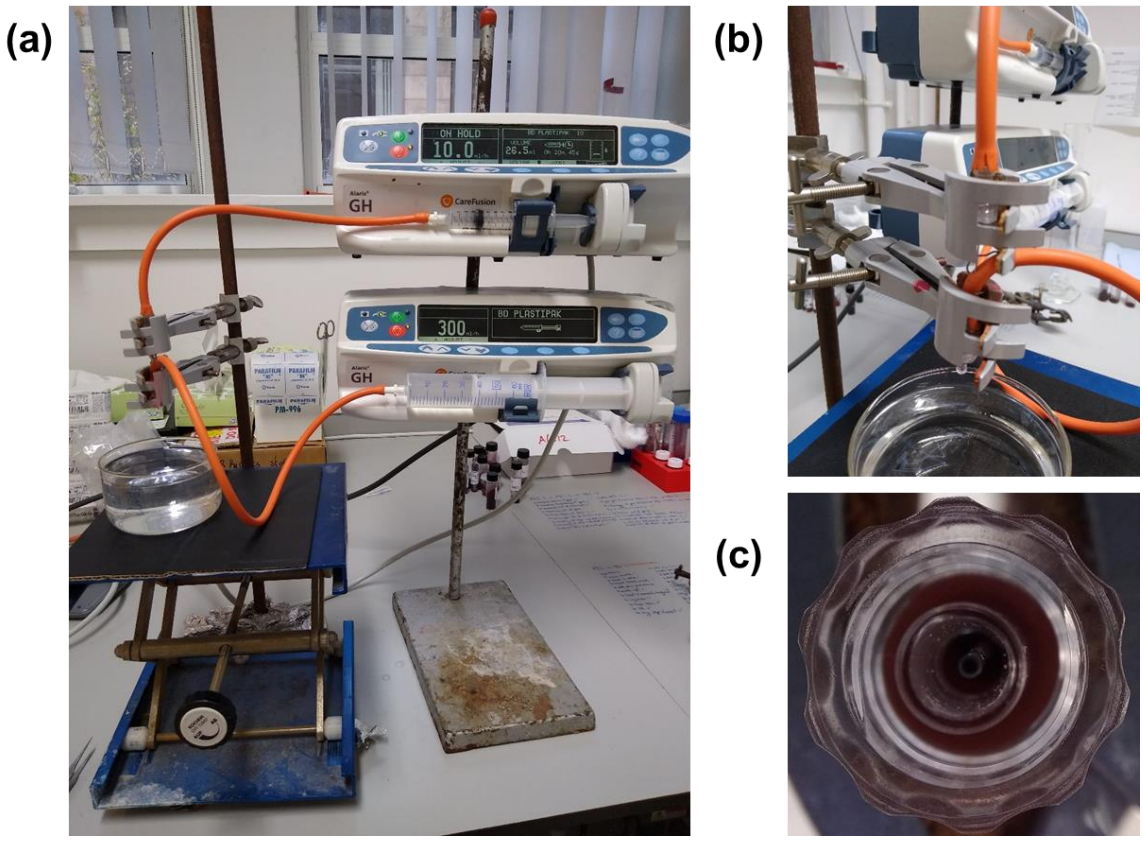

Figure 43. Photographs of the concentric flow setup. (a) Whole setups; (b) close up of tubing and (c) view from underneath showing the concentric alignment of needle and sheath flow. (c) was taken using a clip-on macrolense.

4.6.4.2 Concentric flow setup: Filament within a filament

Using a similar setup but having both the sheath and inner flows as 1ThNapFF solutions, a "filament-in-filament" could be formed. Here, a 1 mL pipette tip was used for the sheath flow (Figure 44) as opposed to a Luer-lock connector as above. The pipette tip was cut approximately 1 cm from the exit of the tip. This shortened tip was fitted into the rubber tubing so the exit nozzle from the tubing was the plastic pipette tip. Then the inner flow needle was pierced through the tubing and aligned within the pipette tip from which the sheath flow was dispensed.

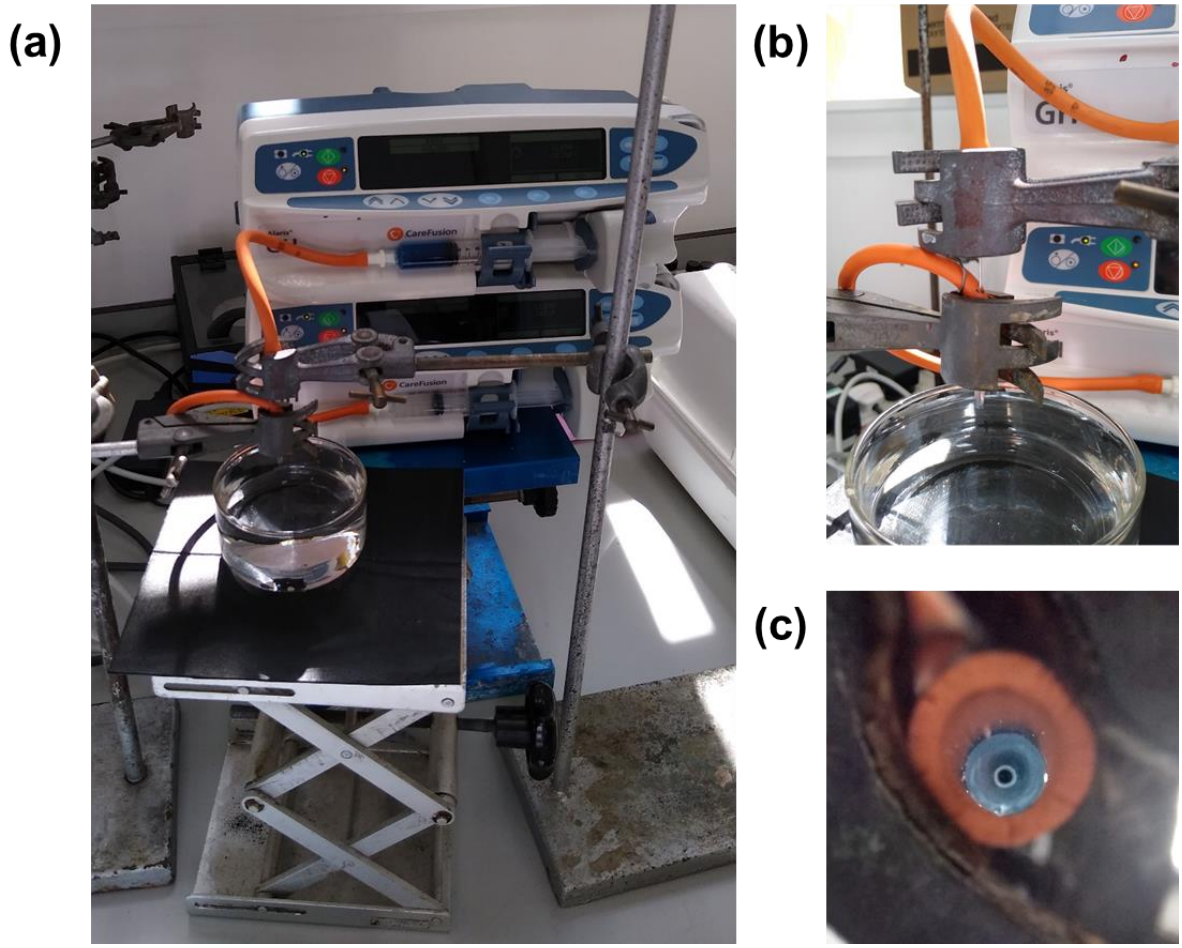

Figure 44. Photographs of the concentric flow setup. (a) Whole setups; (b) close up of tubing and (c) view from underneath showing the concentric alignment of needle and sheath flow.

For this setup an inner flow of 5 mg/mL 1ThNapFF solution and a sheath flow of 10 mg/mL 1ThNapFF solution were selected. The 5 mg/mL 1ThNapFF solution was stained blue with 80 ppm of Nile blue A to distinguish the two layers. Once formation of the filament occurred, the inner flow could be adjusted to vary the thickness of the blue, 5 mg/mL, inner filament within the 10 mg/mL sheath filament.

4.7 Optical microscopy

A Nikon Eclipse LV100 optical microscope with an Infinity 2 camera connected to a computer was used to image the gel filaments. The microscope was used in transmission mode, 5X magnification (LU Plan Fluor lense) and images taken under both normal and cross polarised light. Approximately 20-50 images were taken of each sample. In all CPOM images the direction of polarisers are vertical and horizontal relative to the image. The CPOM light intensity was kept constant by marking the dial positions required for each intensity.

Once the gel structures had been formed and collected on a microscope slide they were imaged. The underside of the slide was dried thoroughly with paper towel and placed on the microscope stage. Droplets of trigger medium was placed on the filament structures to form a pool to keep them hydrated. The gels shrink and lose alignment if not re-hydrated over a 40 minute period (Figure 45). Additionally, this removed any curved water/air boundaries from near the filament structures which resulted in poor images due to the refraction of light (see Figure 45c for this effect visualised).

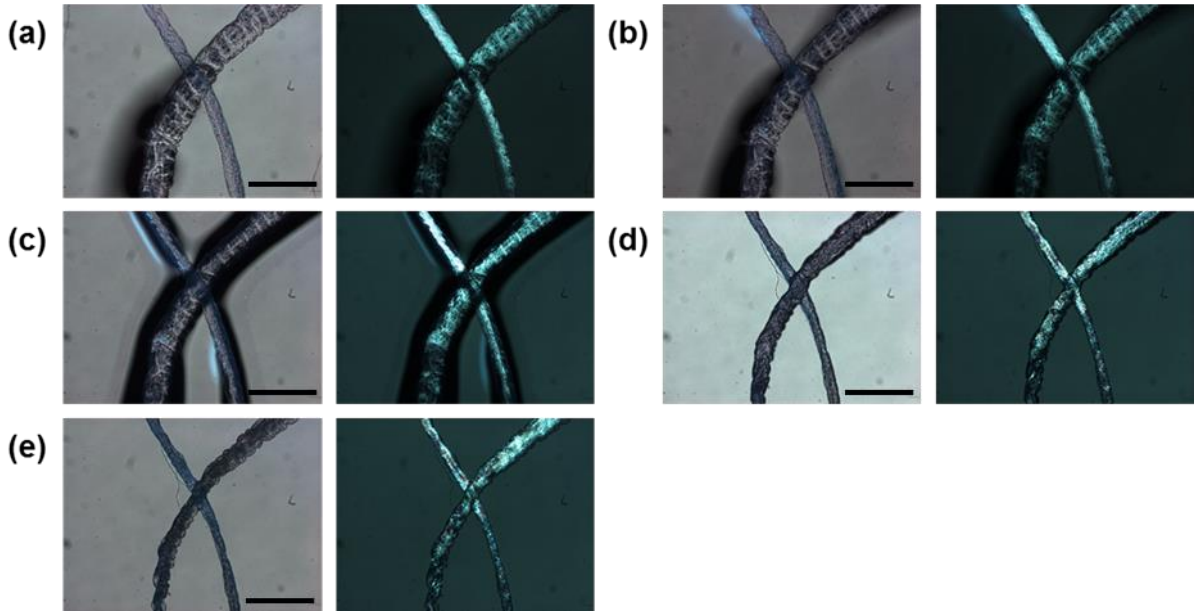

Figure 45. Optical microscope for the drying test showing normal (left) and cross polarised (right) light images at 5X magnification. Images were taken at (a) 0 minutes; (b) 10 minutes; (c) 20 minutes; (d) 30 minutes; (e) 40 minutes. Black scale bars represent 0.6 mm.

4.8 ImageJ analysis

ImageJ (version 1.50e)[53] analysis was used to measure the structure diameters in all of the microscope images. This was done using a 1 mm scale bar supplied with the microscope which is imaged at the same magnification, with which the global scale (pixels/mm) can be set in ImageJ. Out of focus structures were not measured. In each microscope image the diameter of every in focus filament structure was measured at a point approximately in the middle of the structure in view. This allowed for a histogram of filament diameter to be plotted for each sample.

4.9 Nanoindentation

The nanoindentation experiments and analysis were carried out by Dr Matthew Walker and Dr Massimo Vassalli (both at the School of Engineering at the University of Glasgow).

Nanoindentation was used to measure the Young's modulus of the low molecular weight gel filaments and bulk gels. The Young's modulus can vary depending on the experimental setup used.[54] During a nanoindentation experiment, the tip performs a set distance indentation into the sample and the resistance to the deformation is measured. This allows for a force-indentation curve to be created, which is then fitted using a Hertzian model to obtain a Young's modulus. The technique is localised, therefore the tip is scanned across the surface of the sample and many individual measurements collected. These are then processed and presented all together for each sample. A Chiaro nanoindenter (from Optics11Life) was used for nanoindentation under the indentation control operation mode. Tip radii of 8.5-10 μm, probe stiffness of 0.46-0.51 N/m and a Geo factor range of 1.21-1.25 were used. A maximum displacement of 10,000 nm was used, which includes the whole range including the out of contact region (flat baseline prior to reaching the surface). The indentation was performed at a constant speed of 5 μm/s. The forward segment of the force-distance curves were analysed and filtered for high frequency noise and evaluated with a custom-build software[55] developed using python and available online under open source license.[56] The fitting procedure was applied to the first 2000 nm after the contact point, keeping within 10% of the radius of the spherical indenter tip and 10% the thickness of the sample. A contact point method in the analysis software called 'Goodness of fit' was used.[57] The measurements were performed in 50 mM $CaCl_2$ solutions.

The thin (<0.2 mm), spun gel filaments could not be measured using the specific setup available.

4.10 Small angle X-ray scattering

Small angle X-ray scattering experiments were performed at the B21 beam line at Diamond Light Source, Didcot, UK. The beamline operated at a fixed energy of 13.02 keV, a camera length of 3.7046 m, resulting in a Q range of 0.0026 – 0.34 $Å^{-1}$. The beam flux was $4x10^{12}$ photons per second. The beam is offset to the top right hand corner of the Eiger 4M in-vacuum detector (Dectris). Further details of the SAXS setup can be found in a 2020 publication by the beamline scientists.[58]

The samples were measured in polyimide capillaries. To load the samples into the capillaries, a 1 mL syringe and a 19G needle (inner diameter = 0.686 mm) were used for each solution. For each sample 20 x 1 s frames were collected. Loading the capillaries into

the beam and running the experiments was performed *via* mail-in by the beamline scientists (Dr Nathan Cowieson).

The data was processed in the Dawn Science software (version 2.20.0).[59] As part of the processing procedure, a background of air (an empty capillary) and of the solvent (deionised H_2O in a capillary) were subtracted. The 20 frames were averaged and, for samples that scattered isotropically, a full azimuthal integration performed. Where necessary, flare from capillary mis-alignment was masked out. The azimuthal integration yielded the data as I vs *q* plots. These data were then fitted to structural models in the SasView software (version 5.0.2).[37] Many of the samples exhibited anisotropic scattering, which is consistent with aligned structures within the capillaries.[60] This is attributed to shear-aligning when loading the sample into the capillaries. The anisotropic data cannot be azimuthally integrated as is done for a normal isotropic data set. Instead, bow-tie integrations were performed over the regions of high scattering intensity and low scattering intensity. This results in two separate I vs q plots. The I vs q plots for the high scattering intensity regions were fitted to structural models in SasView. When performing a bow-tie integration over the high intensity (vertical) regions, there are kinks in the data due to boundaries between the detector modules. This results in anomalous data points which have been manually removed and gaps in the curve. There are some limitations in this approach because the form factor fitting assumes that the self-assembled structures are non-interacting and randomly oriented. For aligned samples the structures are not randomly oriented. While this approach is not ideal and may lead to some small errors in the fitting, it is not significant enough to not fit the data. Indeed, by virtue of the fact that the particles have aligned, this reinforces the application of a structural model consistent with 1D structures. For the fitting X-ray scattering length densities (SLDs) were calculated using the NIST neutron activation and scattering calculator.[61] An SLD of 14.025×10^{-6} Å^2 was used for 1ThNapFF and a solvent SLD of 9.469×10^{-6} Å^2 was used.

4.10.1 Fitting data

Data that exhibited isotropic scattering were azimuthally integrated and the resultant plots fitted structural models in SasView as has commonly done before for these type of systems.[35,62] The data for the 1.0 mg/mL and 1.5 mg/mL solutions exhibited low scattering intensity and were not fitted to any structural models. Many of the data show anisotropic scattering patterns in the 2D data. This is attributed to shear-alignment of 1D structures in the 1ThNapFF solution as it is injected into the capillary. As discussed in the experimental, bow-tie integrations were performed. An example of the two I vs q plots obtained from this process is shown in Figure S12. For many of the data a large upturn in intensity at the lowest Q was seen. This has previously been attributed to scattering from the network for self-assembled functionalised dipeptides.[34] For each fit, this low Q region was initially

excluded from the fitting and the rest of the data fitted to different cylinder models until a good fit was achieved. For these data typically a cylinder or flexible cylinder model was required to achieve a good fit. This is consistent with the presence of self-assembled worm-like micelles. After this, the values obtained with this flexible cylinder fit were input into a combined flexible cylinder + power law model and the whole Q range fitted. The power law model generally captured this upturn in intensity at low Q.

5 References

1 H. Sai, A. Erbas, A. Dannenhoffer, D. Huang, A. Weingarten, E. Siismets, K. Jang, K. Qu, L. C. Palmer, M. Olvera De La Cruz and S. I. Stupp, *J. Mater. Chem. A*, 2019, **8**, 158–168.

2 R. J. Lindquist, B. T. Phelan, A. Reynal, E. A. Margulies, L. E. Shoer, J. R. Durrant and M. R. Wasielewski, *J. Mater. Chem. A*, 2016, **4**, 2880–2893.

3 A. S. Weingarten, A. J. Dannenhoffer, R. V. Kazantsev, H. Sai, D. Huang and S. I. Stupp, *J. Am. Chem. Soc.*, 2018, **140**, 4965–4968.

4 D. Liu, J. Wang, X. Bai, R. Zong and Y. Zhu, *Adv. Mater.*, 2016, **28**, 7284–7290.

5 M. Wallace, A. Z. Cardoso, W. J. Frith, J. A. Iggo and D. J. Adams, *Chem. Eur. J.*, 2014, **20**, 16484–16487.

6 L. Hu, R. Zhang and Q. Chen, *Nanoscale*, 2014, **6**, 14064–14105.

7 D. W. P. M. Löwik, I. O. Shklyarevskiy, L. Ruizendaal, P. C. M. Christianen, J. C. Maan and J. C. M. Van Hest, *Adv. Mater.*, 2007, **19**, 1191–1195.

8 E. R. Draper, M. Wallace, D. Honecker and D. J. Adams, *Chem. Commun.*, 2018, **54**, 10977–10980.

9 L. Jiang, H. Dong and W. Hu, *Soft Matter*, 2011, **7**, 1615–1630.

10 E. R. Draper, O. O. Mykhaylyk and D. J. Adams, *Chem. Commun.*, 2016, **52**, 6934–6937.

11 G.-F. Liu, D. Zhang and C.-L. Feng, *Angew. Chem. - Int. Ed.*, 2014, **53**, 7789–7793.

12 A. Chalard, L. Vaysse, P. Joseph, L. Malaquin, S. Souleille, B. Lonetti, J. C. Sol, I. Loubinoux and J. Fitremann, *ACS Appl. Mater. Interfaces*, 2018, **10**, 17004–17017.

13 B. D. Wall, S. R. Diegelmann, S. Zhang, T. J. Dawidczyk, W. L. Wilson, H. E. Katz, H. Q. Mao and J. D. Tovar, *Adv. Mater.*, 2011, **23**, 5009–5014.

14 D. J. Adams, M. F. Butler, P. Sanderson, L. Mullen, W. J. Frith and M. Kirkland, *Soft Matter*, 2009, **5**, 1856.

15 A. Li, A. Hokugo, A. Yalom, E. J. Berns, N. Stephanopoulos, M. T. McClendon, L. A. Segovia, I. Spigelman, S. I. Stupp and R. Jarrahy, *Biomaterials*, 2014, **35**, 8780–8790.

16 E. J. Berns, S. Sur, L. Pan, J. E. Goldberger, S. Suresh, S. Zhang, J. A. Kessler and

S. I. Stupp, *Biomaterials*, 2014, **35**, 185–195.

17 J. G. Egan, G. Brodie, D. McDowall, A. J. Smith, C. J. C. Edwards-Gayle and E. R. Draper, *Mater. Adv.*, 2021, **2**, 5248–5253.

18 C. L. Smith, L. L. E. Mears, B. J. Greeves, E. R. Draper, J. Doutch, D. J. Adams and A. J. Cowan, *Phys. Chem. Chem. Phys.*, 2019, **21**, 26466–26476.

19 S. Zhang, M. A. Greenfield, A. Mata, L. C. Palmer, R. Bitton, J. R. Mantei, C. Aparicio, M. O. De La Cruz and S. I. Stupp, *Nat. Mater.*, 2010, **9**, 594–601.

20 T. Christoff-Tempesta, Y. Cho, D.-Y. Kim, M. Geri, G. Lamour, A. J. Lew, X. Zuo, W. R. Lindemann and J. H. Ortony, *Nat. Nanotechnol.*, 2021, **16**, 447–454.

21 M. T. McClendon and S. I. Stupp, *Biomaterials*, 2012, **33**, 5713–5722.

22 R. Marty, R. Szilluweit, A. Sánchez-Ferrer, S. Bolisetty, J. Adamcik, R. Mezzenga, E. C. Spitzner, M. Feifer, S. N. Steinmann, C. Corminboeuf and H. Frauenrath, *ACS Nano*, 2013, **7**, 8498–8508.

23 J. Chen, F. K. C. Leung, M. C. A. Stuart, T. Kajitani, T. Fukushima, E. Van Der Giessen and B. L. Feringa, *Nat. Chem.*, 2018, **10**, 132–138.

24 D. R. Lide and W. M. Haynes, Eds., *CRC Handbook of Chemistry and Physics*, CRC Press, Boca Raton, 90th edn., 2010.

25 A. Chalard, P. Joseph, S. Souleille, B. Lonetti, N. Saffon-Merceron, I. Loubinoux, L. Vaysse, L. Malaquin and J. Fitremann, *Nanoscale*, 2019, **11**, 15043–15056.

26 A. B. Marciel, M. Tanyeri, B. D. Wall, J. D. Tovar, C. M. Schroeder and W. L. Wilson, *Adv. Mater.*, 2013, **25**, 6398–6404.

27 L. R. Valverde, B. Li, C. M. Schroeder and W. L. Wilson, *Langmuir*, 2019, **35**, 10947–10957.

28 S. R. Diegelmann, N. Hartman, N. Markovic and J. D. Tovar, *J. Am. Chem. Soc.*, 2012, **134**, 2028–2031.

29 J. López-Andarias, M. J. Rodriguez, C. Atienza, J. L. López, T. Mikie, S. Casado, S. Seki, J. L. Carrascosa and N. Martín, *J. Am. Chem. Soc.*, 2015, **137**, 893–897.

30 M. P. Del Borgo, A. I. Mechler, D. Traore, C. Forsyth, J. A. Wilce, M. C. J. Wilce, M. I. Aguilar and P. Perlmutter, *Angew. Chem. - Int. Ed.*, 2013, **52**, 8266–8270.

31 H. Guo, J. Zhang, T. Xu, Z. Zhang, J. Yao and Z. Shao, *Biomacromolecules*, 2013, **14**, 2733–2738.

32 Y. Liu, T. Wang, Y. Huan, Z. Li, G. He and M. Liu, *Adv. Mater.*, 2013, **25**, 5875–5879.

33 F. K. C. Leung, T. Kajitani, M. C. A. Stuart, T. Fukushima and B. L. Feringa, *Angew. Chem. - Int. Ed.*, 2019, **58**, 10985–10989.

34 A. Z. Cardoso, L. L. E. Mears, B. N. Cattoz, P. C. Griffiths, R. Schweins and D. J. Adams, *Soft Matter*, 2016, **12**, 3612–3621.

35 E. R. Draper, H. Su, C. Brasnett, R. J. Poole, S. Rogers, H. Cui, A. Seddon and D. J. Adams, *Angew. Chem. - Int. Ed.*, 2017, **56**, 10467–10470.

36 A. P. R. Eberle and L. Porcar, *Curr. Opin. Colloid Interface Sci.*, 2012, **17**, 33–43.

37 SasView, https://www.sasview.org/, (accessed 21 September 2021).

38 L. Chen, T. O. McDonald and D. J. Adams, *RSC Adv.*, 2013, **3**, 8714–8720.

39 S. Richardson, *Rheol. Acta*, 1970, **9**, 193–199.

40 J. Batchelor, J. P. Berry and F. Horsfall, *Polymer*, 1973, **14**, 297–299.

41 A. Koeppel, N. Stehling, C. Rodenburg and C. Holland, *Adv. Funct. Mater.*, 2021, DOI:10.1002/adfm.202103295.

42 M. Sentmanat, O. Delgadillo-Velázquez and S. G. Hatzikiriakos, *Rheol. Acta*, 2010, **49**, 931–939.

43 M. Trebbin, D. Steinhauser, J. Perlich, A. Buffet, S. V. Roth, W. Zimmermann, J. Thiele and S. Förster, *Proc. Natl. Acad. Sci. U. S. A.*, 2013, **110**, 6706–6711.

44 S. M. Recktenwald, S. J. Haward, A. Q. Shen and N. Willenbacher, *Sci. Rep.*, 2019, **9**, 1–11.

45 R. Omidvar, S. Wu and H. Mohammadigoushki, *J. Rheol.*, 2019, **63**, 33–44.

46 A. V. Walter, L. N. Jimenez, J. Dinic, V. Sharma and K. A. Erk, *Rheol. Acta*, 2019, **58**, 145–157.

47 J. Dinic, M. Biagioli and V. Sharma, *J. Polym. Sci. Part B Polym. Phys.*, 2017, **55**, 1692–1704.

48 L. Biette, F. Carn, M. Maugey, M. F. Achard, J. Maquet, N. Steunou, J. Livage, H. Serier and R. Backov, *Adv. Mater.*, 2005, **17**, 2970–2974.

49 R. Akhtar, E. R. Draper, D. J. Adams and J. Hay, *J. Mater. Res.*, 2018, **33**, 873–883.

50 M. C. Nolan, A. M. Fuentes Caparrós, B. Dietrich, M. Barrow, E. R. Cross, M. Bleuel, S. M. King and D. J. Adams, *Soft Matter*, 2017, **13**, 8426–8432.

51 M. J. Farooqi, M. A. Penick, J. Burch, G. R. Negrete and L. Brancaleon, *Spectrochim. Acta - Part A Mol. Biomol. Spectrosc.*, 2016, **153**, 124–131.

52 L. Thomson, R. Schweins, E. R. Draper and D. J. Adams, *Macromol. Rapid Commun.*, 2020, DOI:10.1002/marc.202000093.

53 ImageJ, https://imagej.net/Welcome, (accessed 20 October 2019).

54 C. T. McKee, J. A. Last, P. Russell and C. J. Murphy, *Tissue Eng. - Part B Rev.*, 2011, **17**, 155–164.

55 I. Lüchtefeld, A. Bartolozzi, J. Mejía Morales, O. Dobre, M. Basso, T. Zambelli and M. Vassalli, *J. Nanobiotechnology*, 2020, **18**, 1–11.

56 M. Vassalli and G. Ciccone, CellMechLab/nanoindentation: beta, https://zenodo.org/record/4508646/export/json#.YMpon9VKiCo, (accessed 16 June 2021).

57 N. Gavara, *Sci. Rep.*, 2016, **6**, 1–13.

58 N. P. Cowieson, C. J. C. Edwards-Gayle, K. Inoue, N. S. Khunti, J. Doutch, E. Williams, S. Daniels, G. Preece, N. A. Krumpa, J. P. Sutter, A. D. Tully, N. J. Terrill and R. P. Rambo, *J. Synchrotron Radiat.*, 2020, **27**, 1438–1446.

59 Dawn Science, https://dawnsci.org/, (accessed 21 December 2020).

60 R. P. Murphy, Z. W. Riedel, M. A. Nakatani, P. F. Salipante, J. S. Weston, S. D. Hudson and K. M. Weigandt, *Soft Matter*, 2020, **16**, 6285–6293.

61 NIST Neutron activation and scattering calculator, https://www.ncnr.nist.gov/resources/activation/.

62 D. McDowall, B. Greeves, R. Clowes, K. McAulay, A. Fuentes-Caparros, L. Thomson, N. Khunti, N. Cowieson, M. C. Nolan, M. Wallace, A. I. Cooper, E. R. Draper, A. Cowan and D. J. Adams, *Adv. Energy Mater.*, 2020, DOI:10.1002/aenm.202002469.

Chapter 4

Gel noodles for photocatalysis and extensional relaxation time of an isoleucine-functionalised perylene bisimide

Acknowledgements

I would like to thank co-workers for synthesising the materials used in this Chapter. 1ThNapFF was synthesised by Professor Dave Adams, PBI-I was synthesised by Jacquelan Egan and 2NapFF was synthesised by Lisa Thomson.

The gel noodle photocatalysis work was performed in collaboration with Benjamin Greeves. His aspect of the work covered the photocatalysis setup and data analysis.

Professor Robert Poole and Dr Henry Ng aided greatly with advice on building the dripping-onto-substrate setup as well as how to approach the data processing and analysis.

Abstract

An L-isoleucine functionalised PBI reported in the literature to form highly viscous, shear-thinning worm-like micelle solutions was used for the formation of gel noodles. Both aligned and un-aligned gel noodles were prepared and used for the photocatalytic evolution of hydrogen. The results suggest that the aligned gel noodles produced more hydrogen than the un-aligned ones but there were concerns over differences in the gel morphology. A third, more-aligned system was sought after but attempts at using the spinning technique shown in Chapter 3 were unsuccessful. The PBI-I did not stretch to form thin, well-aligned filaments. Instead, short, broken-up sections of gel noodle were formed. It was hypothesised that differences in the extensional viscosity of the PBI-I solution as compared with the 1ThNapFF solution controlled this. A literature method to measure the extensional relaxation time of fluids, dripping-onto-substrate, was setup. The results supported the hypothesis, where 1ThNapFF behaved as an elastic fluid with long relaxation times whereas the PBI-I solution broke rapidly in extensional deformations.

1 Introduction

When self-assembled structures are present in the pre-gel solution of LMWGs, the rheological properties often exhibit non-Newtonian behaviour. This has been recognised in some studies within the low molecular weight gel literature,[1,2] but it is seldom studied in great depth because it typically requires access to relatively expensive equipment and the data analysis can be complex. When rheological measurements are done, they are typically on the gels, where oscillatory strain and frequency sweeps are used as proof of gel formation.[3–5] The non-Newtonian behaviour of the pre-gel solutions is important from a fundamental understanding as well as for potential applications. For example, researchers have studied the influence of anions in organogelator solutions and found a sharp increase in specific viscosity upon entanglement of the supramolecular fibres.[6] Much work specifically utilises the non-Newtonian material properties for certain applications such as shear-alignment of worm-like micelles (WLM) and gels or the formation of gel noodles.[7,8] Most commonly, the shear viscosity of the pre-gel solutions is studied but some recent studies by Adams and co-workers have studied the extensional viscosity/extensional relaxation time of pre-gel solutions that contain worm-like micelles.[1,2,9]

Studying a fluids response to both shear and extensional flows (as opposed to one of these alone) is crucial for a full characterisation of the materials rheological properties.[10] The rheological properties of a fluid are governed by both the interactions between molecules and the presence of nano- or micro-structural units and the interactions between those units. For example, hydrogen bonding between individual molecules can be a significant factor in determining the viscosity of a solution.[11] The phase volume of the dispersed phase in emulsions has a significant impact on the fluid viscosity and they are typically shear-thinning at high phase volumes.[12] Additionally, the solid-like behaviour of LMWGs derives from the formation of an entangled network of fibrous structures.[5]

Viscosity is described as the liquid's (or material's) resistance to flow. For flow to occur, the liquid must be subjected to a stress, which is defined by the force divided by the area. This results in a deformation of the fluid that is defined by the strain, which is the change per unit length. As a general definition, viscosity is determined by the stress divided by the strain. The direction of the applied stress relative to the fluid/material determines the type of viscosity.[13,14] For fluids, two important types are the shear viscosity and the extensional viscosity.

Before discussing the extensional viscosity, it is first important to define the shear viscosity to draw distinction between them. A common method for determining shear viscosity is by using a rotational rheometer. Shear stress occurs when the force acts parallel to the fluid.

For example, where a fluid is contained between a gap between two plates and one plate moves parallel to the other, a shear stress (σ) is applied. Assuming there is no-slip between the fluid and the plates, a velocity gradient is formed where the fluid directly in contact with the moving plate moves at the same rate as the plate and the fluid directly in contact with the stationary plate is stationary. The displacement occurring with each second determines the rate of strain which is synonymous with the velocity gradient or shear rate (ẏ). With both the shear stress and the shear rate known, the viscosity (η) can be determined (equation 1). This provides a very simplistic description for how rotational rheometers are used to determine the shear viscosity of a fluid.

$$\eta = \frac{\sigma}{\dot{y}} \quad (1)$$

The extensional viscosity is a material parameter that is important for various processes including fibre spinning, electrospinning, inkjet printing, roll coating and drag reduction.[15,16]In contrast to shear deformation, extensional viscosity is described by the ratio of the stress to strain in the uniaxial and steady extension of a uniform cylinder of fluid.[17] In practice, realising the specific requirements (e.g. spatially uniform and steady flows) for the extensional viscosity experimentally are typically challenging.[13] As such, the "transient extensional viscosity" is commonly reported but it has been noted that even this term can lead to confusion and comes with caveats.[13] A 1906 paper by Frederick Thomas Trouton is generally regarded as the first study of extensional flow, in which he refers to "the coefficient of viscous traction and its relation to that of viscosity".[18] Trouton determined that for a Newtonian fluid, the extensional viscosity is three times greater than the shear viscosity. Commonly in research, the extensional relaxation (λ_E) times for fluids are given instead. This is a more simplistic method for analysis but is widely used for polymer and worm-like micelle solutions.[1,19,20] The measurement of extensional viscosity and extensional relaxation time has been an active area of study in recent decades.[13,21,22] One parameter, which has not been widely studied for LMWG pre-gel solutions, is the extensional relaxation time. Extensional relaxation time measurements have been reported for functionalised dipeptide worm-like micelle solutions by the Adams group in recent years, in which a capillary break-up extensional rheometer (CaBER) was used to perform the measurements.[1,2]

1.1 The importance of extensional deformations

It is important to understand the behaviour of fluids under extensional deformations because they have wide ranging consequences in industries including food processing, oil industry, coatings, printing, plastics, materials and lubricants among others.[10,16,23] In particular, extensional deformations play an important role in the micro- and nano-structuring of a material. Extensional flows and deformation have been shown to impart enhanced material properties and alignment of 1D structures (for example for polymers, self-assembled silk proteins and colloidal nanorods).[24,25]

1.1.1 Polymers

When manufacturing polymers and plastics, consistently producing materials to specification as efficiently and economically as possible is vital. As such, the rheological properties of the materials being used need to be fully understood, where variables including temperature, aging, deformation rate as well as the molecular structure and make-up (e.g. polymer size distribution) are important.[23] In this context, extensional flow fields have significant industrial relevance for polymers and plastics where extensional flow plays a key role in fibre spinning and blow moulding processes among others.[26–29] Many (but not all) polymers exhibit an increase in extensional viscosity above a linear range at certain strains, a process termed strain hardening.[30] Strain hardening is both useful and important because it can lead to greater uniformity of deformation (such as during manufacture).[23]

Extensional flows typically lead to orientation of the polymer chains,[31,32] which can result in enhanced material properties as well as improving efficiency during manufacturing.[33] For example, in the spinning of polyethylene terephthalate (PET) fibres, increasing the draw ratio (λ_D) leads to increased alignment of the polymers within the fibre as determined by anisotropic scattering in wide angle X-ray scattering (WAXS) measurements (Figure 1a).[34] The draw ratio compares the fibre thickness before and after part of the mechanical spinning process which stretches the filament. Similarly, when mixed with carbon nanotubes (CNTs) the PET shows increased alignment with increasing the draw ratio (Figure 1b).[33] For the polyamide-6 (PA6) system with CNT, the fibres already show alignment and are unchanged with drawing ratio. There is a critical draw ratio at which the CNTs go from being aligned perpendicular to the fibre long axis to being aligned parallel to it.

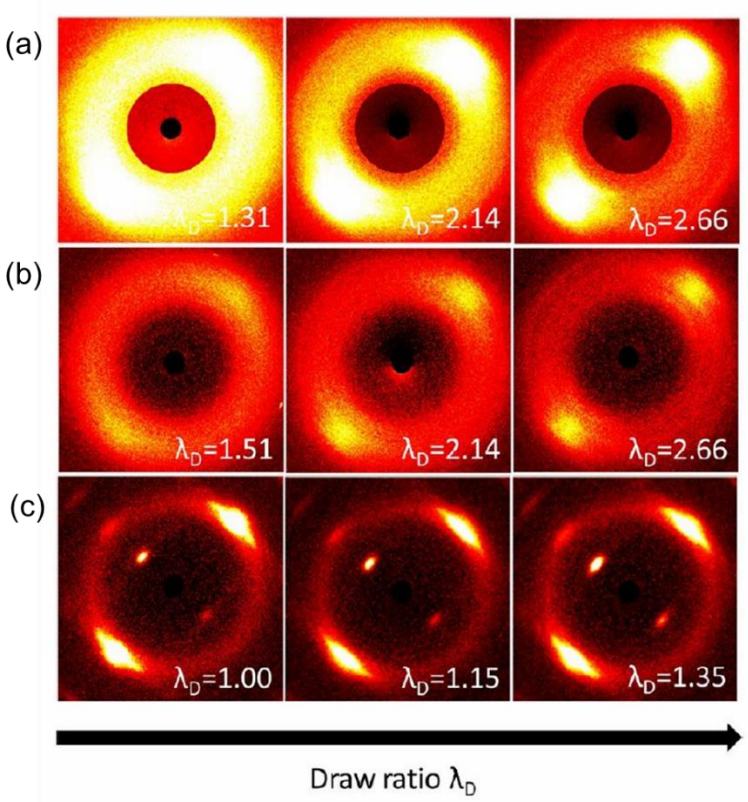

Figure 1. WAXS data for polymeric drawn filaments comprised of (a) PET; (b) PET with 0.5 wt% CNTs and (c) PA6 with 0.1 wt% CNTs. Reprinted with permission from T. Vad, J. Wulfhorst, T. T. Pan, W. Steinmann, S. Dabringhaus, M. Beckers, G. Seide, T. Gries, W. F. C. Sager, M. Heidelmann and T. E. Weirich, Macromolecules, 2013, 46, 5604–5613. Copyright© 2013, American Chemical Society

1.1.2 Silks

There is considerable research studying the influence of extensional flows on silk spinning for the formation of silk fibres. Silk fibroin obtained from the silk moth, *Bombyx mori*, has been widely studied. Silk fibroin is a block copolymer with a high proportion of hydrophobic β-sheet segments connected by hydrophilic linkers.[35] The protein self-assembles, resulting in a polymeric material with high mechanical strength (particularly tensile strength) and toughness, making it an ideal candidate for a wide range of materials. In work using the native silk fibroin obtained from *Bombyx mori* silkworms, a tensile testing instrument was adapted into a filament stretching rheometer, allowing the investigation into how silk proteins respond to extensional deformation.[36] To this end, the effect of extension rate on filament formation was investigated, showing that fibre formation was only achieved at the lower extension rates (Figure 2). This result was surprising, as the higher extension rates corresponded to those found in natural silk spinning. These experiments solely study the influence of extension rate, and the authors concluded that other factors (such as pH and humidity) are at play in natural silk spinning.

The stretching device measures the force during fibre formation which enables a transient extensional viscosity to be calculated by using the effective extension rate and tensile stress difference. To do this, both the filament diameter evolution with time and surface tension must be calculated. The transient extensional viscosities (Figure 2b) show three distinct regions with time. An initial increase with time, followed by a plateau and then a subsequent increase again at later times. The viscosity increase after the plateau is attributed to strain hardening and occurs at shorter times at higher extension rates. The time aspect is removed by plotting Hencky strain against the transient extensional viscosity (Figure 2c). By removing the time element, the filaments at different strain rates are compared and show that the viscosity increase is independent of strain rate. Following this up they demonstrate that alongside extensional flow, pH activation is a key variable in controlling the performance of spun fibres.[25]

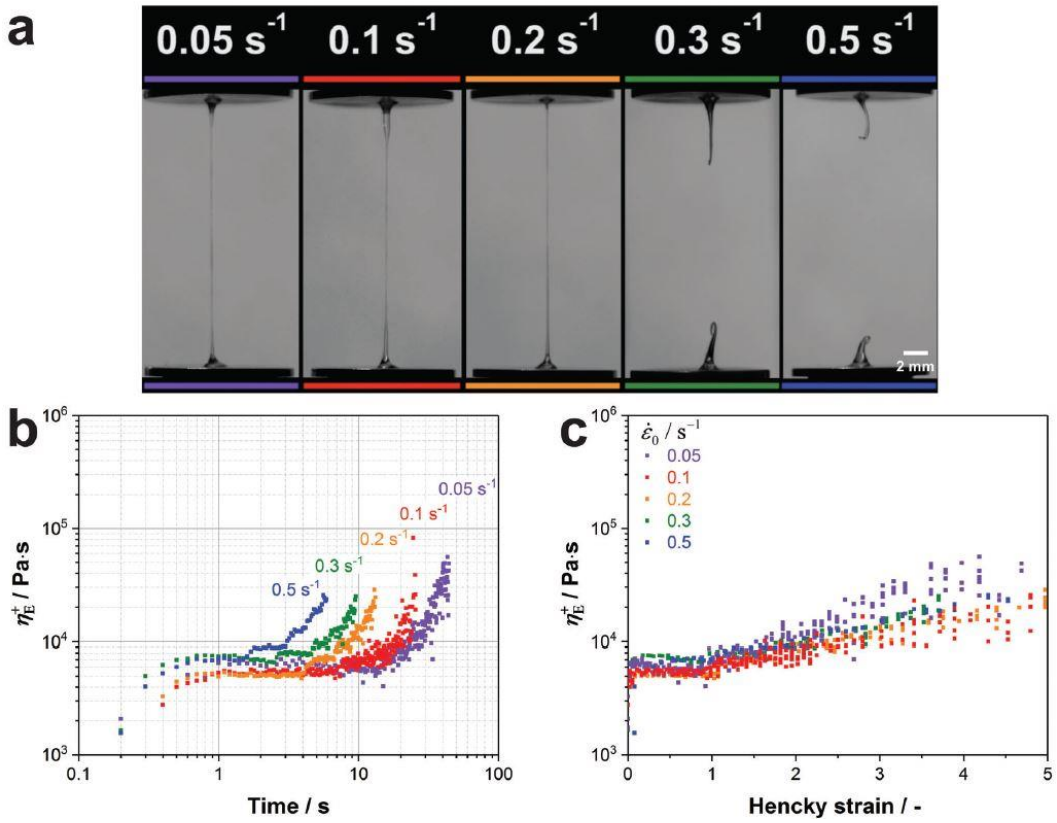

Figure 2. (a) Native silk fibres formed in a tensile testing device at different extension rates; (b) transient extensional viscosity of the silks at different extension rates and (c) Transient extensional viscosity plotted against the Hencky strain. Reproduced from A. Koeppel, P. R. Laity and C. Holland, Soft Matter, 2018, 14, 8838–8845, with permission from the Royal Society of Chemistry under the Creative Commons Attribution 3.0 Unported Licence.

1.1.3 Hydrogel filaments

There have been reports in which a wet spinning technique is used to prepare aligned filaments from polymeric hydrogels.[37] In a similar manner to the spinning technique described in Chapter 3, the polymer solution is injected into a rotating coagulant bath to form the gel filaments. This results in alignment within the filaments which are used as cell culture matrices which direct cell alignment. It is not explicitly mentioned or investigated, but it appears that the extensional deformation induced by the spinning process is crucial for the alignment. If it were not the case, the spinning procedure would not be needed.

1.1.4 Other nanomaterials

Cellulose nanocrystals have been studied as model colloidal rods (dimensions approximately 200 nm x 6 nm) where, in the dilute regime, it was shown that extensional flow fields were more effective at inducing nanorod alignment as compared with shear flows.[38] In other work, extensional deformation in the wet spinning of macroscopic fibres from vanadium oxide nanorod suspensions has been shown to be essential in aligning the nanorods (Figure 3).[24] This work inspired the concentric flow setup shown in Chapter 3 that was used to align the 1ThNapFF gel noodles. Similar setups have also been used for the spinning of artificial silk fibres.[39] Alignment is determined by cross polarised optical microscope (CPOM) measurements.

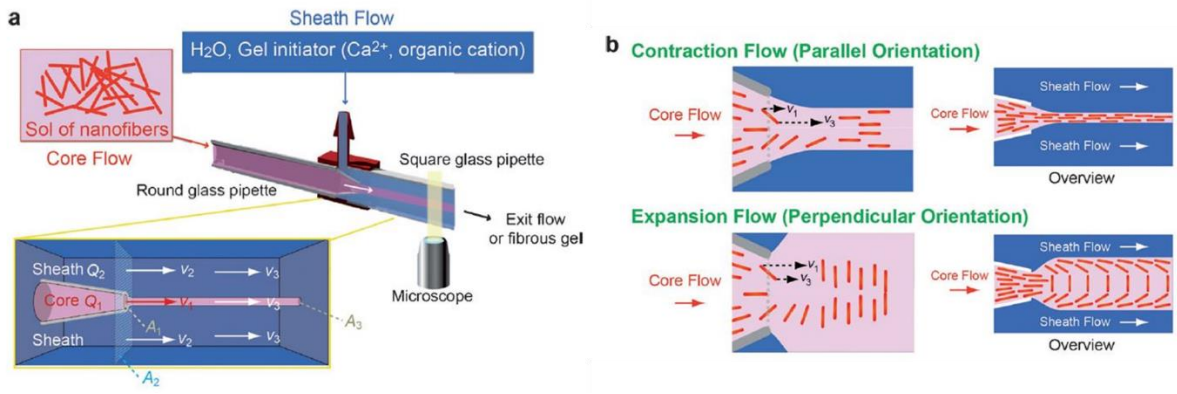

Figure 3. Cartoon schematics of the microfluidic setup used to control the internal morphology of gel threads based on vanadium oxide nanorods. (a) Microfluidic setup where Q_1 is the flow rate of the nanofibre suspension and Q_2 is the gel initiator sheath flow rate resulting in flow velocities V_1 and V_2. (b) Cartoon representation of the nanorod alignment within the gel filaments under two flow regimes. Reprinted from D. Kiriya, R. Kawano, H. Onoe and S. Takeuchi, Angew. Chem. Int. Ed., 2012, 51, 7942–7947 with permission from John Wiley and Sons, Copyright© 2012.

Macroscale fibres comprised of aligned protein nanofibrils have been prepared using extensional deformations imparted in a cross-slot device (Figure 4).[40] First, the protein self-assembly is triggered to form nanofibrils and then the fluid is passed through a cross-slot device (with alginate, polyethylene glycol and calcium chloride) to form aligned fibres.

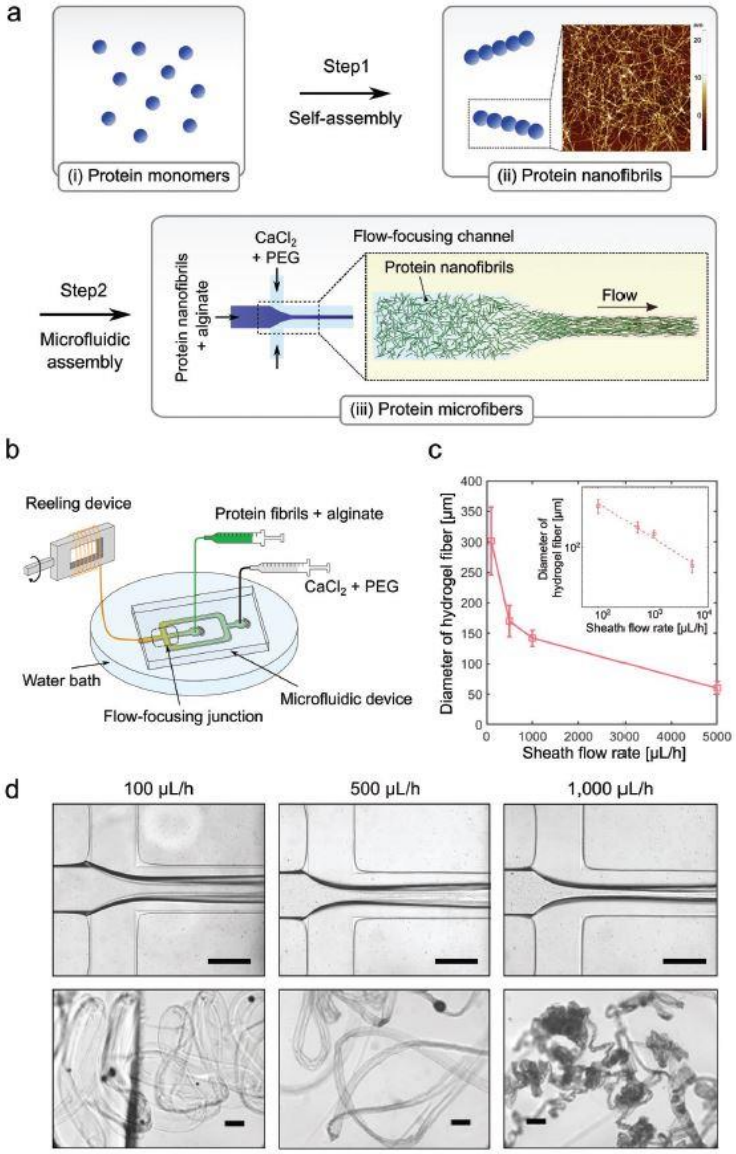

Figure 4. (a) Cartoon schematic of the preparation of aligned protein microfibers; (b) cartoon schematic of the device used to prepare the fibres; (c) hydrogel fibre diameter with the sheath flow rate and (d) images of the fibres produced at different flow rates. Reproduced from A. Kamada, A. Levin, Z. Toprakcioglu, Y. Shen, V. Lutz-Bueno, K. N. Baumann, P. Mohammadi, M. B. Linder, R. Mezzenga and T. P. J. Knowles, Small, 2020, 16, 1–8, with permission from John Wiley and Sons, Copyright© 2020.

Again, although not explicitly discussed or investigated, the drawing of self-assembled nanoribbon solutions in a gelation trigger bath to form mechanically robust threads appears to operate on an extensional process during thread formation.[41] Indeed, the CPOM, SAXS

and WAXS data of these threads (Figure 9; Chapter 3) shows the nanostructure to be highly aligned, as was highlighted in the literature review in Chapter 3. The threads are flexible and can be handled as well as support of 20 mg weight over a 5 cm gap where the thread itself weighs only 0.1 mg.

1.2 Measuring fluids under extensional deformation

The behaviour of a fluid under extensional deformations is important for manufacturing and allows for unique properties and alignment to be achieved. It is therefore important to understand the behaviour of fluids in extensional flow. While there has been considerable interest in making such measurements, they have posed a significant challenge in part due to issues with creating purely extensional deformations on a fluid. Part of the challenge is that different equipment is typically required to study fluids with different extensional viscosities, there is no 'catch all' approach (Figure 5).

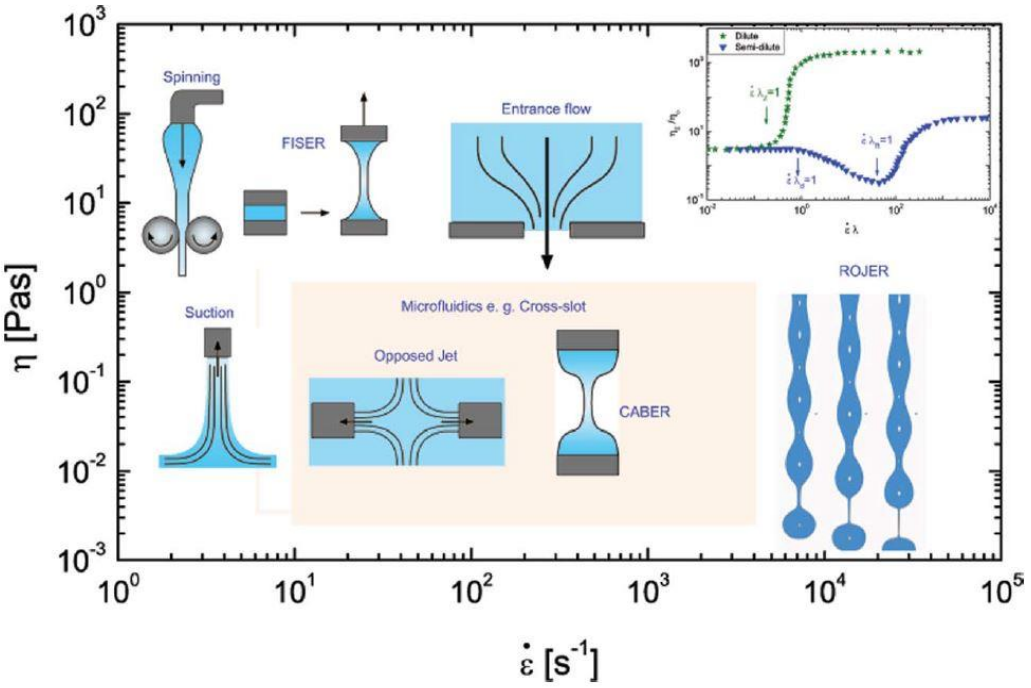

Figure 5. A plot of extension rate vs zero shear viscosity demonstrating the effective operating range for a range of extensional rheometry techniques when studying polymer solutions. Inset is a rate-dependent extensional viscosity response shown by dilute and semi-dilute polymer solutions. Reproduced from V. Sharma, S. J. Haward, J. Serdy, B. Keshavarz, A. Soderlund, P. Threlfall-Holmes and G. H. McKinley, Soft Matter, 2015, 11, 3251–3270, with permission from the Royal Society of Chemistry, Copyright© 2015.

To this end, filament stretching devices have proven to be quite successful. These operate of the analyte fluid being sandwiched between two plates and then one of the plates moves vertically, imposing a stretching deformation. The filament stretching extensional rheometer

(FiSER^{TM}) imparts a vertical exponential velocity with a constant strain rate to create uniaxial extension (Figure 5). During this, both the tensile force exerted on the bottom plate by the fluid and the axial midplane radius of the fluid are measured to obtain a transient extensional viscosity.[42] In the capillary break-up extensional rheometer (CaBER^{TM}), the top plate imparts a single step strain to form the filament (Figure 5).[42] The filament subsequently thins due to capillary forces with the extensional strain rate defined by the fluid properties. The evolution of the midplane filament radius with time is typically measured by a laser micrometer but recent work has demonstrated the importance of filming the thinning process, where the shape of the fluid filament can be observed.[22] Microfluidic devices have also been developed to study the extensional properties of fluids and have been particularly effective for low viscosity fluids.[43] A limitation of many techniques for measuring extensional viscosity and relaxation time is the expense and/or complexity of the equipment.

1.3 Dripping-onto-substrate

In 2015, Sharma's group reported a technique called dripping-onto-substrate (DoS) as a method for measuring the extensional relaxation time of fluids.[44] It involves the dispensing of a droplet of the fluid onto a substrate, resulting in an unstable liquid bridge that subsequently thins and breaks (Figure 6). The thinning rate and dynamics are recorded by video and analysed to measure the rate at which the liquid bridge thins. Importantly, it can be easy and relatively inexpensive to setup.

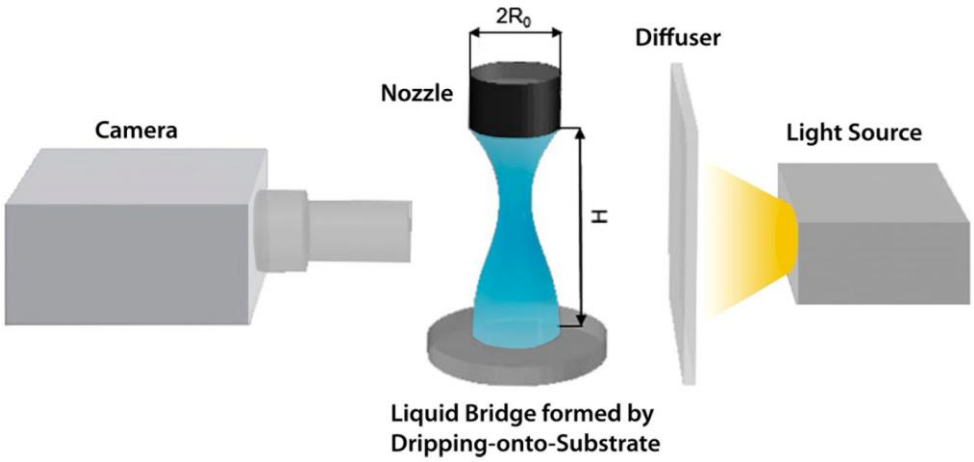

Figure 6. Cartoon schematic of the dripping-onto-substrate setup. Reprinted with permission from J. Dinic, Y. Zhang, L. N. Jimenez and V. Sharma, ACS Macro Lett., 2015, 4, 804–808. Copyright© 2015 American Chemical Society.

In this first work, they demonstrated the effectiveness of DoS for studying dilute poly(ethylene oxide) (PEO) solutions that undergo very fast thinning processes (Figure 7). The fluid is dispensed at a very low flow rate (such that it has negligible effect on the thinning

process) and each fluid is measured at least 5 times. For pure water, the thinning process results in the formation of a cone shaped fluid, which is characteristic for inviscid fluids (Figure 7a). The dilute PEO solutions in water form slender filaments during the thinning process (Figure 7b to 7d) and they often observe the well-known 'beads-on-a-string' phenomena.[45] These are common phenomena for dilute polymer solutions.[20] The thinning of the PEO solutions exhibits two distinct regimes, a power law regime which is then followed by an exponential decay. The initial neck-thinning is dominated by capillary and inertial stresses and is described using an inertia-capillary (IC) scaling equation. The exponential decay regime, termed the elastocapillary (EC) regime, has been described by an equation by Entov and Hinch (equation 2).

$$\frac{R}{R_0} = \left(\frac{G_E R_0}{2\sigma}\right)^{\frac{1}{3}} exp\left(-\frac{t}{3\lambda_E}\right) \quad (2)$$

where G_E is the elastic modulus, λ_E the extensional relaxation time, R_0 radius of the dispensing needle, R filament radius and σ the surface tension. The data is typically fitted to an exponential decay to obtain the extensional relaxation time. The fitting is generally performed when a slender filament (height is 10 x the width) has formed. Here, elastic and capillary forces dominate the filament thinning where stretching and orientation of the polymer oppose the neck thinning. The results show an increase in extensional relaxation time with increasing PEO concentration.

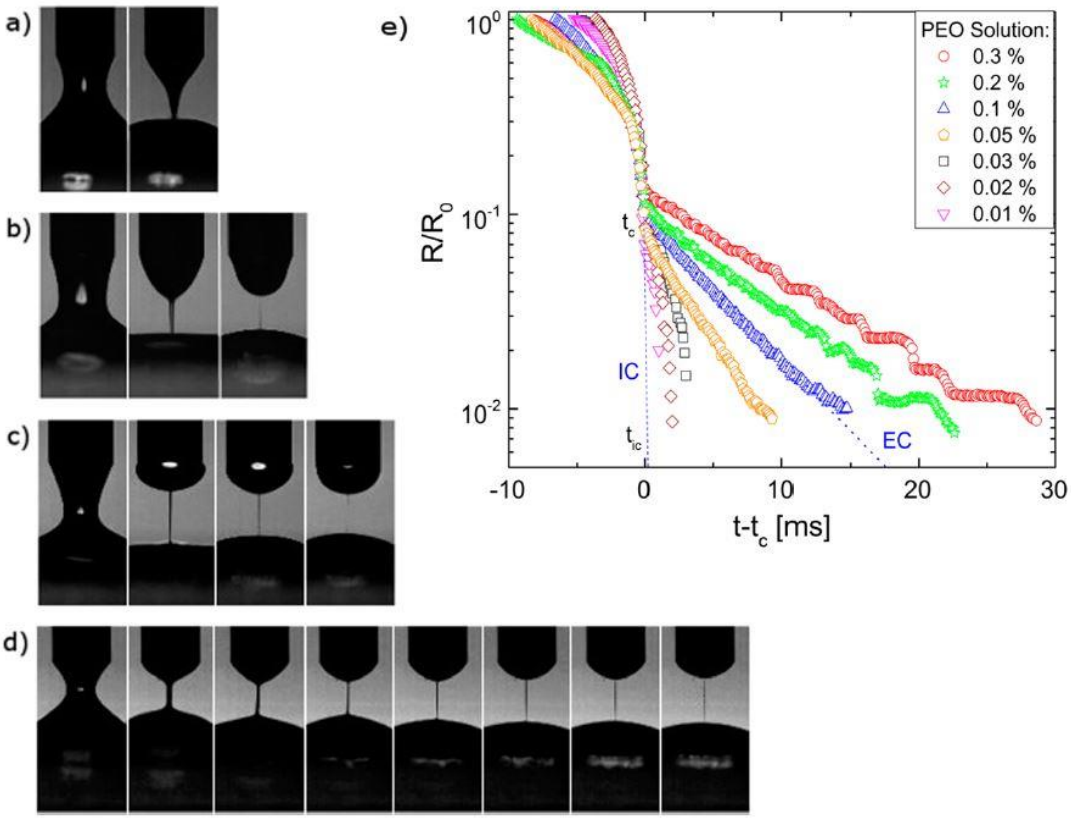

Figure 7. Image sequences from DoS study of PEO at (a) 0.00 wt% (pure water); (b) 0.02 wt%; (c) 0.1 wt%; (d) 0.2 wt%. (e) DoS data of for different PEO solutions with time normalised to the start of the EC regime and filament radius normalised to R/R_0. Reprinted with permission from J. Dinic, Y. Zhang, L. N. Jimenez and V. Sharma, ACS Macro Lett., 2015, 4, 804–808. Copyright© 2015 American Chemical Society.

In later work, the same group presented the applicability of the technique to a wide range of complex fluids.[46] For low viscosity fluids that thin and break very quickly, the technique requires specialist high-framerate cameras that are typically expensive. For polyacrylamide (PAM) solutions that break over the time frame of hundreds of ms or more, the technique becomes very accessible, where a 60 fps digital camera can be used (Figure 8).

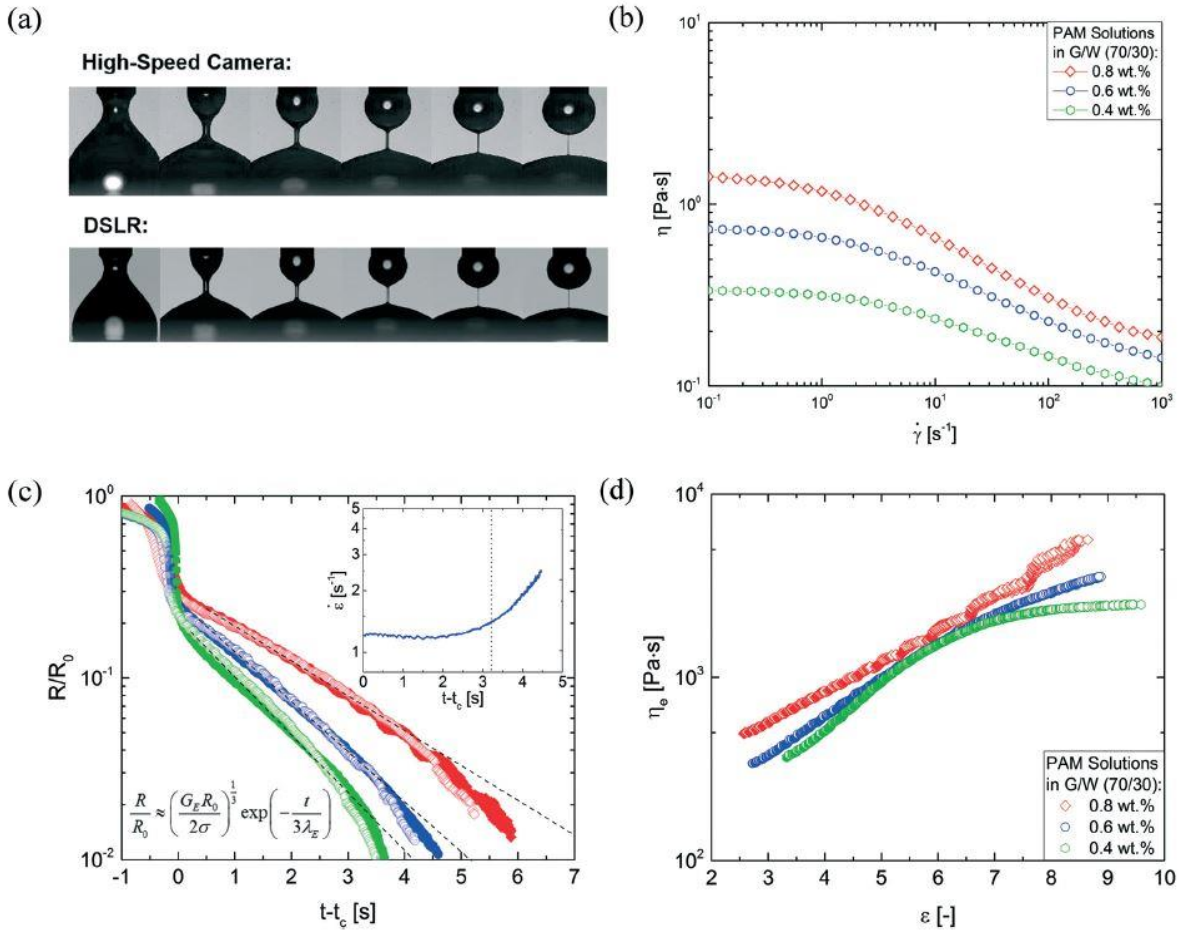

Figure 8. (a) Images from a video of DoS experiments taken with both a high-speed camera and a digital (DSLR) camera; (b) shear viscosity data for polyacrylamide (PAM) solutions (in glycerol:water 70:30); (c) DoS data showing time (t) normalised to the start of the elastocapillary regime (t_c) against filament normalised radius for the PAM solutions. Dashed lines show the region that can be fitted to the inset equation. The inset shows extensional rate variation over time; (d) Extensional viscosity as a function of the Hencky strain. Reproduced from J. Dinic, L. N. Jimenez and V. Sharma, Lab Chip, 2017, 17, 460–473, with permission from the Royal Society of Chemistry, Copyright© 2017.

1.3.1 Worm-like micelles

Worm-like micelles (WLMs) are widely utilised and researched materials that arise from the self-assembly of surfactants.[47–49] The rheological response of WLMs have many similarities to those of polymer solutions but there are also crucial differences. Both polymers and WLMs access stress relief mechanisms through reptation by Brownian motion.[50] WLMs can also access stress relief mechanisms by breaking entanglement points either by micelles breaking apart[51] or through 'ghost-like' crossing where the micelles effectively pull through one another.[52]

The use of DoS to study WLM solutions is relatively limited but there are some important studies. Researchers utilised both CaBER and DoS as methods to detect and compare the worm-like micelle microstructures of two different systems, octyl trimethylammonium bromide/sodium oleate (OTAB/NaOA) and cetylpyridinium chloride/sodium salicylate (CPCl/NaSal).[19] OTAB/NaOA transitions from linear to short linear micelles (L-L) whereas CPCl/NaSal transitions from linear to branched micelles beyond the zero shear viscosity peak. The results show that branched micelles exhibit longer filament lifetimes compared with linear micelles. Of particular interest is the effectiveness of applying DoS to WLM solutions because the pre-gel solutions studied in this thesis act in an analogous way to WLMs. The researchers perform this successfully (Figure 9) where they fitted the data to exponential decay equations to obtain the extensional relaxation times. They were particularly interested in comparing the two techniques due to the possibility of flow-induced micellar breakage due to the step-strain imposed at the start of a CaBER measurement. Interestingly, the results support their hypothesis where the Trouton ratios, filament lifetimes and extensional relaxation times obtained from CaBER are all lower than those obtained from DoS. Both techniques show the same trends with surfactant/salt concentration. The length of the filament breaking process for these surfactant systems is relatively long (Figure 9c and 9d), where the longest is over a minute. For the data analysis time zero (0 s) is set to when the contact line is pinned and no longer moving (i.e., the substrate is fully wetted; Figure 9a and 9b) and for many of the samples the exponential fitting is started at time zero instead of the formation of a slender filament. The DoS results show that there is a complex relationship between the extensional relaxation time and surfactant concentration or salt concentration. In the paper,[19] the authors explored the complex relationship between the micelle morphology (linear or branched) and this relaxation time. This work is important and highlights the applicability of the technique to worm-like micelle systems.

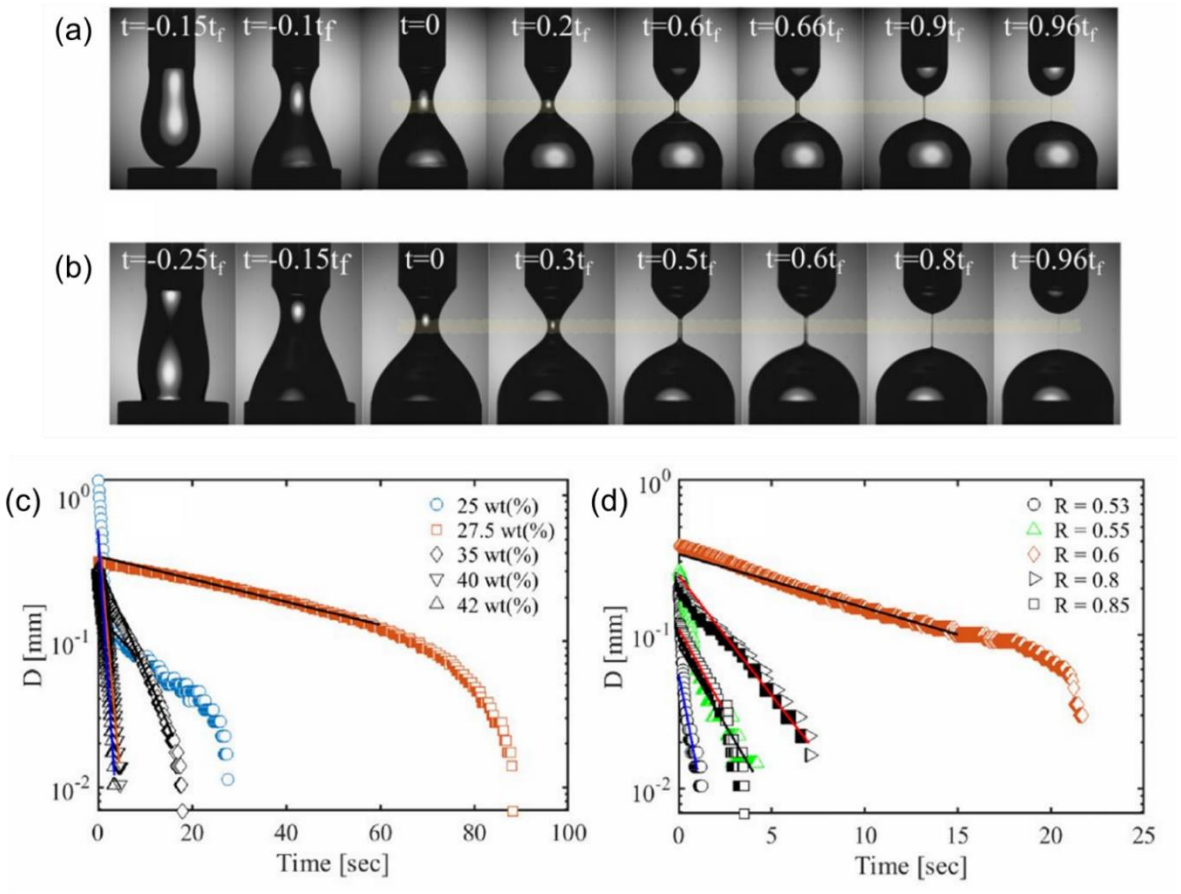

Figure 9. Frames from dripping-onto-substrate experiments on worm-like micelle solutions (a) OTAB/NaOA and (b) CPCl/NaSal. DoS data with exponential decay fits (solid lines) for (c) OTAB/NaOA at a range of OTAB concentrations and (d) CPCl/NaSal at a range of salt to surfactant ratios (R). Reprinted with permission from R. Omidvar, S. Wu and H. Mohammadigoushki, J. Rheol., 2019, 63, 33–44, Copyright 2019, The Society of Rheology.

2 Results and discussion

2.1 Perylene bisimide gel noodles

In Chapter 3, the importance of high viscosity worm-like micelle solutions for the formation of gel noodles was demonstrated. The formation of perylene bisimides (PBI) gel noodles was sought because if both un-aligned and aligned noodles could be formed, it would make a potentially interesting study into the effect of nanostructure alignment on activity. As such, PBIs that self-assemble into worm-like micelles and forms high viscosity solutions were sought. PBI-L and PBI-V have previously been shown to form viscous and shear-thinning worm-like micelle solutions.[53–55] 10 mg/mL PBI-L and PBI-V solutions were prepared at pH 6 and the shear viscosity measured (Figure 10). pH 6 was chosen because the increased degree of protonation of the carboxylic acid should lead to a greater degree of self-assembly, as had previously been seen for these systems.[55] The results show that at this concentration and pH 6, PBI-L and PBI-V form viscous shear-thinning solutions and PBI-L is more viscous at all shear rates studied. Neither PBI-L nor PBI-V were as viscous as the 10 mg/mL 1ThNapFF solution studied in Chapter 3 and neither solution effectively formed gel noodles. In a recent publication, a novel PBI functionalised with L-isoleucine (inset, Figure 10) was shown to form more viscous solutions than both PBI-V and PBI-L.[55] As such, a 10 mg/mL PBI-I solution at pH 6 was prepared and studied. This was shown to be significantly more viscous (almost an order of magnitude) than either PBI-L or PBI-V (Figure 10) and possessed a similar viscosity to 1ThNapFF at the same concentration. The exact reasons for these differences between PBIs with very similar chemical structures cannot be easily obtained. It is likely that the subtle change in molecular results in changes to the self-assembly and molecular packing that leads to longer worm-like micelles with more entanglement.

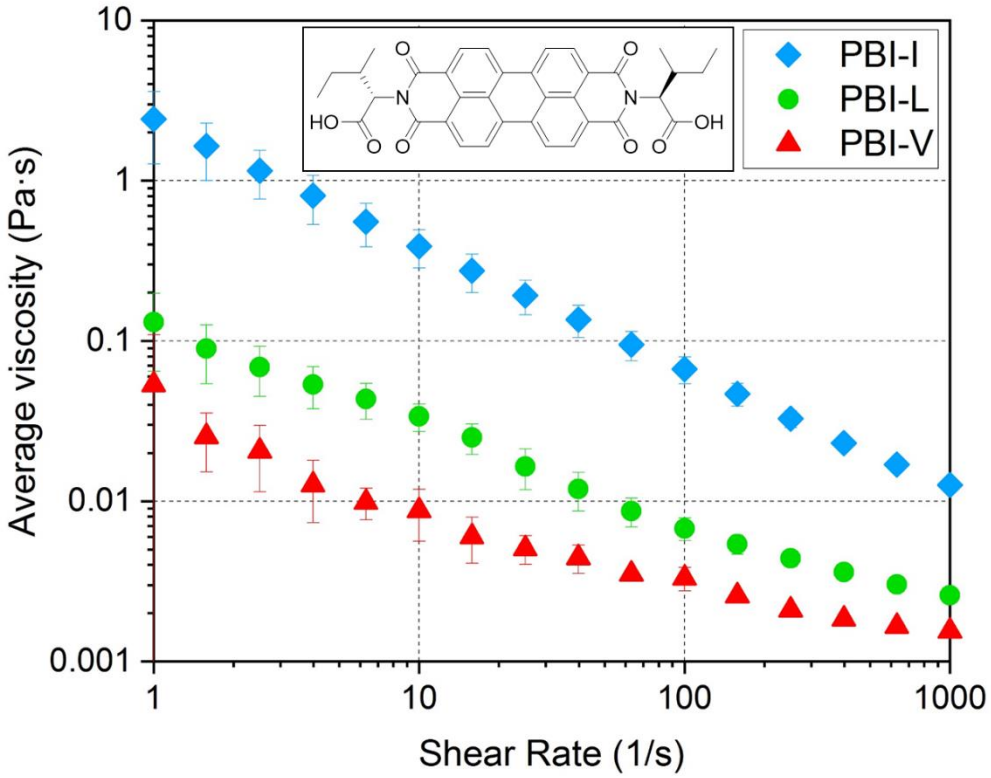

Figure 10. Shear viscosity data for PBI-V, PBI-L and PBI-I at 10 mg/mL, pH 6. The chemical structure of PBI-I is inset at the top of the graph.

2.1.1 PBI gel noodles

Based on the high viscosity of the PBI-I solution, gel noodle formation was attempted using this solution. The highly viscous 10 mg/mL and pH 6 PBI-I solutions proved highly effective at forming gel noodles in a 50 mM $CaCl_2$ trigger medium when using a 2-20 µL pipette (Figure 11a). Crucially, the PBI-I gel noodles exhibited birefringence in CPOM images (Figure 11b). The edges of the gel filament particularly showed consistent alignment. In a similar manner to the 1ThNapFF gel noodles formed from pipettes in Chapter 3 however, the birefringence was not uniform and consistent throughout the structures. Nevertheless, the result did suggest some degree of alignment within the gel structures formed and these materials were studied as part of a photocatalytic system.

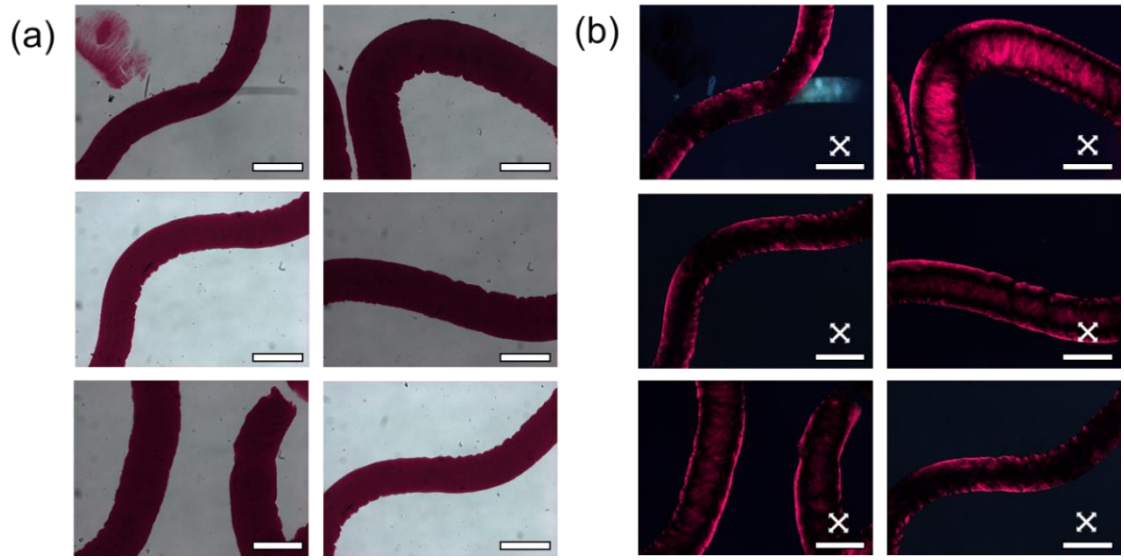

Figure 11. Optical microscope images of 10 mg/mL, pH 6 PBI-I gel noodles formed using a 2-20 µL pipette in 50 mM $CaCl_2$. (a) Normal light and (b) cross polarised light. Scale bars represent 0.5 mm and white crosses indicate polariser direction.

The photocatalysis experiments were performed in a collaborator's lab (Professor Alex Cowan, working with Benjamin Greeves) at the University of Liverpool. These labs did not have access to CPOM equipment, but it was important that any samples to be used for photocatalysis were also imaged using CPOM to show whether they were aligned or not. As such, a custom-built and portable CPOM imaging setup was created. This was an inexpensive setup comprised of a white light emitting diode (LED) backlight, a light diffuser, two plastic polarisers and a smartphone with a macro lens attached (see experimental for more details). The macro lens enables high quality images of small and close-up object to be collected on almost any smartphone. Without the lens, the images were out of focus. The custom-built setup was shown to be effective for both microscope-like imaging as well as showing birefringence in PBI gel noodles (Figure 12). While effective, less control over both ambient light and LED light intensity was found as compared with an instrument manufactured microscope.

The collaborators did not have access to a syringe pump setup, as such, work focussed on using pipettes initially. Additionally, photocatalysis experiments would require small and discrete volumes of material that is harder to achieve with a syringe pump as compared with a 20 µL pipette.

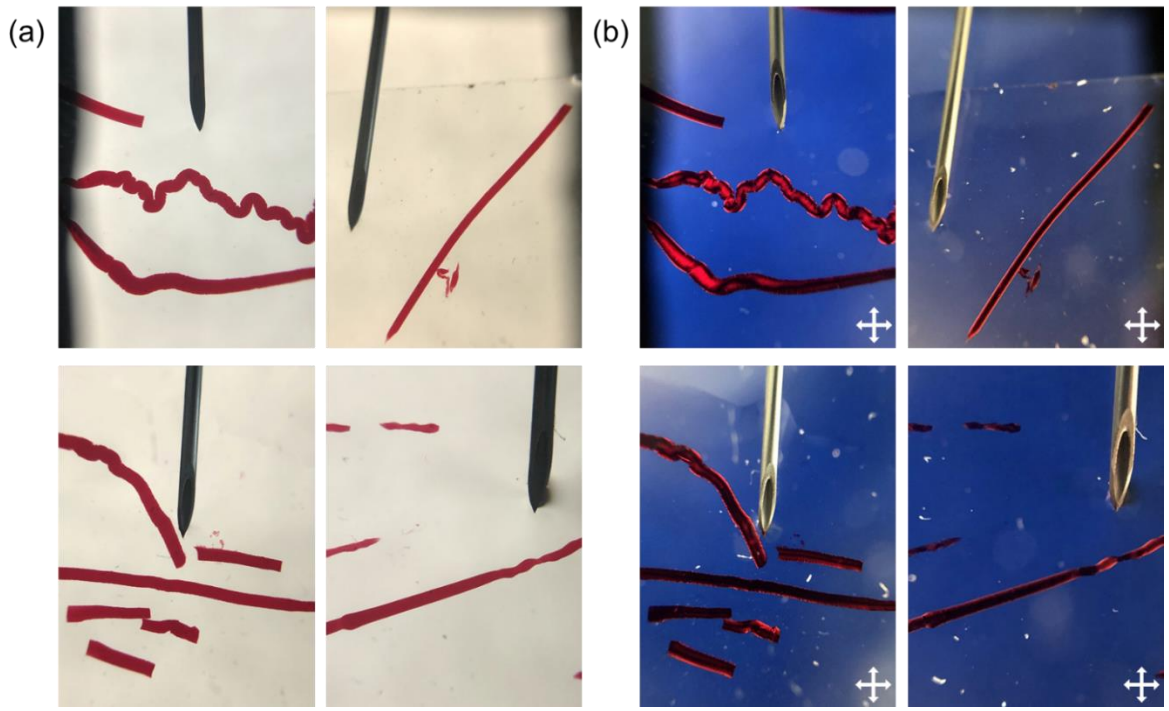

Figure 12. Photographs of PBI-I (10 mg/mL, pH 6) gel noodles taken on the custom built, portable optical microscopy setup with an iPhone 8. (a) Normal light images and (b) cross polarised light images. A 21G (0.82 mm outer diameter) needle was placed in each picture. White crosses indicate polariser direction.

To perform photocatalysis experiments comparing aligned and un-aligned gel noodles, a method for forming un-aligned (non-birefringent) PBI-I gel noodles was required. It was found that due to the highly viscous nature of the PBI-I WLM solutions, it could be pipetted into deionised pH neutral water, forming a ‘solution noodle’ that retained its shape for several minutes before dissolving (Figure 13). The hypothesis for the formation of aligned and birefringent regions within the PBI-I gel noodles is that the shear forces experienced during dispensing from the pipette induce alignment which is then locked-in by gelation from the Ca^{2+}. It was hypothesised that upon injection into water, the aligned WLM regions within the solution noodle would lose alignment with time in the absence of any gelation trigger.

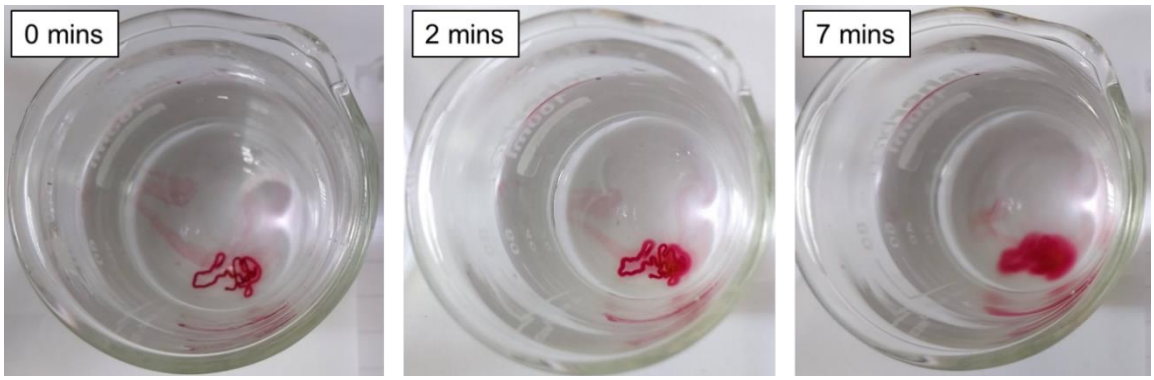

Figure 13. Change in a PBI-I solution noodle in de-ionised water with time.

To test this hypothesis, gel noodles were prepared either by pipetting the solution directly into 50 mM $CaCl_2$ or into deionised water. The process could be video recorded using the custom-built CPOM setup. When directly pipetting into calcium, birefringent gel noodles form immediately (Figure 14a). In contrast, when pipetting into deionised water, noodle-like structures are formed but do not exhibit significant birefringence (Figure 14b). After this, by gently adding concentrated $CaCl_2$ solution into the vial, unaligned gel noodles are formed.

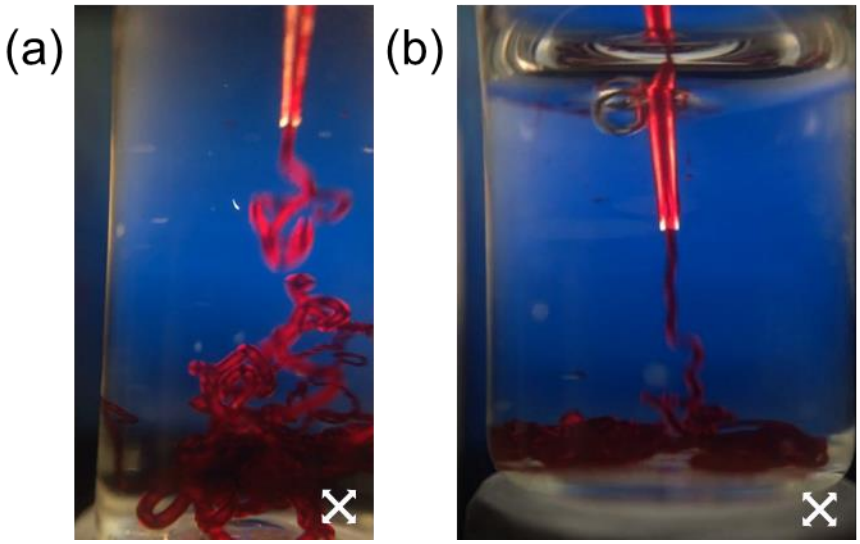

Figure 14. Images collected on the custom-built CPOM setup of a solution noodle with time. (a) Normal light and (b) cross polarised light. White crosses indicate polariser direction.

2.1.2 PBI-I photocatalysis

With the ability to form PBI gel noodles that showed different degrees of birefringence (and thus inferred alignment), hydrogen evolution photocatalysis experiments were performed. An initial study (performed by Benjamin Greeves) in which analogous experiments to those in Chapter 2 were performed showed that PBI-I could be used for photocatalytic hydrogen evolution reaction, with comparable levels of H_2 detected as compared to the active PBIs in Chapter 2.

For the gel noodle photocatalysis experiments, platinum (Pt) nanoparticles and methanol (MeOH) were required to be incorporated into the gel noodle system. Pt nanoparticles were incorporated by adding 1 mol% into the PBI-I solution during preparation. Full details of how the photocatalysis solutions were prepared can be found in the experimental. The procedure was designed such that the final concentration of all components (MeOH, $CaCl_2$ etc) was the same for both the aligned and unaligned samples. The noodles prepared in these solvents did not show significant differences to those seen in the absence of either Pt nanoparticles or MeOH. The noodles were video recorded with the portable CPOM setup as they were prepared. This allowed for a qualitative measure of the alignment (Figure 15). As can be seen, there is a significant difference in the observed birefringence.

In an ideal experiment, a single, well-defined gel noodle that was either aligned or un-alinged would be studied. The first attempts at photocatalysis with 1 gel noodle in a 4 mL glass vial resulted in no H_2 being seen. An increase to studying 7 noodles was attempted but again no H_2 was produced. Then, the use of quartz cuvettes instead of glass vials was investigated but was also unsuccessful. Quartz was selected because it absorbs less light however the headspace was considerably larger, increasing the challenge for detecting H_2. When scaling up, 7 noodles were chosen initially because it meant that the gels did not crowd each other significantly. Too much crowding would result in blocking light from accessing gels on the opposite side of the vial relative to the light source. This would complicate the analysing the results. The overall volume from 7 noodles (70 µL) is a very small amount of PBI considering that a volume of 5 mL (albeit 5 mg/mL PBI) samples was studied in Chapter 2.

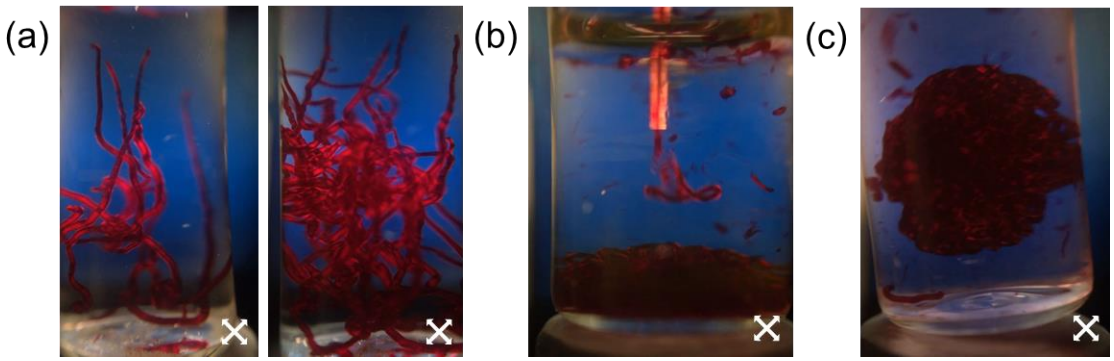

Figure 15. Frames from videos of the formation of PBI-I gel noodles for photocatalysis experiments (a) aligned gel noodles formed from direct injection into pH 5, 50 mM $CaCl_2$ with 20 v/v% MeOH; (b) ‘unaligned’ gel noodles formed by injection into pH 5 water with 40 v/v% MeOG and (c) the clump of gel noodle formed upon the addition of an equal volume of 100 mM $CaCl_2$ (final concentration 50 mM $CaCl_2$).

As such, to increase the amount of PBI in the vial, experiments were performed in glass vials with 25 gel noodles (250 µL of PBI solution) and 4 repeat measurements performed

(data analysis performed by Benjamin Greeves). With this setup, H_2 was generated in small amounts (~0.3 µmol/g/h) for the aligned gel noodles (Figure 16). The un-aligned gel noodles no H_2 was seen. At face value, these results appear to support the hypothesis that alignment improves photocatalytic activity. While the aligned and un-aligned samples show differences in birefringence, the morphology of the gels within the vials is different. The aligned samples are spaced out whereas the un-aligned samples form a 'clump' of gel (Figure 15c). The two systems a likely to possess differences in light absorption and diffusion of the reagants/products within the gel. As such, the difference in alignment, morphology and photocatalysis cannot be easily deconvoluted.

The alignment achieved with the pipette, while good, did not appear to be as well aligned as spun filaments achieved with 1ThNapFF. As part of photocatalysis studies a third sample with greater alignment was desirable. The spinning procedure from Chapter 3 was attempted with PBI-I solutions to see if highly aligned and uniform gel filaments could be formed. The results (Figure 16a) show that long gel noodles do not form, rather short (< 1 cm) lengths of gel noodle are made. The gel noodles do not show a significant increase in birefringence in CPOM imaging (Figure 16b) as compared with those prepared using the pipette.

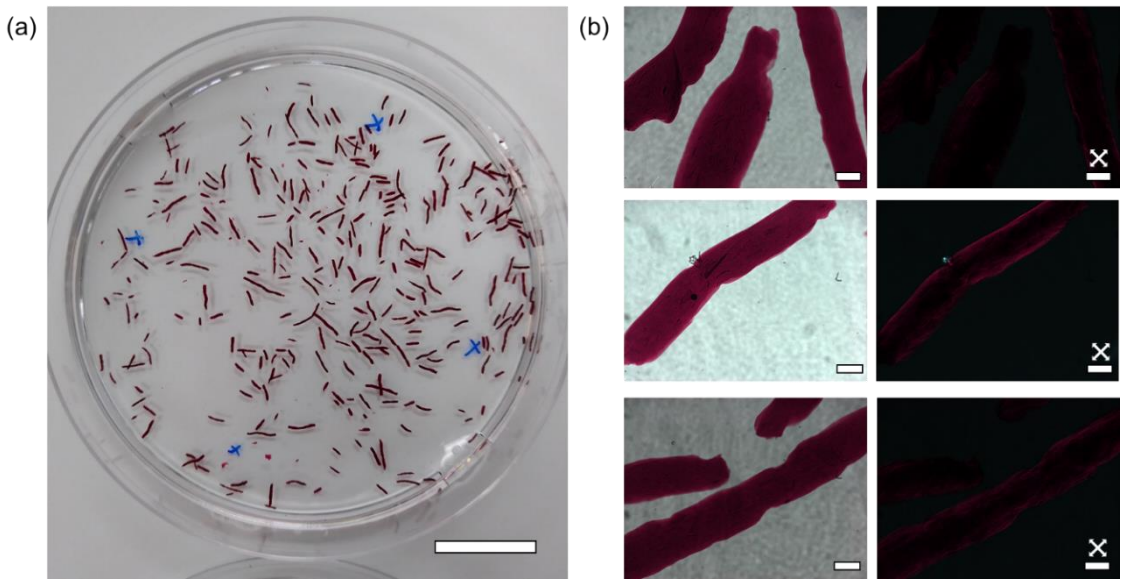

Figure 16. Attempted spinning of PBI-I with (a) a photograph of the spun noodles immediately after spinning. Scale bar represents 2 cm; (b) optical microscope images of the spun noodles with normal light (left-hand side) and cross polarised light (right-hand side). Scale bars represent 0.25 mm, white cross represents polariser direction.

By measuring the size distribution of gel noodles formed (Figure 17), a relatively large size range from 0.30 – 0.65 mm is seen, with less than half the noodles formed having a diameter less than the inner needle diameter. In Chapter 3, the 1ThNapFF spun gel noodles possess size distributions centred on 0.1 mm and showed significant birefringence. A key difference between PBI-I and 1ThNapFF is the stretching and thinning (extensional deformation) that occurs during the spinning process. The PBI-I does not do this, and it was hypothesised that this is a result of differences in the extensional viscosity. To understand the fundamental material properties behind this, a literature setup for measuring extensional relaxation time was developed.

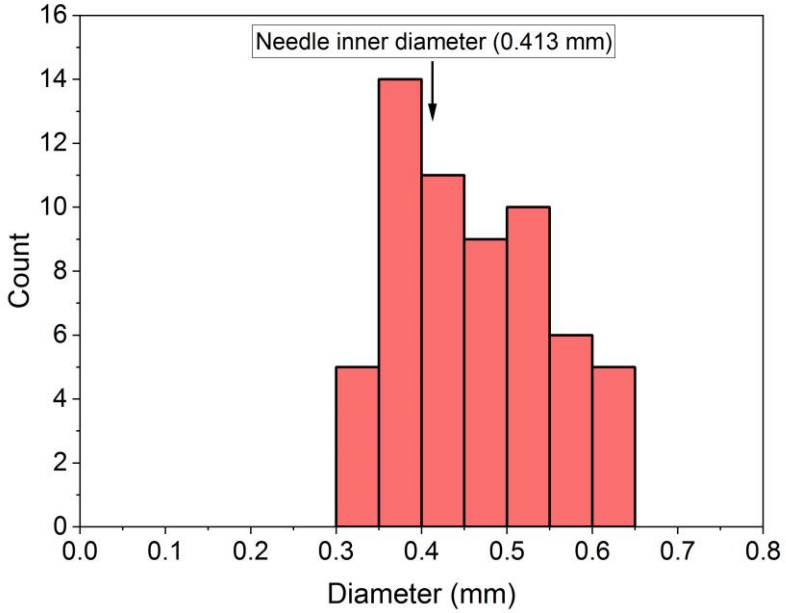

Figure 17. Histogram of PBI-I spun noodle diameter.

2.2 Dripping-onto-substrate

2.2.1 DoS: setup

Based on a literature setup by Dinic *et al.*, a dripping-onto-substrate setup was built.[44] The strength of the technique is that it requires relatively cheap and common place materials to build. Initial work to create a DoS setup for this research project used an Infinity 2 lab camera that captured high quality videos of the droplet being dispensed from the needle (Figure 18a and 18b). Other digital cameras are not designed for close-up imaging, resulting in blurry images that were unsuitable. The setup comprised of the lab camera, a 19G flat-headed needle connected *via* tubing to a syringe pump, 80 gsm paper backlit using a white LED and a glass microscope slide as the substrate. One challenge was that some fluids (but not all) would wet and climb up the needle (Figure 18a). This problem was solved by the application of a layer of vacuum grease to the sides of the needle tip, creating a

hydrophobic surface that prevented wetting (Figure 18a). Following this, the wetting of the substrate posed a problem. The large flat surface of the microscope slide meant that the fluid droplet spread out over a large area (Figure 18b). This wetting is reported to both undesirably influence the liquid bridge thinning process and also would sometimes cause the droplet to move off centre, meaning that the thinning process was not occurring solely in the vertical plane. To solve this, most reports utilise a circular substrate that pins the contact line.[19] Here a 4 mm cylindrical glass substrate was used and worked effectively as compared with the microscope slide (Figure 18b).

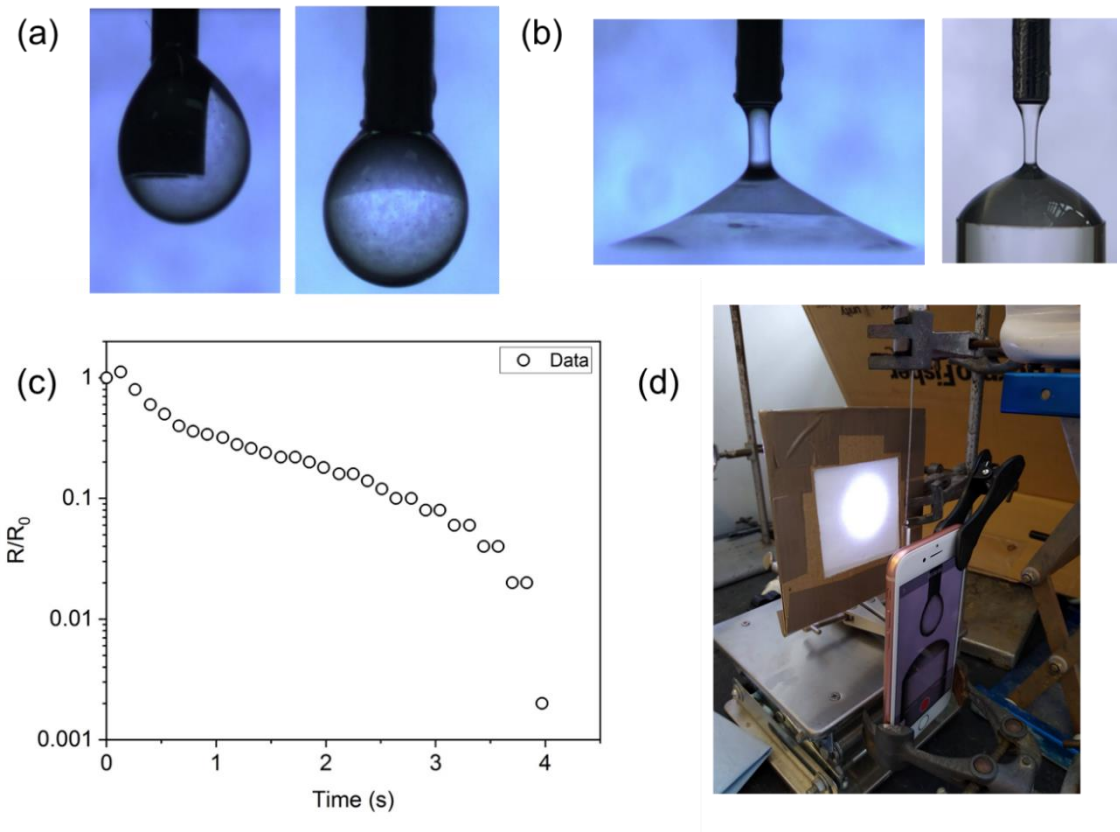

Figure 18. (a) Needle wetting before (left) and after (right) grease; (b) substrate wetting and spreading on a microscope slide (left) and 4 mm glass rod (right); (c) DoS data of 10 mg/mL 1ThNapFF collected on a 7 fps camera (d) image of optimised setup using an iPhone 8 with a macro lens.

To start with a 1ThNapFF solution was studied using the technique (Figure 18c). While the thinning process could be tracked using the technique, very few data points were obtained. The lab camera collected videos at maximum frame rate of 7 fps, resulting in an insufficient number of data points. Additionally, the filament diameter was measured by hand in ImageJ,[56] which was a time consuming process. Ideally, a camera that had a capture rate of 60 fps or greater was required.[46]

To solve this problem in an inexpensive manner, a clip-on macro lens (which facilitates good quality images of close-up and small objects) and a second-hand smartphone (iPhone 8) were used (Figure 19d). The macro lens provided high quality images and the iPhone could collect videos at 30, 60 or 240 fps. At 240 fps, a 5 second thinning process would yield 1200 individual data points (frames). It would be unfeasible to analyse this data manually in ImageJ especially if performing repeats and multiple fluids. As such, a MatLab script that utilises the CannyEdge detection system was written by a collaborator, Dr Henry Ng (School of Engineering, University of Liverpool, UK), which automates the data analysis. With 240 fps, very fast thinning processes (<0.1 s) can be measured (Figure 19a) and large numbers of data points for longer thinning processes can be collected (Figure 19b). In particular, good backlighting creates contrast between the filament and the background, which is essential for the MatLab analysis which detects the filament edge by changes in pixel light intensity.

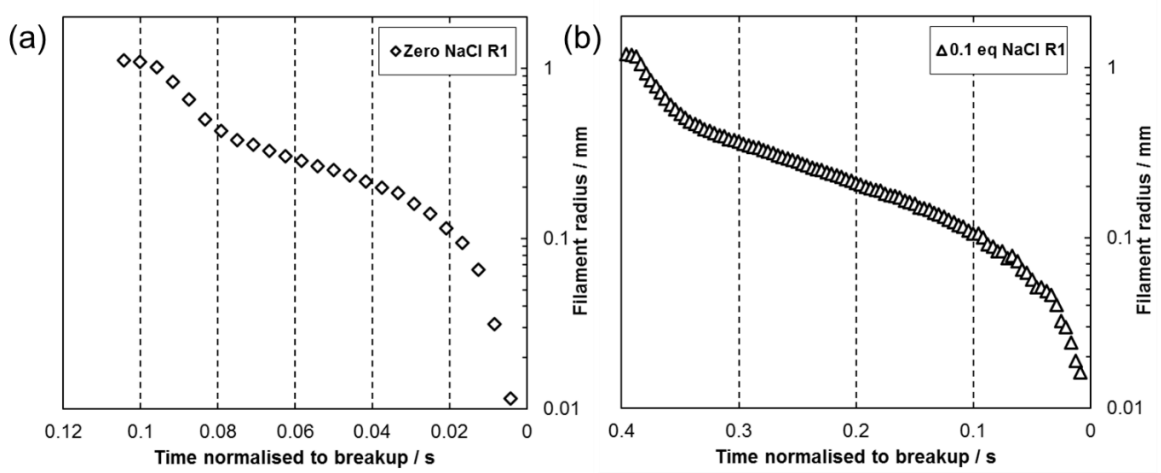

Figure 19. DoS data for 10 mg/mL 2NapFF at pH 10.5 with either (a) 0 eq. NaCl or (b) 0.1 eq NaCl.

2.2.2 DoS: Validation

After ironing out experimental issues with the DoS setup, the next step was to perform validation experiments on known fluids to test if accurate results could be obtained using it.

2.2.2.1 Glycerol

Measurements on a well-documented fluid, glycerol (literature viscosity is η = 0.934 Pa.s at 25°C[57]) were performed because for Newtonian fluids, the fluid viscosity can be calculated from a linear fit to the DoS measurements using equation 3.[21] If the DoS setup could provide a value close to both the measured and literature viscosity, then it is working correctly.

$$(3) \quad R(t) = 0.0709 \left(\frac{\sigma}{\eta}\right)(t_c - t)$$

where σ is surface tension and η is the viscosity.

Firstly, the shear viscosity of the glycerol was measured on a rotational rheometer using a cone and plate geometry and was shown to be approximately 1 Pa.s (Figure 20a). This is close to, but slightly higher than the literature value which may be due to instrument errors. Then DoS was performed on the fluid (Figure 20b) and showed very good reproducibility across 4 repeats. The overall thinning time was around 200 ms and the thinning was close to being linear at the latter stages. A literature value for the surface tension of 0.0625 N/m[57] was used and a linear fit was then used at latter stages of the thinning process (Figure 20c) to obtain a viscosity value. The y-intercept was set to zero as the final data point is often inaccurate due to poor resolution of the thin liquid bridge on this camera. The results across the four measurements (Figure 20d) show good agreement with the literature value.

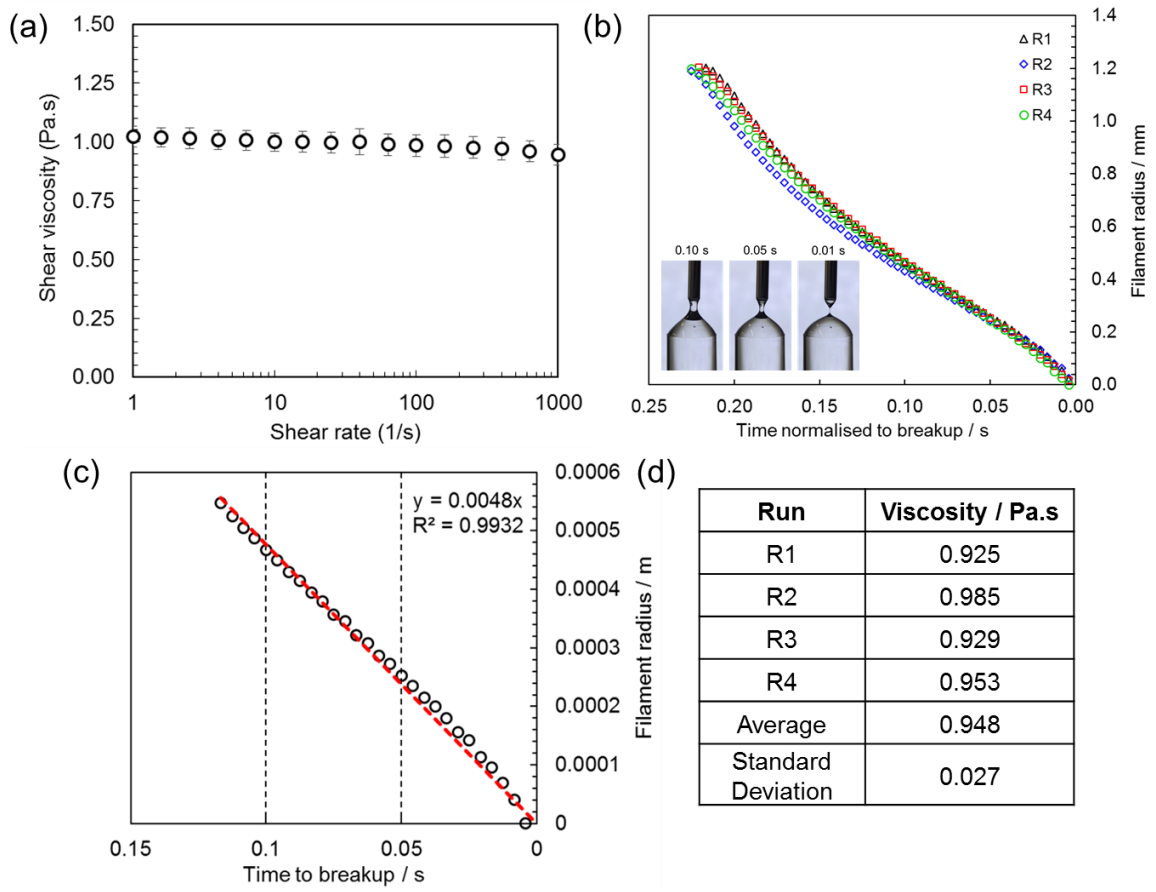

Run	Viscosity / Pa.s
R1	0.925
R2	0.985
R3	0.929
R4	0.953
Average	0.948
Standard Deviation	0.027

Figure 20. (a) Shear viscosity data for glycerol collected on a cone and plate geometry at 25°C; (b) Time vs filament radius data from DoS measurements on glycerol with inset pictures of the liquid bridge and corresponding time stamps; (c) linear fit example for one of the measurements and (d) a table summarising the results.

2.2.2.2 Polyacrylamide

For further validation experiments, polyacrylamide (Figure 21a) solutions were studied and compared with the results from the DoS literature.[46] A 0.4 wt% PAM in glycerol:water (70:30) were measured and showed elastic fluid behaviour with the formation of a slender filament that subsequently thinned and broke. According to the literature fluids exhibiting this behaviour can be fitted to the Entov and Hinch equation (Figure 21c to 21g) to obtain an extensional relaxation time. Across 5 measurements an average extensional relaxation time, λ_E, of 0.54 ± 0.04 s was obtained. This is comparable with the value of 0.50 s reported by Dinic *et al.*[46]

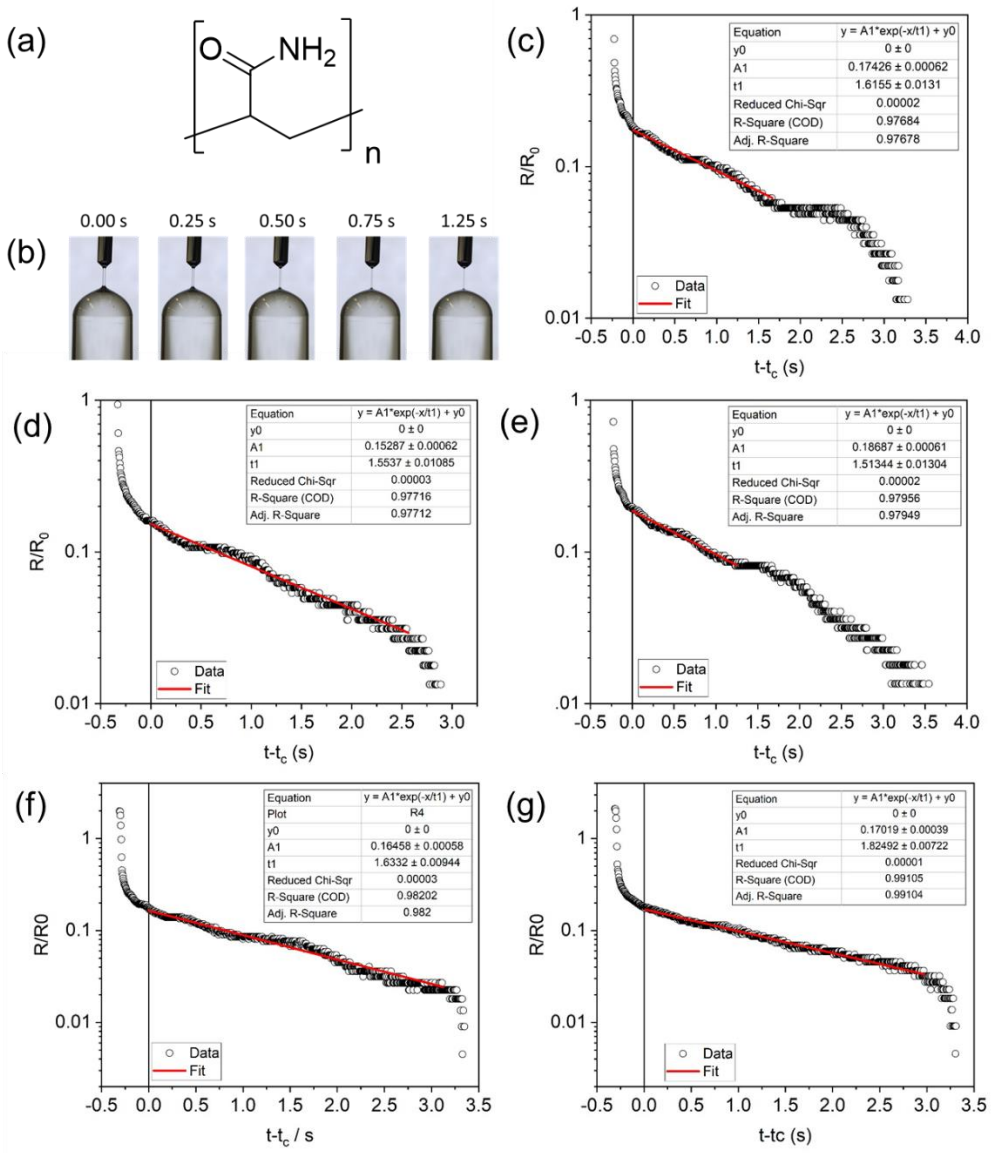

Figure 21. (a) Chemical structure of polyacrylamide (PAM); (b) representative images taken from the data shown in (c); DoS data (open black circles) for 0.4 wt% PAM in glycerol:water (70:30) fitted to the Entov and Hinch equation (red lines) with boxes showing the fitting parameters for runs (c) 1; (d) 2; (e) 3; (f) 4 and (g) 5. Time is normalised to the start of the elastocapillary regime.

Some oscillations are visible in the data which may be due to vibrations in the setup. A similar feature has been seen for polymer solutions in the previously published work.[44] The validation experiments worked very well and showed that the setup was suitable to use but they did highlight some the limitations of the setup. At early stages on the semi-log plot, the thinning process can be tracked well but at the latter stages ($R/R_0 < 0.1$) the data shows well-defined steps. This is due to limitations in image resolution obtained using the smartphone. At these stages, the process is tracked pixel-by-pixel thinning, resulting in these steps. The data in these stages could still be fitted effectively.

2.2.3 DoS: 1ThNapFF

After demonstrating that the technique can be used to measure known systems accurately the next step was to study a pre-gel solution. 1ThNapFF was the focus of Chapter 3, where it was used to successfully spin aligned gel filaments. It was hypothesised that this was due to high extensional viscosity. It was also hypothesised that the worm-like micelle solution should exhibit similar behaviours to that seen for PAM in DoS.

A 10 mg/mL 1ThNapFF solution at pH 11.3 was studied using the DoS setup. As expected, the thinning process behaved as expected for an elastic fluid such as PAM, with the formation of a slender filament that thins and breaks (Figure 22f). Across 5 repeat measurements, the results show that the total time of the thinning process varied between 2 and 7 seconds (Figure 22a to 22e). Interestingly, the PAM solutions formed a thin filament rapidly after droplet contact whereas the 1ThNapFF solutions did not form a thin filament until the latter stages of the process. For 1ThNapFF the process that occurs prior to the slender filament formation appears to follow an exponential decay (seen as a straight line on the semi-log plot). At early stages, a range of factors including surface tension and viscosity dominate the thinning dynamics. It is probable that the 1ThNapFF WLM solutions are different to the PAM solutions in this regard. For example, it should also be noted that the PAM data is collected in a solvent with a high proportion of glycerol.

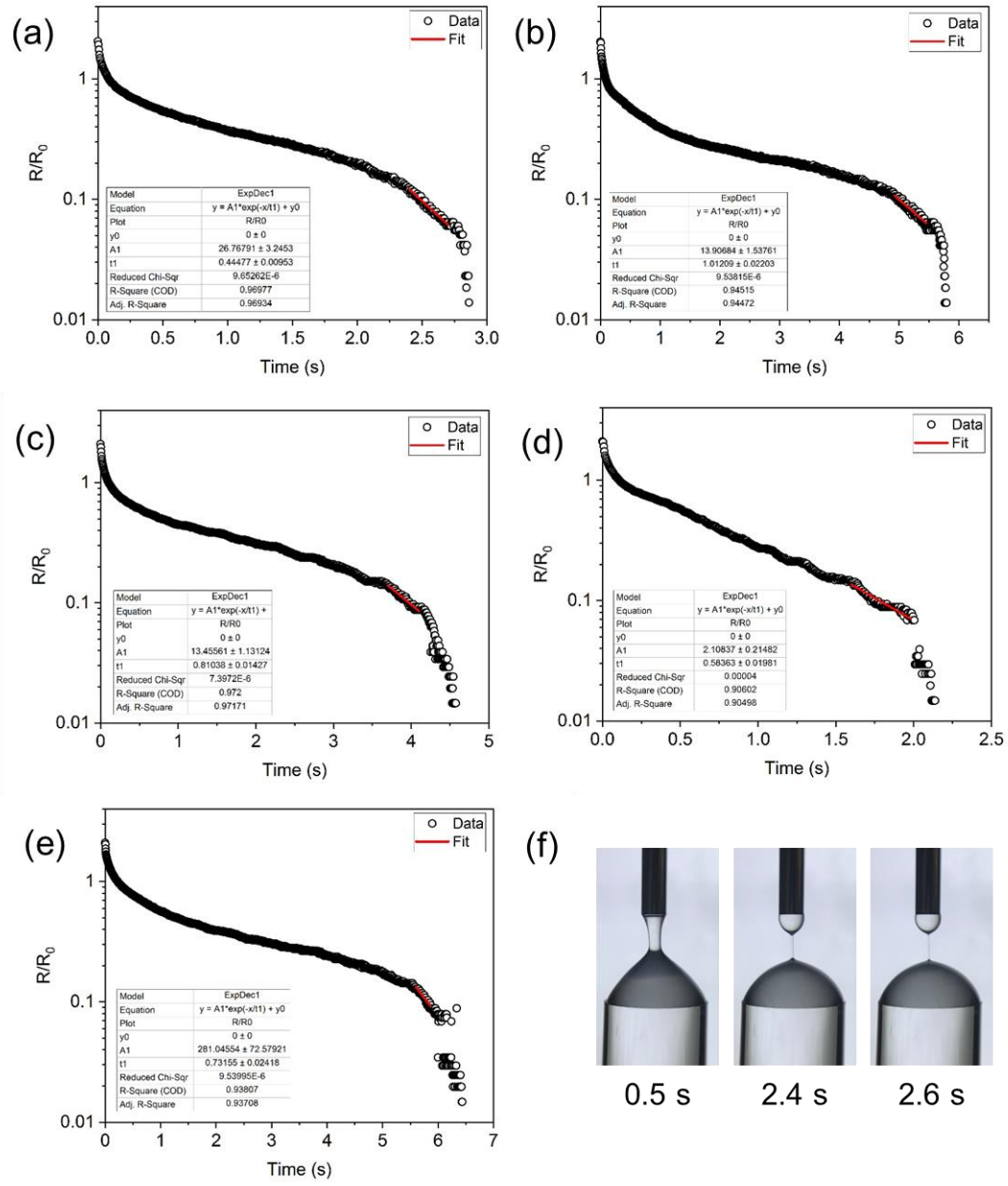

Figure 22. Dripping-onto-substrate data (black hollow circles) for 10 mg/mL 1ThNapFF at pH 11.3 with corresponding exponential decay fits (red lines) with 5 repeats (a) R1; (b) R2; (c) R3; (d) R4; (e) R5 and (f) example frames from R1 with corresponding time stamps, focussing particularly on the slender filament region that is fitted.

To obtain an extensional relaxation time, care was taken to identify the frame at which a slender filament with an aspect ratio of 10 formed. In all cases, when matched to the time on the plots, this frame corresponds with a transition to a short straight-line region in the semi-log plot that could be fitted. All 5 data sets were fitted to obtain extensional relaxation times (Table 1).

Table 1. Extensional relaxation time for 1ThNapFF solutions. Error for the individual runs is obtained from the fitting software and the error for the average value is the standard deviation across the 5 repeats.

Run	λ_E / ms	Error / ms
1	148	3 (fit)
2	337	7 (fit)
3	270	5 (fit)
4	195	7 (fit)
5	243	5 (fit)
Average	239	72 (standard deviation)

A λ_E value of 239 ± 72 ms was obtained for the 1ThNapFF solution. Compared with the PAM data, the λ_E values obtained for 1ThNapFF show a relatively large variation between runs. This coupled with differences in the total time taken for the thinning process shows that there is a degree of irreproducibility studying this WLM solution. Also, for 1ThNapFF the exponential decay region ends at much larger R/R_0 values (approx. 0.08 for 1ThNapFF) as compared to the PAM data. The PAM data can be fitted down to an R/R_0 of 0.03, meaning that the PAM solutions follow the elasto-capillary regime form longer, to form thinner filaments. This may highlight a key difference between polymer solutions and WLM solutions. As thinner filaments form the WLMs may start to break apart. In summary, these results demonstrate that these WLM solutions can be successfully studied using the DoS technique.

2.2.4 DoS: PBI-I

The DoS setup was used to study the 10 mg/mL PBI-I solutions used for noodle formation and photocatalysis experiments. The PBI-I solution behaved differently to any polymer or worm-like micelle solution studied previously (Figure 23). The PBI-I did not exhibit the behaviour of elastic fluids which form thin filaments towards the latter stages of the break-up process. Instead, the fluid forms a curved neck that thins up until it breaks. The shape of the liquid bridge bears some similarity to that of glycerol however when studied on a linear-linear scale plot, no straight line region (at least at this frame rate) is seen at the latter stages of breakup. Dinic *et al* studied a range of complex fluids with DoS and showed materials that bear some similarities to the thinning seen here.[46] After breaking, the droplet on the substrate does not form a near-spherical/curved shape as is typically expected for a droplet on a surface attempting to minimise surface tension. Instead, the droplet shows a point at the top (Figure 23), suggesting a different complex fluid behaviour is occurring.

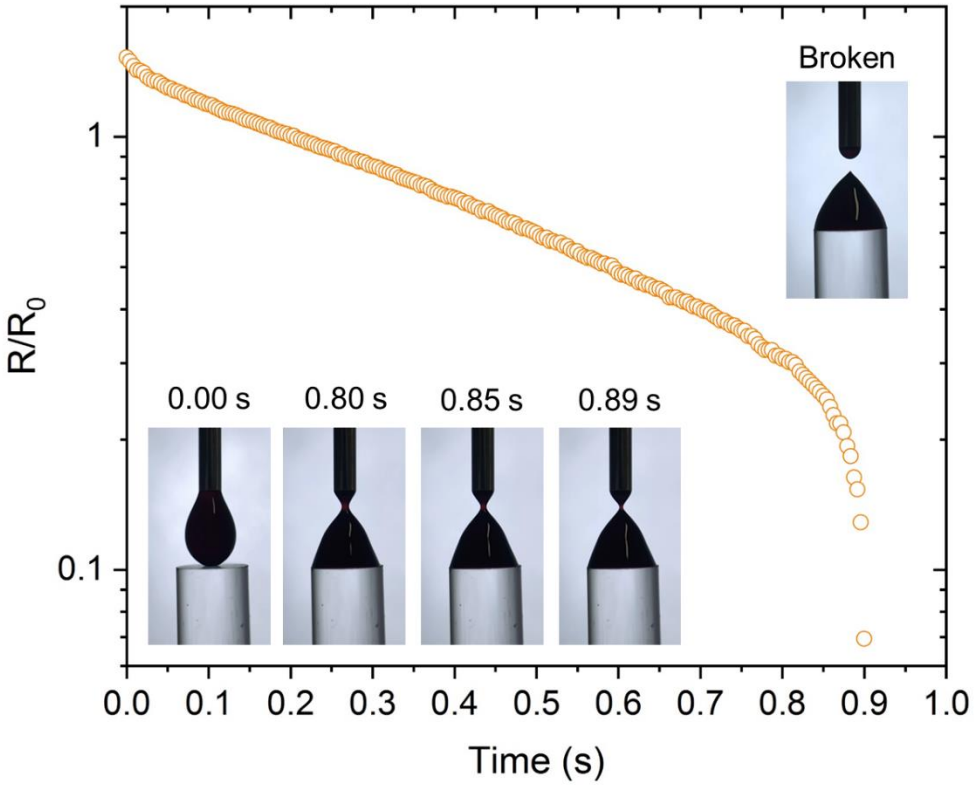

Figure 23. 10 mg/mL PBI-I pH 6 DoS data for one measurement (Run 5) with corresponding time-stamped frames for the thinning process.

Similar thinning processes are seen across the 5 repeat measurements (Figure 24) with some difference in the overall time for breakage to occur. Without performing any further analysis, it is clear that the PBI-I does not behave as is seen for PAM or 1ThNapFF and does not possess the ability to form slender filaments with a large extensional relaxation time. This is likely a significant variable as to why spun PBI noodles cannot be formed. Instead, the structures break-up into numerous short noodle regions, which are not significantly stretched (as inferred from the size distribution relative to the needle) during the spinning.

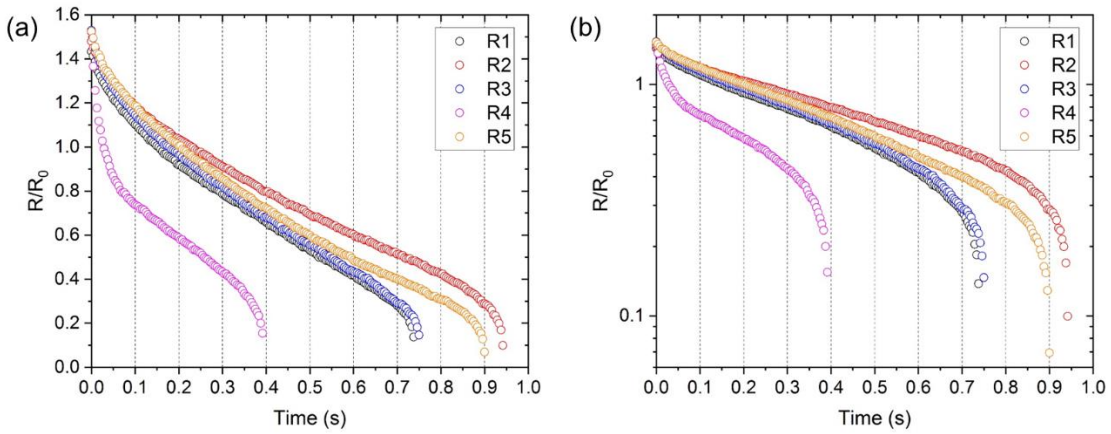

Figure 24. DoS data for 10 mg/mL PBI-I, showing the 5 repeats on both (a) linear-linear and (b) linear-logarithmic scales.

2.2.5 DoS: 2NapFF

To the test the capabilities of the setup when comparing LMWG pre-gel solutions, the influence of both counter ion and a heat/cool cycle was investigated on the functionalised dipeptide 2NapFF (Figure 25a). These parameters have previously been shown to control viscosity, self-assembled structure as well as extensional relaxation time (measured using a CaBER) at a lower concentration.[1,2] 25 mg/mL 2NapFF solutions at pH 10.5 (prepared by Lisa Thomson) were made using either NaOH (Na) or tetrabutylammonium hydroxide (TBA). The solutions were either studied as prepared or subjected to a heat/cool (H/C) procedure, where the solution was heated to 60°C for 1 hour and then cooled back to room temperature and left for 3 hours. This resulted in four different solutions which were studied using DoS and are termed Na, TBA, Na H/C or TBA H/C.

For the Na and TBA H/C samples, the thinning process was similar to that seen for 1ThNapFF and extensional relaxation times could be measured (Figure 25b). The TBA and Na H/C samples did not break over measurable time scales. The TBA sample formed a filament 20 minutes after contacting the substrate, which dried out instead of breaking (Figure 25c). The Na H/C sample exhibited solid-like/gel-like behaviour as seen by the irregularly shaped droplet (Figure 25d). After contacting the substrate, the droplet did spread out but “jammed” and no further thinning was seen. Strictly speaking, just because a sample does not break in the DoS setup, it does not mean that the extensional relaxation time is very high. At early stages a range of variables are at play and in neither sample did a slender filament (aspect ratio = 10) form. Qualitatively however, both showed “stringy” behaviour when being handled and it is expected that they would both possess long extensional relaxation times.

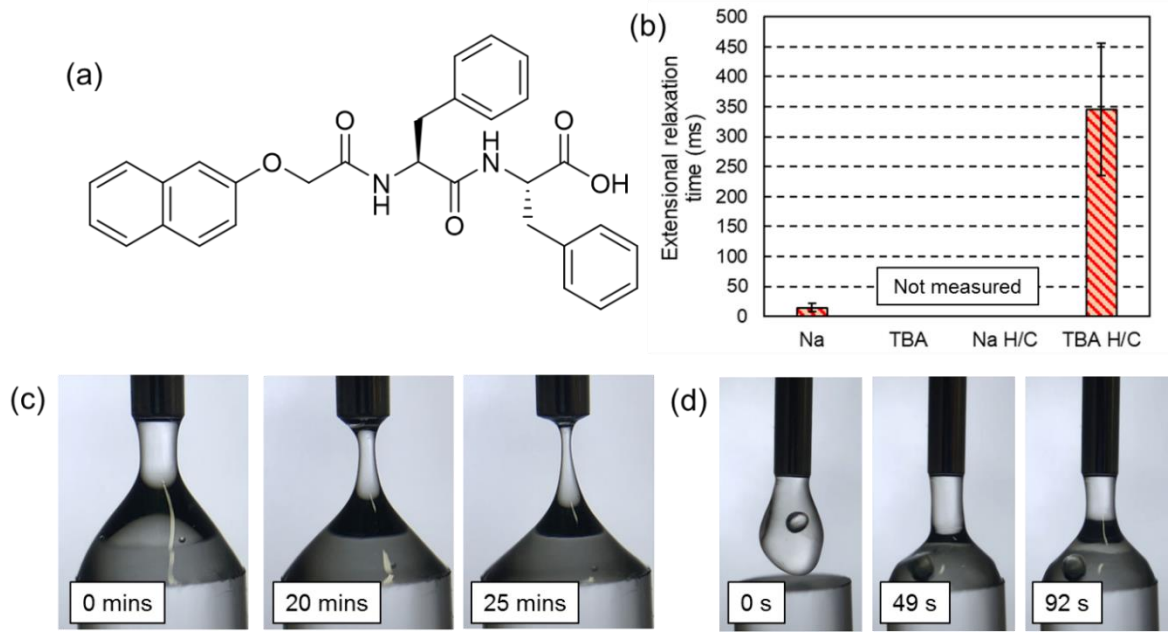

Figure 25. (a) Chemical structure of 2NapFF; (b) summary of the extensional relaxation time results; (c) frames taken from the thinning of the TBA sample pre-heating and (d) frames taken from the thinning of the Na sample post-heat/cool.

Across 5 repeat measurements for the Na sample, the liquid bridge broke around 800 ms after the droplet contacted the substrate (Figure 26). The fluid exhibited elastic fluid behaviour (Figure 26b), where a slender filament formed at later times. As was seen for 1ThNapFF, the early thinning process appears to follow an exponential decay, but it was not fitted because a slender filament is yet to form. ImageJ was used to determine when a slender filament (aspect ratio = 10) had formed and this frame used as the start of the exponential decay. The fitting was successful and shows an extensional relaxation time of 14.6 ± 6.5 ms but highlights the limitations of this specific setup. At these late stages, the limitation in both camera resolution as well as frame rate are clearly apparent, and the fitting is performed using a relatively small number of data points. Nevertheless, the result highlights a significant difference as compared to the TBA H/C sample.

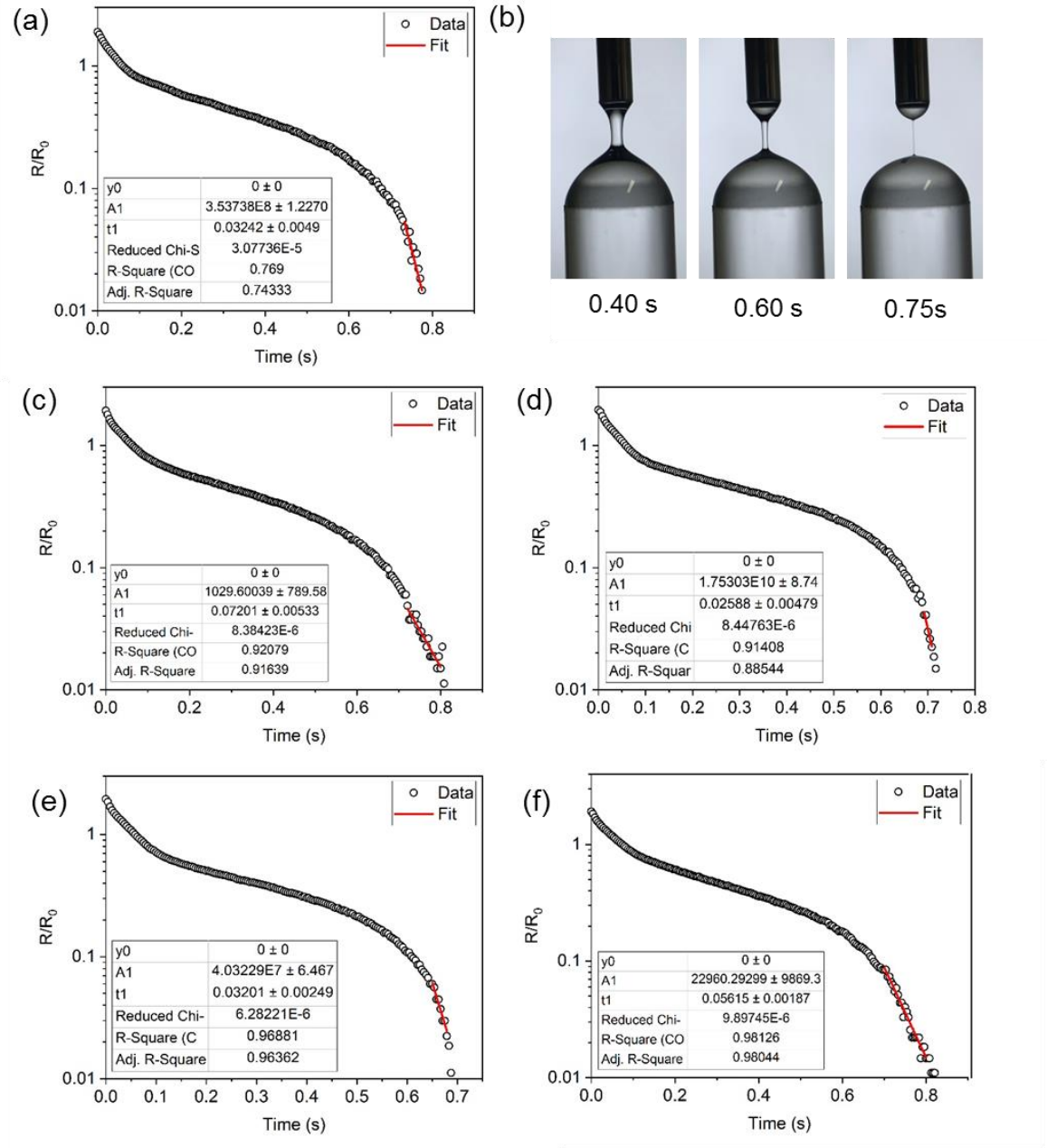

Figure 26. 25 mg/mL 2NapFF with NaOH DoS data with corresponding fits to the slender filament region with 5 repeats. (a) R1; (b); frames from R1 with corresponding time stamps; (c) R2; (d) R3; (e) R4; (f) R5.

For TBA H/C, the liquid bridge thinning followed slightly different behaviour. The early stage of the thinning process which has been seen for these worm-like micelle solutions took multiple minutes and could not be captured and analysed due to limitations in device storage space and processing power (minutes of footage would provide tens of thousands of individual frames!).

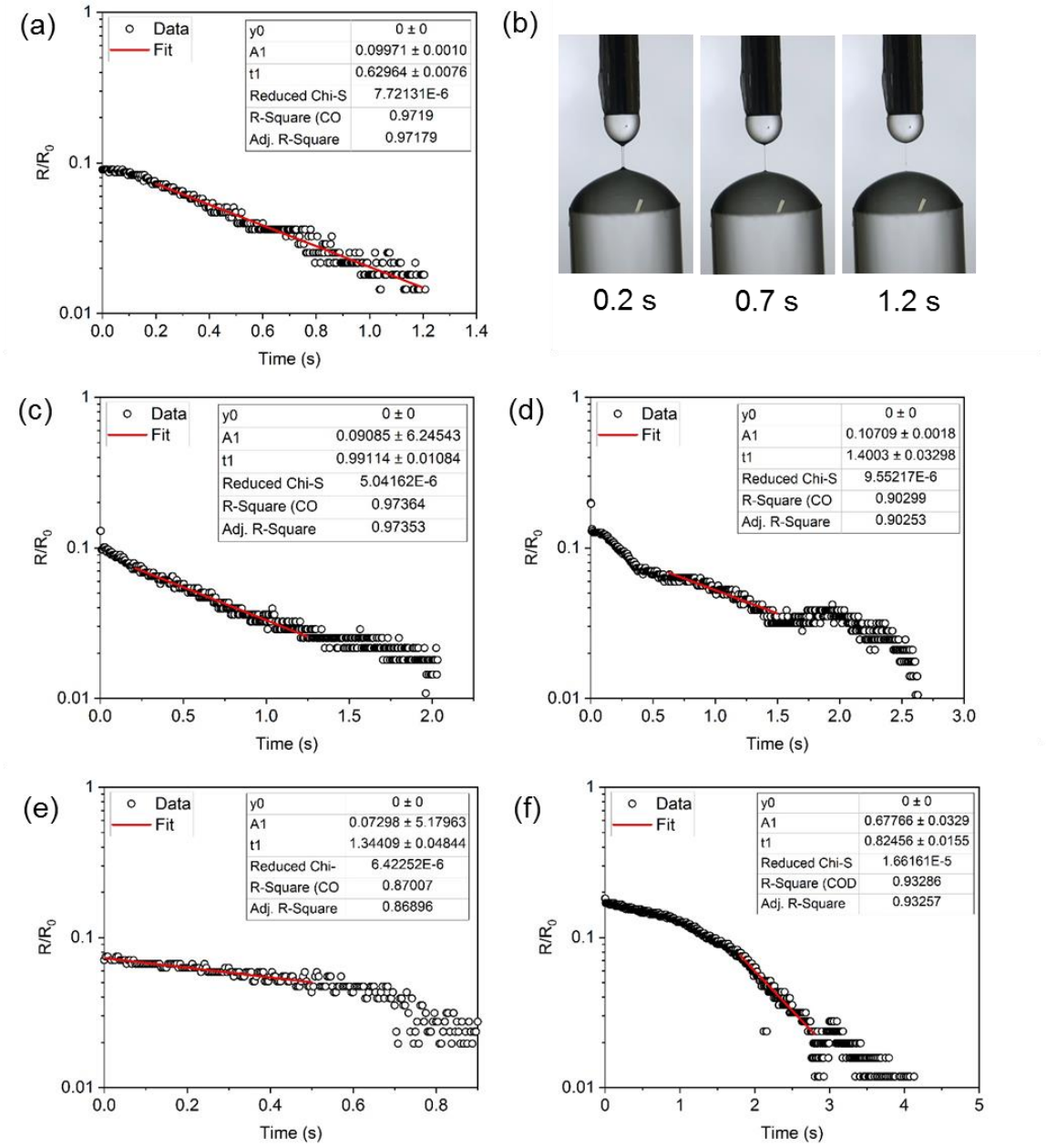

Figure 27. 25 mg/mL 2NapFF with TBAOH post-heat/cool DoS data with corresponding fits to the slender filament region with 5 repeats. (a) R1; (b); frames from R1 with corresponding time stamps; (c) R2; (d) R3; (e) R4; (f) R5.

To solve this issue, the camera recording was started shortly before the formation of the slender filament. As such, unlike the previously shown data, time zero does not correspond to the point of droplet contact on the substrate. The TBA H/C sample also exhibited elastic fluid behaviour where a slender filament formed and thinned and broke (Figure 27b). The overall time for this process to occur varied (Figure 27). In part this was because the camera start time was not well defined but there was also a variation in the calculated extensional relaxation times. The point at which a slender filament formed was used to determine the

start of the exponential decay fitting, resulting in an extensional relaxation time of 346 ± 110 ms.

The results show that a combination of changing the counter-ion and using a heat/cool cycle for one functionalised dipeptide results in a range of different behaviours under extensional flow. Interestingly, as compared to the 1ThNapFF solution, the Na and TBA H/C 2NapFF solutions form thinner filaments. This is shown by the 2NapFF samples reaching much smaller R/R_0 values before breaking. For 1ThNapFF, the slender filaments reach R/R_0 values of approximately 0.06 – 0.08 before deviating from the exponential decay region and rapidly breaking. For both Na and TBA H/C 2NapFF samples, R/R_0 values in the region of 0.02 – 0.03 are reached. The underlying reasons for this difference are not simple to determine. It may be, for example, that the 2NapFF micelle are more resilient to the forces in extensional flow whereas the 1ThNapFF micelles start to break apart under the same conditions.

3 Conclusions

Building upon the work in Chapter 3, an L-isoleucine functionalised PBI (reported in the literature) at a specific pH and concentration formed highly viscous and shear-thinning solutions that could be used to readily prepare both aligned and unaligned gel noodles. The result highlights the sensitivity of the self-assembly process, where a very subtle molecular change (L-leucine to L-isoleucine) results in vastly different fluid properties meaning that previously inaccessible materials (the gel noodles) can be prepared. Attempts at photocatalysis experiments with the gel noodles were challenging and did not provide convincing results. Creating a third set of conditions (well-aligned spun gel noodles) with PBI-I was desired but proved unsuccessful. The PBI-I and 1ThNapFF solutions both form wormlike micelle solutions with similar shear viscosities. It was hypothesised that differences in the extensional viscosity of the fluids was to reason that PBI-I could not be spun. A literature technique called ‘dripping-onto-substrate’ (DoS) was built and validated using known fluids. DoS was used to compare the behaviour of both 1ThNapFF and PBI-I solutions under extensional deformations. 1ThNapFF behaved as an elastic fluid (similar to other wormlike micelle solutions and polmyer solutions) with an average extensional relaxation time of 239 ms. PBI-I did not behave as an elastic fluid and rapidly broke under extensional deformation. The difference in the ability of the two fluids to be spun is attributed to the extensional viscosity. This serves as a good demonstration that shear viscosity and extensional viscosity are not the same but the latter is studied less frequently. Additionally, it highlights the complexity of these systems and the requirement to use numerous techniques to fully characterise and understand them.

4 Experimental

4.1 Sample preparation

4.1.1 Solution preparation

– 6 MDa PAM (from Merck Life Science UK) was used directly from the supplier with no further purification. This specific polymer size was used because it matched that which Dinic *et al* used.[46] PAM solutions were prepared by first preparing a glycerol:water mixture in a ratio of 70:30 by volume. The PAM was weighed into a 40 mL Falcon tube and then the glycerol:water mixture added. The dissolve the polymer, the Falcon tube was placed on a roller for 3 days until the polymer had dissolved.

Glycerol (from Merck Life Science UK) was used without further purification. The glycerol was used immediately after being opened and kept sealed. Glycerol is highly hygroscopic, which would influence the water content within the prepared samples.

1ThNapFF was synthesised by Professor Dave Adams according to a previously reported method.[58] 1ThNapFF solutions were prepared by weighing 1ThNapFF into a vial. The required volume of deionised H_2O was added followed by the required volume of a 0.5M NaCl aqueous solution. The absolute amounts of H_2O and NaCl solutions varied based on the number of NaCl equivalents were required for that sample. Following this, NaOH was added to deprotonate the 1ThNapFF. To avoid overshooting the pH and the subsequent addition of acid which would change the final NaCl concentration, an insufficient amount of NaOH (0.8 equivalents) were first added using a 2M NaOH aqueous solution. Then, the solutions were stirred overnight, and the pH adjusted up to 11.3 by the addition of 2M or 0.1M NaOH (the different concentrations were required depending on how large a pH change was required).

PBI-I was synthesised by Jacquelan Egan (University of Glasgow) according to a previously reported method.[55] PBI-V and PBI-L was synthesised following previously reported methods that were covered in Chapter 2 and 3.[53,59] 10 mg/mL PBI solutions were prepared by weighing 50 mg of material into a 14 mL glass vial and then the required volume of deionised water. For the photocatalysis experiments, 1 mol% Pt nanoparticle solution was added (0.81 mL). When Pt nanoparticle was added 0.81 mL less deionised water was added. Finally, 2 equivalents (relative to the PBI) of 1M NaOH was added. The total volume of both water and base added was 5 mL. A stirrer bar was added, and the solution stirred overnight. The next day, when the PBI was fully dissolved, the pH was checked. Then the pH was adjusted down to pH 6.00 – 6.10 using 2M and 0.1M HCl. As pH was lowered, the solution viscosity (especially for PBI-I) became noticeably greater.

2NapFF was synthesised by Lisa Thomson according to a previously reported method.[60] Solutions were prepared by Lisa Thomson. 3 mL 2NapFF solutions were prepared at a concentration of 25 mg/mL. The 2NapFF powder was weighed into a Sterilin vial and the predetermined volume of deionised water added. Then 1 molar equivalent of 0.1M hydroxide (either Na or TBA hydroxide) was added to make the final volume of 3 mL. The solutions were stirred overnight and then pH adjusted to pH 10.5 the next day. As is detailed in Section 3.6, the solutions are loaded into 10 mL syringes for the DoS measurement. After measuring the pre-heat/cool DoS data, the syringes containing the 2NapFF solutions were placed in an oven at 60°C for 1 hour. Then they were removed and allowed to cool for 3 hours before measuring them with DoS.

4.2 Photocatalysis experiments

4.2.1 Photocatalysis sample preparation

Either aligned or un-aligned gel noodles were prepared for photocatalysis.

The aligned noodles were prepared in 50 mM $CaCl_2$ with 20 v/v% MeOH present. The un-aligned noodles were prepared in deionised water to which an equivalent volume of 100 mM $CaCl_2$ with 40 v/v% MeOH was added to bring about a final concentration of 50 mM $CaCl_2$ and 20 v/v% MeOH. The $CaCl_2$/MeOH solutions were pH adjusted to pH 5 and purged with argon and kept in a sealed contained. The fluid was accessed using using a needle and a syringe through the septum of the container.

For the aligned noodles, 3.6 mL of 50 mM $CaCl_2$ with 20 v/v% MeOH was added to a 4 mL vial with a lid and septum. For the un-aligned noodles 1.8 mL of de-ionised water with 40 v/v% MeOH was added to the vial and then the PBI pipetted in to form noodles. The vial was left for 2 minutes to allow the gel noodles to de-align and then an equivalent volume of 100 mM $CaCl_2$ with 40 v/v% MeOH was carefully added (a needle and syringe was used and the needle tip lowered to the surface of the solution to reduce turbulence when adding the fluid) to form a final volume of 3.6 mL, so as to be comparable to the aligned noodles.

In order to pipette the PBI solution into the vials, the lids were temporarily removed (for a few minutes). Argon was used to purge the solutions and is denser than air, meaning the solutions were not re-purged afterwards.

PBI-I gel noodle were formed either by hand using a pipette or spun using a syringe pump and spin coated according to methods in Chapter 3 which are also reported in the literature.[61] The noodles were prepared by sequential 10 µL injections of the PBI solution.

4.2.2 Lamp setup

A 300 W Newport Xenon lamp (with no filters) was used to irradiate the samples resulting in an intensity of 100 mW/cm^2 at the samples. The distance from the lamp was adjusted such that the W/cm^2 was constant throughout the experiments.

4.2.3 Gas chromatography

Gas chromatography to detect H_2 and CO was performed using an Agilent Technologies 6890N. The GC utilised a pulsed discharge detector (D-3-I-HP, Valco Vici) and a 5 Å molecular sieve column (ValcoPLOT, 30 m long, 0.53 mm inner diameter) with N6 helium as the carrier gas (flow rate of 5 mL/min). A calibrant gas of 500 ppm H_2, 200 ppm CH_4 and 200 ppm CO (with CO_2 balance gas) was used to calibrate the instrument. Methane could not be detected using this setup.

4.3 Rotational rheometer measurements

Shear and oscillatory rheology measurements were performed on an Anton Paar Physica 101 rheometer. For the shear viscosity measurements, a 50 mm cone and plate geometry was used. The temperature was controlled and fixed at 25ºC for the measurement. The sample poured onto the plate to reduce pre-shear before the measurement. A shear rate range of 1 – 100 s^{-1} or 1 – 1000 s^{-1} was investigated. For each solution, 3 repeat measurements were performed and an average viscosity at each shear rate was calculated.

4.4 Optical microscopy

A Nikon Eclipse LV100 optical microscope with an Infinity 2 camera connected to a computer was used to image the gel filaments. The microscope was used in transmission mode, 5X magnification (LU Plan Fluor lense) and images taken under both normal and cross polarised light. An image of a 1 mm scale bar was collected to quantitatively measure length in ImageJ. For noodles, the diameter

4.5 Portable CPOM setup

A portable microscopy setup was designed to allow for CPOM measurements of gel noodles when working with collaborators in labs that did not have access to CPOM. This involved a white LED light source, 80 gsm paper as a light diffuser, two polarisers and a smartphone (iPhone 8) with a macro lens (Figure 28).

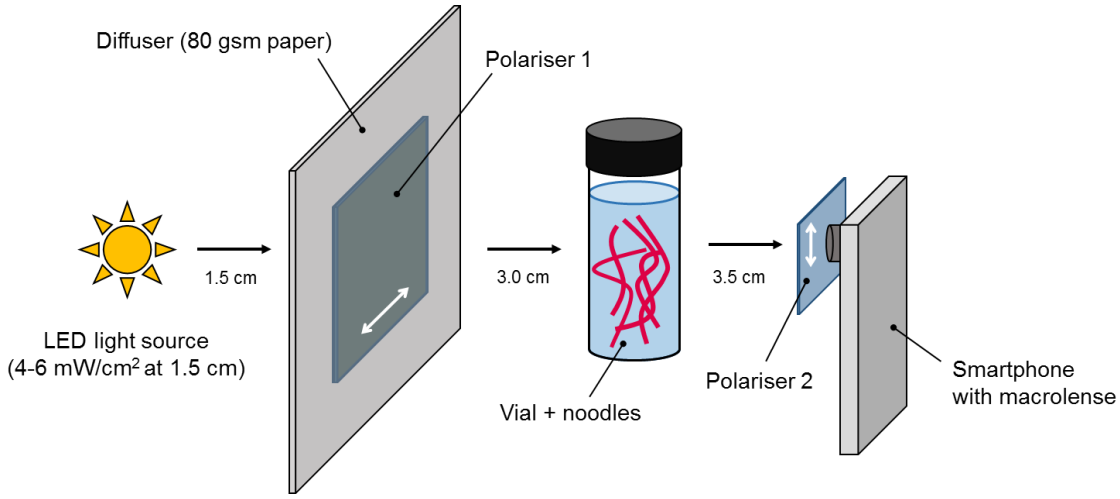

Figure 28. Cartoon schematic of the portable CPOM setup. White arrows on each polariser indicate the polariser orientation.

4.6 Dripping-onto-substrate

4.6.1 Setup

The DoS setup was created based on the publications by Dinic *et al*.[44,46] An iPhone 8 smart phone camera with a clip-on macro lens was used to record the thinning process. The clip-on maco lens enables good quality imaging on small, close-up objects. The zoom function on the iPhone camera was then used to get the DoS process in full frame. Depending on the speed of filament breakup either the standard (30 frames per second (fps)) or slo-mo (240 fps) video functions were used. A 4 mm diameter circular glass substrate that was sanded flat at the end was used to pin the contact line and reduce the effects of wetting. A 19-gauge flat-headed needle connected to a 10 mL syringe (BD Plastipak) was used to dispense the fluid. The fluid dispensing rate was set to 1 mL/hr and controlled by an Alaris CareFusion syringe pump. A fixed needle to substrate distance of 4 mm was used.

4.6.2 Measurement

To reduce the effects of pre-shear, the fluids were loaded into the syringe by first pulling the plunger out of the back of the syringe. The nozzle was briefly sealed with Blu-tac and the fluid poured into the back. The plunger was returned to the back of the syringe and inverted such that the fluid flowed to plunger with the air above. Then the excess air was dispensed. It is important to remove the air to avoid bubbles and causing inaccuracy in the flow rate as the syringe pump will compress any air trapped in the pump leading to additional unwanted forces and pressures. The syringe was loaded and the fluid dispensed at a flow rate of 5 mL/hr until the first droplet appeared at the end of the syringe. Then the fluid dispensing rate was set to 1 mL/hr for the measurement. For fast thinning processes this flow rate is slow enough that it does not affect the liquid bridge thinning. For slower thinning processes

(>5 s), the flow must be stopped before the droplet makes contact with the substrate. Upon stopping the syringe driving, the droplet continues to grow for a couple of seconds and it can be timed such that the flow is stopped and it contacts the substrate after the flow is stopped. The flow cannot be stopped during the thinning process because pressing the button causes vibrations throughout the setup. For each fluid, 5 experiments were performed (5 repeat droplets) and the thinning recorded.

4.6.3 Data processing

Video recordings were saved as .mov files on the iPhone by default. To perform the MatLab analysis, the videos were converted to individual frame-by-frame .tiff files. The conversion process require different software for each step as follows.

1. VLC media player (version 3.0.12) converts .mov to .mp4.[62]

In-built tools within the VLC media software was used to convert the .mov file to a .mp4 file.

2. FFmpeg (2021-04-04 build) converts .mp4 to .avi.[63]

In order to convert the .mp4 files to the uncompressed .tiff files, they were first converted to the .avi file format using FFmpeg using the following command line, “ffmpeg -i *filename*.mp4 -pix_fmt nv12 -f avi -vcodec rawvideo *filename*.avi”

3. ImageJ (version 1.52n) converts .avi to .tiff.[56]

The .avi files were then opened in ImageJ and saved as an “Image Sequence” to a dedicated folder for that video. This resulted in a folder of .tiff files showing the process frame-by-frame.

4. The .tiff files were processed in MatLab (version R2021a)[64] and the ‘canny edge’ detection system used to extract the evolution of filament diameter with time.

The filament radius was extracted at the half-way along the slender filament after it had formed. The pixels/mm value was calibrated for each experiment using the outer diameter of the 19G needle (1.27 mm) as a scale bar.

4.6.3.1 Data handling

Converting .mp4 videos into an uncompressed format resulted in the creation of very large files. For example, a single 4 s video at 240 fps would result in 960 frames which would require approximately 6 GB of storage space and also require a lot of time and computer power to analyse. Multiplying this be 3 – 5 measurements per fluid and then analysing multiple fluids, a large amount of storage and time is needed. The .avi and .tiff files are intermediate files between the raw .mov and the final filament radius vs time output and can be deleted to save storage space.

4.6.4 Data analysis

An analysis that has been previously applied to polymer solutions and worm-like micelle solutions was used to analyse the data.[19,46] The initial droplet contact and thinning is dominated by numerous factors including surface tension, viscosity and inertial forces. At later stages, a slender filament (where the height = 10x width), which subsequently thins and breaks. This process is called the elastocapillary regime, previously described by Entov and Hinch (equation 2, page 14).[65] The thinning of the slender filament is therefore fitted to an exponential decay to obtain the extensional relaxation time (λ_E). The fitting as performed in the Origin 2020 software using the "ExpDec1" equation which takes the form as shown in equation 4.

$$(4) \quad y = A1\ exp\left(-\frac{x}{t1}\right) + y0$$

ImageJ was used to analyse the frames and determine when the slender filament formed.

Surface tension measurements were not accessible during this work meaning that G_E could not be calculated.

5 References

1 E. R. Draper, H. Su, C. Brasnett, R. J. Poole, S. Rogers, H. Cui, A. Seddon and D. J. Adams, *Angew. Chem. - Int. Ed.*, 2017, **56**, 10467–10470.

2 K. McAulay, P. A. Ucha, H. Wang, A. M. Fuentes-Caparrós, L. Thomson, O. Maklad, N. Khunti, N. Cowieson, M. Wallace, H. Cui, R. J. Poole, A. Seddon and D. J. Adams, *Chem. Commun.*, 2020, **56**, 4094–4097.

3 J. P. Wojciechowski, A. D. Martin, E. Y. Du, C. J. Garvey, R. E. Nordon and P. Thordarson, *Nanoscale*, 2020, **12**, 8262–8267.

4 C. Colquhoun, E. R. Draper, R. Schweins, M. Marcello, D. Vadukul, L. C. Serpell and D. J. Adams, *Soft Matter*, 2017, **13**, 1914–1919.

5 A. Dawn and H. Kumari, *Chem. Eur. J.*, 2018, **24**, 762–776.

6 K. W. K. Tong, S. Dehn, J. E. A. Webb, K. Nakamura, F. Braet and P. Thordarson, *Langmuir*, 2009, **25**, 8586–8592.

7 S. Zhang, M. A. Greenfield, A. Mata, L. C. Palmer, R. Bitton, J. R. Mantei, C. Aparicio, M. O. De La Cruz and S. I. Stupp, *Nat. Mater.*, 2010, **9**, 594–601.

8 E. R. Draper, O. O. Mykhaylyk and D. J. Adams, *Chem. Commun.*, 2016, **52**, 6934–6937.

9 E. R. Draper, M. Wallace, R. Schweins, R. J. Poole and D. J. Adams, *Langmuir*, 2017, **33**, 2387–2395.

10 V. Evageliou, *Int. J. Food Sci. Technol.*, 2020, **55**, 1853–1861.

11 S. Perticaroli, B. Mostofian, G. Ehlers, J. C. Neuefeind, S. O. Diallo, C. B. Stanley, L. Daemen, T. Egami, J. Katsaras, X. Cheng and J. D. Nickels, *Phys. Chem. Chem. Phys.*, 2017, **19**, 25859–25869.

12 H. A. Barnes, *Colloids Surf. A: Physicochem. Eng. Asp.*, 1994, **91**, 89–95.

13 C. J. S. Petrie, *J. Nonnewton. Fluid Mech.*, 2006, **137**, 15–23.

14 J. W. Goodwin and R. W. Hughes, *Rheology for Chemists An Introduction*, The Royal Society of Chemistry, Cambridge, 2000.

15 J. W. Goodwin and R. W. Hughes, in *Rheology for Chemists An Introduction*, The Royal Society of Chemistry, Cambridge, 1st edn., 2000, p. 272.

16 C. J. S. Petrie, *J. Nonnewton. Fluid Mech.*, 2006, **137**, 1–14.

17 C. J. S. Petrie, in *Advances in the Flow and Rheology of Non-Newtonian Fluids*, eds. D. A. Siginer, D. De Kee and R. P. Chhabra, 1999, pp. 613–636.

18 F. T. Trouton, *Proc. Roy. Soc. A*, 1906, **77**, 426–440.

19 R. Omidvar, S. Wu and H. Mohammadigoushki, *J. Rheol. (N. Y. N. Y).*, 2019, **63**, 33–44.

20 L. Campo-Deaño and C. Clasen, *J. Nonnewton. Fluid Mech.*, 2010, **165**, 1688–1699.

21 G. H. McKinley, *Rheol. Rev.*, 2005, **3**, 1–48.

22 C.-H. H. Ng and R. J. Poole, *Meas. Sci. Technol.*, , DOI:10.1088/1361-6501/abeea8.

23 H. Münstedt, *Int. Polym. Process.*, 2018, **33**, 594–618.

24 D. Kiriya, R. Kawano, H. Onoe and S. Takeuchi, *Angew. Chem. - Int. Ed.*, 2012, **51**, 7942–7947.

25 A. Koeppel, N. Stehling, C. Rodenburg and C. Holland, *Adv. Funct. Mater.*, 2021, DOI:10.1002/adfm.202103295.

26 Z. Starý, M. Papp and T. Burghelea, *J. Nonnewton. Fluid Mech.*, 2015, **219**, 35–49.

27 M. L. Sentmanat, *Rheol. Acta*, 2004, **43**, 657–669.

28 E. L. Cabarcos, R. K. Bayer, H. G. Zachmann, F. J. B. Calleja and W. Meins, *Polym. Eng. Sci.*, 1989, **29**, 193–201.

29 R. Arrigo, G. Malucelli and F. P. La Mantia, *Polymers (Basel).*, 2021, **13**, 1–35.

30 H. Münstedt and F. R. Schwarzl, in *Deformation and Flow of Polymeric Materials*, Springer, Berlin, Heidelberg, 1st edn., 2014, p. 408.

31 K. Koyama and O. Ishizuka, *J. Polym. Sci. Part B Polym. Phys.*, 1989, **27**, 297–306.

32 T. Yaoita, T. Isaki, Y. Masubuchi, H. Watanabe, G. Ianniruberto and G. Marrucci, *Macromolecules*, 2012, **45**, 2773–2782.

33 M. Battisti, L. Perko, S. Arunachalam, S. Stieger and W. Friesenbichler, *Polym. Eng. Sci.*, 2018, **58**, 3–12.

34 T. Vad, J. Wulfhorst, T. T. Pan, W. Steinmann, S. Dabringhaus, M. Beckers, G. Seide, T. Gries, W. F. C. Sager, M. Heidelmann and T. E. Weirich, *Macromolecules*, 2013, **46**, 5604–5613.

35 D. N. Rockwood, R. C. Preda, T. Yücel, X. Wang, M. L. Lovett and D. L. Kaplan, *Nat. Protoc.*, 2011, **6**, 1612–1631.

36 A. Koeppel, P. R. Laity and C. Holland, *Soft Matter*, 2018, **14**, 8838–8845.

37 Y. Yang, X. Liu, D. Wei, M. Zhong, J. Sun, L. Guo, H. Fan and X. Zhang, *Biofabrication*, 2017, **9**, 45009.

38 V. Calabrese, S. J. Haward and A. Q. Shen, *Macromolecules*, 2021, **54**, 4176–4185.

39 J. Pérez-Rigueiro, R. Madurga, A. M. Gañán-Calvo, G. R. Plaza, M. Elices, P. A. López, R. Daza, D. González-Nieto and G. V. Guinea, *Biomimetics*, , DOI:10.3390/biomimetics3040029.

40 A. Kamada, A. Levin, Z. Toprakcioglu, Y. Shen, V. Lutz-Bueno, K. N. Baumann, P. Mohammadi, M. B. Linder, R. Mezzenga and T. P. J. Knowles, *Small*, 2020, **16**, 1–8.

41 T. Christoff-Tempesta, Y. Cho, D.-Y. Kim, M. Geri, G. Lamour, A. J. Lew, X. Zuo, W. R. Lindemann and J. H. Ortony, *Nat. Nanotechnol.*, 2021, **16**, 447–454.

42 G. H. McKinley, O. Brauner and M. Yao, *Korea-Australia Rheol. J.*, 2001, **13**, 29–35.

43 F. J. Galindo-Rosales, M. A. Alves and M. S. N. Oliveira, *Microfluid. Nanofluidics*, 2013, **14**, 1–19.

44 J. Dinic, Y. Zhang, L. N. Jimenez and V. Sharma, *ACS Macro Lett.*, 2015, **4**, 804–808.

45 Y. Christanti and L. M. Walker, *J. Rheol. (N. Y. N. Y).*, 2002, **46**, 733–748.

46 J. Dinic, L. N. Jimenez and V. Sharma, *Lab Chip*, 2017, **17**, 460–473.

47 A. L. Kwiatkowski, V. S. Molchanov and O. E. Philippova, *Polym. Sci. - Ser. A*, 2019, **61**, 215–225.

48 K. D. Danov, P. A. Kralchevsky, S. D. Stoyanov, J. L. Cook, I. P. Stott and E. G. Pelan, *Adv. Colloid Interface Sci.*, 2018, **256**, 1–22.

49 C. A. Dreiss, *Soft Matter*, 2007, **3**, 956–970.

50 R. G. Larson, *The Structure and Rheology of Complex Fluids*, Oxford University Press, New York, 1999.

51 H. Rehage and H. Hoffman, *Mol. Phys.*, 1991, **74**, 933–973.

52 J. P. Rothstein and H. Mohammadigoushki, *J. Nonnewton. Fluid Mech.*, 2020, DOI:10.1016/j.jnnfm.2020.104382.

53 E. R. Draper, J. J. Walsh, T. O. McDonald, M. A. Zwijnenburg, P. J. Cameron, A. J.

Cowan and D. J. Adams, *J. Mater. Chem. C*, 2014, **2**, 5570–5575.

54 E. R. Draper, L. J. Archibald, M. C. Nolan, R. Schweins, M. A. Zwijnenburg, S. Sproules and D. J. Adams, *Chem. - A Eur. J.*, 2018, **24**, 4006–4010.

55 J. G. Egan, G. Brodie, D. McDowall, A. J. Smith, C. J. C. Edwards-Gayle and E. R. Draper, *Mater. Adv.*, 2021, **2**, 5248–5253.

56 ImageJ, https://imagej.net/Welcome, (accessed 20 October 2019).

57 D. R. Lide and W. M. Haynes, Eds., *CRC Handbook of Chemistry and Physics*, CRC Press, Boca Raton, 90th edn., 2010.

58 M. C. Nolan, A. M. Fuentes Caparrós, B. Dietrich, M. Barrow, E. R. Cross, M. Bleuel, S. M. King and D. J. Adams, *Soft Matter*, 2017, **13**, 8426–8432.

59 M. J. Farooqi, M. A. Penick, J. Burch, G. R. Negrete and L. Brancaleon, *Spectrochim. Acta - Part A Mol. Biomol. Spectrosc.*, 2016, **153**, 124–131.

60 L. Chen, K. Morris, A. Laybourn, D. Elias, M. R. Hicks, A. Rodger, L. Serpell and D. J. Adams, *Langmuir*, 2010, **26**, 5232–5242.

61 D. McDowall, M. Walker, M. Vassalli, M. Cantini, N. Khunti, C. J. C. Edwards-Gayle, N. Cowieson and D. J. Adams, *Chem. Commun.*, 2021, **57**, 8782–8785.

62 VLC Media Player, https://www.videolan.org/vlc/, (accessed 15 April 2021).

63 FFmpeg, https://ffmpeg.org/, (accessed 16 April 2021).

64 MATLAB, https://uk.mathworks.com/products/matlab.html, (accessed 27 April 2021).

65 V. M. Entov and E. J. Hinch, *J. Nonnewton. Fluid Mech.*, 1997, **72**, 31–53.

Chapter 5

Conclusions

1 Conclusions

The overriding theme of this work is controlling the self-assembled structures and alignment of those structures to modulate activity. Conventionally, the molecular structure determines the properties of a material. As such, there is significant research interest in synthesising new chemicals to obtain a desired effect. In this work, while chemical structure is important, the exact nature of the self-assembled structures determine the photocatalytic activity of a set of five perylene bisimides (PBIs). The formation of one-dimensional (1D) nanofibres with a specific molecular packing and surface charge were required for optimum photocatalysis. What defines the material properties is complex, where desired activities can also be achieved through changing the self-assembly as opposed to the chemical structure.

As well as changing the self-assembled structures, the orientation of those 1D structures can be controlled. For materials that self-assemble into 1D structures (such as nanofibres), these structures typically adopt a random orientation due to Brownian motion. An interesting question is, how would nanofibre alignment influence activity? This can be achieved through the formation of gel filaments (or so-called ‘noodles’). A functionalised dipeptide was studied as a model system and gel noodles formed only when 1D structures were present, resulting in viscous shear-thinning pre-gel solutions. Gel noodles with both aligned and unaligned nanostructures could be readily prepared.

For a specific PBI, the pre-gel solution at pH 6 resulted in a highly viscous shear thinning solution that could also be used to form aligned gel noodles. Unaligned noodles could also be formed by modifying the preparative method, allowing for photocatalysis to be performed on samples with the two different alignments. The photocatalysis study showed small levels of activity but differences in sample morphology meant that the results were inconclusive.

In trying to expand the study to a third system with better alignment, a spinning technique that worked well for the functionalised dipeptide was used but was unsuccessful for the PBI. The functionalised dipeptide and PBI solutions possessed very similar shear viscosities but behaved very differently when spun. The spinning technique imposed an extensional deformation on the pre-gel solution, resulting in thin well-aligned gel noodles. It was hypothesised that the difference in extensional viscosity between the two fluids determined whether or not the spinning technique was successful. A setup to perform these measurements was created and showed that while the functionalised dipeptide behaved as an elastic fluid with long extensional relaxation times, the PBI did not. This highlights that while two fluids form worm-like micelle solutions and possess similar shear viscosities, a wide range of techniques are required to fully characterise them and draw out differences.

In summary, this work highlights the importance of the self-assembly process and the variables that influence it in achieving specific functionality with any given low molecular weight gelator. This demonstrates that low molecular weight gels are highly versatile materials, but the structure-activity relationship can often be complex, where a wide range of measurement techniques are required. For example, in Chapter 2 very specific self-assembled structures are needed to achieve optimum photocatalysis. To characterise these differences, a range of measurements techniques were required. This should provide an example to other researchers that specific and sometimes seemingly irrelevant variables (e.g. subtle pH changes) are important. There may be many low molecular weight gelators for which certain, highly active, self-assembled structure regimes have been missed. This research also represents a first (to the best of our knowledge) for the application of the dripping-onto-substrate technique to measure the extensional flow properties of pre-gel solutions in this field. The results highlight that shear viscosity and extensional viscosity are two very different parameters and the consequences of this determine whether or not well-aligned gel filaments can be formed. Other researchers should consider performing a wide range of measurements to fully understand the structure-activity relationship of any given low molecule weight gelator.